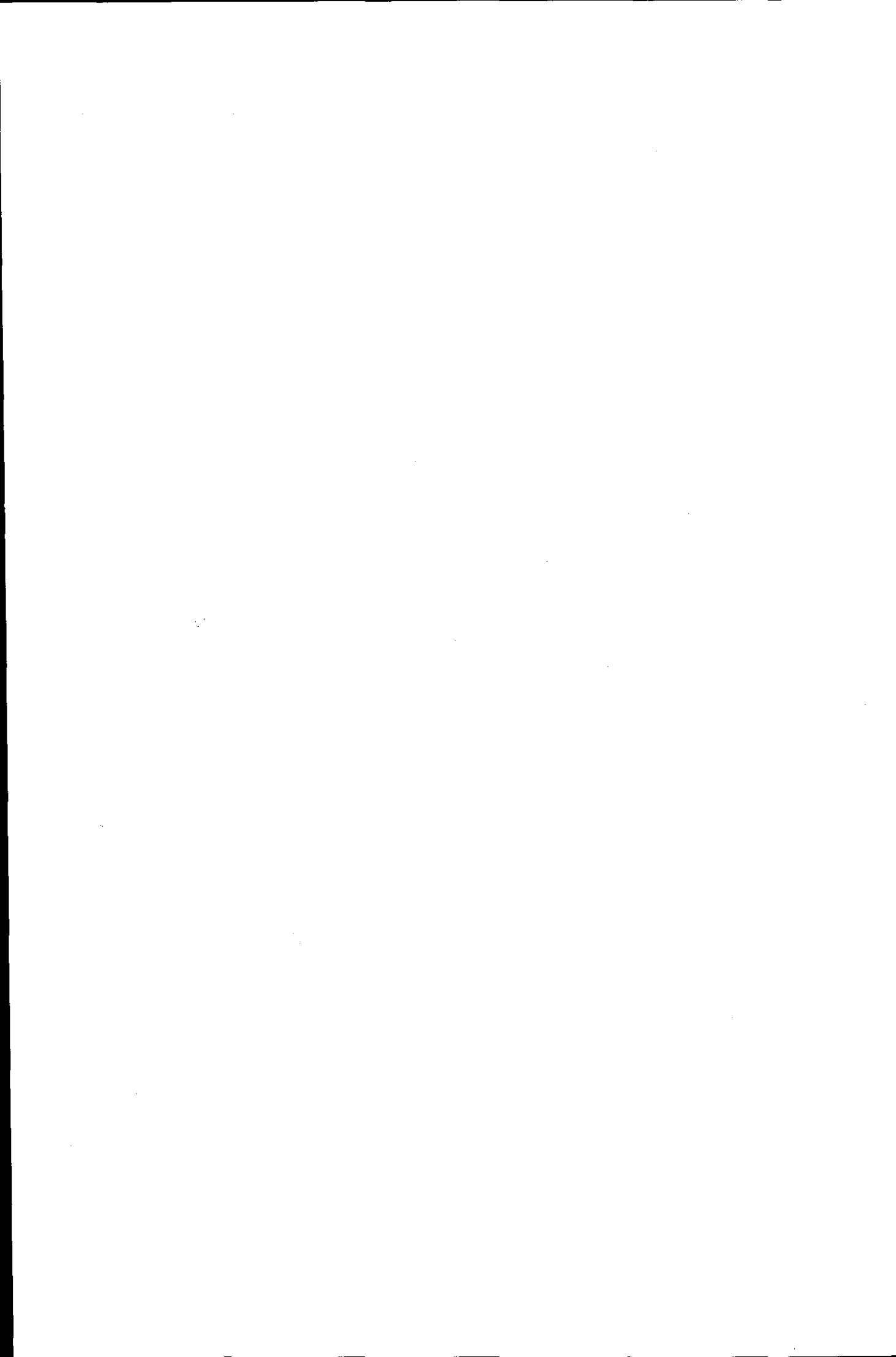# BRITISH THESIS SERVICE

DX233012

Awarding Body : **Loughborough**

Thesis By : **BALAKRISHNAN Sashi**

Thesis Title : **TRANSIENT ELASTOHYDRODYNAMIC ANALYSIS OF PISTON SKIRT LUBRICATED CONTACT UNDER COMBINED AXIAL LATERAL AND TILTING MOTION**

We have assigned this thesis the number given at the top of this sheet.

THE BRITISH LIBRARY
DOCUMENT SUPPLY CENTRE

Transient Elastohydrodynamic Analysis of Piston Skirt Lubricated Contact Under Combined Axial, Lateral and Tilting Motion

By
Sashi Balakrishnan

A Doctoral Thesis

Submitted in partial fulfillment of the requirements for the award of Doctor of Philosophy of Loughborough University

October 2002

ABSTRACT

Most modern engines utilise pistons with an offset gudgeon pin. In internal combustion engines, the offset is to the major thrust side of the piston. The piston thrust side is the part of the piston perpendicular to the gudgeon pin that carries the majority of side loading during the power stroke. Primary reason for having the gudgeon pin positioned eccentrically is to prevent the piston from slamming into the cylinder bore after the connecting rod journal passes the top dead centre. This phenomenon is referred to as piston slap, and is more pronounced in compression ignition and high performance engines due to higher combustion pressure than that of commercial spark ignition engines. The coming together of the piston and the bore results in scuffing, at best, or, catastrophic failure at worst. Clearance space between bore and piston is filled by a lubricant film. The main role of the lubricant is to separate the piston and bore by reacting to the applied load.

Investigating the above problem requires a holistic approach, whereby a dynamic three degree-of-freedom piston model is coupled with a lubrication model to represent the actual system. The dynamic model determines the motion of the piston in combined axial, lateral and rotation about the gudgeon pin. The reactive forces due to lubricant films on the major and minor thrust sides of the piston play significant roles in piston dynamics and are evaluated by either quasi-static or transient solution of the lubricant contact conjunctions.

The novel quasi-static analysis is carried out in the sense of its detailed approach, including many key practical features not incorporated in other analyses, hitherto reported in literature. These features include first and foremost the development of a specific contact mechanics model for evaluation of conforming contacts for piston skirt against liner or bore. The quasi-static analysis includes many practical feature not encountered in other literature on the subject, such as detailed surface irregularities and

modification features, and with thermal distortion. The analysis has been extended to thermohydrodynamics, as well as micro-hydrodynamics, all with high computational mesh densities, and robust methods of solution in space and time domains, including effective influence Newton-Raphson method and linear acceleration integration scheme.

The transient tribo-elasto-multi-body dynamics problem includes physics of motion study from film thickness prediction and secondary motion evaluation of the order of micrometers and minutes of arc to large rigid body dynamics, including simultaneous solution of the contact problem at both major and minor thrust sides. Such a comprehensive solution has not hitherto been reported in literature.

The thesis discusses many aspects of piston dynamics problem, through the broad spectrum of vehicle manufacture, with many pertinent practical engineering issues. In particular, it provides solutions for high performance Formula 1 racing engines. This is the first ever comprehensive analysis of piston tribodynamics for this range of engines at very high combustion pressures.

This study has shown the paramount influence of profile of piston in promoting lubrication between the contiguous bodies, as evident from the pattern of lubricant flow through the contact. Deformation of the bodies increases the volume of lubricant in the contact. During the reversal in direction of piston motion, when the entraining velocity momentarily cases and reversal takes place, the load is held by an elastic squeeze film.

Keywords: Conformal contact, piston secondary motions, Transient tribodynamics of piston assembly, squeeze film action, inlet boundary reversal.

Acknowledgement

I would like to express my gratitude to Dr. H. Rahnejat, for his invaluable advice, encouragement and understanding. I would also like to thanks to my parents for their deeply support

Finally, I would like to thank all my friends, for their help and support.

Contents

Chapter 1: Introduction

Chapter 2: Literature Survey

Chapter 3: Multi-body Dynamics of IC Engines

Chapter 4: Piston Lubrication

Chapter 5: Quasi-Static Analysis

Chapter 6:Transient Tribodynamics of piston skirt to Liner Contact

Chapter 7: Conclusion

Reference

Nomenclature: Chapter 3

a	height measured from centre of gudgeon to piston crown (m)
b	height of the centre of mass of piston measured from piston crown (m)
C_g	offset of centre of mass measured along the z-axis from gudgeon (m)
C_p	offset of gudgeon pin from centre line (m)
e_b	lateral displacement of lower end of the piston skirt (N)
e_l	lateral displacement of gudgeon pin (m)
e_t	lateral displacement of upper end of the piston skirt (m)
f_{con}	connecting rod force (N)
f_g	gas force (N)
f_{gg}	inertial force of gudgeon due to primary motion (N)
f_{gp}	inertial force of piston due to primary motion (N)
f_{ig}	inertial force of gudgeon due to secondary motion (N)
f_{ip}	inertial force of piston due to secondary (N)
f_{r1}	reaction due to lubricant at major thrust side (N)
f_{r2}	reaction due to lubricant at minor thrust side (N)
I_p	piston inertia about its centre of mass $(kg.m^2)$
m_g	mass of gudgeon pin (kg)
m_p	mass of gudgeon pin (kg)

m_{fr1}, m_{fr1}	hydrodynamic reaction moments, (Nm)
p_l	piston length, (m)
t	time, (s)
β	tilt of piston, (rad)
ϕ	conrod angle, (rad)
θ	crank angle (rad)
$\dot{\theta}$	crank angular velocity (rad/s)
$\ddot{\theta}$	crank angular acceleration $\left(rad/s^2\right)$

Nomenclature: Chapter 4

a	Half-length of piston circumference πR_p, (m)
b	Half-length of piston, $0.5\,P_l$, (m)
$\tilde{a}, \tilde{b}$	Computational domain, (m)
c_p	Constant, 1.96×10^8, $\left(N\!/_{m^2}\right)$
x, y, z	Cartesian Coordinates
w'	Applied load per unit length, $\left(N\!/_{m}\right)$
p	Applied pressure, $\left(N\!/_{m^2}\right)$
p_l	Piston length, (m)
r_{bx}	bore radius in the inlet direction, (m)
r_{by}	Circumferential radius of bore, (m)
r_{px}	Barrel radius of piston, (m)
r_{py}	Circumferential radius of piston, (m)
E	Modulus of elasticity, $\left(N\!/_{m^2}\right)$
G_s	Shear modulus of elasticity, $\left(N\!/_{m^2}\right)$
Z_1	viscosity pressure index (dimensionless constant)
$\overline{h}$	Non-dimensional film

$\bar{P}$ Non-dimensional pressure

δ Elastic deformation, (m)

γ Second derivative of viscosity $\left(Pa\,s^2\right)$

η_0 absolute viscosity at $p = 0$ and a constant temperature, $\left(Pa\,s\right)$

η_k kinematic viscosity, $\left(mm^2\!\!\diagup_s\right)$

η dynamic viscosity, $\left(Pa\,s\right)$

η_∞ Constant, 6.31×10^{-5} $\left(Pa\,s\right)$

σ Normal stress component, $\left(N\!\!\diagup_{m^2}\right)$

ν Poisson Ratio

τ Shear Stress, $\left(N\!\!\diagup_{m^2}\right)$

ξ pressure-viscosity coefficient of lubricant dependent on temperature

$\bar{\rho}$ Non-dimensional density

$\bar{\eta}$ Non-dimensional viscosity

$\wp$ Thermo-viscous constant

List of Figures

Chapter 1

Chapter 2

Chapter 3

Chapter 4

Chapter 5

Chapter 6

List of Tables

Chapter 3

Chapter 1

1.1- Introduction: Addressing the Automotive Industry's Concerns

Faced with stringent Government regulations (**EPA** (2002)), be it regarding safety or environmental concern, the automotive industry is striving to make their product as environmentally sustainable as possible while keeping it competitive to private and fleet customers, both in terms of price and performance specifications. Vehicle manufacturers face constant pressure to comply with ever tightening of legislations regarding NOx and noise emission, from governmental agencies. With ever increasing sale of vehicles in Western Europe, as shown in figure 1.1, the European Commission drafted series of legislations, the *Euro*, to curtail NOx emission by automobiles.
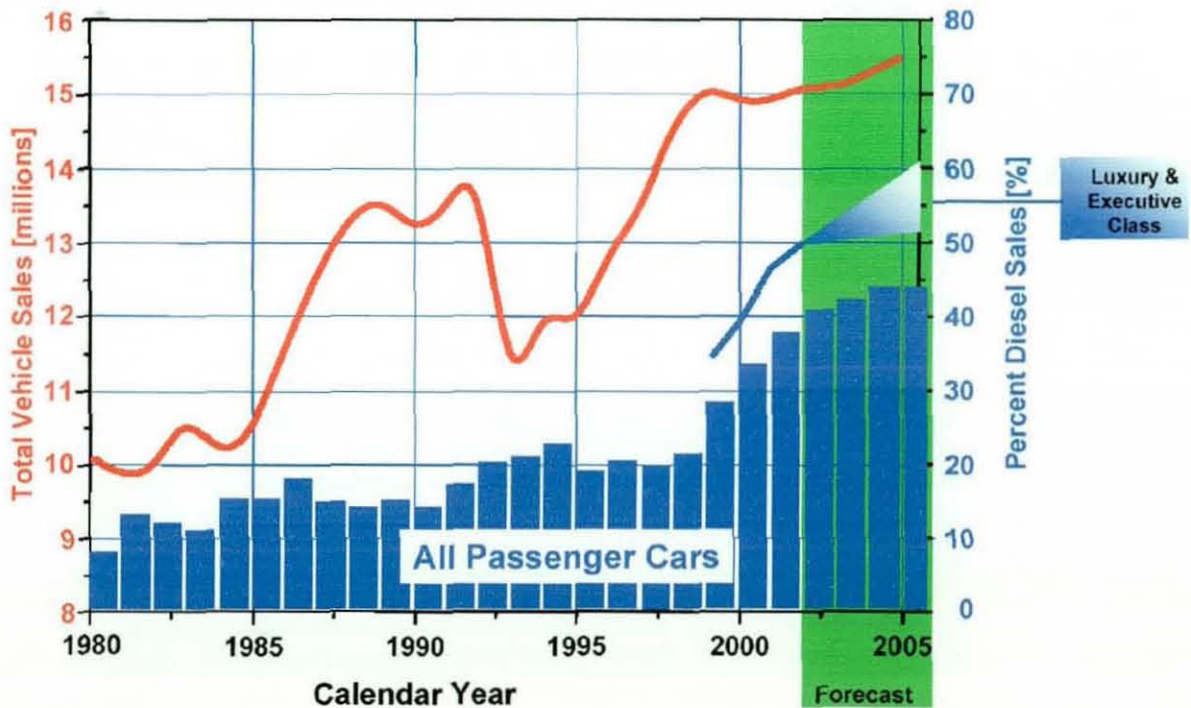
Figure 1.1: Sales volume of new cars in Western Europe (taken from source:
Hofbauer(2002))

The forth-coming target, *Euro* 4, sets the level of acceptable particulate emission, at or below 0.025 g/km. Currently, this target is beyond the reach of many manufacturers (indicated by coloured dots in figure 1.2). Although this may seem like an out of reach target thrown at engineers, figure 1.2 does suggest a path forward in the right direction to achieve the required reduction in particulate emission by 2005 and for the future. Advanced combustion technique in both gasoline and diesel engines has shown marked reduction in harmful exhaust emission. Homogenously charged compressed ignition (*HCCI*) diesel engines and gasoline direct injection (*GDI*) combustion, ensure more complete combustion process, thereby, reducing particulate emission. Combined with new fuel delivery to the combustion chamber (such as common-rail direct injection (*CDI*)), the diesel engine indicates a strong potential to fulfil the stringent level requirements in the future.
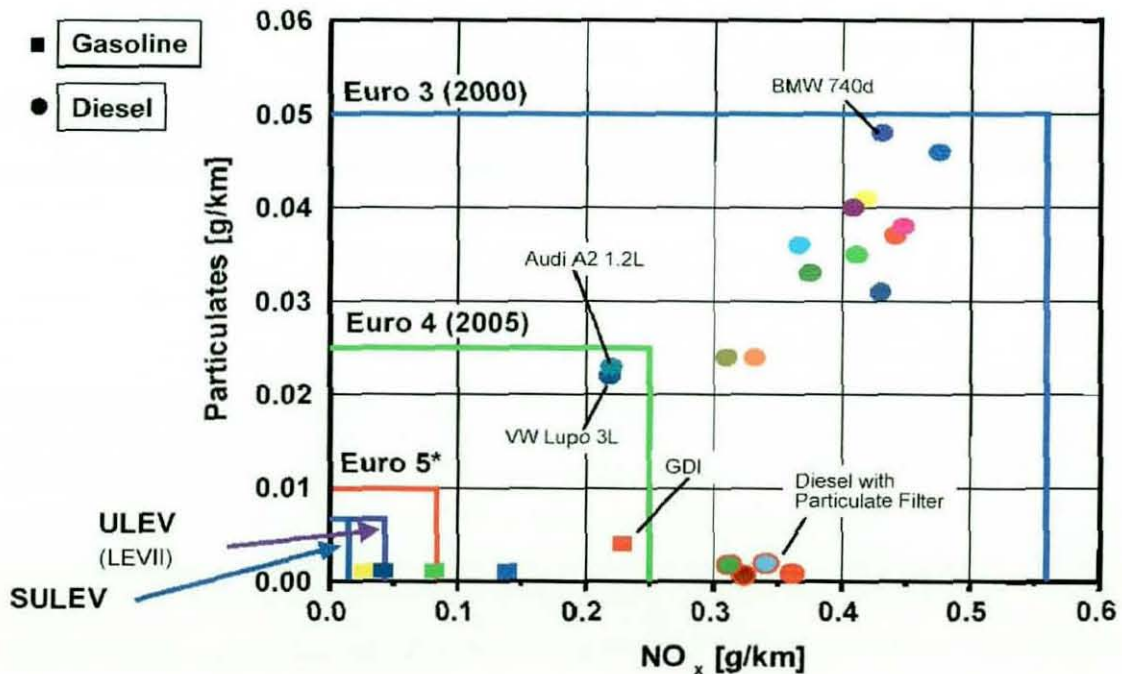
Figure 1.2: Current particulate emission level of vehicles (taken from source: **Hofbauer** (2002))

Aided by the Government incentives in the form of tax relief for small displacement engines (**DVLA** (2001)) and new and cleaner diesel vehicles, sales volume of diesel

2

vehicles is clearly on the rise (*UK Economic & Market Report* (2002) and also see figure 1.1). In the past, diesel engines were unrefined, sluggish and environmentally unfriendly. This is no longer true. Modern diesel engines are powerful, smooth and very refined, so much so that it has been introduced as an alternative engine in the line-up of flagship models. This segment of luxury cars were dominated by large displacement gasoline/petrol engines. Attention paid to improve the performance and refinement of diesel engines has yielded some positive outcomes. The new generation diesel engines are as refined, as quiet (see figure 1.3) and as powerful as their gasoline counterpart (eg. Ford, VW, Toyota to name a few). A typical example of such an engine, is the soon to enter production, Mercedes-Benz 4.0 litres V-8 engine developing 238bhp and boasts a maximum torque of 560Nm available from just 1800rpm, meanwhile being able of covering 100km with just 9 litres of diesel fuel (**Mercedes** (2002)). This is achieved by integrating a common-rail direct injection system, coupled with a twin-turbo system with electrically adjustable guide vanes, water charge-air cooling and four-valve-per cylinder technology.
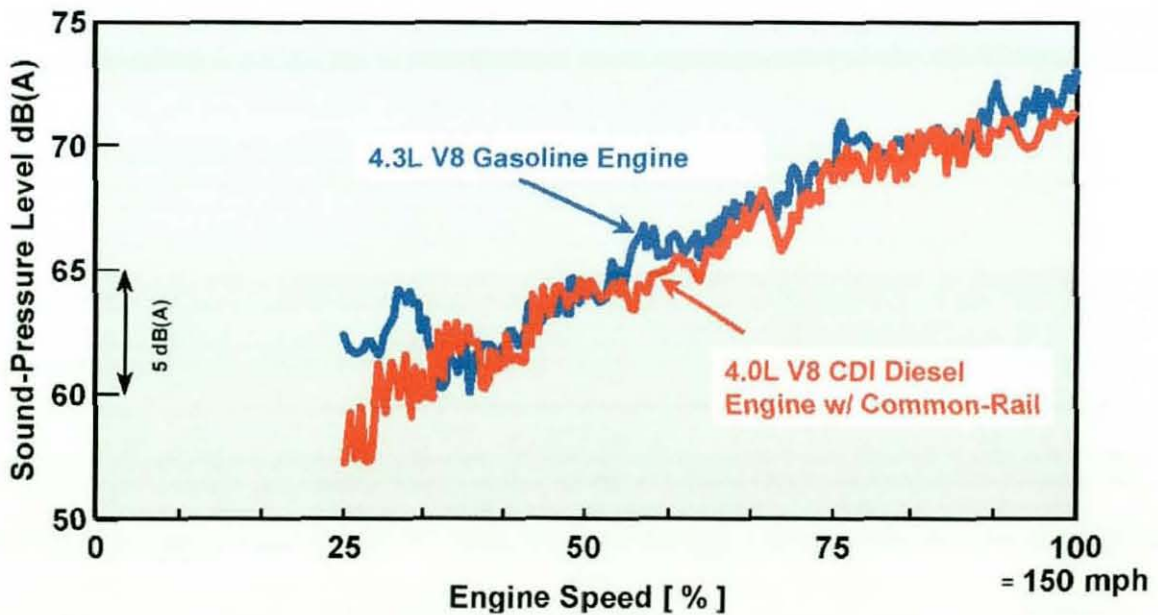
Figure 1.3: Noise in cabin from that of a large displacement diesel engine compared to that of a large displacement gasoline engine measured at speed of 150 mph (taken from source: **Hofbauer** (2002))

The gasoline counterpart engine, a 5 litres V-8, however, boasts a higher output power of 302 bhp, but a lower peak torque value of 460Nm at 2700rpm and consumes 13.9 litres of fuel to cover the same 100km. The above-mentioned specification comparison is typical feature of diesel and gasoline engines of large and small displacement type.

Along with Mercedes-Benz, pioneers in large displacement diesel engine in luxury and sports cars and BMW (4.0 litres V-8), Volkswagen has recently built a state-of-the-art, compact, powerful and frugal 4 litres V-10 diesel variant (shown in figure 1.4) for its flagship line-up, the Phaeton (VW (2002)). Involvement of such large volume car manufacturer is promising news. With technology transfer from higher line-up production model to lower line-up, such technology is bound to be introduced to large volume production diesel cars.
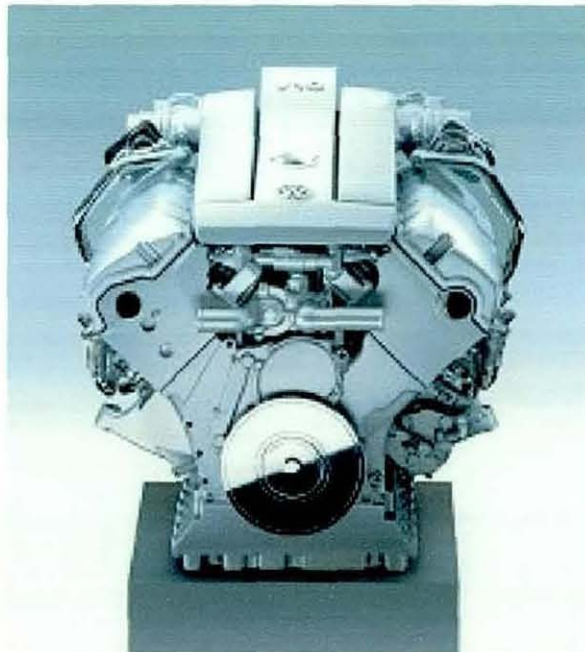
Figure 1.4: New generation, low emission CDI common-rail diesel engine (taken from source: **Volkswagen** (2002))

As far as product quality and improvement is concerned, the automotive industry has come a long way since the era of Ford's Model T, first launched in 1908 (**Inventors (2002)**). At the same time, an average motorist's expectations and demands (**Visteon (2000)**) have equally risen for a more refined and luxurious car. Therefore, a modern car, compared to its predecessor, has much higher level of equipment, better ride and handling, better overall built quality, improved safety features, both active and passive. Active research and development carried out in the automotive field also means that all the above-mentioned aspects have been dramatically improved. Above-mentioned points seem to reflect a positive trend in the heading of the industry, but with the penalty of weight increase with each new model. Therefore, the improvements made to reduce the particulate emission level seem to be offset by an increase in weight. Overall, all the pointers lead the automotive manufacturers to justify investment for further development of diesel engines of the future (**Taylor (1998)**).

1.2 Improving Engine Performance

Thermal losses within the internal combustion engine, as identified by **Andersson** (1991), account for 60-65% of all losses in an engine (see figure 1.5). From the remaining 35-40%, approximately 15% of the energy is dissipated as mechanical losses by all the articulating inertial members within the internal combustion engine, piston assembly, journal and big end bearings, valve train, ancillaries and transmission. Piston assembly accounts for a sizeable proportion of the 15%, making it a suitable target for researchers in trying to improve engine power output. The use of stiffer and lighter engine components has resulted in considerable engine improvement due to a reduction in inertia of reciprocating components (**March** and **Croker** (1998)).

1.3 Investigating the Diesel Engine

In a four stroke internal combustion engine, the forcing frequency is the cyclic firing of the various pistons. The forcing frequency is, therefore, the half engine rotational frequency in such an engine, since all the cylinders fire every 720° rotation of the

crankshaft. Therefore, the signature of the vibration of the system contains the fundamental forcing frequency at half-engine order and all its multiples (**Bremer** (1979)). This is commonly referred to as engine "roughness", which dominates the noise and vibration spectra of modern vehicle engines. Pistons are one of such afore-mentioned component, constructed from light-weight aluminium alloys. Since combustion pressures in a compression ignition engine is higher than that in spark ignition engines, (see figure 3.3) engine components of the latter undergoes higher levels of stress. As discussed in the previous section, most of the mechanical losses in piston assembly is attributed to frictional losses, generated by the piston skirt and piston ring pack, interacting with the cylinder liner or bore.
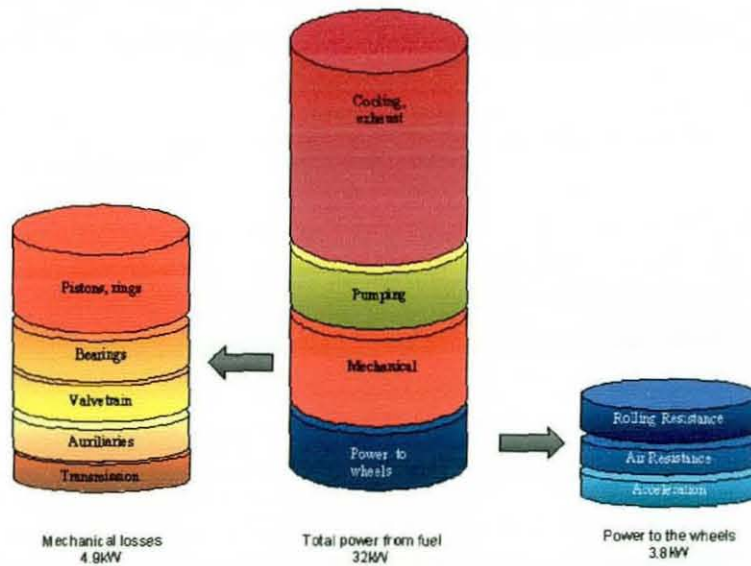
Figure 1.5: Frictional losses in an internal combustion engine simulating urban driving, as measured by **Anderson** (1991)

As piston assembly accounts for a sizeable proportion of mechanical and frictional losses in internal combustion engines (IC), it is essential to undertake remedial actions in order to minimise these. There are a number of key motivations in development of new IC engines. These are:

- Better fuel efficiency and lower emission through reduction of frictional losses.

- Enhanced combustion strategies that produce higher BMEP and lower NOx output.

- Reduced inertial dynamics in order to lessen Noise, Vibration and Harshness (NVH) signature of the engine. This less resulted from the use of light-weight, but durable materials with good structural integrity.

- Decreased package space requirement for engine installation.

Therefore, the role of lubricant in separating these two contiguous bodies is critical to an engine, to avoid catastrophic failure. Owing to this, much research has been carried out in understanding tribo-dynamics of piston (**Knoll** and **Peeken** (1982), **Oh** *et al* (1987) , **Liu** *et al* (1998)) and ring pack lubrication (**Dowson** *et al* (1983), **Ma** *et al* (1995a and 1995b), **Taylor** (1993)), including study of wear pattern (**Hartfield-Wünsch** *et al* (1993), **Brown** *et al* (1993) and **Graddage** *et al* (1993)) formed on piston skirt and inside the bore or cylinder liner. The clearance between reciprocating piston in the bore and the deformation of the former leads to the formation of a lubricant film and generation of hydrodynamic pressures in the contact conjunction (**Knoll** and **Peeken** (1982)).

Since the external load on a piston is mainly from the combustion pressure, the dynamics of the piston assembly governs the magnitude of clearance or gap available to be filled by lubricant. Therefore, to understand the piston lubrication, a study encompassing the lubrication condition of a deformable body under transient condition has to be carried out. In brief, a tribo-elasto-multi-body dynamics analysis of piston under transient condition has to be carried out, which is the theme of this thesis (**Boysal** and **Rahnejat** (1998)).

1.4- Aims and Objectives

As the title of the thesis suggests, the solution for the problem described above calls for an integration of dynamics of piston together with a conformal contact lubrication model in a simultaneous solution. Therefore, the first approach is to develop a module to replicate the three degrees of freedom of piston's reciprocating, tilting and transversal

motion within the confinement of the cylinder bore. A lubrication module has to be created, specifically for solving the Reynolds' equation for generated pressures and lubricant film shape and thickness. Both the individual models have to be verified to ensure the validity of the obtained results. Ideally, any comparison with experimentally measured data or observations matching the results obtained via the numerical analysis will further lend validity to the model. A suitable time-marching integration scheme would then have to be chosen to couple the two modules to simulate piston skirt lubrication under transient conditions. A suitable production diesel engine has to be identified to implement the numerical model, and possibly, extending the investigation to other engines, operating in extreme conditions. Along with the progress in achieving the targets mentioned above, the hope is to gain a greater understanding of the piston lubrication problem fundamentally.

1.5- Methods employed in investigating this problem

To achieve the above objectives the following steps were undertaken, in an integrated manner within this thesis:

- A numerical module, simulating three degrees of freedom, rigid-body-motion of a piston reciprocating in cylinder bore was developed using time integration scheme. This included the external combustion force.
- The above model was verified against a multi-body dynamics model developed in a commercial code.
- An elastohydrodynamic lubrication model of the conformal contact of two contiguous bodies was developed.
- Verification of the lubrication model was carried out to establish the validity of the results. The analysis was carried out for two different engines, first being a 1.8 litres production diesel engine and the other being a high performance racing engine.

- The lubrication module was coupled to the numerical piston model to investigate lubrication condition, of the aforementioned diesel engine, under combined squeezing, tilting and reciprocating action of the piston.

1.6- Structure of the Thesis

Thus far, background to general trend and concerns of automotive industry, its current interests and direction of developments (as far as engine lubrication is concerned), were highlighted in sections 1.1 to 1.3, thereby providing an impetus for undertaking this research, leading to the compilation of this thesis. The thesis is divided into seven chapters, beginning with the current chapter.

In chapter 2, a literature review of various aspects that have influenced the progress of the research is shown. In particular, it contains a survey of piston lubrication investigations, both in experimental and simulation studies. Comprehensive survey on elastohydrodynamic lubrication, the main context of this thesis, is also presented there.

Thorough analytical treatment of engine dynamics from basic principles, including the derivations of equations of motion for the three degree-of-freedom motion of piston assembly in Newton-Euler formulation is presented in chapter 3. This model was verified, using a commercially available multi-body dynamics code called *ADAMS* (acronym for Automated Dynamic Analysis of Mechanical Systems).

The theory of hydrodynamic lubrication and the derivation of Reynolds' equation from first principles, using Navier-Stokes and continuity of flow equation is expounded in chapter 4. Non-dimensionalisation and discretisation of Reynolds' equation, using finite difference method is explained there. The solution for pressures, utilising effective-influence Newton-Raphson method, solved simultaneously with the elastic film shape and load balance equations is also shown. The deflection of the piston skirt, from general theory of elasticity is illustrated. The method of solution for the piston elastohydrodynamics is detailed in chapter 4.

In chapter 5, results from quasi-static analysis of piston skirt lubrication at various positions (at top-dead-centre, combustion, mid-span where piston's translation velocity is the highest, and finally at the bottom-dead-centre), were presented and discussed. The module was adapted to replicate geometry of piston skirt to that of a high performance racing vehicle. These are also presented in chapter 5.

The two aforementioned modules were developed using the theories outlined in chapter 3 and chapter 4, were combined using *Newmark's* linear acceleration integration scheme (Newmark (1962)) to simulate the piston skirt lubrication under transient conditions for a diesel engine. The results obtained from the analysis are shown in chapter 6.

Chapter 7 outlines the overall conclusions of the research carried out under this project and which are included in this thesis. The aims of the research are revisited and the degree of achievement in this regard has been gauged. A critical assessment of the thesis has been carried out, including the underlying assumptions made in the different methods of analysis developed and used. Finally, chapter 7 proposes suggestions for future work to be carried out to extend the research and development findings contained in this thesis.

2. Literature Review

2.1 Introduction

Early known application of piston is said to be in pumps to raise water. Invented around 3rd century BC by a Greek named Ctesibius (**Technology Museum of Thessaloniki (2001)**), the pump exploited the successive suction and compression achieved in a pair of cylinders in order to raise fluids. In 1680, the French inventor Henri Papin (**Inventors (2002)**) developed the first model steam engine, a single-piston powered by the air pressure generated by expanding steam. The work done by the steam in displacing the piston vertically was, turned into a rotational motion by the connecting rod-crank assembly, essentially a crank slider mechanism. From thereon, the piston assembly has become an integral part of an engine in converting energy into motion. In figure 2.1, the piston-assembly of that in a modern high performance vehicle is shown.

Figure 2.1: Piston-conrod assembly components

2.2 Piston assembly components

The piston assembly (see figure 2.1) consists of the following components:

- piston
- connecting rod
- crank
- gudgeon pin
- compression rings
- oil control ring

Pistons are designed specifically to an engine, depending on its application. For example, three distinctive piston skirt profiles are shown in figure 2.2(a) and 2.2(b). The first piston skirt is that of a motorcycle engine and the second is that of a high performance engine. Notice the difference in the extent of the skirt in circumferential direction. In order to reduce inertia and friction, the pistons in an engine such as that in a Formula 1 (*F1*) racing car has less volume of material than that of a high performance road car (**Howell-Smith** (2002)). The pistons in a typical *F1* car survive for about 450km, before needing replacement (**Howell-Smith** (2002)), whereas in a road vehicle, this distance is significantly longer.

Figure 2.2(a): Piston skirt design variation according to application (shown on the left is a full skirt piston and on the right short skirt)
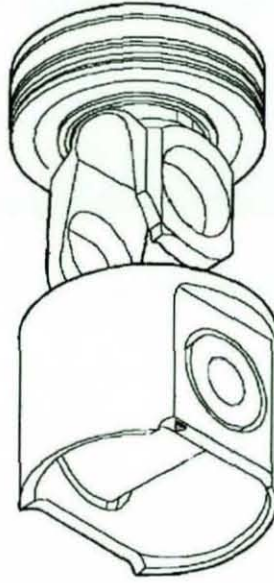
Figure 2.2(b): Articulated piston skirt design (taken from source Ricardo)

In figure 2.2(b), the piston skirt and crown are two separate parts, connected together by a gudgeon pin. Such pistons, also known as articulated pistons, are known to be used in large diesel engines such as tractors, excavators and trucks.

2.3 Secondary Dynamics of Piston Assembly

Most modern engines utilise pistons with an offset gudgeon pin. In internal combustion engines, the offset is to the major thrust side of the piston. The piston thrust side is the part of the piston perpendicular to the gudgeon pin that carries the majority of side loading during the power stroke. Primary reason for having the gudgeon pin positioned eccentrically is to prevent the piston from slamming into the cylinder bore after the connecting rod journal passes the top dead centre. This problem is referred to as piston slap. The aim of an ideal motion of piston with offset gudgeon pin is for the piston to gently rock from side to side within the bore, thereby eliminating slap (**Betts** (1997)).

13
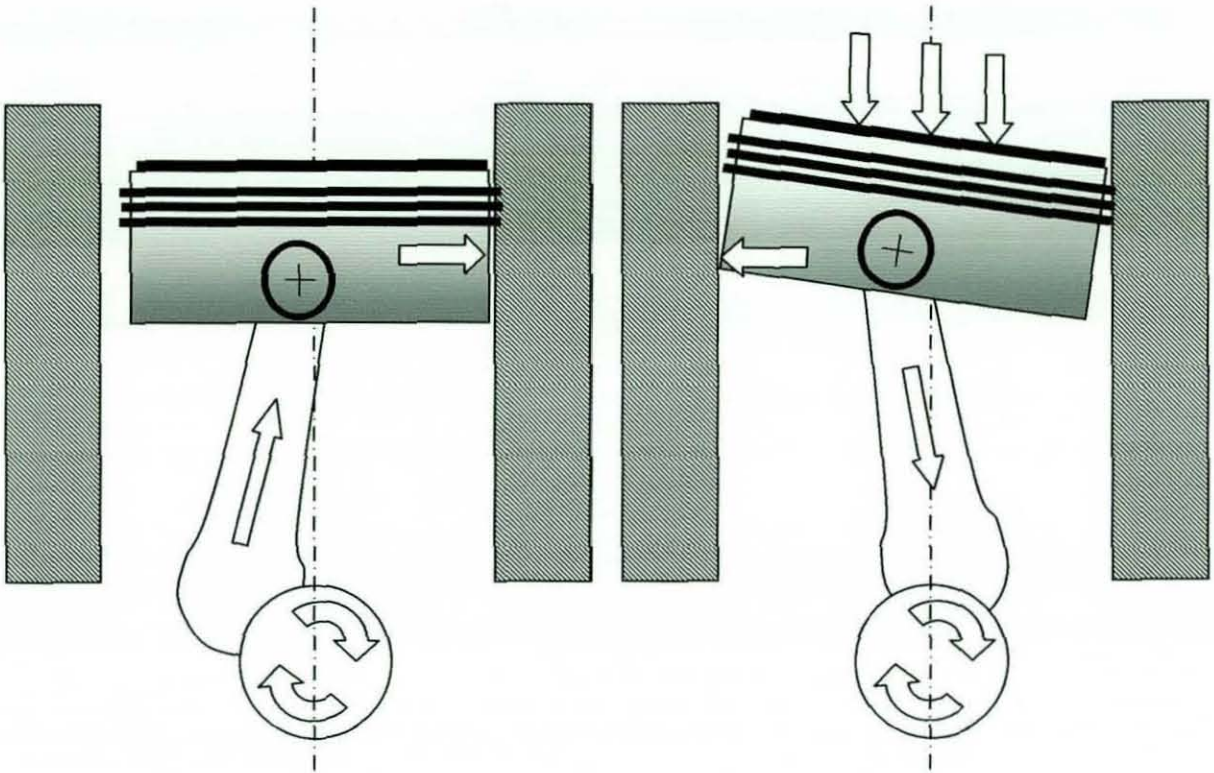
Figure 2.3 (a)   Figure 2.3 (b)

Figure 2.3(a) illustrates a piston travelling upwards into the cylinder during the compression stroke. In this illustration, the crank rotation is clockwise and the pin offset is to the major thrust side of the piston. It can be seen that the piston is being forced against the minor thrust side during this stroke.

In figure 2.3(b), the piston is at the top dead centre. The arrows at the top of the piston drawing indicate pressure applied to the piston crown due to the compressing air/fuel mixture. This exaggerated figure shows greater force acting on the minor thrust side of this piston. Consequently, the additional force causes moment about the gudgeon pin rotating the piston, pushing the major thrust side of the piston skirt towards the cylinder wall.
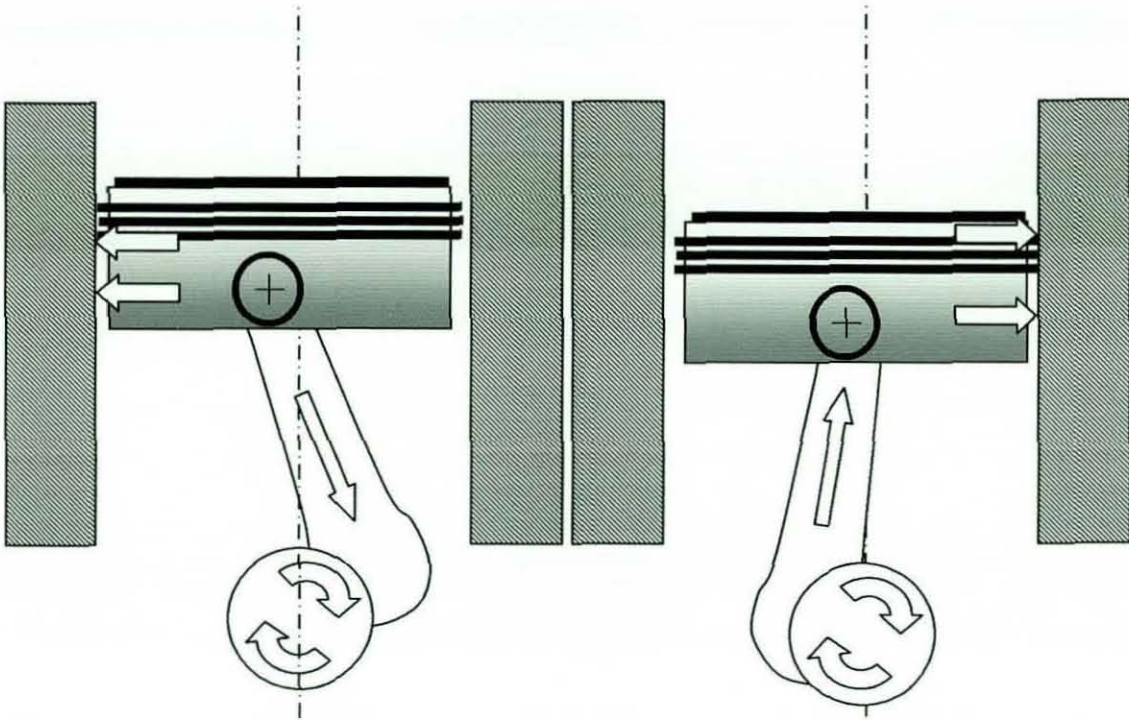
Figure 2.3 (c)

Figure 2.3 (d)
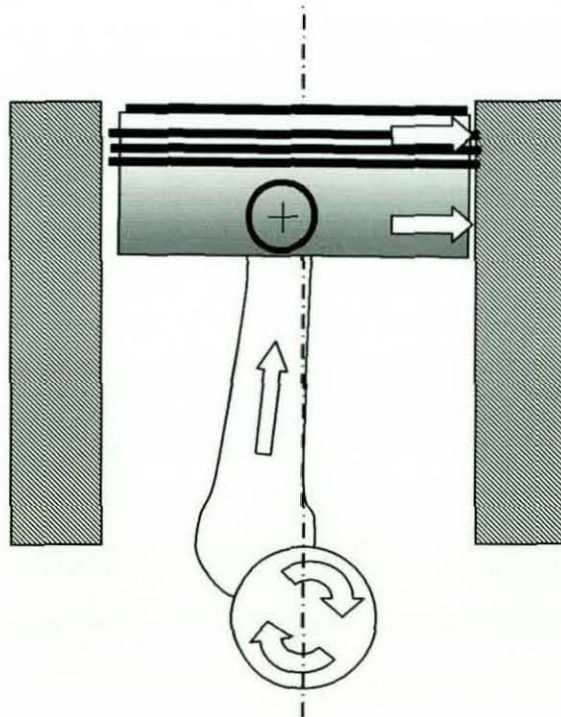
Figure 2.3 (e)

Figure 2.3: Secondary motion of piston

Figure 2.3(c) illustrates the power stroke, which shows the expanding combustion gasses pushing the piston into the cylinder. The reactive forces, created by rotational resistance of the crankshaft, continue pushing the major thrust side of the piston against the cylinder wall. Figure 2.3(d) shows how the piston changes side from the major thrust side to the minor thrust side during the exhaust stroke. The piston reaches the top-dead centre, as shown in figure 2.3(e), while dragging itself along the minor thrust side. During the intake stroke, the piston would move downwards, along the minor thrust side. It is during the next cycle; combustion stroke that the piston begins to tilt towards the major thrust side, as shown in figure 2.3(a), and the cycle repeats itself.

Piston slapping noise is usually apparent when an engine is started from cold, mainly due to different rates of expansion of piston, rings, and the cylinder liner itself, and partly due to the absence of lubricant between the interacting bodies. The difference in the rate of expansion of material, as mentioned above, is mainly due to the usage of different alloy compositions for engine parts.
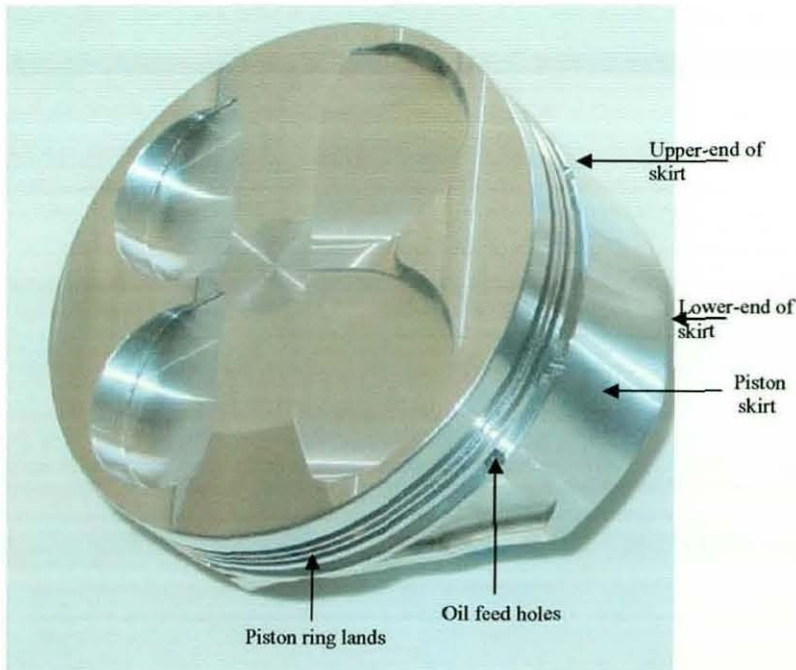
Figure 2.4: Terminology used to define the piston geometry in the thesis

2.4 Lubrication: A Historical Perspective

Since dawn of human civilisation, man has acknowledged the importance of overcoming friction (**Dowson** (1968)). Documented evidence of the use of wheel, by the Babylonians, dates back to 3500 BC with the use of animal fat to lubricate the wheels on axle. The Egyptians rubbed animal fat on logs, essentially roller bearings, to move large stone block used in constructing the great pyramids.

2.4.1 The importance of Lubrication in Engineering

In a mechanical system, interaction between parts moving relative to each other or parts that are transmitting power undergo tremendous stress and experience high friction. The onset of friction and stresses can result in catastrophic failure of such parts, due to abrasive wear, seizure, fatigue spalling and pitting. The introduction of a lubricant between these mating members simply ensures, that the two contiguous surfaces, moving relative to each other, are constantly separated by a film of fluid, which can be sheared with minimum effort, without causing any damage to the surfaces (**Forbes** and **Taylor** (1943), and **Furuhama** *et al* (1981) and **Uras** and **Petterson** (1983) and **Graddage** *et al* (1993)). It is, therefore, necessary to arrange wherever possible, an everlasting presence of a lubricant film of sufficient thickness, to ensure that no solid contact occurs between the opposing surfaces (during reversals of piston as mentioned in section 2.3), thereby, minimising the undesired effects of friction and wear considerably. In most engineering applications, the form of lubricant used is usually mineral oil.

2.4.2 Principle of Lubrication

When one surface moves relative to the other in a lubricated contact (shown in figure 2.5), lubricant is dragged into the narrow conjunction (**Cameron** (1970)). As the passage

constricts, and the volume of lubricant entering the conjunction remains constant, the incompressible fluid generates pressure to force its path through the conjunction.
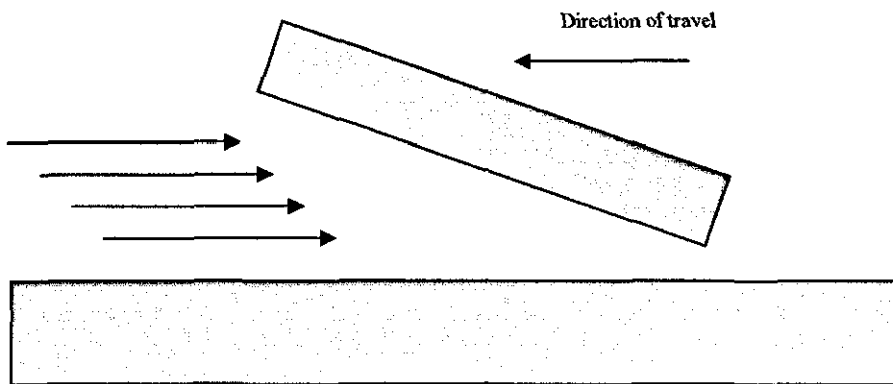
Figure 2.5: Entrapment of lubricant in a converging gap

Although the Babylonians and the Egyptian used oil to lubricated moving parts, the understanding of principles of lubrication, from an engineering standpoint arrived in the late 19th century, when an engineer by the name of **Beauchamp Tower** (1883) found that lubricant leaked from a hole in the shell of a journal bearing, especially when the particular side was loaded. While all effort to plug the leak failed, Tower realised that the oil was somehow pressurised by an unknown mechanism, generating enough force to push out any plug forced in place to stop the leak. Almost concurrently, a Russian scientist; **Petroff** (original text: (1883); reference source: **Dowson** (1968)), was studying the variation in frictional characteristic in a journal bearing with different types of oil and that the journal bearing friction could be explained as a hydrodynamic phenomenon, when assuming that the lubricant was sheared between a coaxial shaft and a bearing.

About the same time, **Osborne Reynolds** (1886) was working for an analytical model to prove that lubricant can physically separate the bodies in contact, and moving relative to each other, and published his work in the Proceeding of the Royal Society. Using **Newton's** (original text: (1687); reference source: **Hamrock** (1994)), model for slow viscous action, and the energy equations and the **Navier's** (1821) - **Stokes'** (1845)

18

equations of motion for a fluid element, Reynolds was able to mathematically describe the phenomenon observed by Tower, that when a viscous fluid is drawn into a space of decreasing height by the imposed surface velocities of the bearing elements, load carrying pressures in the oil film would be generated. The mathematical formulation is the well known Reynolds' equation, which describes the physical wedge condition of lubricant in a narrow conjunction. The derivation of the Reynolds' equation from the Navier-Stokes equations is shown in chapter 4.

In the case of mechanical components, having low geometrical conformity (for example pair of gear teeth in contact, rollers contacting a plane, cams and followers and etc.), the contact area is generally very small (**Dowson** and **Higginson** (1959)). Therefore, under highly loaded conditions, the pressures within this area of contact would be enormous. Therefore, in a lubricated condition, as two surfaces come together under mutual approach and under rolling or sliding motion, they tend to deform elastically at the point of contact, forming a gap filled with the lubricant, whose size can often exceed that of the hydrodynamically generated lubricant film thickness. This often results in the formation of a central flattened contact zone (as indicated by **Grubin** (1949)). As the lubricant in the contact experiences high pressures, its viscosity under such conditions varies dramatically, as showed by **Barus** (1895) and **Roelands** (1966). The lubricant becomes semi-amorphous, similar to cheese (see section 4.2.2). The combination of pressure and viscosity leads to the deformation of the elastic bodies and prevents the mating surfaces from direct interaction. The deformed gap is filled by the lubricant, thereby giving rise to higher film magnitude within the contact (**Dowson** (1959)). The formation of lubricant film due to such action is known as elastohydrodynamic lubrication (EHL).

2.4.3 Solution of Deformation

Boussinesq (1885) made important contributions to all branches of mathematical physics. His contributions to the study of turbulence were praised by **St Venant** (1868), and those on theory of elasticity by **Love** (1948). Although he approached mathematics only in order to apply it practically, he still made important contributions. Notably, in 1880 he

19

came upon non-analytic integrals of hydrodynamic equations. **Hertz** (1896) found an analytical solution defining the contact stresses for elastic bodies in contact. For a more general case of deformation in two dimensional elastic half-space, the limits of integral, known as "singular integral equation" **(Johnson (1985))** was employed by **Muskhelishvili** (1963) to uncouple them (refer to equations [4.26] and [4.27]). Based on this, the derivation of deflection equation for the piston is presented in chapter 3.

Approach in solving for deflection of conforming bodies in contact (spherical or cylindrical) was provided by **Paul** and **Hashemi** (1979). Another methodology to solve for the deflection of bodies in conformal contacts is by finite element approximation **Zienkiewicz** and **Taylor** (2000). Solution for pressures due to a uniform line load along a semi infinite solid was given by **Timoshenko** and **Goodier** (1951). This analytical solution was extended to solve for pressure for a distributed load. In finite element, the discretisation of a continuum allows for the stress-strain relationship in an element to be expressed relative to adjacent elements by the use of shape functions. **Szabo** and **Lee** (1969) derived stiffness matrices to express elasticity of a plane using Galerkin's method.

2.4.4 Measuring Pressures in Lubricated Contacts

Early pressure distribution measurements were obtained by **Higginson** (1962) for conformal contact between a bronze disc and a rubber block. **Kannel** (1965) managed to measure pressures in the lubricated contact region of steel rolling discs, using thin manganin micro-transducers. **Ioannides** and **Pareti** (1986) showed that actual pressures measured in an elastohydrodynamic contact are much higher than their numerically predicted counterparts. **Safa** (1986) extended the method of depositing the pressure transducer to study the elastohydrodynamic pressure distribution of rolling line contacts in a disc machine. The case of a point contact of a sphere against a flat glass race was studied using the same transducer technology by **Johns-Rahnejat** (1988).

2.4.5 Measurement of lubricant film thickness

Various methods have been successfully developed to measure and visualise the oil film thickness in lubricated contacts. These include the use of capacitance method (**Dyson** (1980)), X-ray (**Sibley** *et al* (1961) and **Kannel** (1965)), optical interferometry (**Archard** (1963), **Wedeven** and **Cameron** (1968), **Wymer** and **Cameron** (1974) and **Safa** and **Gohar** (1986)) and laser-induced fluorescence (**Ting** (1979), **Inoue** *et al* (1989) and **Brown** *et al* (1993)). Extensive detail on the use of optical interferometry to measure oil film thickness has been explained in the thesis of **Mostofi** (1981). Proximity sensors, such as eddy current probes have also been reported to have been successfully implemented in measuring the piston secondary motion (**Graddage** *et al* (1993)) in a large displacement engine. However, the most successfully implemented tool for visualising and measuring the lubricant in the contact between piston skirt and piston ring with cylinder bore (**Ting** (1979), **Inoue** *et al* (1989) and **Brown** *et al* (1993)) has been the laser-induced fluorescence (LIF). A brief outline of the laser-induced fluorescence technique to measure film thickness is given in the following section.

2.4.5.1 Lubricant Film Measurement using Laser-Induced Fluorescence

Fluorescence arises when the molecules in the oil film are electronically excited by a laser light source due to photon absorption and return to their ground state. This process occurs within lapse of a few nano-seconds. During their return to the ground state, photons are emitted, but at a lower energy level than that of the excitation source (i.e. the light). The spectral emission can be discriminated by appropriate optical filtering techniques (**Greene** (1969)). The spatial resolution depends on the area illuminated by the excitation source. An early qualitative work on observation of the oil film distribution in the lubricated conjunction between a Perspex liner and piston with ring pack was carried out by **Greene** (1969). **Ting** (1979) successfully extended this method and implemented it to measure the oil film thickness by comparing the illumination intensity distribution with that of a calibrated data (**Hoult** *et al* (1988)).

21

2.5 Experimental study of piston skirt lubrication

As mentioned earlier in section 1.2, the piston assembly accounts for majority of the frictional losses. Early experimental studies to measure friction between the piston skirt and cylinder bore/liner were carried out by **Forbes** and **Taylor** (1943), and **Furuhama** *et al* (1981) and **Uras** and **Petterson** (1983). More recent experimental study by **Graddage** *et al* (1993) of the piston's secondary motion in a 4MW power output diesel engine, was measured using eddy current probes (also referred to as proximity sensors) and thermal distortions by thermocouples. This study was conducted to understand the reason for catastrophic failure of the crankcase by the means of crack propagation, suspected to be the result of inadequate lubrication. The performance of a variety of pistons with different skirt profiles were gauged, under different operating conditions, in the above mentioned engine. The collected data were analysed and led to the conclusion that the originally failed piston skirt profiles were inadequate to promote sufficient lubrication within the contact.

In the experiment carried out by **Toshihide** *et al* (1993) to measure relative wear (and therefore assessing the relative friction contributions) of the various components of the piston and valve-train, the parts were coated with different radioactive isotopes. The sump oil sample revealed that the highest content of radioactive isotope was that coated onto the piston ring.

Attempts made to reduce frictional losses are usually by modifying the piston design (i.e. the profile along circumferential and along the skirt) and using lighter material (**Howell-Smith** (2002)). All research in this field have the main aim of improving lubrication between the piston skirt and bore and thereby reducing friction (**Taylor** and **Coy** (1996)).

Early on, the importance of having a well lubricated contact condition between the piston skirt and cylinder bore was appreciated, especially at the two reversal points, top-dead centre and bottom-dead centre. Studies undertaken by **Okrent** (1964) focussed on the deflection of journal bearing and its influence upon lubrication. Although attention was

22

paid to the noise problems (due to secondary motions) of piston (**Haddad** and **Howard** (1980)), the emphasis was on reducing friction. Experimental studies were intensely carried out to understand the physics of the lubrication throughout the crank cycle. Until the recent development in laser measurement technique (see section 2.4.5.1), the lubricant film trapped between the piston and bore was only been able to be measured using capacitance discharge methods (**Lewicki** (1955))

2.6 Numerical Investigation of Piston Skirt Lubrication

One of the first papers, reporting a simulation of piston skirt lubrication of a large V-8 spark ignition engine was undertaken by **Li** *et al* (1981). The secondary motion of the piston was solved without taking lubrication into consideration. The results showed that the location of the gudgeon pin has a critical influence on the secondary dynamics of the piston. The clearance and viscosity of the lubricant were also found to be important. The results obtained showed that the location of the gudgeon has a direct influence upon the piston skirt to cylinder liner friction. The solution of the second order differential lateral accelerations was ignored, and the analysis was carried out to obtain a repeated cyclic pattern.

Knoll and **Peeken** (1982) carried out a study of hydrodynamic lubrication of piston skirt in a motored engine and identified the following parameters to be important in inducing secondary dynamics:

- gas and inertial forces
- piston clearance
- off-set of gudgeon pin
- hydrodynamic friction acting on skirt and gudgeon pin
- elastic deformation during impoact of piston

Reynolds' boundary condition was applied and solution for the deflection was based on finite element method. The conclusion derived from their study re-emphasised the

23

importance of the parameters identified above. **Oh** *et al* (1987) referred to the piston design (i.e. piston's upper and lower end relief radii and ovality, see figures 4.8(a) and 4.8(b)) as key factors in reducing friction between the piston skirt and the cylinder liner. Using the finite element package, Nastran, to compute deformation and thermal distortion, the simulation was carried out for a motored engine. **Oh** *et al* (1987) deduced from realistic pressures and lubricant films in the contact that the profile of the piston has to be modelled accurately. A comparative study between two different piston skirt designs indicated the important of skirt axial profile in reducing friction. **Goenka** and **Meenik** (1992) carried out a sensitivity analysis to study the friction between liner and piston skirt of a motored engine (using an in-house computer code developed by General Motors), and by varying the clearance space, the gudgeon pin position and the mass of the piston. Two separate analyses were carried out, one assuming the piston skirt was elastic and the other rigid. Again, a finite element code was used to solve the deformation of the piston skirt (in the case of the elastic piston skirt), assuming that the cylinder bore to be rigid. This study showed the effect of friction behaviour within the contact by varying each of the above parameters in isolation. By comparing the results obtained from the numerical analysis with the experimental data, the authors concluded that a rigid analysis showed a greater deviation from the experimentally measured friction than that obtained from the elastohydrodynamic analysis. A numerical analysis to compare hydrodynamic lubrication of a conventional piston with that of an articulated piston in a large engine was undertaken by **Dursunkaya** and **Keribar** (1992). The articulated piston skirt design, was found to give rise to larger tilt angle of the crown about the gudgeon pin, when compared with that of a conventional piston. Therefore, the articulated skirt travelled more parallel to the liner than the rigid skirt. No comments were made on the possibility of impact or contact between the lower part of the crown with the top face of piston skirt (see figure 2.2(b)).

A two part comprehensive analysis was undertaken by **Zhu** et al ((1992) and (1993)) to simulate piston lubrication in an engine at severe operating conditions. The first part of the investigation was focussed on obtaining rigid body piston lubrication analysis and extended to include the piston skirt distortion, including thermal effect in the second part.

24

The conclusions derived are reaffirmation of the importance of the parameters identified above.

To study structure borne noise due to piston slap in a 4-stroke 4-cylinder engine, **Offner** and **Priebsch** (2000) built an elasto-multi body model to simulate a piston traversing in a cylinder bore. Extensive finite element analysis was carried to obtain frequency response from the impact of piston against cylinder bore. Although this analysis was relatively comprehensive, the lubrication was not solved for full cycle of the piston. It was assumed that hydrodynamic reaction action was not significant in all other positions except at TDC (top-dead-centre) and BDC (bottom-dead-centre) in order to minimise computation time. However, results from experimental study **(Graddage** *et al* (1993)) indicate that the pressures generated by lubricant film at such positions can be significant.

Chapter 3

3.1 Introduction

In this chapter, a numerical model of a three degrees-of-freedom piston assembly system, representing piston axial, lateral and tilting motions is developed. The first model is developed based on the *Newton-Euler* (**Xie** *et al* (1998)) method and a second model is developed in a commercial multi-body dynamics code called *ADAMS**, which is based on constrained *Lagrangian* dynamics. The underlying principles behind the two theories are explained in section 3.2. The formulation for the model based on the *Newton-Euler* method is described in section 3.3. In the sub-sections, derivation of the equations of motion and method of solution, using *Newmark's* linear acceleration method is shown. In section 3.4 and its sub-sections, theory of multi-body dynamic modelling, using *Lagrangian* dynamics for the construction of the piston-connection rod-crank assembly (hereinafter referred to as piston assembly) model in *ADAMS*, and the results and discussions are presented. Details pertaining to the geometric data and operating conditions are provided in sub-sections 3.3.3 and 3.4.4.

3.2 Numerical Formulation: Newton-Euler or Lagrangian Method?

The classic approach to a simple problem of deriving equations of motion commences by drawing a free-body diagram. The action and reaction forces, constraining and restraining elements are specified. For a given system, the equations of motion are then derived. This is known as the *Newton-Euler* method.

As opposed to the *Newton-Euler* method, the *Lagrange's* method is more generic (**Chance (1967)**) and is based on the application of differential geometry. Kinetic and

---

* *ADAMS* is an acronym for Automatic Dynamic Analysis of Mechanical Systems and is a Trademark of MSC (Maxwell-Schwindler Corporation of USA)

potential energy equations of an assembly of parts are obtained and solved by differential calculus for the inertial and applied forces, including the restraining and constraining forces. The reactions due to the constraining elements are accounted for through the use of differential properties of the constraint functions and the *Lagrange's* multipliers, thereby leading to automatic generation of equations of motion (**Orlandea** *et al* (1977)).

A general guide to selecting the appropriate method lies in the problem that is to be investigated. The *Newton-Euler* method is best suited for systems that have relatively well-defined active degrees of freedom (**Rahnejat** (1998)), and the applied and reaction forces can be easily determined; leading to a smaller number of equations defining the motions of the system, since redundant degrees of freedom are ignored.

In the case of the *Lagrange's* method, equations of motion are rendered by the consideration of the principle of virtual work, in other words they can be self-generated. The disadvantage of this method is that it results in a much larger equation set. On the positive side, since the equations of motion are automatically generated, mistakes in resolving the action and reaction forces are eliminated, in turn, making it the ideal method to study very complex mechanisms and large system dynamics problems.

3.3 Derivation of Equations of Motion

The piston assembly is three degrees of freedom system. Therefore, the motions that the piston is allowed to undertake (see figure 3.1):

- Translational action along x-axis
- lateral oscillation along z-axis
- tilting motion; rotation about y-axis of the gudgeon pin

The vertical motion of the piston is considered purely kinematic, because the analysis is carried out for a given input of combustion pressure data for a fixed engine speed. Therefore, the relationship for the vertical acceleration, velocity and displacement are derived purely based on kinematics, **Oh** *et al* (1987). In the following section, derivations of acceleration, velocity and displacement of piston along the vertical *x*-axis is shown.

3.3.1 The Kinematic Crank Slider Mechanism

The piston assembly is, in essence, a crank slider mechanism. The displacement, velocity and acceleration of the piston relative to a datum position, from the top-dead-centre (TDC), can be expressed as a simple harmonic motion. Figure 3.1 below, shows a piston assembly. In the following sections, derivation of the equations, describing the three degrees of freedom of the piston assembly is outlined.
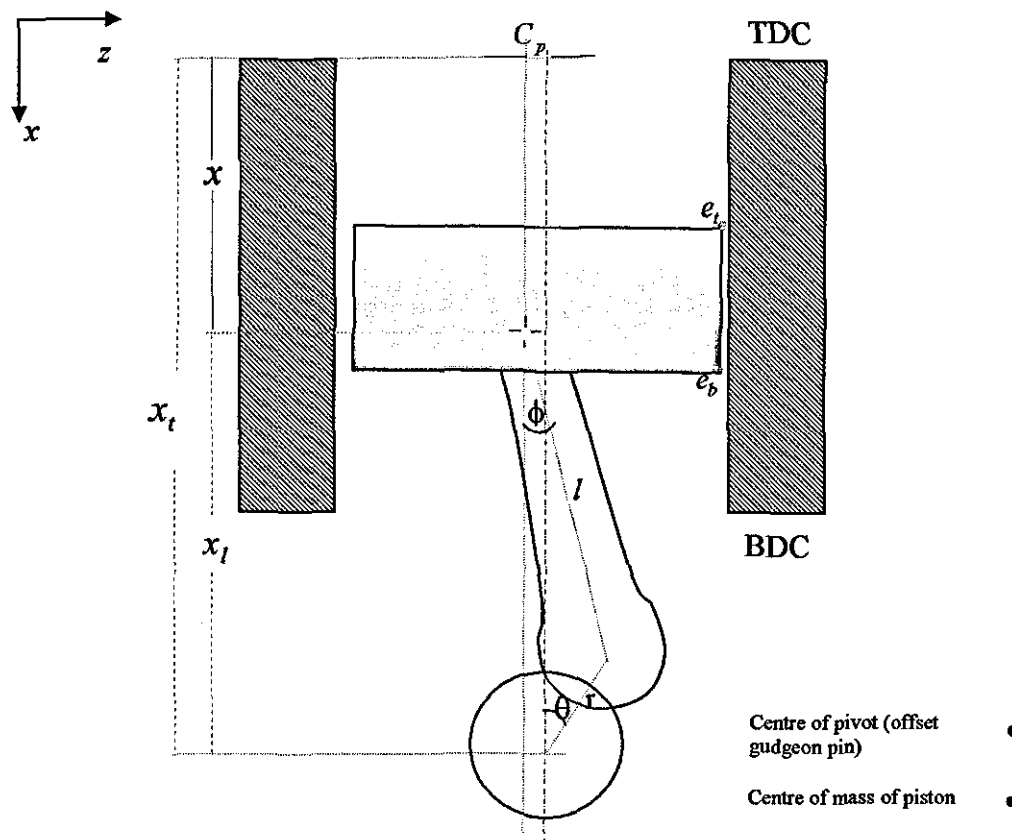
Figure 3.1: Free body diagram of piston assembly

27

3.3.2 Derivation of Equations of Motion

Using the geometric relationship, from figure 3.1, (in the lateral direction, z) the connecting rod length, l, can be written in terms of the crank radius and the offset C_p as:

$$l\sin\phi = C_p + r\sin\theta \qquad \text{[3.1]}$$

Meanwhile, along the x direction, displacement can be written as:

$$x = x_t - x_l = (l+r) - (l\cos\phi + r\cos\theta) \qquad \text{[3.2]}$$

The aim is to write the equations describing the piston's vertical displacement and velocity in terms of the crank angle, θ. By using trigonometric relationship, ϕ can be expressed in terms of θ as:

$$\cos\phi = \sqrt{1 - \frac{(C_p + r\sin\theta)^2}{l^2}} \qquad \text{[3.3]}$$

Using binomial expansion to expand equation [3.3], $\cos\phi$ can be expressed as:

$$\cos\phi = 1 - \frac{1}{2}\frac{(C_p + r\sin\theta)^2}{l^2} + \frac{1}{8}\left(\frac{(C_p + r\sin\theta)^2}{l^2}\right)^2$$
$$- \frac{1}{16}\left(\frac{(C_p + r\sin\theta)^2}{l^2}\right)^3 + \frac{5}{128}\left(\frac{(C_p + r\sin\theta)^2}{l^2}\right)^4 \qquad \text{[3.4]}$$

Therefore, substituting equation [3.4] into equation [3.2] yields,

$$x = (l+r) - \left[r\cos\theta + l \left[\begin{array}{c} 1 - \dfrac{1}{2}\dfrac{(C_p + r\sin\theta)^2}{l^2} + \dfrac{1}{8}\left(\dfrac{(C_p + r\sin\theta)^2}{l^2}\right)^2 \\[4mm] - \dfrac{1}{16}\left(\dfrac{(C_p + r\sin\theta)^2}{l^2}\right)^3 + \dfrac{5}{128}\left(\dfrac{(C_p + r\sin\theta)^2}{l^2}\right)^4 \end{array} \right] \right] \qquad [3.5]$$

Simplifying equation [3.5], the following equation is obtained:

$$x = l + r - r\cos\theta - l\left(\begin{array}{c} 1 + \Omega + \Omega_1\sin\theta + \Omega_2\cos 2\theta + \Omega_3\sin 3\theta - \Omega_4\cos 4\theta + \\ \Omega_5\sin 5\theta + \Omega_6\cos 6\theta + \Omega_7\sin 7\theta + \Omega_8\cos 8\theta \end{array} \right) \qquad [3.6]$$

where:

$$\Omega = \frac{\vartheta_1}{2l^2} - \frac{1}{16l^4}\left(\vartheta_1^2 + \frac{\vartheta_2^2 + \vartheta_3^2}{2}\right) + \frac{1}{16l^6}\left(\vartheta_1^3 + \frac{\vartheta_1\vartheta_2^2 + 3\vartheta_1\vartheta_3^2 + 3\vartheta_2^2\vartheta_3}{2}\right)$$
$$- \frac{5}{128l^8}\left(\vartheta_1^4 + \frac{\vartheta_3^4 + 3\vartheta_2^4}{8} - \vartheta_1^2\vartheta_2^2 + 3\vartheta_1^2\vartheta_3^2 + 2\vartheta_1\vartheta_2^2\vartheta_3 + \vartheta_2^2\vartheta_3^2\right)$$

$$\Omega_1 = \frac{\vartheta_2}{2l^2} - \frac{\vartheta_2\vartheta_3 - 2\vartheta_1\vartheta_2}{16l^4} + \frac{12\vartheta_1\vartheta_2\vartheta_3 - 4\vartheta_1^2\vartheta_2 + 3\vartheta_2^3 + 6\vartheta_2\vartheta_3^2}{64l^6}$$
$$- \frac{160\vartheta_1^2\vartheta_2\vartheta_3 + 200\vartheta_1\vartheta_2\vartheta_3^2 + 85\vartheta_2^3\vartheta_3 + 10\vartheta_2\vartheta_3^3}{1024l^8}$$

$$\Omega_2 = -\frac{\vartheta_3}{2l^2} + \frac{4\vartheta_1\vartheta_3 - \vartheta_2^2}{32l^4} - \frac{12\vartheta_1^2\vartheta_3 - 2\vartheta_1^2\vartheta_2 + 6\vartheta_2^3\vartheta_3 + \vartheta_3^3}{64l^6}$$
$$+ \frac{80\vartheta_1^3\vartheta_3 - 20\vartheta_1^2\vartheta_2^2 + 80\vartheta_1\vartheta_2^2\vartheta_3 + 50\vartheta_1\vartheta_3^3 + 10\vartheta_2^4 + 25\vartheta_2^2\vartheta_3^2}{512l^8}$$

$$\Omega_3 = \frac{\vartheta_2\vartheta_3}{16l^4} - \frac{12\vartheta_1\vartheta_2\vartheta_3 - \vartheta_2\vartheta_3^2 + \vartheta_2^3}{64l^6} + \frac{160\vartheta_1^2\vartheta_2\vartheta_3 + 20\vartheta_1\vartheta_2\vartheta_3^2 + 50\vartheta_2^3\vartheta_3 + 5\vartheta_2\vartheta_3^3}{1024l^8}$$

$$\Omega_4 = \frac{\vartheta_3^2}{32l^4} - \frac{6\vartheta_1\vartheta_3^2 + 3\vartheta_2^2\vartheta_3 + \vartheta_2^3}{64l^6} - \frac{60\vartheta_1^2\vartheta_3^2 + 17\vartheta_1\vartheta_2^2\vartheta_3 - 20\vartheta_2^2\vartheta_3^2}{512l^8}$$

29

$$\Omega_5 = \left(\frac{3\vartheta_2\vartheta_3^2}{64l^6} - \frac{60\vartheta_1\vartheta_2\vartheta_3^2 + 15\vartheta_2^3\vartheta_3 - 5\vartheta_2\vartheta_3^3}{1024l^8} \right)$$

$$\Omega_6 = \left(\frac{\vartheta_3^3}{64l^6} - \frac{10\vartheta_1\vartheta_3^3 + 15\vartheta_2^2\vartheta_3^2}{512l^8} \right)$$

$$\Omega_7 = \frac{5\vartheta_2\vartheta_3^3}{512l^8}$$

$$\Omega_8 = \frac{5\vartheta_3^4}{1024l^8}$$

and:

$$\vartheta_1 = C_p^2 + \frac{r^2}{2}, \qquad \vartheta_2 = 2C_p r, \qquad \vartheta_3 = \frac{r^2}{2}$$

This expression includes all higher order terms up to and including the 8th expansion term, which is chosen in order to include engine order responses up to the 8th order. Engine order is defined as the crankshaft angular velocity (or radiancy). For 4-cylinder 4-stroke engines, the main vibration contributions (frequencies) extend up to the 8th engine order response (**March** and **Croker** (1998)).

Expression for velocity is obtained by differentiating equation [3.6] as:

$$\dot{x} = r\dot{\theta}\sin\theta - l\dot{\theta}\left(\begin{array}{l} \Omega_1\cos\theta - \Omega_2\sin 2\theta + \Omega_3\cos 3\theta - \Omega_4\sin 4\theta + \\ \Omega_5\cos 5\theta - \Omega_6\sin 6\theta + \Omega_7\cos 7\theta - \Omega_8\sin 8\theta \end{array} \right) \qquad [3.7]$$

Similarly, differentiating the above equation, [3.7], the acceleration is obtained as:

$$\ddot{x} = r\ddot{\theta}\cos\theta - l\ddot{\theta}\left(\begin{array}{l} -\Omega_1\sin\theta - \Omega_2\cos 2\theta - \Omega_3\sin 3\theta - \Omega_4\cos 4\theta - \\ \Omega_5\sin 5\theta - \Omega_6\cos 6\theta - \Omega_7\sin 7\theta - \Omega_8\cos 8\theta \end{array} \right) \qquad [3.8]$$

30

Since the analysis is carried out for a steady engine speed, 3700rpm **(Gupta (2002))** for the diesel engine, and 18500rpm for the high performance engine **(Howell-Smith (2002))**, the above equations, [3.6],[3.7] and [3.8] are used to describe the motion of the piston in the vertical direction. The equations describing the rotational motion about the gudeon/wrist pin bearing and the lateral motion of the piston are derived below.

Referring to figures 3.1 and 3.2, using geometric relationship, the tilt of piston, β and the lateral motion e_l, can be substituted by deviation of top of piston, e_t, and deviation of bottom of piston, e_b from the centre-line axis (shown in figure 3.2 as dot-dash line). This is written as:

$$e_t = e_l + a\beta \qquad [3.9]$$

and

$$e_b = e_l - (p_l - a)\beta \qquad [3.10]$$

Differentiating e_t and e_b in equations [3.9] and [3.10] yields the velocity terms:

$$\dot{e}_t = \dot{e}_l + a\dot{\beta} \qquad [3.11]$$

$$\dot{e}_b = \dot{e}_l - (p_l - a)\dot{\beta} \qquad [3.12]$$

Equation [3.9] and [3.10] describes the relationship between the lateral motion and tilt with the deviation of the top and bottom of piston **(Xie *et al* (1998))**.

Referring to figure 3.2, balancing the forces in lateral direction, z, yields:

$$f_z = f_{ip} + f_{ig} + f_{r2} - f_{r1} - f_{con}\sin\phi \qquad [3.13]$$

and in vertical direction, x:

$$f_x = f_{gp} + f_{gg} + f_g - f_{con}\cos\phi \qquad [3.14]$$

31

Taking moments about the gudgeon/wrist pin bearing results in:

$$m_z = f_{ip}(a-b) + (f_g \times C_g) - (f_{gp} \times C_p) + m_c + m_{fr1} + m_{fr2}$$
[3.15]

Rewriting equation [3.14] in terms of f_{con},

$$f_{con} = \frac{1}{\cos\phi}(f_{gp} + f_{gg} + f_g)$$
[3.16]
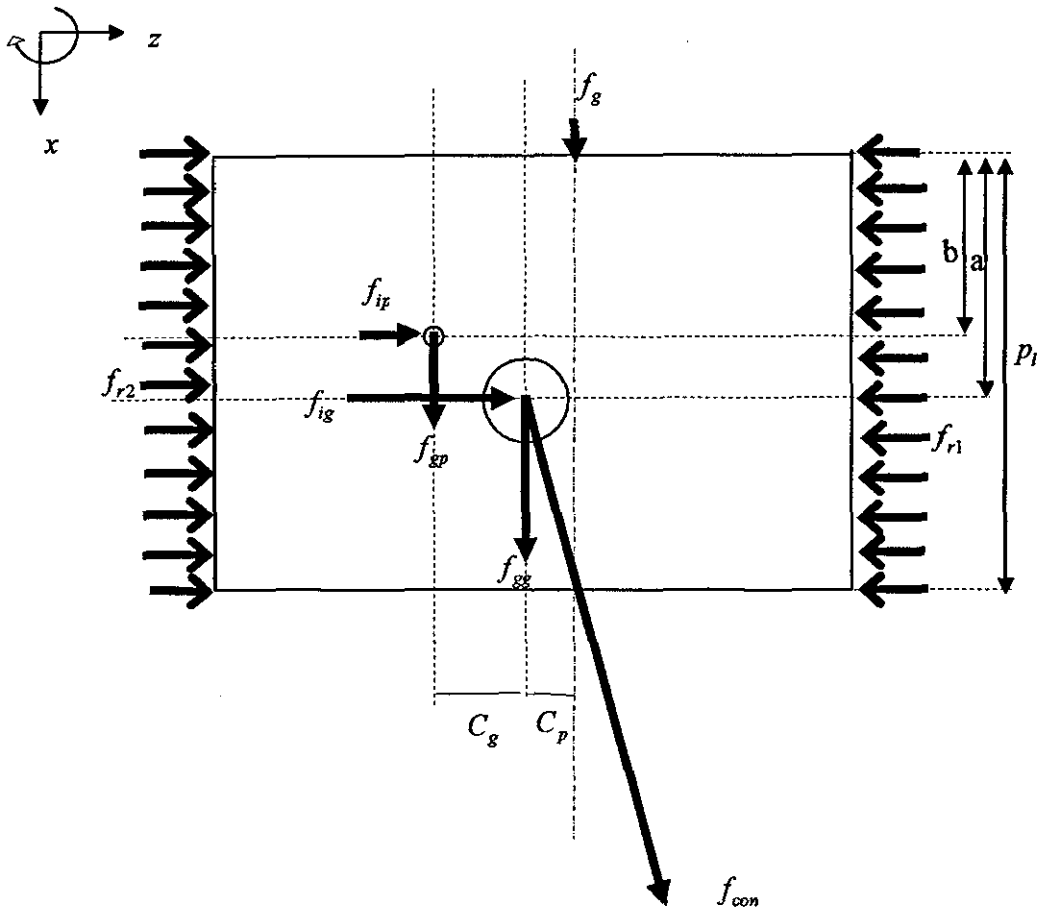
Figure 3.2: Free-body diagram of piston

and substituting equation [3.16] into equation [3.13] yields:

$$f_z = f_{ip} + f_{ig} + f_{r2} - f_{r1} - \tan\phi\left(f_{gp} + f_{gg} + f_g\right) \qquad [3.17]$$

The inertial forces and moments caused by the secondary motion of the piston (**Xie** *et al* (1998)) can be expressed as:

$$f_{ip} = m_p\left(\ddot{e}_t + \frac{b}{p_l}\left(\ddot{e}_t - \ddot{e}_b\right)\right) \qquad [3.18]$$

$$f_{ig} = m_g\left(\ddot{e}_t + \frac{a}{p_l}\left(\ddot{e}_b - \ddot{e}_t\right)\right) \qquad [3.19]$$

$$m_c = \frac{I_p}{p_l}\left(\ddot{e}_t - \ddot{e}_b\right) \qquad [3.20]$$

In equations [3.15] and [3.17], the force components in the vertical direction can be lumped together to simplify the equations and yield the following expressions:

$$m_s + m_{fr1} + m_{fr2} = -m_c - f_{ip}\left(a - b\right) \qquad [3.21]$$

where:

$$m_s = \left(f_g \times C_g\right) - \left(f_{gp} \times C_p\right)$$

and:

$$f_s = f_{ip} + f_{ig} + f_{r2} - f_{r1} \qquad [3.22]$$

where:

$$f_s = \tan\phi\left(f_{gp} + f_{gg} + f_g\right)$$

Substituting equations [3.18], [3.19] and [3.20] into equations [3.21] and [3.22], the following matrix expression is obtained:

$$\begin{bmatrix} m_g\left(1-\dfrac{a}{p_l}\right)+m_p\left(1-\dfrac{b}{p_l}\right) & m_g\dfrac{a}{p_l}+m_p\dfrac{b}{p_l} \\ \dfrac{I_p}{p_l}+m_p(a-b)\left(1-\dfrac{b}{p_l}\right) & m_p(a-b)\dfrac{b}{p_l}-\dfrac{I_p}{p_l} \end{bmatrix}\begin{bmatrix} \ddot{e}_t \\ \ddot{e}_b \end{bmatrix}=\begin{bmatrix} f_{r1}+f_{r2}+f_s \\ m_{fr1}+m_{fr2}+m_s \end{bmatrix} \qquad [3.23]$$

Lubricant reaction forces and their applied moments, f_{r1}, f_{r2}, m_{fr1} and m_{fr2} are obtained by solving the *Reynolds'* equation for both the major and minor thrust side, as shown in the following chapter. $\ddot{e}_t$ and $\ddot{e}_b$ are the lateral acceleration terms of the piston's upper end and lower end (see figure 2.4). In the following section, using *Newmark's* linear acceleration integration method, the velocity and displacement terms are obtained.

3.3.3- *Solving Integration Using Newmark's Linear Acceleration Method*

Nathan M. Newmark is very well known for his contributions to the design of earthquake-resistant structures. He is dubbed the pioneer in earthquake studies. In the late 1940s and early 1950s, Newmark served as earthquake consultant to the forty-three story Latino Americana Tower in Mexico City. During this period, he developed a numerical method stable enough to predict displacements of highly non-linear structures due to earthquake (**University Karlsruhe**). The widely used Newmark time integration scheme consists of approximating the displacement and velocity vectors as:

$$x_{n+1}=x_n+\dot{x}\Delta t_n+\Delta t_n^{\,2}\left(\left(\frac{1}{2}-\beta\right)\ddot{x}_n+\beta\ddot{x}_{n+1}\right) \qquad [3.24]$$

$$\dot{x}_{n+1}=\dot{x}_n+\Delta t_n\left((1-\gamma)\ddot{x}_n+\gamma\ddot{x}_{n+1}\right) \qquad [3.25]$$

The Newmark scheme is second order accurate and depends on two real parameters β and γ. The parameter values are directly linked to accuracy and stability of the *Newmark*

integration scheme (**Newmark (1962)**). The values of β and γ are determined by the application it is used for, as indicated below:

$\beta = \frac{1}{6}$ and $\gamma = \frac{1}{2}$, which lead to a linear acceleration approximation (a conditionally stable scheme)

$\beta = \frac{1}{4}$ and $\gamma = \frac{1}{2}$, which lead to a constant average acceleration: choice of parameters corresponds to a trapezoidal rule (an unconditionally stable scheme in linear analyses)

$\beta = \frac{1}{2}$ and $\gamma = \frac{1}{2}$, which is the *Fox-Goodwin* method, accurate up to fourth order (a conditionally stable scheme)

Therefore, rewriting equation [3.23] to solve for $\ddot{e}_t$ and $\ddot{e}_b$:

$$\ddot{e}_t = \frac{\left(\left(-\frac{I_p}{l} + m_p \frac{b}{l}(a-b)\right)(f_{r1} + f_{r2} + f_s) - \left(m_g \frac{a}{l} + m_p \frac{b}{l}\right)(m_{fr1} + m_{fr2} + m_s)\right)}{\left(\frac{m_g(l-a)}{l} + m_p\left(1 - \frac{b}{l}\right)\right)\left(-\frac{I_p}{l} + m_p \frac{b}{l}(a-b)\right) - \left(m_g \frac{a}{l} + m_p \frac{b}{l}\right)\left(\frac{I_p}{l} - m_p(a-b)\left(1 - \frac{b}{l}\right)\right)}$$

[3.26]

$$\ddot{e}_b = \frac{\left(a_{21}(f_{r1} + f_{r2} - f_s) + a_{11}(m_{fr1} + m_{fr2} + m_s)\right)}{\left(\frac{m_g(l-a)}{l} + m_p\left(1 - \frac{b}{l}\right)\right)\left(-\frac{I_p}{l} + m_p \frac{b}{l}(a-b)\right) - \left(m_g \frac{a}{l} + m_p \frac{b}{l}\right)\left(\frac{I_p}{l} - m_p(a-b)\left(1 - \frac{b}{l}\right)\right)}$$

[3.27]

Using *Newmark* linear acceleration time integration scheme to approximate the velocity and displacement, where $\beta = \frac{1}{6}$ and $\gamma = \frac{1}{2}$, the lateral acceleration terms can be integrated to solve for the velocity terms $\dot{e}_t$ and $\dot{e}_b$, and the displacement terms e_t and e_b. Therefore, the following expressions are obtained.

$$\dot{e}_{t_{(n+1)}} = \dot{e}_{t_n} + \Delta t_n \left(\frac{1}{2} \ddot{e}_{t_n} + \frac{1}{2} \ddot{e}_{t_{(n+1)}} \right) \qquad [3.28]$$

$$\dot{e}_{b_{(n+1)}} = \dot{e}_{b_n} + \Delta t_n \left(\frac{1}{2} \ddot{e}_{b_n} + \frac{1}{2} \ddot{e}_{b_{(n+1)}} \right) \qquad [3.29]$$

$$e_{t_{(n+1)}} = e_{t_n} + \dot{e}_{t_n} \Delta t_n + \Delta t_n^2 \left(\frac{1}{3} \ddot{e}_{t_n} + \frac{1}{6} \ddot{e}_{t_{(n+1)}} \right) \qquad [3.30]$$

$$e_{b_{(n+1)}} = e_{b_n} + \dot{e}_{b_n} \Delta t_n + \Delta t_n^2 \left(\frac{1}{3} \ddot{e}_{b_n} + \frac{1}{6} \ddot{e}_{b_{(n+1)}} \right) \qquad [3.31]$$

The initial and boundary conditions and convergence criterion employed in the transient analysis using this integration scheme is detailed in sections 4.6.1, 4.6.2 and 4.6.3.

3.3.4 Operating Conditions

The simulation conditions in the analysis of a diesel engine running at 3700rpm at $t_0 = 0$ are as follows:

- Transverse position, $x_0 = 0$ m (at TDC)
- Transverse velocity, $\dot{x}_0 = 0$ m/s
- Transverse acceleration, $\ddot{x}_0 = 5315$ m/s^2
- Angular velocity, $\dot{\theta}_0 = 387.46$ rad/s
- Angular acceleration, $\ddot{\theta}_0 = 0$ rad/s^2
- Duration of simulation, $t = 0.2s$

whereas, the simulation conditions for the analysis of an *FI* engine running at 18500rpm are:

- Transverse position, $x_0 = 0.0423$ m (at TDC)

- Transverse velocity, $\dot{x}_0 = 0$ m/s

- Transverse acceleration, $\ddot{x}_0 = 86,000$ m/s^2

- Angular velocity, $\dot{\theta}_0 = 1937.0$ rad/s

- Angular acceleration, $\ddot{\theta}_0 = 0$ rad/s^2

- Duration of simulation, $t = 0.2s$
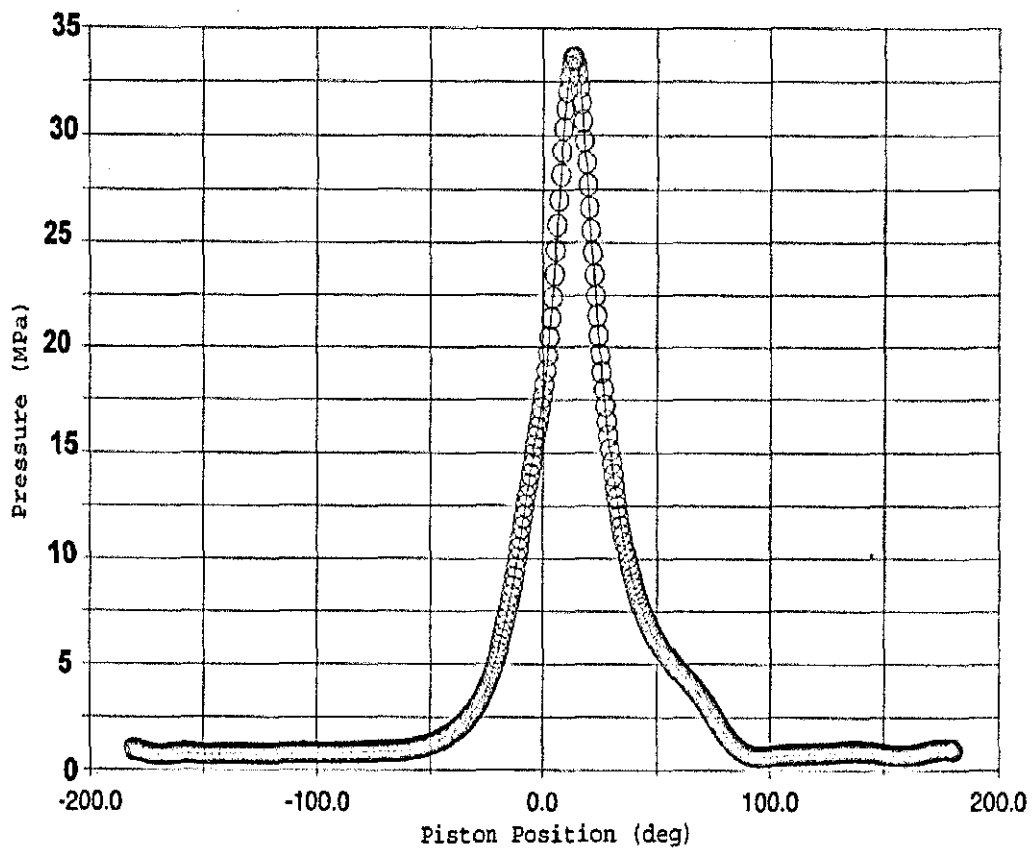
Figure 3.3: Combustion pressure of a diesel engine experimentally obtained at 3700 rpm
(taken from source: **Kelly** (1999))

37
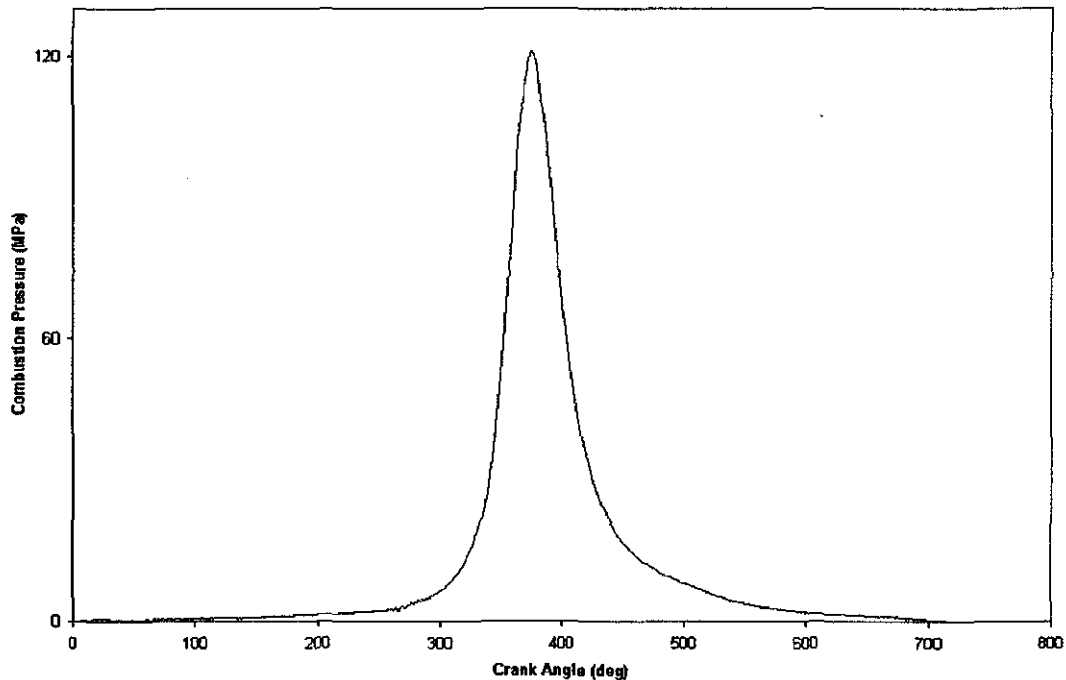
Figure 3.4: Peak combustion pressure in a 3.0 litres V10 engine (experimentally obtained data, given by Perfect Bore Ltd.)

In this chapter, the simulation of the secondary dynamics of the piston was ignored because, without the inclusion of the lubricant reaction forces in equation [3.23], the piston would simply rotate about the gudgeon pin and travel along the lateral direction. However the combined transient dynamic of the secondary motion analysis of piston with lubricant forces is shown in chapter 6.

3.3.5 Results

Figures 3.5, 3.6 and 3.7 show the variation of displacement, velocity and acceleration of the piston with time. Maximum displacement is the function of the crank-throw, r as described in equation [3.6], in this case, is 64 mm. The displacement of piston, x, indicates the position of piston in the bore, therefore, determining the position of piston profile, at any instant of time, on the computation grid (see chapter 4). The velocity

profile (shown in figure 3.6) is the entraining speed, u_A of the lubricant into the contact. During the points of reversals, at TDC and BDC, piston experiences a maximum acceleration/deceleration of $5330 \, m/s^2$. These results are verified by comparing it with that obtained from the piston in ADAMS.

Another set of figures, 3.8, 3.9 and 3.10 show the variation of displacement, velocity and acceleration with time for an F1 engine at 18500rpm. The maximum displacement of the piston in this case is 42.28mm. At mid-stroke, the translational velocity of piston is the highest, at 42.5m/s.

These results were used to solve the quasi-static analysis at various positions of piston along the bore both for the diesel engine (results are presented in section 5.3) and the F1 engine (shown in section 5.4).
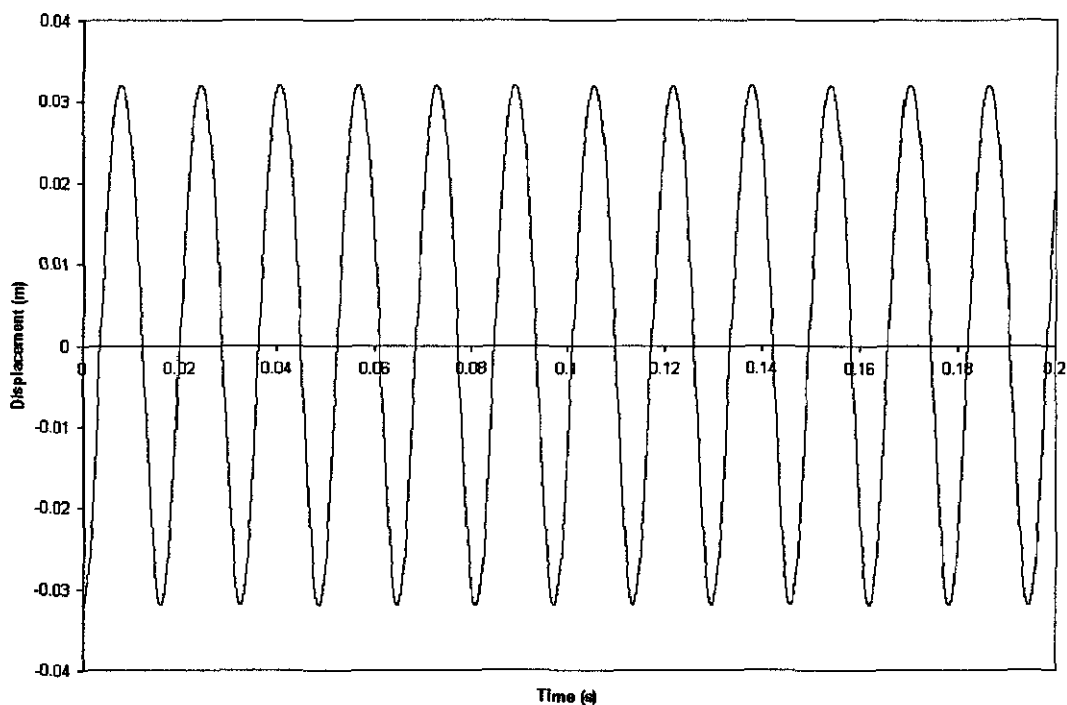
Figure 3.5: Displacement characteristic for a diesel engine at 3700rpm
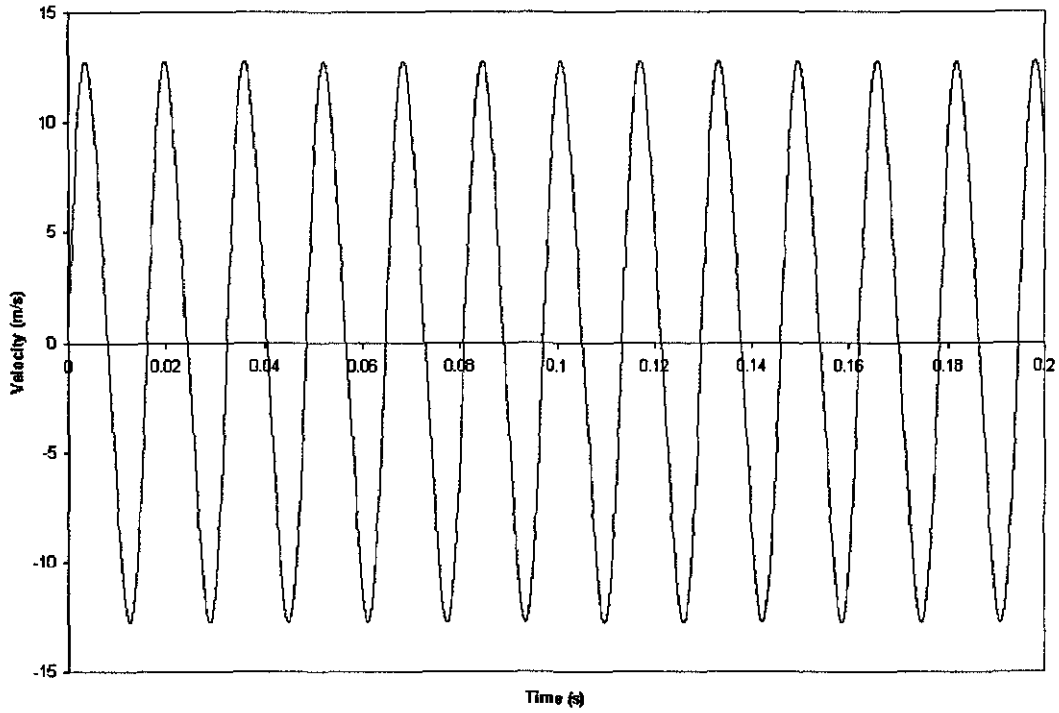
Figure 3.6: Velocity characteristic for a diesel engine at 3700rpm
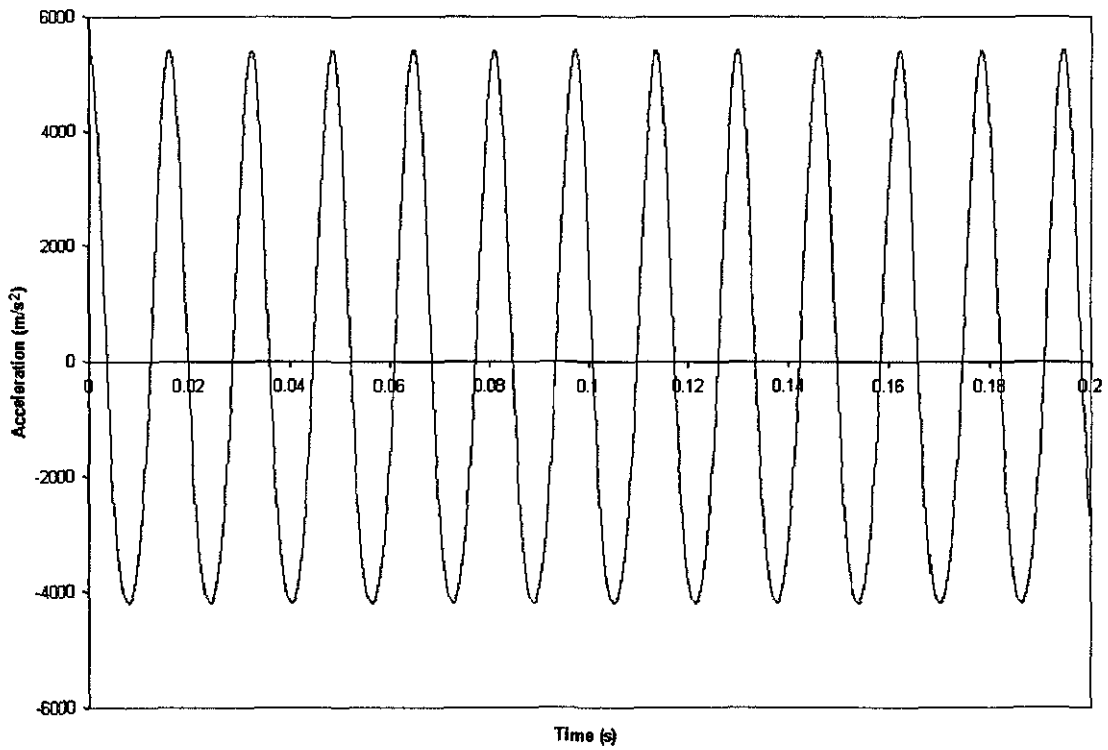
Figure 3.7: Acceleration characteristic for a diesel engine at 3700rpm

40
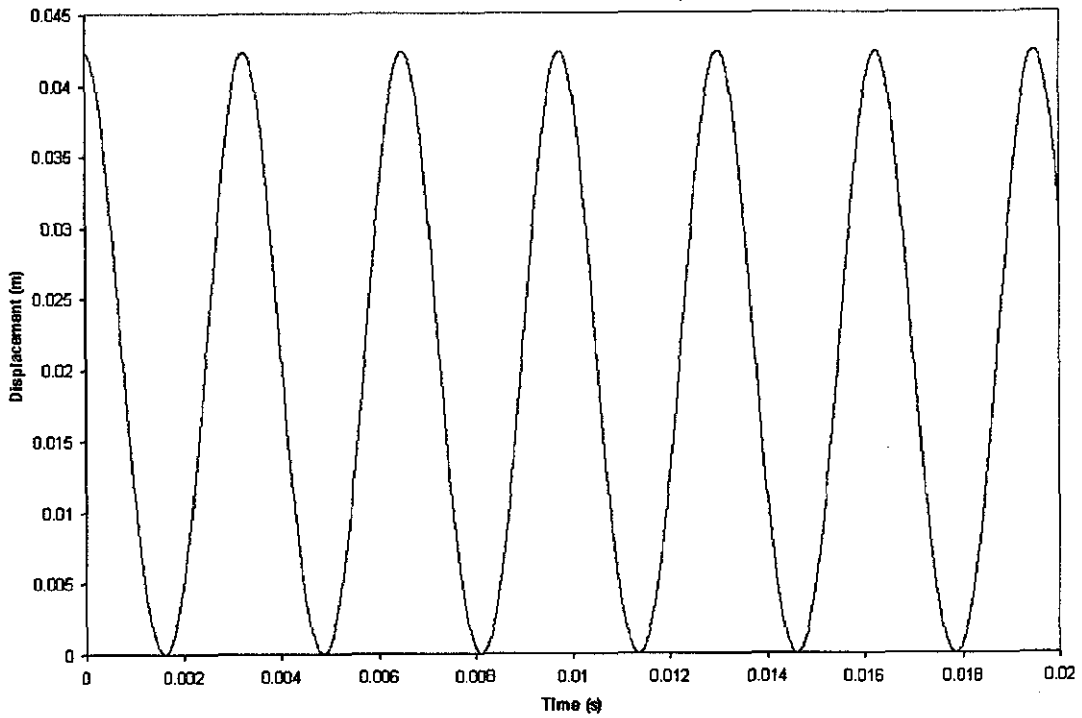
Figure 3.8: Displacement characteristic for a F1 engine at maximum engine speed of 18500rpm
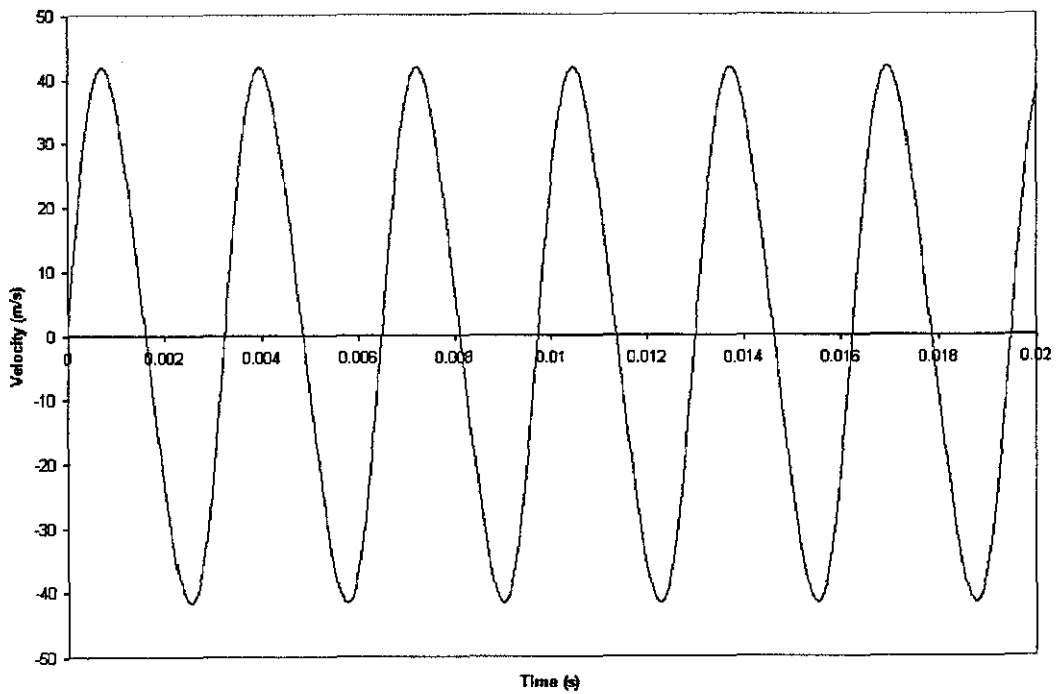
Figure 3.9: Velocity characteristic for a F1 engine at maximum engine speed of 18500rpm
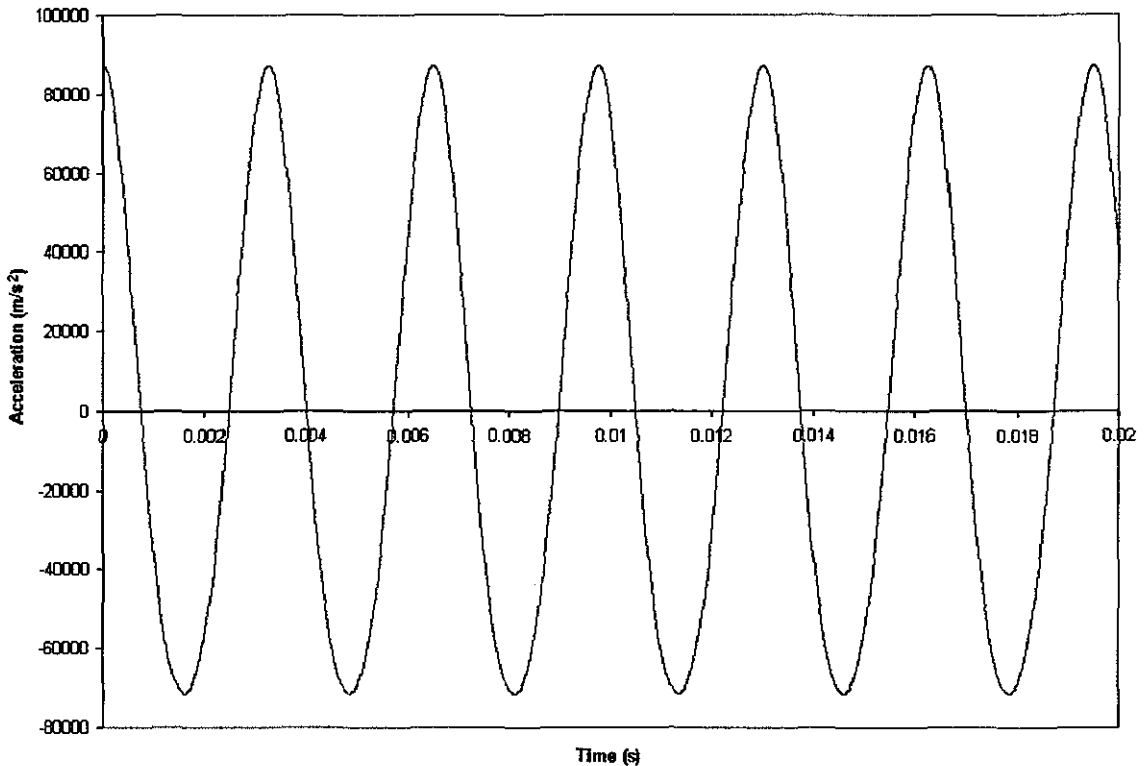
Figure 3.10: Acceleration characteristic for a F1 engine at maximum engine speed of 18500rpm

3.4 The Multi-body Dynamic Method

The dynamics of many assembled real systems such as vehicle systems are quite complex. In particular, such systems often include non-linear characteristics, such as sources of compliance (as in stiffness and damping). The assembly of parts or components, having relative degrees of freedom with respect to one another introduces constraints that are also represented by complex non-linear functions. The set of equations; the equations of motion, algebraic constraint functions and applied forces/torques require matrix formulation for simultaneous solution. Often the resulting matrices are quite large in dimensions and include many zero entries. The solution methodology, therefore, requires handling of large sparse matrices that cannot be

efficiently inverted to obtain the solution vector. In addition to this, the nature of the non-linear dynamic problems is such that in many cases a large range of response frequencies may exist. Thus, a suitable formulation and solution method must be employed in order to obtain the required system response in small discrete steps of time.

Considering the presented constraints, the simulation models should be developed, using powerful simulation software such as *ADAMS*. A description of *ADAMS'* modelling methodology is provided in section 3.4.4. In this chapter the mathematical approach in problem formulation, using multi-body theory is highlighted.

3.4.1 Lagrange's Equation for Constraint Systems

For each part of the multi-body piston assembly model, a set of equations of motion is established using the *Lagrange's* equation for constrained systems (**Lagrange** (1788)):

$$\frac{d}{dt}\{\frac{\partial K}{\partial q}\} - \frac{\partial K}{\partial q} - F_q + \sum_{n=1}^{m} \lambda_n \frac{\partial C_n}{\partial q} = 0 \qquad [3.32]$$

where, K is kinetic energy, F_q represents the generalised forces, C_n represents the constraint function and λ_n represents the *Lagrange* multipliers, n represents the number of constraint functions and $\{q\}$ is the vector of generalised co-ordinates. The generalised forces are given by **Euler** (1767) as:

$$F_q = \frac{\partial U}{\partial q} \qquad [3.33]$$

where U is the potential or strain energy.

For an unconstrained part in space, six equations of motion yields $\{q\} = \{x, y, z, \varphi, \gamma, \phi\}$, where $\bar{x}, \bar{y}, \bar{z}$ are the position vectors and φ, γ, ϕ are the first, second and third Euler angles. For constrained systems such as the piston assembly, some of the equations of

43

motion are represented by zero entries in the final Jacobian matrix. The constraint function formulation is shown in the following section.

3.4.2 Constraint Functions
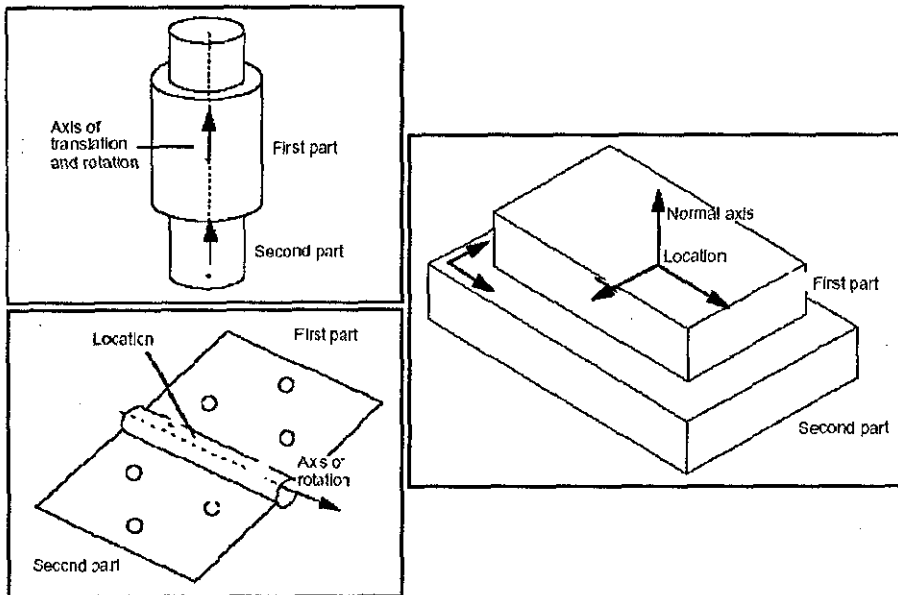
Figure 3.11: Holonomic constraints used in building the piston assembly (taken from source: *ADAMS View* manual)

The constraint functions C in equation [3.32] depend on the types of joints (see figure 3.11) that are employed to represent the physical constraints in the piston assembly. For example, for the motion of piston in a bore, an in-plane joint is used. There is, in the case of an in-plane joint, one constraint function, removing the freedom of the piston to leave the $y - z$ plane. This constraint is:

$$\vec{s}_{ij} \cdot \vec{z}_j = 0 \qquad\qquad [3.34]$$

Likewise, for a cylindrical joint, the four constraining functions are:

$$\vec{z}_i \cdot \vec{x}_j = 0, \ \vec{z}_i \cdot \vec{y}_j = 0, \ \vec{s}_{ij} \cdot \vec{x}_j = 0, \ \vec{s}_{ij} \cdot \vec{y}_j = 0 \qquad [3.35]$$

and for a revolute joint, the five constraints are expressed as:

$$\vec{y}_i \cdot \vec{x}_j = 0, \ \vec{y}_i \cdot \vec{z}_j = 0, \ \vec{x}_i \cdot \vec{z}_j = 0, \ \vec{s}_{ij} \cdot \vec{x}_j = 0, \ \vec{s}_{ij} \cdot \vec{z}_j = 0 \qquad [3.36]$$

where $\vec{x}$, $\vec{y}$, $\vec{z}$ are the position vectors of points i and j on two adjacent bodies, subjected to the constraints set by the above equations. $\vec{s}_{ij}$ is the position vector of the point i in the frame of reference of point j. Equation [3.34] constrain the translational motion of point i with respect to the axis of point j in the z-axis (**Rahnejat** (1998)). $\vec{S}_{ij}$ is the instantaneous relative position of point i with respect to point j.

$$\vec{S}_{ij} = (\vec{R}_i + \vec{r}_i) - (\vec{R}_j + \vec{r}_j) \qquad [3.37]$$

where: $\vec{R}_i, \vec{R}_j$ are the position vectors of points i and j with respect to the fixed Cartesian global frame of reference, $\vec{r}_i, \vec{r}_j$ are the position vectors of points i and j from local part frames of reference attached for example to the piston and the engine, in this case. Clearly, the various joints in the multi-body model described are formulated in the same manner to constrain the unwanted degrees of freedom.

3.4.3 Formulation of Generalised Forces

The applied forces in the model, as well as the sources of compliance are modelled as generalised forces $\vec{F}_q$ as shown in the *Lagrange's* equation [3.32]. This includes the combustion force and the contact force (described in section 3.4.14).

3.4.4 The Jacobian Matrix

The set of differential equations of motion, scalar constraint functions, applied forces and force characteristics of the various sources of compliance have to be solved in each small step of time. The vector of unknowns includes the system state variables; position, velocity and acceleration of all parts, and the *Lagrange* multipliers representing the joint reactions. Thus, in the matrix from the set of equations are represented as:

$$[J]\{q,\lambda\}^T = \{F_q\} \qquad\qquad [3.38]$$

where [J] is the *Jacobian* matrix, $\{q,\lambda\}^T$ is the required solution vector in all small time steps, dt, and $\{\vec{F}_q\}$ is the vector of applied forces. The *Jacobian* matrix is of the following form (**Orlandea (1977)**, **Chance (1967)** and **Rahnejat (1998)**):

$$[J] = \begin{bmatrix} \left[\dfrac{s}{dt}\dfrac{\partial K}{\partial \dot{q}} + \dfrac{\partial K}{\partial q} \right] & \left[\dfrac{\partial C}{\partial \lambda} \right] \\ \left[\dfrac{\partial C}{\partial q} \right] & [0] \end{bmatrix} \qquad\qquad [3.39]$$

where, [J] is the *Jacobian* matrix, s represent the position of a point, K represents the kinetic energy, C represents the constant function, q is the vector of generalised co-ordinates, λ represents the *Lagrange* multiplier and t is time.

The *Jacobian* matrix, as shown in equation [3.39], consists of a number of sub-matrices, relating to the mass/inertial contributions, constraint functions and the corresponding joint reactions, given as *Lagrange's* multipliers. The *Jacobian* matrix contains many zero entries, thus being referred to as sparse. The *Jacobian* matrix is also quite large in dimensions, as it embodies appropriate coefficients for 6 equations of motion per model part as defined above, and all the formulated constraint functions for the joints in the

model. In fact fewer than 10% of all the elements of the matrix are usually non-zero (**Kushwaha** (2000), **Kelly** (2000), **Hegazy** (1999)). The solution to equation [3.38] is obtained in small variable time steps, *dt*, employing the predictor-corrector technique (see Section 3.4.9), *Newton-Raphson* method (see section 3.4.7) for the solution of a non-linear set of simultaneous equations, and step-by-step integration using a "stiff" (see section 3.4.10) algorithm for a widely split eigenvalue problem.

3.4.5 The Solution Methodology

The *Jacobian* matrix is a sparse matrix. This is a matrix, where most of its elements are zero. The *Jacobian* matrix also contains the terms that provide a mix of linear and non-linear algebraic equations (i.e. constraints functions and generalised forces) and differential equations of motion. The *Jacobian* matrix for a multi-body system is usually a very large square matrix. Therefore, it is difficult, if not impossible, to invert such a matrix in order to solve the simultaneous set of equations given by equation [3.39]. Thus, *Cholesky's* factorisation process is used for this purpose (**Schiehlen** (1990)). The sets of equations in most multi-body systems are non-linear in nature. *Newton-Raphson* method is employed for the solution of these non-linear equations. The vector of the state variables includes a set of derivatives, usually of the first order since the problem is normally presented in first order by using the following substitutions:

$$\varsigma = \frac{dq}{dt} \qquad\qquad [3.40]$$

$$\varsigma' = \frac{d^2q}{dt^2} \qquad\qquad [3.41]$$

where q is the generalised co-ordinate set (i.e. the state variables), ς is the vector of the state variables in the first order formulation, ς' is the vector of the state variable derivatives and t is time.

This means that the state variables and the state variable derivatives in each time step must be evaluated by the process of discretisation of the differential equations of motion using a time marching integration method. This process is carried out using recursive backward difference formulas in a predictor-corrector procedure, also employing the *Gear* integration algorithm (**MDI** (1994), **Kushwaha** (2000), **Hegazy** (2000) and **Centea** (1997)).

3.4.6- LU Decomposition (Cholesky factorisation)

For a set of linear equations which has to be repeatedly solved with different inhomogenous terms, the *LU* decomposition is recommended (**Orlandea** *et al* (1977)). The *LU* decomposition represents the replacement of the *Jacobian* matrix by a product of two triangular matrices, known as the lower and the upper triangular matrices. In the lower triangular matrix all the non-zero elements occupy the triangle on or below the diagonal, whilst in the upper triangular matrix all such terms reside on or above the diagonal. Therefore:

$$[L]\cdot[U]=[J] \qquad \text{[3.42]}$$

where: $[J]$ is the Jacobian, $[L]$ is the lower matrix and $[U]$ is the upper matrix.

Thus, the equation [3.40] becomes:

$$[J] \cdot \{q, \lambda\}^T = \{F_q\} \qquad [3.43]$$

where: $[J]$ is the *Jacobian*, $\{q, \lambda\}^T$ is the solution vector and $\{F_q\}$ is the vector of applied forces.

The *LU* decomposition can be used to solve equation [3.43] as follows:

$$[J] \cdot \{q, \lambda\}^T = ([L] \cdot [U]) \cdot \{q, \lambda\}^T = [L] \cdot ([U] \cdot \{q, \lambda\}^T) = \{F_q\} \qquad [3.44]$$

Equation [3.44] can then be represented by a pair of matrix equations. The first step is to solve for $\{V\}$ vector as indicated below:

$$[L] \cdot \{V\} = \{F_q\} \qquad [3.45]$$

and afterwards by solving:

$$[U]\{q, \lambda\}^T = \{V\} \qquad [3.46]$$

This set of matrix equations is sufficient for the solution of a linear system. However, the set of equations in the multi-body systems described in this thesis is non-linear, requiring the use of *Newton-Raphson* method.

3.4.7 The Newton - Raphson Method

The *Newton-Raphson* method can be employed for the solution of a system of non-linear equations. This method is based upon the approximation of a characteristic curve $f(q, \lambda)$ with a straight line near the point of solution, where $f(q, \lambda) = 0$.

$f(q, \lambda)$ is the solution curve for the problem at hand. The solution is obtained by an iterative process, where current values for the characteristic curve are obtained from

49

previously determined solutions and the gradient of the curve in the vicinity of the point of solution, as:

$$f(q,\lambda)_{n+1} \approx f(q,\lambda)_n + \frac{\partial f}{\partial q} \cdot \nabla q_{n+1} \qquad [3.47]$$

$$[J] = \frac{\partial f}{\partial q} \qquad [3.48]$$

$$\nabla q_{n+1} = q_{n+1} - q_n \qquad [3.49]$$

where f is the solution curve, *[J]* is the Jacobian and ∇q_{n+1} is the vector of backward differences.

The historical data in the above equations is obtained by approximating the solution trend from previous known values, using polynomial fits in the predictor-corrector procedure, based on *Newton* interpolations.

3.4.8 Newton Interpolations

A set of data points can be interpolated using polynomial, spline or rational functions, *Fourier* series or other possible ways. Polynomial interpolation uses a polynomial to fit a given set of points. The most important one-dimensional interpolation schemes are the *Lagrange* interpolation, *Newton* interpolation, *Lagrange* interpolation using *Chebysev* points, *Hermite* interpolation or a cubic spline interpolation (**Nakamura** (1992)).

The predictor-corrector procedure described in section 3.3.4 uses *Newton* interpolation because the order of the polynomial can be changed easily and the evaluation of the errors can be obtained readily.

There are two versions of the *Newton* interpolations: the Newton forward interpolation and the *Newton* backward interpolation.

A function f, can be represented by a set of discrete points (x_n, f_n). A subset of these points can be selected. The set (i.e $n = 0,1,2,3$ or $n = 3,4,5,6,7$) has $m+1$ points (m being 3 and 4 respectively in this example). An interpolation polynomial function $p(x)$ has to be found to fit the given points (see Figure 3.12).

The forward differences $\Delta^n f_n$ are defined by **Nakamura** (1992) as:

$$\Delta^0 f_n = f_n \qquad\qquad [3.50]$$

$$\Delta f_n = f_{n+1} - f_n \qquad\qquad [3.51]$$

$$\Delta^k f_n = \Delta^{k-1} f_{n+1} - \Delta^{k-1} f_n \qquad\qquad [3.52]$$

where, f_n is a function given by a set of consecutive data points (x_n, f_n), n is a point within a specific set of points, k is the order of forward difference with $0 \leq k \leq m$ and $m+1$ is the number of points in the selected set.
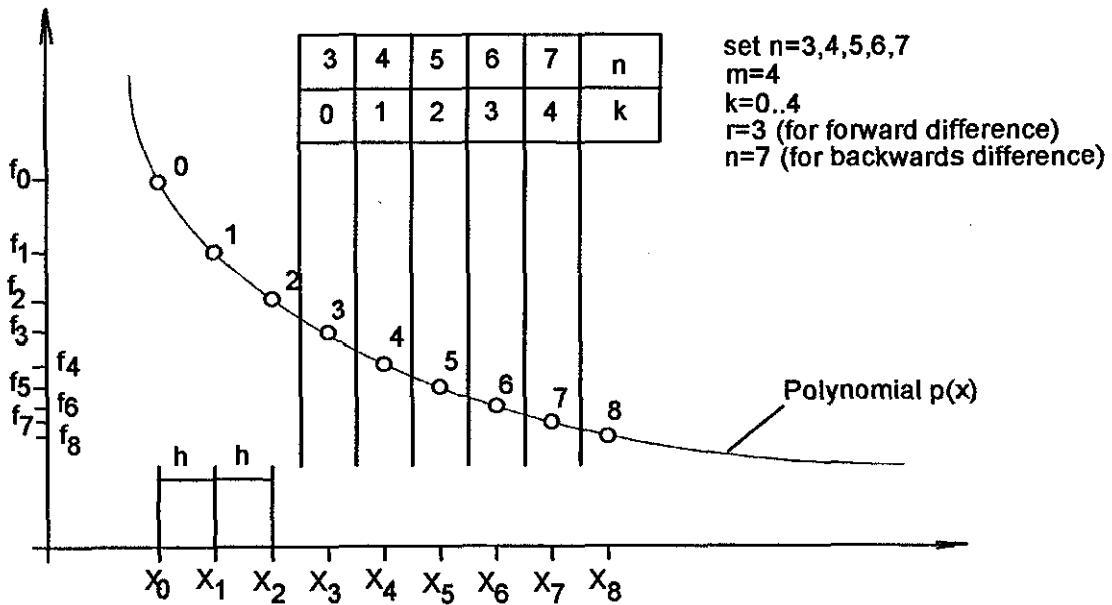
Figure 3.12: The interpolation polynomial

The backward differences $\nabla^n f_n$ are defined as:

$$\nabla^0 f_n = f_n \qquad\qquad [3.53]$$

$$\nabla f_n = f_n - f_{n-1} \qquad\qquad [3.54]$$

$$\nabla^k f_n = \nabla^{k-1} f_n - \nabla^{k-1} f_{n-1} \qquad\qquad [3.55]$$

where, f_n is a function given by a set of consecutive data points (x_n, f_n), n is a point in a chosen set of points defined within the total number of given points, $m+1$ is the total number of points within the selected set and k is the order of backward difference with $0 \le k \le m$.

The equivalence relationship between the forward difference and the backward difference is given by **Nakamura** (1992) as:

$$\nabla^k f_k = \Delta^k f_{n-k} \qquad \text{[3.56]}$$

and the *Newton* forward interpolation formula which defines an interpolation function f is defined as:

$$p(x) = p(x_r + s \cdot h) = \sum_{k=0}^{m} \binom{s}{k} \Delta^k f_0 \qquad \text{[3.57]}$$

where, p is the value of the function which has to be found by interpolation, x_r is the abscissa of the first point in the selected set, h represents the constant distance between any two consecutive points on the abscissa ($h = x_1 - x_0 = x_2 - x_1$ - see Figure 3.12), and s is the local co-ordinate defined as:

$$s = \frac{x - x_r}{h}, \quad 0 \le s \le k \qquad \text{[3.58]}$$

where, subscript r is the order of the first abscissa from the selected set of data points, x is the current abscissa and h is the constant interval along the abscissa.

The *Newton* backward interpolation formula is defined as:

$$p(x) = p(x_n + s \cdot h) = \sum_{k=0}^{m} \binom{s+k-1}{k} \cdot \nabla^k f_n \qquad \text{[3.59]}$$

where, p is the value of the polynomial function which has to be fitted by interpolation through the given points, x_n is the abscissa of the last point in the selected set, h represents the constant distance between any two consecutive points on the abscissa and s is the local co-ordinate defined as:

$$s = \frac{x - x_n}{h}, \quad -k \le s \le 0 \qquad \text{[3.60]}$$

where, n is the order of the last abscissa point from the selected set, x is the current value and h is the constant interval.

By introducing the equation [3.56] in [3.59], the equation of the backward differences can be expressed in terms of forward differences (**Nakamura** (1992)) as:

$$p(x) = \sum_{k=0}^{m} \binom{s+k-1}{k} \cdot \Delta^k f_{n-k} \qquad [3.61]$$

where, $p(x)$ is the interpolation polynomial, s is the actual co-ordinate defined in equation [3.60], k is the counter and n is the order of the point from which the backward interpolation commences.

Both the forward and the backward *Newton* interpolations are mathematically equivalent. The selection of one or the other expression depends on how the formulae are applied. The predictor-corrector procedure uses the *Newton* backward interpolation because data points are all in the backward position.

3.4.9 Predictor-Corrector Method

A predictor-corrector method consists of a predictor step and a subsequent corrector step in each time interval. The predictor provides an estimate for the solution vector at the new point, whilst the corrector improves the accuracy of the solution. A polynomial is fitted to the previous solutions and interpolation is carried out to obtain the slope at various points.

The interpolation polynomial p is fitted to the function ς' (referred to as f in section 3.4.7) defined in time steps (the abscissa x from section 3.4.7 is the time t) at points n, $n-1$..., $n-m$ may be written using the *Newton* backward interpolations formulae [3.61], as shown by **Nakamura** (1992):

$$p_m(t) = \sum_{k=0}^{m}(-1)^k \binom{s+k-1}{k} \cdot \Delta^k \varsigma'_{n-k} \qquad [3.62]$$

where, p in the polynomial interpolated function, $\binom{s+k-1}{k}$ is the binomial coefficient, $m+1$ is the number of points within the chosen set of points, k is the loop counter, $\Delta^n \varsigma'_{n-m}$ is the forward difference term and s represents the local co-ordinate, defined by substituting the abscissa x in equation [3.60] with time t:

$$s = \frac{t-t_n}{h} \qquad [3.63]$$

where, t is the time at the point where the interpolation polynomial has to be found and t_n is the abscissa of the last used point.

By using the *Runge-Kutta* method, in order to calculate the following point ς_{n+1} at $t_{n+1} = t_n + h$ with a known value of ς_n, the following integral, is evaluated by **Nakamura** (1992):

$$\varsigma_{n+1} = \varsigma_n + \int_{t_n}^{t_{n+1}} f(\varsigma,t) \cdot dt \qquad [3.64]$$

Substituting equation [3.62] into equation [3.64], the *Adams-Bashford* predictor formula for m^{th} order is obtained as:

$$\varsigma_{n+1}^p = \varsigma_n + h\left[b_0 \cdot \varsigma'_n + b_1 \cdot \Delta \varsigma'_{n-1} + \cdots + b_m \cdot \Delta^m \varsigma'_{n-m} \right] \qquad [3.65]$$

55

where, the superscript p represents the predictor phase, $b_0..b_n$ represent the polynomial coefficients and the vector ς is given by a set of already calculated points..

The polynomial coefficients b_k in equation [3.65] are defined as:

$$b_k = \int_0^1 \binom{s+k-1}{n} \cdot ds \qquad [3.66]$$

where, s is the local co-ordinate, k is the counter and n represents the point of interest.

The first few values of b_n, shown by **Nakamura** (1992), are:

$$b_0 = 1 \qquad [3.67]$$

$$b_1 = \frac{1}{2} \qquad [3.68]$$

$$b_2 = \frac{5}{12} \qquad [3.69]$$

$$b_3 = \frac{3}{8} \qquad [3.70]$$

$$b_4 = \frac{521}{720} \qquad [3.71]$$

The corrector formula may be derived in the same manner. The polynomial interpolation for the slope in this phase is given by the following relationship:

$$p(t) = \sum_{k=0}^{m} \binom{s+k-2}{k} \cdot \Delta^k \varsigma'_{n+1-k} \qquad [3.72]$$

where, p is the polynomial interpolated function, $\binom{s+k-2}{k}$ is the binomial coefficient, $m+1$ is the number of points of the chosen set of points, k is the loop counter, $\Delta^n \varsigma'_{n-m}$ is the forward difference term and s represents the local co-ordinate defined by substituting the abscissa x in equation [3.60] with the time t defined in equation [3.63].

The *Newton* backward difference formula, fitted in the case of the corrector, using forward integration differences is, therefore, obtained by substituting equation [3.72] into equation [3.64]:

$$\varsigma_{i+1}^c = \varsigma_i + h\left[c_0 \cdot \varsigma'_{i+1} + c_1 \cdot \Delta\varsigma'_i + \cdots + c_m \cdot \Delta^m \varsigma'_{i-m} \right] \qquad [3.73]$$

where, the superscript c represents the corrector phase and c_n represents the polynomial coefficients defined as:

$$c_k = \int_0^1 \binom{s+k-2}{k} \cdot ds \qquad [3.74]$$

where, s is the local slope.

The first few values of c_n follow from **Nakamura** (1992) are:

$$c_0 = 1 \qquad [3.75]$$

$$c_1 = -\frac{1}{2} \qquad [3.76]$$

$$c_2 = -\frac{1}{12} \qquad [3.77]$$

$$c_3 = -\frac{1}{24} \qquad [3.78]$$

$$c_4 = -\frac{19}{720} \qquad [3.79]$$

The advantage of the predictor-corrector methods is their computational efficiency, **Nakamura** (1992), being evaluated in a lower number of steps (regardless of the order of the predictor-corrector method) as required by the fourth order *Runge-Kutta* method. Furthermore, the technique permits detecting at each step the local error with a small computational effort.

The disadvantage of the method is that it cannot start by itself, because of the need to use previous data points. Another method such as *Runge-Kutta* may be used to start the iterative process.

3.4.10 Gear Stiff Integration

Stiffness refers to a very short time constant of an ordinary differential equation. Stiff differential equations frequently arise in physical equations due to the existence of greatly differing time constants (**Gear** (1971)). A system is stiff when its largest inactive eigenvalue is much larger that its largest active eigenvalue.

A numerical integrator approximates the solution by a polynomial which satisfies the system governing equations at discrete time intervals. The error of integration during one integration step is related to the first omitted derivative in the truncated *Taylor* series that represents the polynomial. Therefore, fixed step size integrators can behave well with systems having close eigenvalues. When the smallest eigenvalue is active, costly unnecessary computation can result. The variable step-size *Gear*-type integrators, **Gear** (1971), allow the integration step size to be automatically altered according to an estimate of the local truncation error, making them particularly suitable and fast in dealing with stiff systems.

The *Gear* stiff integrator is used in *ADAMS* is called *Gstiff*. It stores the information relating to the "historical" polynomial as the analysis moves in time in the form of a

58

Nordsieck vector, which is a particular form of representation of the *Taylor* series (**Nakamura** (1992)). Every time a new value is calculated, a corresponding error is also calculated. If the estimated error is greater than a specified error tolerance, a new smaller time step is used and the value obtained is better fitted to the curve.

3.4.11 Integration error control

Each integration step consists of two phases: predictor and corrector. The predictor (**MDI** (1994)) uses the previous values of each variable to predict the value of the variable at the end of the current integration time step. The corrector uses the predicted values as the initial guesses to solve the system state equations using *Newton-Raphson* iterations.

The integrator error is the difference between the solution of a differential equation and its direct analytical solution. The difference between analytical solution and the numerical approximation at any time, t, is called the "*Global Integration Error*", where the "*Local Integration Error*" is the error which occurs during a single integration step time, *dt*.

Using the information about the numerical method an upper bound for the *Local Integration Error* can be estimated. The argument related to *Gstiff* integrator controls the integration error associated with the state variable ς. The integration error for state variable derivates, $\dot{\varsigma}$, will be less than or equal to *error/dt*, where *dt* is the integration step size. The integration for acceleration and forces will be the order of $\leq error/dt^2$. These integration error limits apply to the solution approximation to the differential and algebraic equations by Taylor series polynomial for the predictor phase. According to *Taylor's* remainder theorem, the principle term in the local truncation error in an interval of time *dt* is:

$$R_k \leq \varsigma^{k+1} \cdot \hat{f} \cdot \frac{dt^{k+1}}{(k+1)!}$$

[3.80]

where, *k+1* indicates the (k+1)th derivate term with respect to time and $\hat{f}$ is a multiplier maximising the value of ς^{k+1}. During the corrector phase the integrator ensures that the largest change in a variable will not exceed *error/1000*. Two methods used to ensure the satisfaction of the upper limit are:

the absolute method:
if $v_c \leq 1$ then

$$\chi \leq \frac{error}{1000}$$ [3.81]

the relative method
if $v_c > 1$ then

$$\frac{\chi}{v_{max}} \leq \frac{error}{1000}$$ [3.82]

where, v_c is the absolute value of the corrected variable with the largest change during an iteration, v_{max} is the largest past value of v_c and χ is the absolute value of change in v_c, **MDI** (1994).

3.4.12 Modelling Procedure

ADAMS is multi-body simulation software used to study the behaviour of systems consisting of rigid bodies undergoing large displacements (see section 3.2). It can be used to predict characteristics of a new design, to evaluate the performances of an existing design or to investigate extreme operating conditions. It has an open-ended architecture that allows users to create extensions using data set features and external subroutines (**MDI** (1994)).

A model consists of part geometry and mass properties, reference frame definitions, body types, body compliance description, topological and analytical constraints and externally applied forces. The spatial generalised co-ordinates consist of three Cartesian co-ordinates for each part's centre of mass with respect to the global reference frame and three *Euler* angles defining the orientation of the central principal axes of inertia of each part relative to mutually perpendicular, inertially fixed axes, **MDI** (1994).

First step in modelling is to define reference frames and co-ordinate systems. The program allows these to be inertially fixed or moving. Then, physical components of the mechanical system are modelled using idealised *ADAMS* parts, which can be either rigid bodies, flexible bodies or particles.

Markers are orthogonal triads of unit vectors which mark points of interest on a part. The markers are necessary in order to define joints, forces, centre of mass and inertia, etc. Markers can also be used when the displacement of a certain location of a part with respect to other points in the model is of interest, by placing two markers on the appropriate locations and requesting the desired information.

Parts are elements which possess mass and inertia properties and geometric properties in order to visualise the model or to use the animation. The mass, inertia and geometric properties of the parts are usually given by the product suppliers. If not given, the values can be measured. The parts (their mass or inertial properties) used to construct the single cylinder piston model is described shown in table 3.1.

After defining the parts, the next step in building an *ADAMS* model is to describe the possible relative motions between the parts of the system by specifying the type of mechanical joints (holonomic constraints). The joints are perfectly rigid constraints allowing only a relative motion of the two parts in accordance to the joint type. The holonomic constraints used to connect the individual parts (to each other and ground) are

presented In table 3.2. The constraint equations for the corresponding constrains are shown in previous section, 3.2.

Joints can be defined between two parts, referred to as I part and J part, by specifying their names, location and orientation or by specifying markers on the two parts. *ADAMS* permits description of the components of the system in terms of graphic (see figures 3.11, 3.13) primitives and icons which are used to track the motion of the system visually. The graphic representation of the models described, are presented in figure 3.13.

3.4.13 Single Cylinder Engine Model

A single cylinder internal combustion engine multi-body model, developed in this thesis, using ADAMS (see figure 3.13) comprises an assembly of inertial elements; piston, connecting rod and crankshaft. The assembly of parts has been achieved by the use of holonomic constraint (see figure 3.11) functions (**MDI (1994)**) (see section 3.4.2), provided in *ADAMS*.
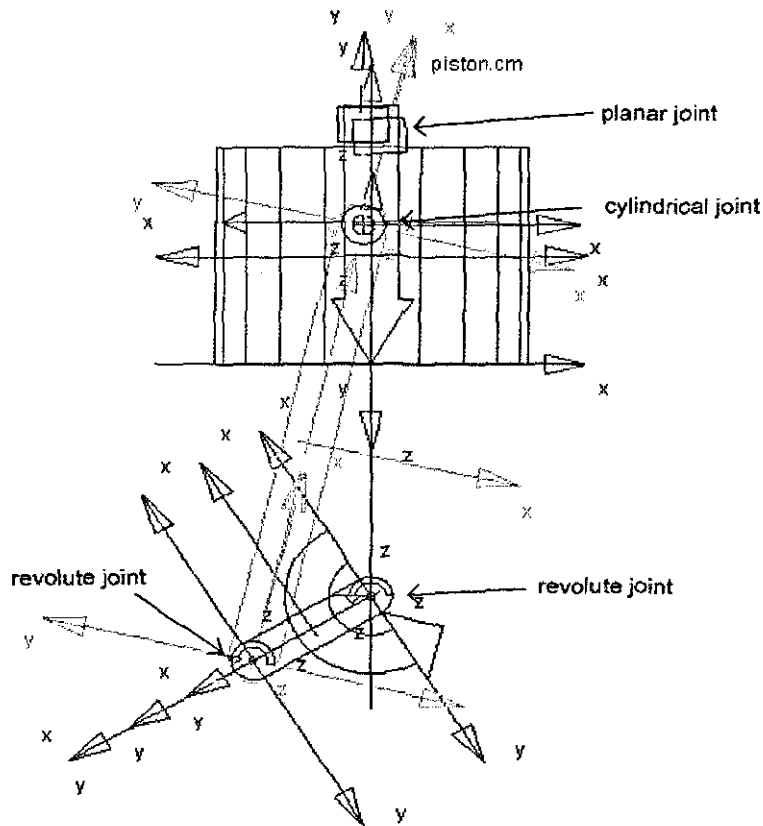
Figure 3.13: Screen-capture of piston-assembly model from *ADAMS*

All the rigid body inertial properties of the parts; mass and mass moments of inertia are given in table 3.1. The joints and other constraining elements in the multi-body dynamic model are given in table 3.2. The table indicates the number of constraints imposed by each holonomic constraint in the assembly of the model.

Part Name	Mass (kg)	Ixx (Kgmm²)	Iyy (Kgmm²)	Izz (kgmm²)
Piston	0.5 – 0.8	500 – 900	500 – 900	450 – 870
Conrod	0.8 – 1.0	2000 – 5000	400 – 650	2000 – 5000
Crank	0.2 – 0.5	75 – 90	75 – 90	100 – 150

Table 3.1: Parts in the multi-body single cylinder engine model

I_Part	J_Part	Constraint Type	DOF Removed
Piston	Conrod	Cylindrical	4
Piston	Ground	In Plane	1
Connection rod	Crank	Revolute	5
Crank	Ground	Revolute	5
Ground	Piston	Contact	0

Table 3.2: Constraints in the multi-body single – cylinder engine model

To allow the piston to "float" in the cylinder bore, a contact force was introduced, between ground (in this case, acts as bore) and piston. A clearance was specified as design variable parameter, allowing the contact force to be activated when the piston penetrates into the bore, which occurs when the specified clearance is breached. The clearance, c_i is specified as $50.0\mu m$. The contact force is modeled here is based upon *IMPACT-Function-Based-Contact* (**MDI** (2001). The force is essentially modeled as a nonlinear spring-damper, with the stiffness of piston (function of material, in this case steel) multiplied by penetration, e_t or e_b of piston into the bore. In the following section, a brief description of the generation of the contact force explained.

3.4.14 Contact force

The *CONTACT* statement, defines contact between two geometric entities in *ADAMS* dataset (**MDI** (2001)). The *CURVE* and the *EXTERNAL* graphics types are the generic geometry modeling entities, which describes the surface where the points (such as shown
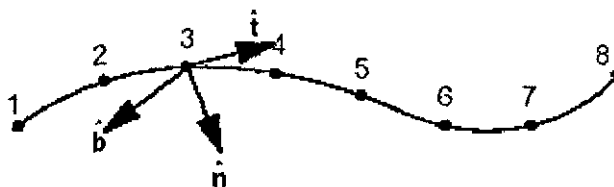
Figure 3.14: Points generated by *ADAMS/Solver* on geometry to define contact

in figure 3.14) are attached onto. If there is no contact, there is no force. If no contact exists, the geometry modeling system calculates the location of the individual contact points and the outward normals to the two geometries at the contact point. *ADAMS/Solver* calculates the normal and slip velocities of the contact point from this information. *ADAMS/Solver* then uses the velocities to calculate the contact force at each individual contact. The calculation of the outward normal velocity for geometry is important because it defines where the point on the body lies and, therefore, determines the direction of the contact normal force. The contact force is modeled based on classical Hertzian contact, as first approximation. The evaluation of contact stiffness, based upon the curvature of contacting solids and their moduli of elasticity is carried out inline with method originally proposed by **Petrenko** ((1916), this method is highlighted more recently by **Rahnejat** (1984)).

3.4.15 Operating conditions

The operating condition, in this case is similar to that in section 3.3.4 for a 1.8 litres diesel engine, except for the inclusion of the secondary dynamics of piston in this analysis. The cavity or clearance of $50.0\mu m$, between piston and bore is assumed to be void. Results obtained from the simulation are presented and discussed in the following sections.

3.4.16 Results

Once the simulation results were obtained, the numeric results are plotted in *ADAMS/Post*. In figures 3.15, 3.16 and 3.17, plots of displacement, velocity and acceleration against time are shown. The results obtained from Newton-Euler method were identical to that obtained from the multi-body analysis. In addition to the primary motions of the piston, using the contact model described in section 3.4.14, the secondary

motions of the piston were also obtained. In figures 3.18 and 3.19 (zoomed for the duration of 0.1-0.13s corresponding to 2 revolutions, for clarity of visualisation), the lateral displacement and orientation of the piston are shown. The deviation of piston from vertical axis, in figure 3.18, shows the excursion of piston from its centre-line, where the positive displacement indicates the lateral motion of piston from the minor thrust side towards the major thrust side, simultaneously rotating in anti-clockwise direction. Note that the displacement has a radial amplitude of about 0.1mm which is greater than the initial radial clearance, thus causing an impact force due to elastic deformation of the contiguous solids. Correlating with the following figure, figure 3.20 provides the magnitude of the force at the corresponding initial secondary motion, at time, $t = 0.1012$ s, which indicates that the impact generates a negative force, meaning that the impact has occurred at the major thrust side. Piecing together the three figures, 3.11, 3.19 and 3.20, suggests the lower end of the piston skirt had come into contact with the liner. This is consistent with the experimental observations (**Phen** *et al* (1993), **Brown** *et al* (1993) and **Graddage** *et al* (1993)) and numerical predictions (**Dursunkaya** *et al* (1992) and **Li** *et al* (1982)). Note that the high frequency impact reversals in figure 3.20 are due to the absence of a lubricant film, thus allowing unhindered motion of the piston towards the liner and repetitive rebounds.
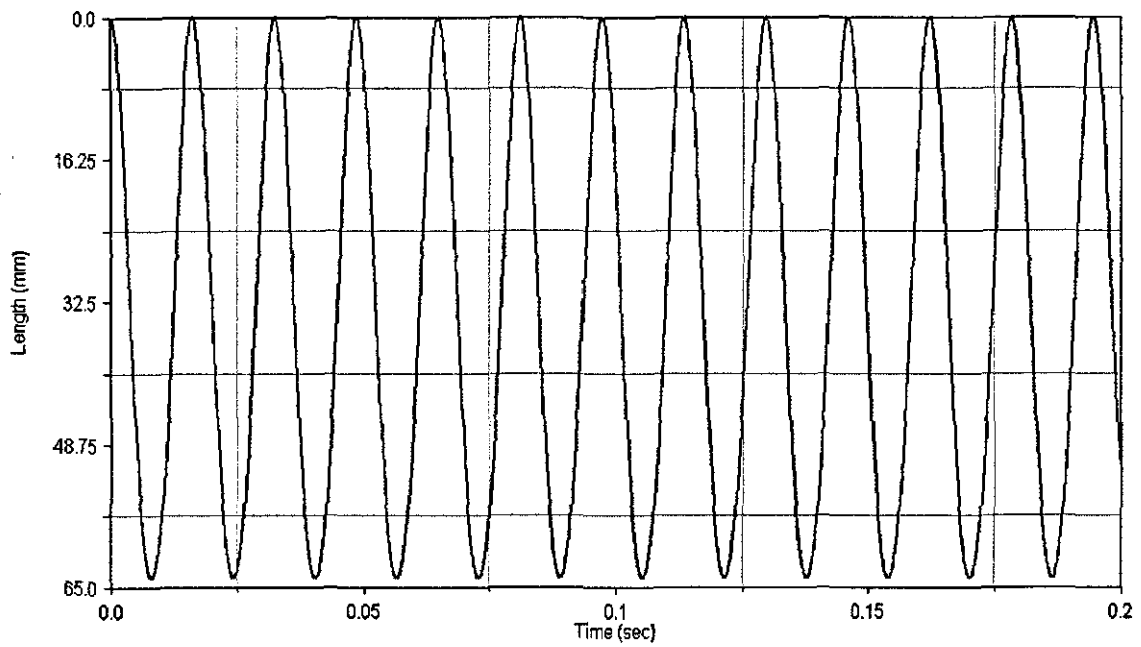
Figure 3.15: Vertical displacement of piston
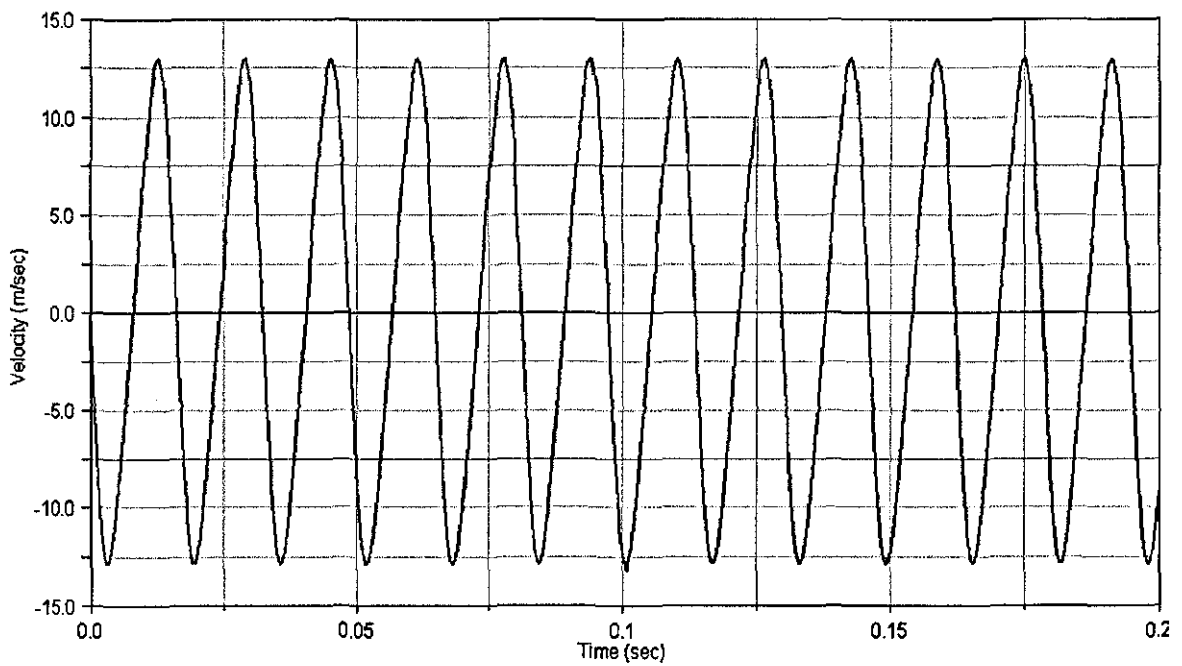
Figure 3.16: Vertical velocity of piston

67
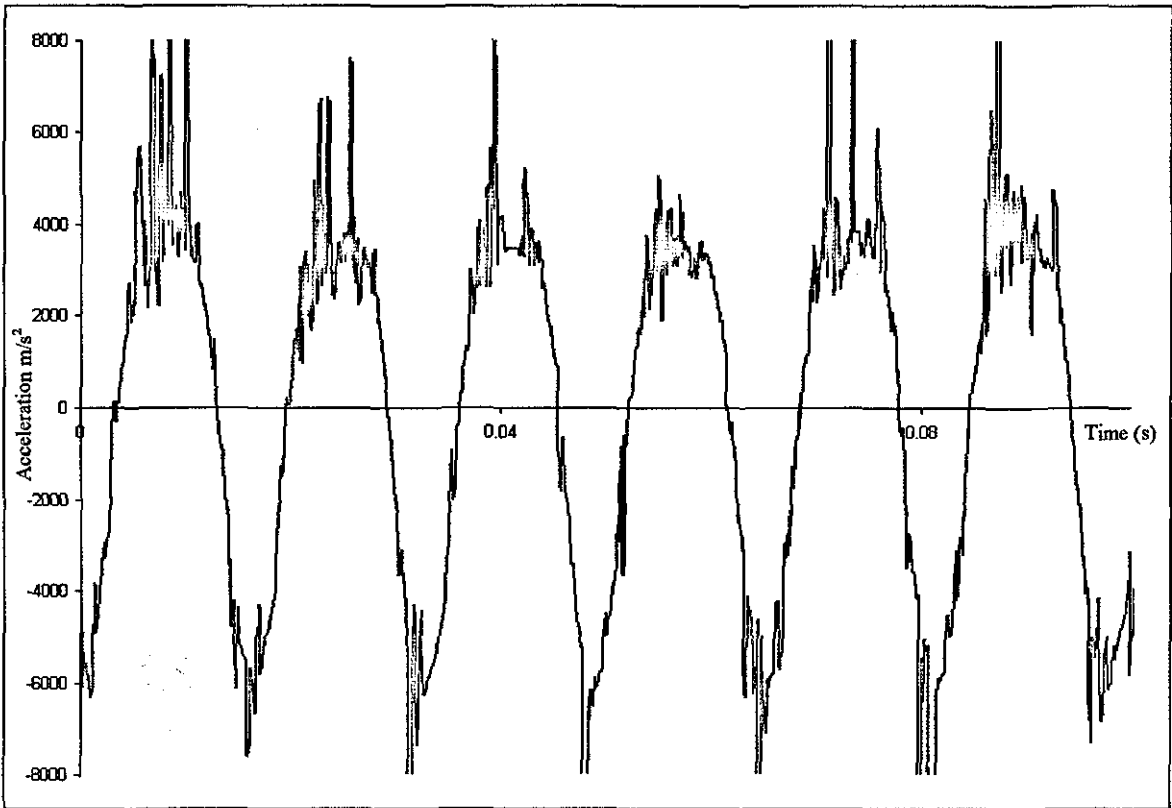
Figure 3.17: Vertical acceleration of piston
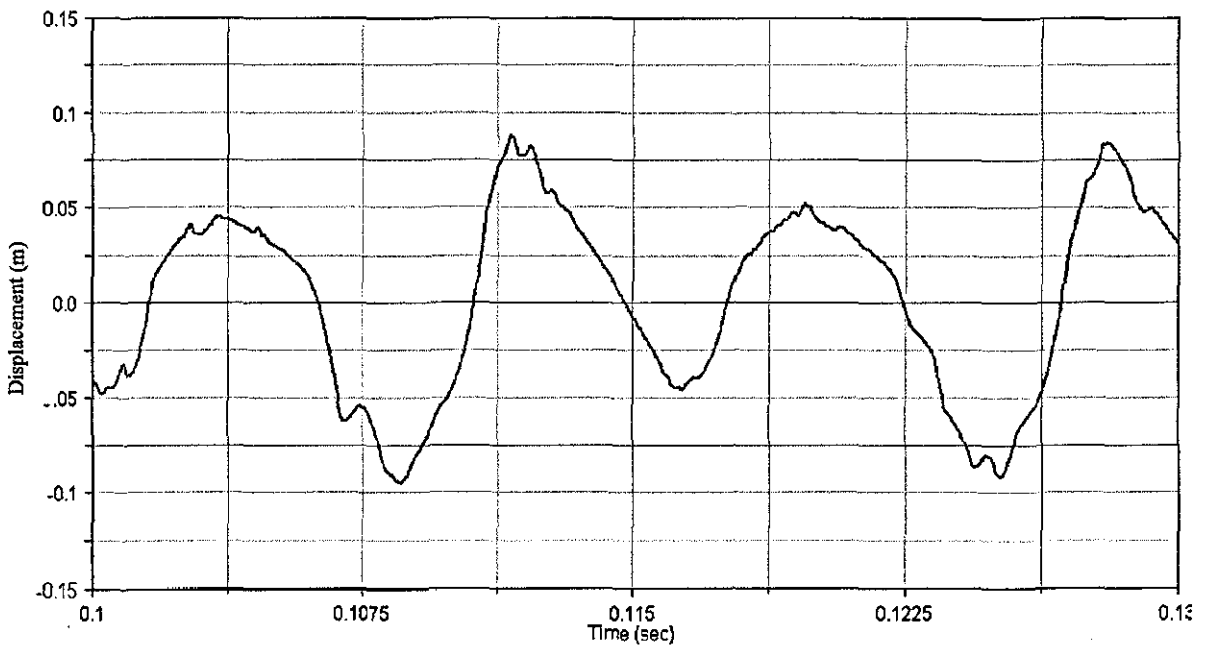
Figure 3.18: Lateral displacement of piston

68
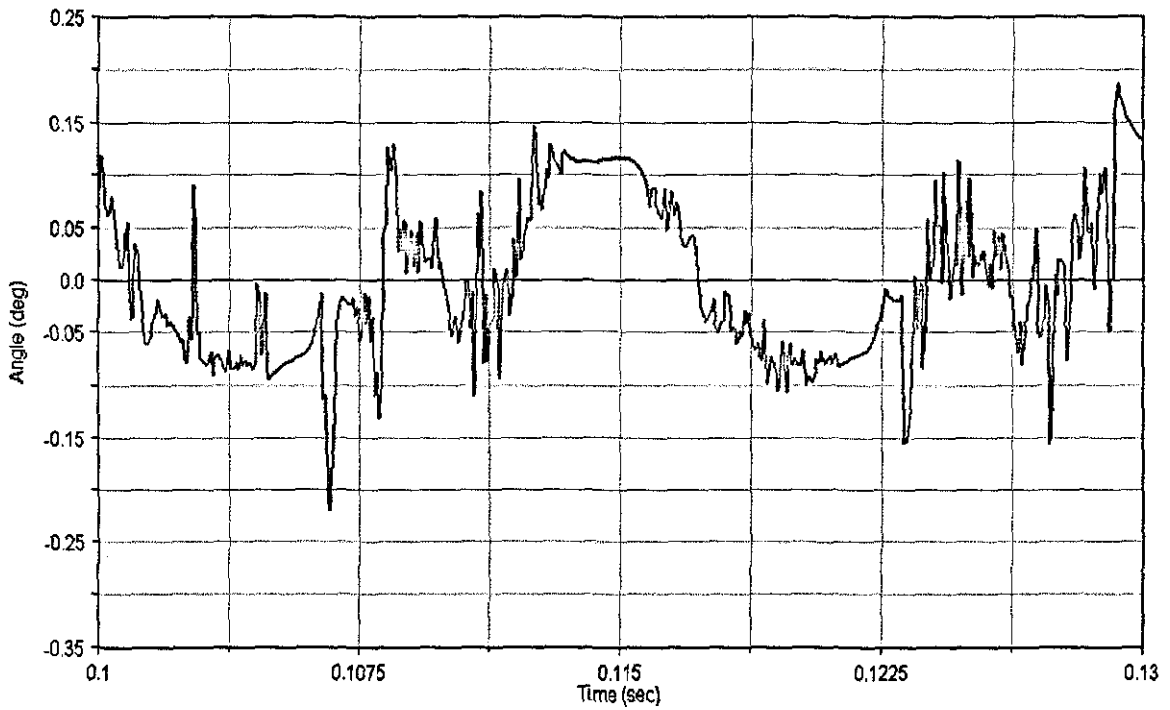
Figure 3.19: Tilt of piston about the gudgeon pin
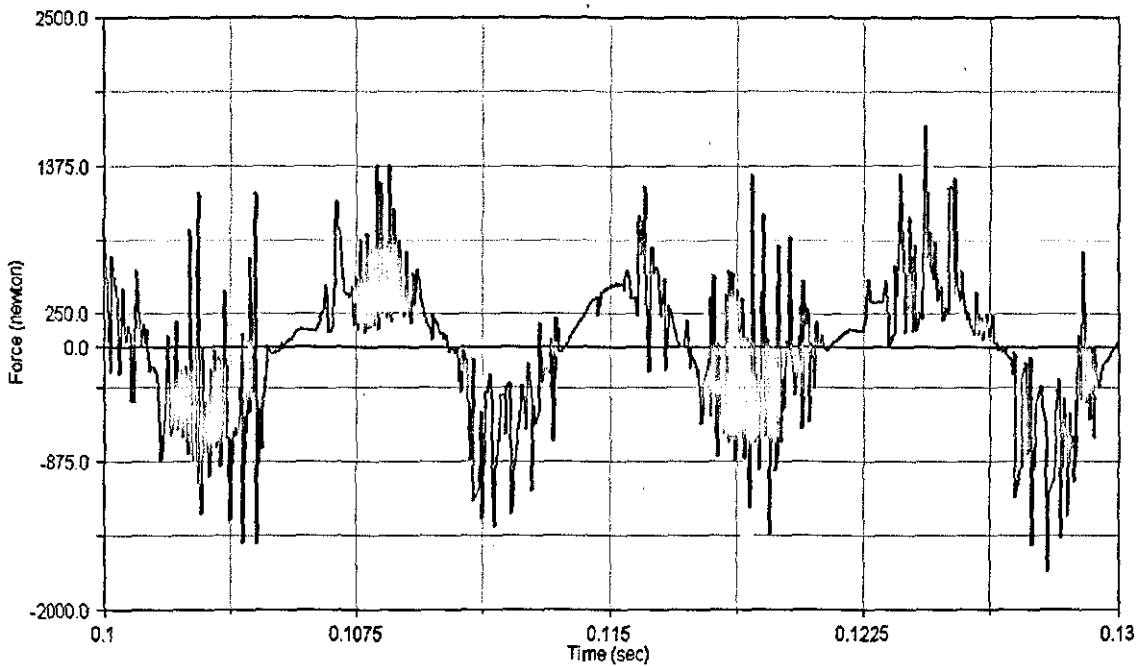
Figure 3.20: Lateral forces due to piston impacting against the cylinder liner

69

3.5 Closure

A mathematical model describing, the primary and secondary motion of the piston assembly was successfully developed. Results obtained from this model were then verified against those obtained through multi-body dynamic analysis in *ADAMS*. In addition, results of lateral displacement and tilt (secondary motion) of the piston in the *ADAMS* single cylinder engine model was simulated for a dry contact against cylinder bore.

In the following chapter, a mathematical model developed to describe the lubrication in a conformal contact is shown. These mathematical models (addressed as modules hereinafter) form the basis to the transient analysis.

Chapter 4

4.1 Introduction

In this chapter, derivation of equations that form the basis of elastohydrodynamic lubrication for conformal contacts is highlighted. Background information on lubricant rheology is explained in section 4.2. Equations used for computing the deformation of solids due to lubricant pressure are derived in section 4.3. In the following section; 4.4, the derivation of Reynolds' equation for use in quasi-static analysis is outlined, by simplifying the Navier-Stokes equations. Extension of Reynolds' equation to include the effect of elastic squeeze film, for a transient analysis, is provided in section 4.5.

4.2 Lubricant Rheology
4.2.1 Density

Density is a measure of mass per unit volume, with the S.I. unit, $\left[\frac{kg}{m^3}\right]$. Specific gravity is measure of the ratio of mass of a given volume of lubricant at temperature, t_1, with that of distilled water at temperature, t_2. For petroleum products, the specific gravity used, is usually quoted for temperature of 15.6°C.

4.2.1.1 Pressure Influence on Density

In relatively moderate pressures, the effect of pressure on density of lubricants is small. However, at very high pressures, typically seen in concentrated counterformal contacts, density change is appreciably significant and need to be included. Experimental results obtained by **Dowson** *et al* (1966) have shown that the relative change of density of lubricant due to pressure varies linearly, but not greatly in magnitude. Maximum increase in density of lubricants due to very high pressures is found to be only 33% greater than that under atmospheric condition, as shown in figure 4.1. This characteristic can be safely

assumed for almost all lubricants. This relationship, found by **Dowson** and **Higginson** to be:

$$\bar{\rho} = \frac{\rho}{\rho_0} = 1 + \frac{0.6p}{1 + 1.7p}$$

[4.1]

Hamrock *et al* (1987) found that for six base fluids at constant temperature (fluids listed in figure 4.1) of 20°C, the solidification pressure played an important part in determining the rate of volumetric variation of these fluids with pressure. Where pressures generated in lubricated conjunctions exceeds that of the solidification pressure of a fluid, the volume variation with pressures become almost insignificant. Whereas, when the applied pressures are lower than the solidification pressure, the variation of volume becomes apparent and indeed significant. Extend to which a lubricant is affected by pressure also depends on its atomic structure, as illustrated in figure 4.1 (the numbers beside the name indicates average molecular weight).
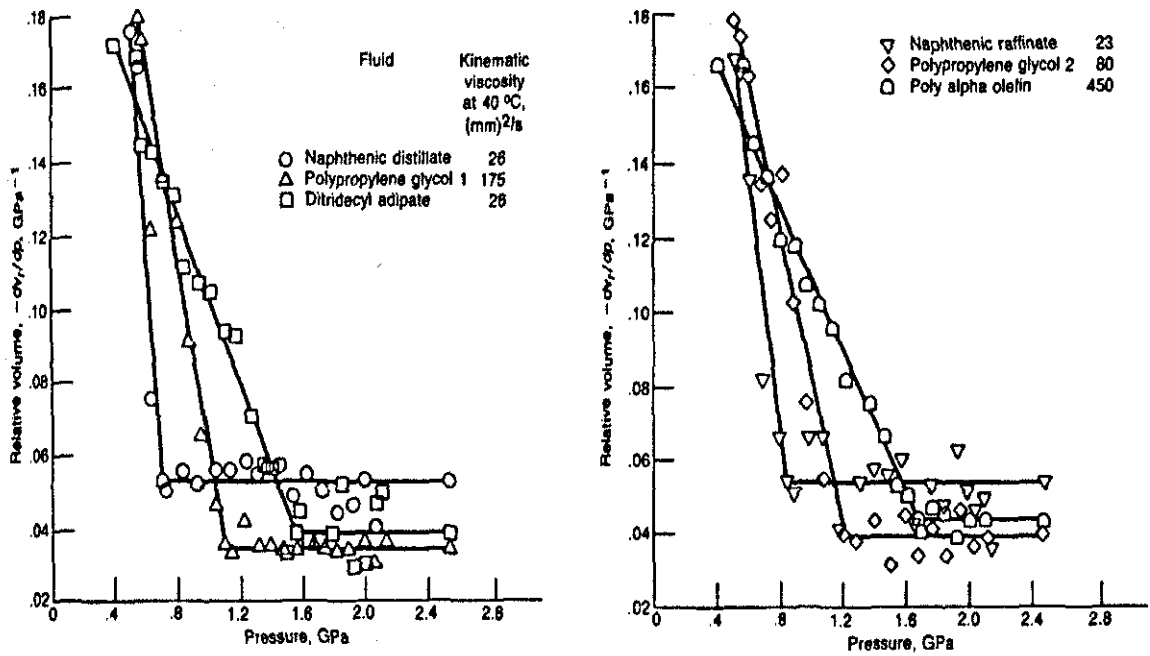
Figure 4.1: Volume variation with pressure (from Hamrock (1994))

4.2.2 Viscosity

Viscosity can be described as internal resistance within fluid to flow. Due to hydrophilic nature of lubricant fluids, they cling to surfaces they are resting or flowing along. Extending this idea to fluids flowing in a channel between a stationary and a moving plate, the bottom-most fluid layer, closest to the stationary plate remains stationary, while the upper-most layer, closest to the moving surface, moves along with the velocity u_A.
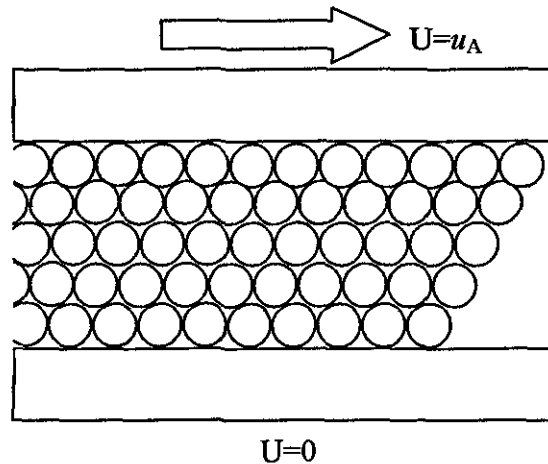
Figure 4.2: Laminar flow in Newtonian fluids

This is illustrated in figure 4.2. Therefore, the relationship between the velocity gradient that exists between the layers of fluid and their displacement is known as shear rate, Ψ. The velocity gradient is proportional to the shear stress, τ. In turn, dynamic viscosity, η, can be described as:

$$\eta = \frac{\tau}{\Psi}$$
[4.2]

Fluids or lubricants that exhibit the above relationship are known as Newtonian fluids. This model was proposed by **Newton** (1674) and is known as *Newtonian slow viscous action* model, in which the molecules of the fluid are considered as spherical and undeformable and the flow to be slow in motion and viscous. Fluids, deviating from such

behaviour, are referred to as non-Newtonian fluids. Another measure of viscosity, known as kinematic viscosity, η_k, i.e. flow in capillary tube, is influenced by weight of the fluid and can be defined in terms of the density and dynamic viscosity as:

$$\eta_k = \frac{\eta}{\rho} \qquad [4.3]$$

4.2.2.1 Temperature Influence on Viscosity

Temperature influence on viscosity is important in engineering applications. This relationship can be obtained from viscosity-temperature *ASTM* (American Society of Testing Materials) chart or by equations (such as equation [4.4]). Standard experiment to measure temperature influence on viscosity is by using capillary tube viscometer under controlled temperature. By curve-fitting experimental data, the viscosity dependency on temperature is expressed (**Crouch** and **Cameron** (1961)) as:

$$\eta = \eta_s e^{-\wp \Delta t} \qquad [4.4]$$

The relationship between viscosity of mineral and synthetic lubricant and temperature can best be said as inversely proportional.

4.2.2.2 Pressure Influence on Viscosity

Viscosity of a lubricant was defined by **Maxwell** (1866) as the *resistance of a fluid to shear deformation*. The effect of pressure on lubricant is of utmost important, especially at higher magnitudes of pressure. This dependency is defined by the chemical structure of the lubricant. The pressure-viscosity dependence proposed by **Barus** (1893) is:

$$\ln \frac{\eta}{\eta_0} = \xi p \qquad [4.5]$$

74

The above equation is valid as an approximation and is inaccurate, when pressures involved are very high (in the order of GPa). Therefore, by curve-fitting experimental data, **Roelands** (1966) formulated the following expression to describe viscosity in terms of pressure of lubricants under isothermal conditions:

$$\ln \eta + 1.2 = (\ln \eta_o + 1.2)\left(1 + \frac{p}{2000}\right)^{Z_1} \qquad [4.6]$$

Rearranging equation [4.6], dynamic viscosity in terms of pressure can be written as:

$$\bar{\eta} = \frac{\eta}{\eta_0} = \exp^{(\ln \eta_o + 9.67)\left(-1+\left(1+5.1\times 10^{-9} p\right)\right)} \qquad [4.7]$$

It must be noted that in Roelands's equation, [4.7], the lubricant viscosity is defined, using three different parameters (i.e. the atmospheric viscosity (η_o), the asymptotic iso-viscous pressure (ξ) and the pressure-viscosity index (Z_1)), while in the Barus's case only the pressure-viscosity coefficient (α) is used. In effect, if the Barus's expression was employed, the exponential pressure-viscosity dependence in his equation, [4.5], can be approximated to a non-exponential dependence by the substitution of the inverse of the asymptotic iso-viscous pressure as:

$$\alpha = \frac{1}{\xi} \qquad [4.8]$$

The values of the individual parameters for a given lubricant in the Roelands's equation can be obtained by consulting the tables that define the lubricant properties. Pressure-viscosity coefficient of lubricant can now be expressed in terms of Z_1 (**Blok** (1965)) as:

$$\xi = Z_1 \left(5.1\times 10^{-9} \left(\ln \eta_0 + 9.67\right)\right) \qquad [4.9]$$

4.3 Derivation Elasticity Equation

4.3.1 General Elasticity

The relationship between normal stress components, Poisson's ratio and shear stress components for an isotropic, homogeneous and perfectly elastic material (**Timoshenko (1951)**) can be written as:

$$(1-v)\nabla^2\sigma_x + \frac{\partial^2}{\partial x^2}\left(\sigma_x + \sigma_y + \sigma_z\right) = 0 \qquad\qquad \text{[4.10]}$$

$$(1-v)\nabla^2\sigma_y + \frac{\partial^2}{\partial y^2}\left(\sigma_x + \sigma_y + \sigma_z\right) = 0 \qquad\qquad \text{[4.11]}$$

$$(1-v)\nabla^2\sigma_z + \frac{\partial^2}{\partial z^2}\left(\sigma_x + \sigma_y + \sigma_z\right) = 0 \qquad\qquad \text{[4.12]}$$

$$(1-v)\nabla^2\tau_{xy} + \frac{\partial^2}{\partial x \partial y}\left(\sigma_x + \sigma_y + \sigma_z\right) = 0 \qquad\qquad \text{[4.13]}$$

$$(1-v)\nabla^2\tau_{yz} + \frac{\partial^2}{\partial y \partial z}\left(\sigma_x + \sigma_y + \sigma_z\right) = 0 \qquad\qquad \text{[4.14]}$$

$$(1-v)\nabla^2\tau_{zx} + \frac{\partial^2}{\partial z \partial x}\left(\sigma_x + \sigma_y + \sigma_z\right) = 0 \qquad\qquad \text{[4.15]}$$

Solution to any elasticity problem must satisfy the above condition and boundary condition.

where: $\nabla^2 = \dfrac{\partial^2}{\partial x^2} + \dfrac{\partial^2}{\partial y^2} + \dfrac{\partial^2}{\partial z^2}$

Stress field for an applied load, in Cartesian coordinates can be expressed as (**Hamrock (1994)**):

$$\sigma_x = -\frac{2w_z' x^2 z}{\pi\left(x^2 + z^2\right)^2} \qquad\qquad \text{[4.16]}$$

$$\sigma_y = -\frac{2w_z' y^2 z}{\pi\left(y^2 + z^2\right)^2} \qquad\qquad \text{[4.17]}$$

$$\sigma_z = -\frac{2w_z' z^3}{\pi \left(x^2 + z^2\right)^2} \qquad\qquad [4.18]$$

$$\tau_{xz} = -\frac{2w_z' xz^2}{\pi \left(x^2 + z^2\right)^2} \qquad\qquad [4.19]$$

Using Hooke's law, plane strain components in a solid can be expressed as:

$$\tilde{e}_x = \frac{\partial \delta_x}{\partial x} = \frac{1}{E'}\left[\sigma_x - v\left(\sigma_y + \sigma_z\right)\right] \qquad\qquad [4.20]$$

$$\tilde{e}_y = \frac{\partial \delta_y}{\partial y} = \frac{1}{E'}\left[\sigma_y - v\left(\sigma_z + \sigma_x\right)\right] = 0 \qquad\qquad [4.21]$$

$$\tilde{e}_z = \frac{\partial \delta_z}{\partial z} = \frac{1}{E'}\left[\sigma_z - v\left(\sigma_x + \sigma_y\right)\right] \qquad\qquad [4.22]$$

$$\tilde{e}_{xz} = \frac{\partial \delta_x}{\partial z} + \frac{\partial \delta_z}{\partial x} = \frac{\tau_{xz}}{G_s} = \frac{2(1+v)}{E'}\tau_{xz} \qquad\qquad [4.23]$$

For plane strain condition, equation [4.21] becomes:

$$\sigma_y = v\left(\sigma_z + \sigma_x\right) \qquad\qquad [4.24]$$

Substituting equation [4.24] into equations [4.20] and [4.22], yields:

$$\tilde{e}_x = \frac{\partial \delta_x}{\partial x} = \frac{1-v^2}{E'}\sigma_x - \frac{(1+v)v}{E'}\sigma_z \qquad\qquad [4.25]$$

and:

$$\tilde{e}_z = \frac{\partial \delta_z}{\partial z} = \frac{1-v^2}{E'}\sigma_z - \frac{(1+v)v}{E'}\sigma_x \qquad\qquad [4.26]$$

Integrating the above equations, [4.25] and [4.26], results in the following equations:

$$\delta_x = -\frac{w_z'}{\pi}\left[\frac{(1-2v)(1+v)}{E'}\tan^{-1}\left(\frac{x}{z}\right) - \frac{(1+v)xz}{E'\left(x^2 + z^2\right)}\right] + \tilde{A}(z) \qquad\qquad [4.27]$$

77

$$\delta_z = -\frac{w_z'}{\pi}\left[\frac{\left(1-\nu^2\right)}{E'}\left[\ln\left(x^2+z^2\right)-\frac{z^2}{\left(x^2+z^2\right)}\right]+\frac{\nu\left(1+\nu\right)x^2}{E'\left(x^2+z^2\right)}\right]+\tilde{B}(x) \qquad [4.28]$$

Since the interest here is to obtain an expression defining the deflection along the normal ($z-axis$), equation [4.27] is ignored. Therefore, in equation [4.28], $\tilde{B}(x)$ is determined by the relative position of line load and the fixed datum (where it is measured from).

4.3.2 Approximate Semi-infinite Solution for Conformal Contacts

Unlike the analytic solution provided by classical Hertzian theory for the conforming contact of bodies of revolution resulting is a circular contact configuration, it is not possible to obtain an exact analytic solution for the case of contact of closely conforming ellipsoidal and cylindrical bodies. An approximate solution, therefore, can be sought using numerical approximation. For the case of the contact of concentric conforming cylinders such as piston skirt to cylinder bore or liner, use of finite element analysis has been prevalent, as previously mentioned in chapter 2. In particular, for computational efficiency, Galerkin method has been employed by various authors. A finite difference solution has particular advantages as mentioned in chapter 5. To make the solution possible, a number of assumptions has to be made. The major assumption is the approximation of the contact conditions to those of semi infinite solids, thus replacing the par of cponforming bodies of revolution by a model of an equivalent near a plane. To ensure that such an approximation is valid, it is necessary to show that the gap at the edge of the contact model is representative of the radial clearance in the actual conforming contact. Furthermore, this also justifies the solution of the lubricated contact in the Cartesian frame of reference as opposed to more representative usual solution in polar coordinates. Finally, it is noted that the dimensions of the contact, although large due to contact conformity (as shown by the results in chapter 5 and 6) are still considerably smaller than the principle radii of the contiguous bodies in contact, providing yet another justification for the use of semi-infinite assumption.

Therefore, elastic deformation, at a point (x,y) of a semi-infinite solid subjected to pressure p at point (x_1,y_1) (**Timoshenko** (1951) and Hamrock (1994)) can be expressed as:

$$d\delta_{z_{(x,y)}} = \frac{2pdx_1dy_1}{\pi E'r}$$

[4.29]

Referring to figure 4.3, deformation at (x,y) due to uniform columnar pressure over $2\tilde{a} \times 2\tilde{b}$ can be expressed as:
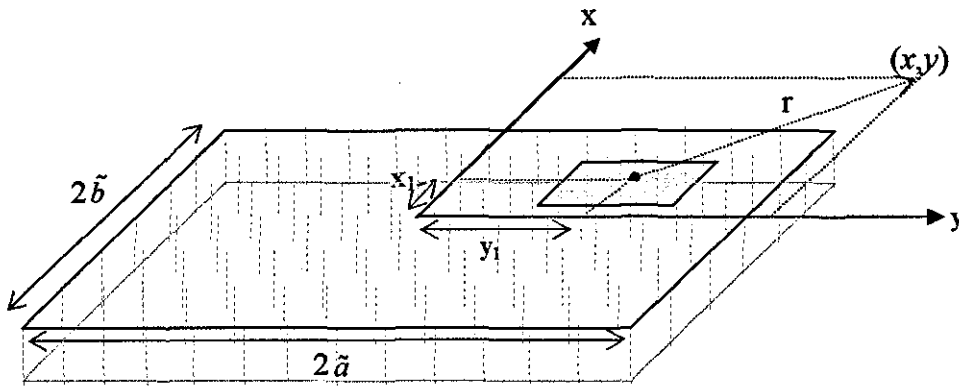
Figure 4.3: Pressure on a semi-infinite solid

$$\delta_{z_{(x,y)}} = \frac{2p}{\pi E'} \int_{-\tilde{b}}^{\tilde{b}} \int_{-\tilde{a}}^{\tilde{a}} \left[\frac{dx_1dy_1}{\left[(y-y_1)^2 + (x-x_1)^2 \right]^{\frac{1}{2}}} \right]$$

[4.30]

The above integral can be expressed in terms of deflection at point (x,y) on a semi-infinite solid as:

$$\delta_{z_{(x,y)}} = \frac{2}{\pi E'} \sum_{i=1}^{n} \sum_{j=1}^{m} pD^*$$

[4.31]

where:

$$D^* = (x+\tilde{b})\ln\frac{(y+\tilde{a})+\left[(y+\tilde{a})^2+(x+\tilde{b})^2\right]^{\frac{1}{2}}}{(y-\tilde{a})+\left[(y-\tilde{a})^2+(x+\tilde{b})^2\right]^{\frac{1}{2}}}+(y+\tilde{a})\ln\frac{(x+\tilde{b})+\left[(y+\tilde{a})^2+(x+\tilde{b})^2\right]^{\frac{1}{2}}}{(x-\tilde{b})+\left[(y+\tilde{a})^2+(x-\tilde{b})^2\right]^{\frac{1}{2}}}$$

$$+(x-\tilde{b})\ln\frac{(y-\tilde{a})+\left[(y-\tilde{a})^2+(x-\tilde{b})^2\right]^{\frac{1}{2}}}{(y+\tilde{a})+\left[(y+\tilde{a})^2+(x-\tilde{b})^2\right]^{\frac{1}{2}}}+(y-\tilde{a})\ln\frac{(x-\tilde{b})+\left[(y-\tilde{a})^2+(x-\tilde{b})^2\right]^{\frac{1}{2}}}{(x+\tilde{b})+\left[(y-\tilde{a})^2+(x+\tilde{b})^2\right]^{\frac{1}{2}}}$$

[4.32]

D^* is also known as the influence coefficient or deformation matrix and relates the applied pressure at any point on the semi-infinite solid to the deflection point of interest. The total deflection at a node (k,l) due to columnar pressures acting at point (i,j) can be expressed as:

$$\delta_{z_{k,l}} = \frac{2}{\pi E''}\sum_{j=1}^{n}\sum_{i=1}^{m}p_{i,j}D_{i,j}^{k,l} \qquad [4.33]$$

where:

$$m = |k-i+1| \qquad [4.34]$$
$$n = |l-j+1| \qquad [4.35]$$

4.4 Elastohydrodynamic Lubrication

Reynolds' (1886) derived his equation based on the Navier-Stokes equation and continuity of flow condition. The following section explains Navier-Stokes equation and continuity of flow equation, and, the derivation of the Reynolds' equation, based on certain assumptions, explained in section 4.4.2.2.

4.4.1 Navier-Stokes and Continuity of Flow Equations

As the lubricant is dragged into the converging wedge by a rolling, sliding or combination of both rolling and sliding action of a body, moving along a surface, as seen in figure 4.4, pressure in the lubricant rises and falls as it passes through the narrowest channel and exits. Pressure gradient becomes exceedingly high at the point just before the exit. Since the pressure at the outlet is quite low compared to the region just prior to it, the fluid is pushed out, thus relaxing the lubricant pressures at the exit boundary. This is a continuous process until the rolling/sliding velocities of the two solids cease to exist.
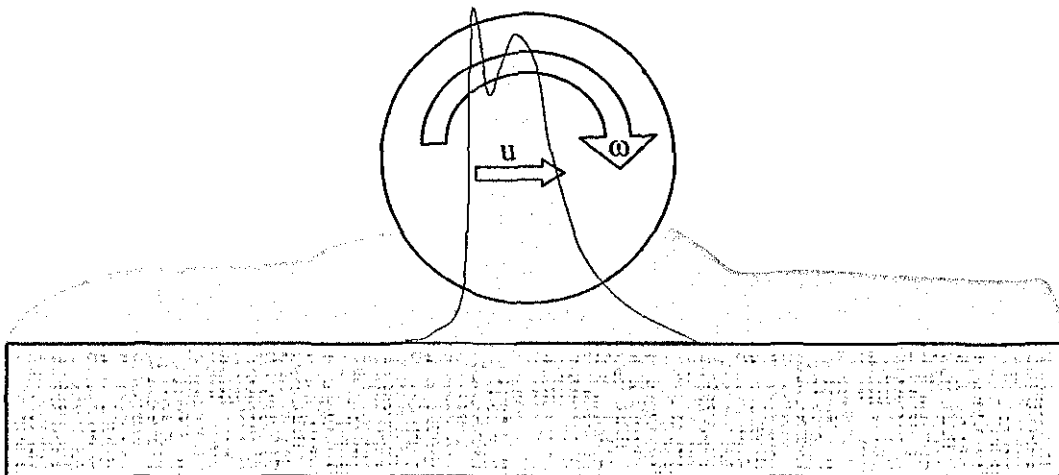
Figure 4.4: Hydrodynamics pressure generation in flow between two contiguous bodies

Referring to figure 4.5, stress-strain relations for a unit element of fluid in an arbitrary space, for Newtonian flow in the most general form of Navier-Stokes equation, in terms of velocity, deformations and the flow continuity, can be written as:
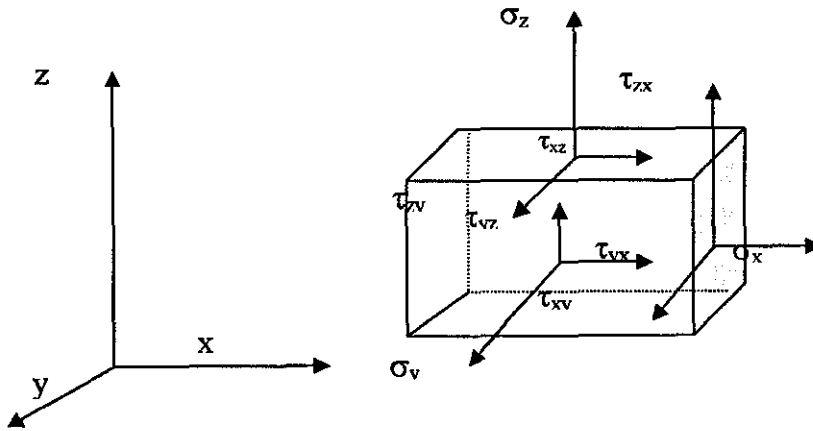
Figure 4.5: Forces on a unit element of fluid

$$\rho\frac{Du}{Dt} = F_x - \frac{\partial p}{\partial x} + \frac{\partial}{\partial x}\left\{2\eta\frac{\partial u}{\partial x} + \gamma\left(\frac{\partial u}{\partial x} + \frac{\partial v}{\partial y} + \frac{\partial w}{\partial z}\right)\right\} + \frac{\partial}{\partial y}\left\{\eta\left(\frac{\partial u}{\partial y} + \frac{\partial v}{\partial x}\right)\right\} + \frac{\partial}{\partial z}\left\{\eta\left(\frac{\partial w}{\partial x} + \frac{\partial u}{\partial z}\right)\right\} \quad [4.36]$$

$$\rho\frac{Dv}{Dt} = F_Y - \frac{\partial p}{\partial y} + \frac{\partial}{\partial y}\left\{2\eta\frac{\partial v}{\partial y} + \gamma\left(\frac{\partial u}{\partial x} + \frac{\partial v}{\partial y} + \frac{\partial w}{\partial z}\right)\right\} + \frac{\partial}{\partial z}\left\{\eta\left(\frac{\partial v}{\partial z} + \frac{\partial w}{\partial y}\right)\right\} + \frac{\partial}{\partial x}\left\{\eta\left(\frac{\partial u}{\partial y} + \frac{\partial v}{\partial x}\right)\right\} \quad [4.37]$$

$$\rho\frac{Dw}{Dt} = F_z - \frac{\partial p}{\partial z} + \frac{\partial}{\partial z}\left\{2\eta\frac{\partial w}{\partial z} + \gamma\left(\frac{\partial u}{\partial x} + \frac{\partial v}{\partial y} + \frac{\partial w}{\partial z}\right)\right\} + \frac{\partial}{\partial x}\left\{\eta\left(\frac{\partial w}{\partial x} + \frac{\partial u}{\partial z}\right)\right\} + \frac{\partial}{\partial y}\left\{\eta\left(\frac{\partial v}{\partial z} + \frac{\partial w}{\partial y}\right)\right\} \quad [4.38]$$

where $\frac{D}{Dt}$ is the Stokesian derivative, that describes the flow with respect to time, is defined as:

$$\Diamond = \frac{\partial}{\partial t} + u\frac{\partial}{\partial x} + v\frac{\partial}{\partial y} + w\frac{\partial}{\partial z}$$

The terms, $\rho\frac{Du}{Dt}, \rho\frac{Dv}{Dt}, \rho\frac{Dw}{Dt}$ corresponds to the inertial terms and the right-hand side terms represent the viscous terms, the body forces and the pressure gradient, acting on the fluid element (see figure 4.6).
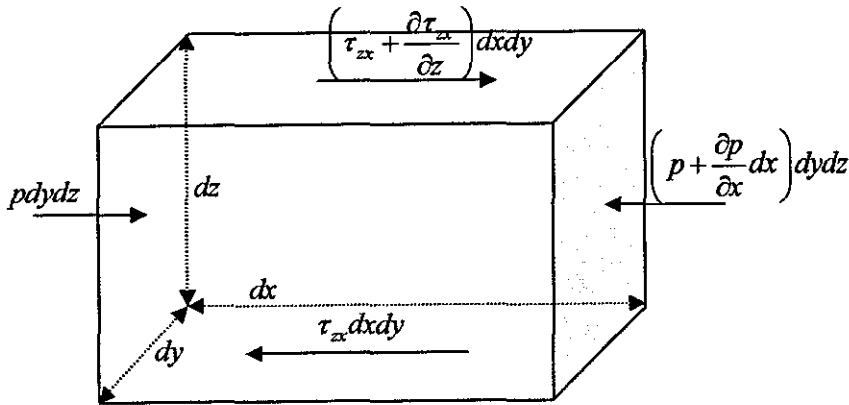
Figure 4.6: Flow of a column of fluid

The continuity of flow equation that represents the conservation of mass is:

$$\frac{\partial \rho}{\partial t} + \frac{\partial}{\partial x}(\rho u) + \frac{\partial}{\partial y}(\rho v) + \frac{\partial}{\partial z}(\rho w) = 0 \qquad [4.39]$$

4.4.2 Reynolds Equation

In order to obtain the hydrodynamic flow equation in a narrow convergent gap, the following assumptions were made by Reynolds (1886):

i. The viscosity and the density of the fluid are considered to be constant. This assumption holds for iso-viscous conditions, where the hydrodynamic pressures are relatively low, so that the effect of pressure on the bulk physical properties of the fluid (such as its density and viscosity) can be ignored. This enables the above equations to be simplified to:

$$\rho \nabla u = F_X - \frac{\partial p}{\partial x} + (\eta + \xi)\frac{\partial}{\partial x}\left(\frac{\partial u}{\partial x} + \frac{\partial v}{\partial y} + \frac{\partial w}{\partial z}\right) + \eta\left(\frac{\partial^2 u}{\partial x^2} + \frac{\partial^2 u}{\partial y^2} + \frac{\partial^2 u}{\partial z^2}\right) \qquad [4.40]$$

$$\rho \nabla v = F_Y - \frac{\partial p}{\partial y} + (\eta + \xi)\frac{\partial}{\partial y}\left(\frac{\partial u}{\partial x} + \frac{\partial v}{\partial y} + \frac{\partial w}{\partial z}\right) + \eta\left(\frac{\partial^2 v}{\partial x^2} + \frac{\partial^2 v}{\partial y^2} + \frac{\partial^2 v}{\partial z^2}\right) \qquad [4.41]$$

83

$$\rho \nabla w = F_z - \frac{\partial p}{\partial z} + (\eta + \xi) \frac{\partial}{\partial z} \left(\frac{\partial u}{\partial x} + \frac{\partial v}{\partial y} + \frac{\partial w}{\partial z} \right) + \eta \left(\frac{\partial^2 w}{\partial x^2} + \frac{\partial^2 w}{\partial y^2} + \frac{\partial^2 w}{\partial z^2} \right) \qquad \text{[4.42]}$$

ii. For incompressible fluids such as mineral oils the dilation term is ignored, thus:

$$\left(\frac{\partial u}{\partial x} + \frac{\partial v}{\partial y} + \frac{\partial w}{\partial z} \right) = 0 \qquad \text{[4.43]}$$

iii. Due to the small size of the element of fluid, its inertial properties are negligible, when compared to the contributions made by the shear deformation terms in the Navier-Stokes equations. Therefore:

$$\nabla u = \nabla v = \nabla w = 0 \qquad \text{[4.44]}$$

iv. The effect of body forces (such as the gravitational effect) on a fluid element is considered to be negligible. Thus:

$$F_X = F_Y = F_Z = 0 \qquad \text{[4.45]}$$

When the above assumptions are applied to the Navier-Stokes equations, the following special forms of the equations are obtained:

$$\frac{\partial p}{\partial x} = \eta \left(\frac{\partial^2 u}{\partial x^2} + \frac{\partial^2 u}{\partial y^2} + \frac{\partial^2 u}{\partial z^2} \right) \qquad \text{[4.46]}$$

$$\frac{\partial p}{\partial y} = \eta \left(\frac{\partial^2 v}{\partial x^2} + \frac{\partial^2 v}{\partial y^2} + \frac{\partial^2 v}{\partial z^2} \right) \qquad \text{[4.47]}$$

$$\frac{\partial p}{\partial z} = \eta \left(\frac{\partial^2 w}{\partial x^2} + \frac{\partial^2 w}{\partial y^2} + \frac{\partial^2 w}{\partial z^2} \right) \qquad \text{[4.48]}$$

v.   The pressure gradient across the fluid film in the z-direction neglected, because the lubricant film is very thin, therefore: $\dfrac{\partial p}{\partial z} = 0$.

vi.   An order of magnitude analysis can be carried out to show that the variation of velocities u and v with respect to z are large compared to all other velocity gradients. This is because of the geometry of the contact domain. Hence:

$$\frac{\partial^2 u}{\partial x^2} = \frac{\partial^2 u}{\partial y^2} = 0; \quad \frac{\partial^2 v}{\partial y^2} = \frac{\partial^2 v}{\partial x^2} = 0; \quad \frac{\partial^2 w}{\partial z^2} = \frac{\partial^2 w}{\partial x^2} = \frac{\partial^2 w}{\partial y^2} = 0 \qquad [4.49]$$

vii.   The fluid film entraining velocities need not change in direction of entraining motion. This means that the flow is laminar (i.e. streamlined).

viii.   It is assumed that no slip occurs between the solid surfaces in pure entraining motion. This means that at the boundaries between the lubricant film and the solids:

$$z = 0; \quad u = u_A; \quad v = v_A = 0; \quad z = h; \quad u = u_B; \quad v = v_B = 0 \qquad [4.50]$$

where, z in the above equation represents the vertical distance (i.e. the gap measured) from a fixed datum, and u and v are the surface velocities of the solids in the x and y directions respectively.

When the above assumptions are applied to equations [4.46] to [4.48], the resulting equations are as follows:

$$\frac{\partial p}{\partial x} = \eta \frac{\partial^2 u}{\partial z^2} \qquad [4.51]$$

$$\frac{\partial p}{\partial y} = \eta \frac{\partial^2 v}{\partial z^2} \qquad [4.52]$$

85

The above two equations can be integrated twice with respect to z to solve for the velocity distributions in the x and y directions, whilst employing the boundary conditions as outlined in assumption *(viii)*. Once the velocity distributions are obtained, they can be coupled with the continuity of flow equation to derive the Reynolds' equation in two-dimensions as stated below.

$$\frac{\partial}{\partial x}\left(\frac{\rho h^3}{\eta}\frac{\partial p}{\partial x}\right) + \frac{\partial}{\partial y}\left(\frac{\rho h^3}{\eta}\frac{\partial p}{\partial y}\right) = 12\left(u_{AV}\frac{\partial}{\partial x}(\rho h) + v_{AV}\frac{\partial}{\partial y}(\rho h) + \frac{\partial}{\partial t}(\rho h)\right) \qquad [4.53]$$

The left-hand side terms are known as Poiseuille terms, which describe flow rate due to pressure gradients within the lubricated area. The two terms on the right-hand side are known as the Couette terms, describing the film action in a convergent gap. These terms are functions of the average velocities in entraining motion, including side-leakage. These average velocities are given as:

$$u_{AV} = \frac{u_A + u_B}{2}; \quad v_{AV} = \frac{v_A + v_B}{2} \qquad [4.54]$$

Since the lubricant entraining direction, in the case of piston sliding in the bore, is in the translation direction only, entraining velocity in y direction can be ignored. The variation of lubricant film thickness with time, described by the last term in the right-hand side of equation [4.53], can be ignored. Therefore, the Reynolds' equation for a quasi-static analysis can now be expressed as:

$$\frac{\partial}{\partial x}\left(\frac{\rho h^3}{\eta}\frac{\partial p}{\partial x}\right) + \frac{\partial}{\partial y}\left(\frac{\rho h^3}{\eta}\frac{\partial p}{\partial y}\right) = 12u_{AV}\frac{\partial}{\partial x}(\rho h) \qquad [4.55]$$

4.4.3 The Elastic Film Shape
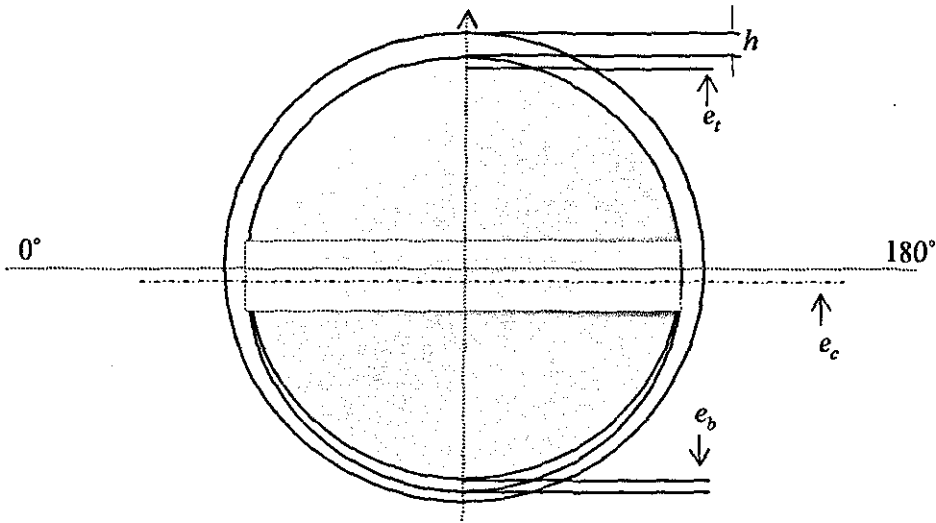
Figure 4.7: Lubricant film between bore and piston (shown without compression rings) as seen from top, into the bore

The elastic film shape refers to the profile of the film between the piston and the bore. Elastic film shape takes into account the undeformed gap size and the deflection of the bodies, as described in equation [4.31]. Figure 4.7 shows the piston in a tilted position, indicated by e_t and e_b. The generated pressures depend on the combustion load, amount of tilt, piston velocity and the rheological properties of the fluid.

The lubricant film denoted by h, is determined by the geometry of the piston, including the tilt and lateral motion, and deflection. The film shape can be unwrapped from around
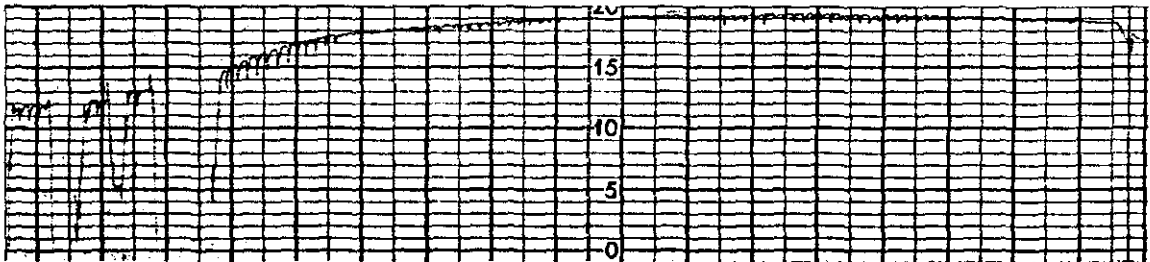
Figure 4.8(a): Piston profile of a high performance engine: in axial direction

the bore, for 180° circumferentially, and viewed as a profile with a large radius on a plane. Piston profile varies largely, depending on the application of the engine it is fitted to.

LOBED SECTION

Filter   Mag.
  1   100

.. is 20
microns
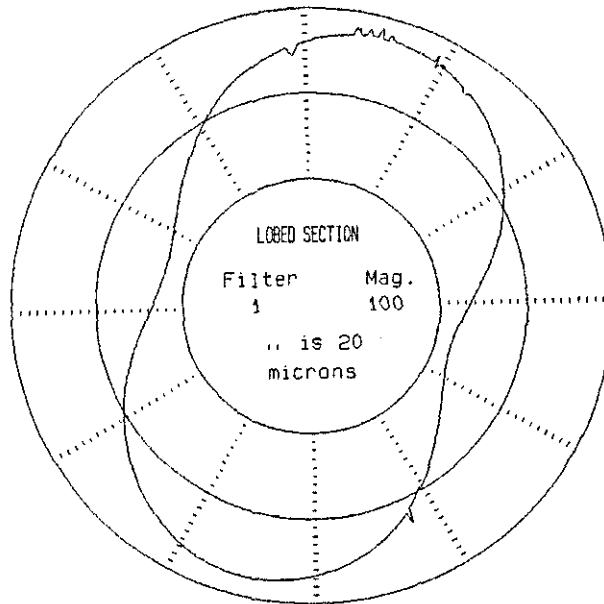
Figure 4.8(b): Piston profile of a high performance engine: in circumferential direction

In figures 4.8(a) and 4.8(b), experimentally measured profile of a piston from a performance engine, in axial and circumferential directions, using a Talyround, is shown. In general, along the length of the piston skirt, there are relief radii at the lower end and upper end of the piston skirt. Therefore, representing the profile of piston, $s(x,y)$, The equivalent radii in x and y directions can be expressed as:

$$\frac{1}{R_x} = \frac{1}{r_{px}} + \frac{1}{r_{bx}}$$

[4.56]

$$\frac{1}{R_y} = \frac{1}{r_{by}} - \frac{1}{r_{py}}$$

[4.57]

88

In the axial direction, the radius of bore, r_{bx}, is very large and is usually considered infinite. Therefore, the radius in the axial direction, the equivalent profile can be written as $R_x = r_{px}$.

In the circumferential direction, the difference in radius of bore and piston is the radial clearance, and therefore, can be written as:

$$r_{by} = r_{py} + c$$

$$R_y = \frac{r_{py}(r_{py} + c)}{c}$$

Typically, the skirt radius (along the tranverse direction) is in the range of 500m to 3000m, (**Howell-Smith (2002)**), and a small radial clearance in the range of $5\mu m$ to $50\ \mu m$.
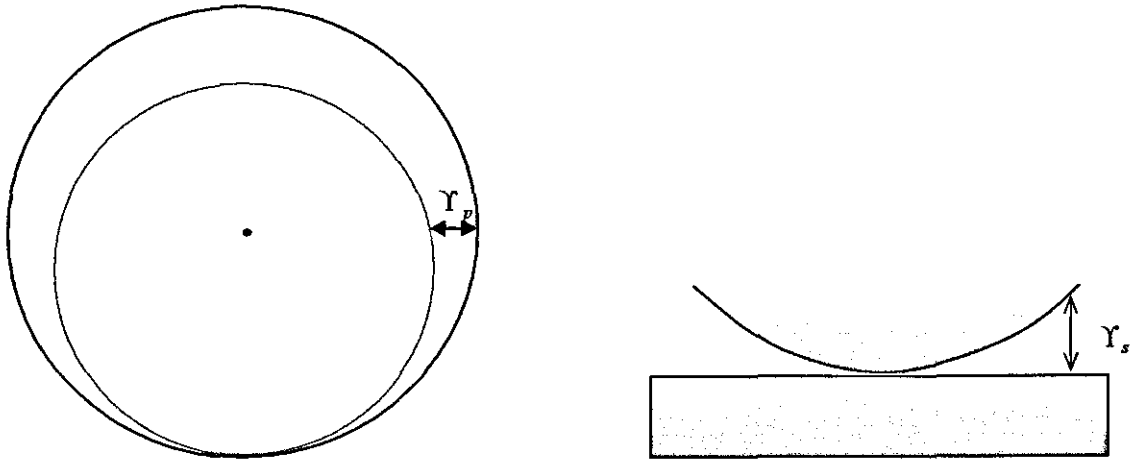
Figure 4.8(c): Circumferential piston clearance shown in polar coordinates (left) and in equivalent radius (right)

It can be noted that the two radii are similar for an aligned contact leading to a sizeable semi-rectangular contact, particularly in the mid section of the skirt. The undeformed

profile of the contiguous bodies in the circumferential and in the axial direction for a crowned or barrelled shape piston can be written as:

$$s_{i,j} = \frac{\left(x_{i,j} - m\right)^2}{2R_x} + \frac{\left(y_{i,j} - n\right)^2}{2R_y}$$ [4.58]

In figure 4.8(c), the gap Υ_p in the polar coordinate system is found to be 59.59×10^{-6} and the gap Υ_s found through equivalent radius in Cartesian coordinate system is 61.64×10^{-6}. Tilt of the piston is about the gudgeon pin (refer to section 3.3.2). Therefore, assigning n_{gx} to the node where gudgeon pin is located along the axial direction, the tilt and lateral displacement (referring to equations [3.10] and [3.11]) of the piston is given as:

$$s_{t_{i,j}} = s_{i,j} + e_l + \Delta x \times \left(i - n_{gx}\right) \times \tan\beta$$ [4.59]

Since the profile, given by equation [4.59] of the contiguous bodies and the elastic deformation relationship, from equation [4.31], has been established, the elastic film shape equation can be expressed as:

$$h_{i,j} = s_{t_{i,j}} + \delta_{z_{i,j}} + h_0$$ [4.60]

4.4.3 Non-dimensionalisation of Reynolds' Equation

The Reynolds' equation, [4.53], is in dimensional form. In numerical analysis, to present this equation in its current format would yield computation problems, mainly due to the nature of the magnitude of the parameters involved. The magnitude of film thickness, pressure, viscosity, density is diverse, ranging from the order of 10^{-9} for film thickness, to 10^9 for pressure. Algebraic operation of such very large and very small numbers gives rise to numerical inaccuracy and may cause computation instability. To avoid such problem, non-dimensionalisation or normalisation techniques are employed. Non-dimensionalisation is substitution of all real variables in an equation with a fraction of one or more real parameters, whereas, with normalisation, a suitable parameter is chosen

to scale the magnitude, usually by division. The non-dimensionalisation parameters chosen here are as follows:

$$\bar{\eta} = \frac{\eta}{\eta_0}$$

$$\bar{x} = \frac{x}{b}$$

$$\bar{y} = \frac{y}{a}$$

$$\bar{h} = \frac{hp_l}{a^2}$$

$$\bar{u} = \frac{u\eta_0}{E'P_l}$$

$$\bar{\rho} = \frac{\rho}{\rho_0}$$

$$\bar{p} = \frac{p}{E'}$$

Substituting the non-dimensional parameters into equation [4.53], the Reynolds' equation can be expressed in dimensionless form as:

$$\frac{a^2}{b^2}\frac{\partial}{\partial\bar{x}}\left(\frac{\bar{\rho}\bar{h}^3}{\bar{\eta}}\frac{\partial\bar{p}}{\partial\bar{x}}\right) + \frac{\partial}{\partial\bar{y}}\left(\frac{\bar{\rho}\bar{h}^3}{\bar{\eta}}\frac{\partial\bar{p}}{\partial\bar{y}}\right) = 12\bar{u}_x\frac{P_l^3}{a^2b}\frac{\partial}{\partial\bar{x}}\left(\bar{\rho}\bar{h}\right) \qquad [4.61]$$

4.4.4 Computation Mesh Generation

In a classic elastohydrodynamic lubrication problems, involving circular point contacts (**Jalali-Vahid** (1999)), finite line contacts (**Kushwaha** (2000)), the procedure is to determine the elastostatic foot-print contacts, then to determine the inlet, outlet boundary and side extensions. **Hamrock** and **Dowson** (1976) found that for a circular point or elliptical contact and finite line contact, the inlet distance had to be at least 4.2 times the elastostatic half-width of the contact foot-print and for the outlet to be 1.12 times of that. Such conditions are imposed to ensure a fully flooded condition for the analysis.
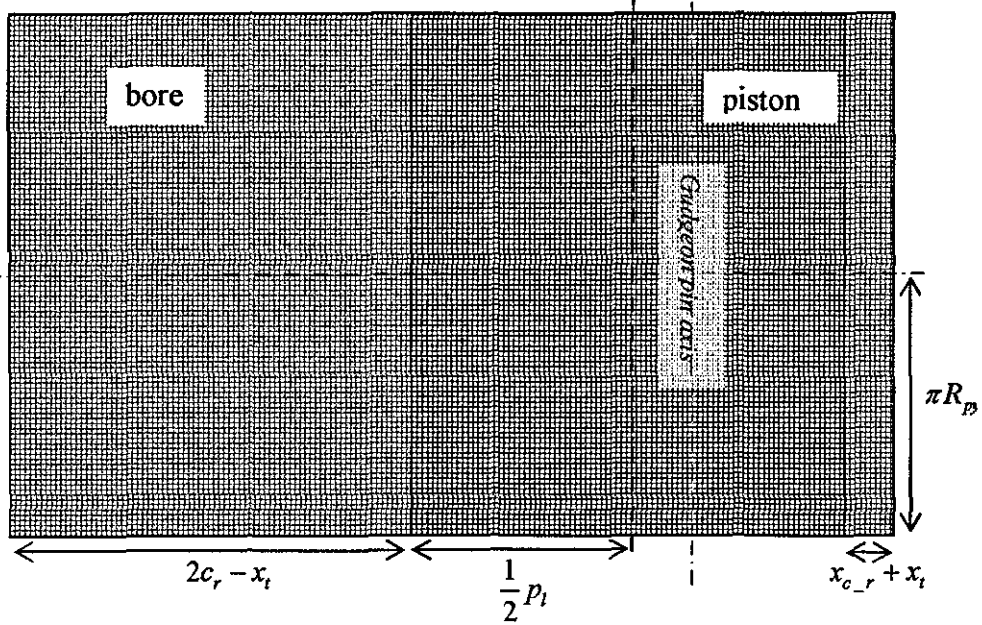
Figure 4.9: Computation domain generated for the analysis

Therefore, the computation domain for this thesis, in the axial direction is set as the bore length and for circumference, the perimeter of the bore. Figure 4.9 illustrates the mesh generated for the analysis. The number of nodes in the axial direction was taken as 200 and for the circumferential direction as 160.

4.4.5 The finite difference approximations

The finite difference method used here is based on the illustrated method in section 3.4.8 (also see figure 3.12). By combining the forward and backward differencing schemes, one can obtain the first derivative of the same function at x_0. This is termed as the *central difference* approximation.

$$f'(x_0) = \frac{f(x_0 + h) - f(x_0 - h)}{2h}$$

[4.62]

92

These first order numerical differentials can be further differentiated to obtain their second order derivatives.

The discretised form of the Reynolds' equation is developed, using two of the standard difference approximations described above. The equation is numerically discretised for pressure, $\bar{P}$ at point x_0, by making use of the presumed solution at its neighbouring points. The function $f(x)$ in this case is the Reynolds' equation itself.

For reasons of achieving good accuracy, the standard *central difference* formulation is used to approximate the residual function f^R of the Reynolds' equation. To satisfy the stability requirements, a mixed second order central and first order backward differencing scheme (see section 3.4.8) is employed to approximate the function generated from the Jacobian matrix f^J (as shown in section 4.4.7) for the Reynolds equation [4.61]. The procedure is outlined below.

A very small part of the mesh generated, as shown in figure 4.10, is used to illustrate the finite difference formulation of the Reynolds' equation [4.62] at point (i,j). The root finding method shown in figure 4.11 can be related to figure 4.10 by making the following replacements in the dimensionless $\bar{X}$ and $\bar{Y}$ directions as:

$$x_0 = \bar{x}(i,j) \qquad x_0 + h = \bar{x}(i+1,j) \qquad x_0 - h = \bar{x}(i-1,j)$$

$$y_0 = \bar{y}(i,j) \qquad y_0 + h = \bar{y}(i,j+1) \qquad y_0 - h = \bar{y}(i,j-1)$$
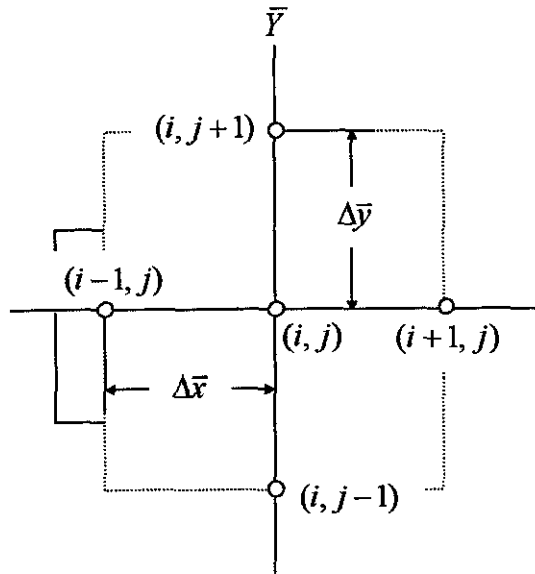
Figure 4.10: Part of computation domain grid points
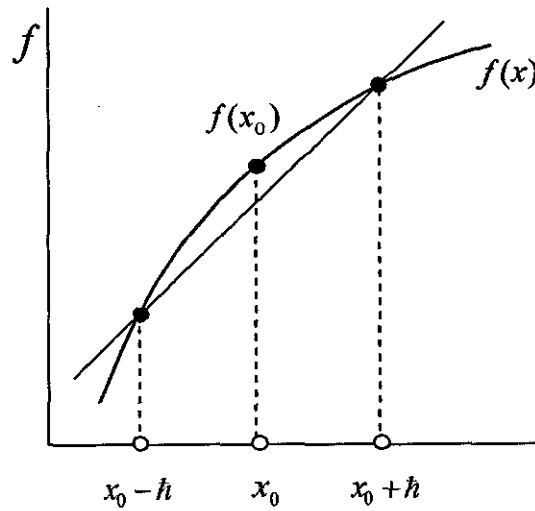
Figure 4.11: Root finding in central difference method

Therefore, using central difference method as outlined above, the first Poiseuille term (i.e. pressure induced term) in the discretised Reynolds' equation, [4.61], can be written as:

$$\frac{a^2}{b^2}\frac{\partial}{\partial \bar{x}}\left(\frac{\bar{\rho}\bar{h}^3}{\bar{\eta}}\frac{\partial \bar{p}}{\partial \bar{x}}\right)_{(i,j)} = \frac{a^2}{b^2}\left[\frac{\left(\frac{\bar{\rho}\bar{h}^3}{\bar{\eta}}\frac{\partial \bar{p}}{\partial \bar{x}}\right)_{(i+\frac{1}{2},j)} - \left(\frac{\bar{\rho}\bar{h}^3}{\bar{\eta}}\frac{\partial \bar{p}}{\partial \bar{x}}\right)_{(i-\frac{1}{2},j)}}{\Delta \bar{x}}\right] \qquad [4.63]$$

Similarly, the second Poiseuille term can be expressed as:

$$\frac{\partial}{\partial \bar{y}}\left(\frac{\bar{\rho}\bar{h}^3}{\bar{\eta}}\frac{\partial \bar{p}}{\partial \bar{y}}\right)_{(i,j)} = \left[\frac{\left(\frac{\bar{\rho}\bar{h}^3}{\bar{\eta}}\frac{\partial \bar{p}}{\partial \bar{y}}\right)_{(i,j+\frac{1}{2})} - \left(\frac{\bar{\rho}\bar{h}^3}{\bar{\eta}}\frac{\partial \bar{p}}{\partial \bar{y}}\right)_{(i,j-\frac{1}{2})}}{\Delta \bar{y}}\right] \qquad [4.64]$$

In the right-hand side of the equation, the Couette term can be expressed as:

$$\left(12\bar{u}_x\frac{p_l^3}{a^2 b}\frac{\partial}{\partial \bar{x}}\left(\bar{\rho}\bar{h}\right)\right)_{(i,j)} = 12\bar{u}_x\frac{p_l^3}{a^2 b\Delta \bar{x}}\left[\left(\bar{\rho}\bar{h}\right)_{i+1,j} - \left(\bar{\rho}\bar{h}\right)_{i-1,j}\right] \qquad [4.65]$$

The numerator in the right-hand side of equations [4.63] and [4.64] has to be discretised further for pressure variation in, x and y direction respectively. Taking the first term of the numerator in the right-hand side of equation [4.63], the term can now be expressed as:

$$\left(\frac{\bar{\rho}\bar{h}^3}{\bar{\eta}}\frac{\partial \bar{p}}{\partial \bar{x}}\right)_{(i+\frac{1}{2},j)} = \left(\frac{\bar{\rho}\bar{h}^3}{\bar{\eta}}\right)_{(i+\frac{1}{2},j)}\left(\frac{\bar{P}_{(i+1,j)} - \bar{P}_{(i,j)}}{\Delta \bar{x}}\right) \qquad [4.66]$$

Similarly, for the second term of the numerator in equation [4.63], in its discretised form appears as:

$$\left(\frac{\bar{\rho}\bar{h}^3}{\bar{\eta}}\frac{\partial \bar{p}}{\partial \bar{x}}\right)_{(i-\frac{1}{2},j)} = \left(\frac{\bar{\rho}\bar{h}^3}{\bar{\eta}}\right)_{(i-\frac{1}{2},j)}\left(\frac{\bar{P}_{(i,j)} - \bar{P}_{(i-1,j)}}{\Delta \bar{x}}\right) \qquad [4.67]$$

Similarly, in the second Poiseuille term, the numerators, in its discretised form can be expressed as:

$$\left(\frac{\overline{\rho}\overline{h}^3}{\overline{\eta}}\frac{\partial\overline{p}}{\partial\overline{y}}\right)_{\left(i,j+\frac{1}{2}\right)} = \left(\frac{\overline{\rho}\overline{h}^3}{\overline{\eta}}\right)_{\left(i,j+\frac{1}{2}\right)}\left(\frac{\overline{P}_{(i,j+1)}-\overline{P}_{(i,j)}}{\Delta\overline{y}}\right)$$ [4.68]

and

$$\left(\frac{\overline{\rho}\overline{h}^3}{\overline{\eta}}\frac{\partial\overline{p}}{\partial\overline{y}}\right)_{\left(i,j-\frac{1}{2}\right)} = \left(\frac{\overline{\rho}\overline{h}^3}{\overline{\eta}}\right)_{\left(i,j-\frac{1}{2}\right)}\left(\frac{\overline{P}_{(i,j)}-\overline{P}_{(i,j-1)}}{\Delta\overline{y}}\right)$$ [4.69]

Equations [4.63] to [4.69] are gathered and substituted into the non-dimensional Reynolds' equation, [4.61], yielding the following expression:

$$\frac{a^2}{b^2}\left[\frac{\left(\frac{\overline{\rho}\overline{h}^3}{\overline{\eta}}\right)_{\left(i+\frac{1}{2},j\right)}\left(\frac{\overline{P}_{(i+1,j)}-\overline{P}_{(i,j)}}{\Delta\overline{x}}\right)-\left(\frac{\overline{\rho}\overline{h}^3}{\overline{\eta}}\right)_{\left(i-\frac{1}{2},j\right)}\left(\frac{\overline{P}_{(i,j)}-\overline{P}_{(i-1,j)}}{\Delta\overline{x}}\right)}{\Delta\overline{x}}\right]$$

$$+ \left[\frac{\left(\frac{\overline{\rho}\overline{h}^3}{\overline{\eta}}\right)_{\left(i,j+\frac{1}{2}\right)}\left(\frac{\overline{P}_{(i,j+1)}-\overline{P}_{(i,j)}}{\Delta\overline{y}}\right)-\left(\frac{\overline{\rho}\overline{h}^3}{\overline{\eta}}\right)_{\left(i,j-\frac{1}{2}\right)}\left(\frac{\overline{P}_{(i,j)}-\overline{P}_{(i,j-1)}}{\Delta\overline{y}}\right)}{\Delta\overline{y}}\right]$$ [4.70]

$$= 12\overline{u}_x\frac{p_i^3}{a^2b\Delta\overline{x}}\left[\left(\overline{\rho}\overline{h}\right)_{i+1,j}-\left(\overline{\rho}\overline{h}\right)_{i-1,j}\right]$$

This equation is now termed the discretised Reynolds' equation.

96

4.4.6 Solving the Reynolds' Equation With Modified Low Relaxation Newton-Raphson Method

It has already been established in Chapter 3, that the Newton-Raphson method is an ideal numerical procedure for finding an approximate solution to non-linear differential equations. Due to the highly non-linear, second order partial differential nature of equation [4.61], the utilisation of the Newton-Raphson method to solve the Reynolds' equation is ideal. This is obtained by achieving the convergence of generated lubricant pressures for a given applied load. This technique is proven to be highly stable for achieving high stability and convergence accuracy even for a wide range of contact loads, as proven by **Jalali-Vahid** (1999). As shown in section 3.4.8, the Newton-Raphson formulation, in terms of the truncated Taylor series to first order is written as:

$$f(X_{n+1}) = f(X_n) + f'(X_n) \cdot (X_{n+1} - X_n) + \varepsilon_r \qquad [4.71]$$

For a multi-variable function, $f(x,y)$, the above equation can be expanded and written in terms of the truncated Taylor series to first order as:

$$f(x_{n+1}, y_{n+1}) = f(x_n, y_n) + (x_{n+1} - x_n) \cdot \frac{\partial[f(x_n, y_n)]}{\partial x_n} + (y_{n+1} - y_n) \cdot \frac{\partial[f(x_n, y_n)]}{\partial y_n} + \varepsilon_r \quad [4.72]$$

The first order differentials (i.e. the derivatives) can be replaced by a Jacobian matrix $[J]$, which contains the set of the derivatives of the function with respect to all the dependent variables. This can be expressed as:

$$[J_n] = \frac{\partial f(x_n, y_n)}{\partial(x_n, y_n)} \qquad [4.73]$$

The pressure term, $\bar{p}$ in the Reynolds' equation is the multi-variable function, since its evaluation at point (i, j) depends upon the pressures at four of its other neighbouring

points (i.e. at $(i-1, j-1),(i-1, j+1),(i+1, j-1)$ and $(i+1, j+1)$). It must be noted that the selection of the pressures at these points is based on the numerical experience of many researchers, such as **Lee** (1994), who showed that the pressures at any other neighbouring points in the computational grid (i.e. at $(i-1, j-1),(i-1, j+1),(i+1, j-1)$ or $(i+1, j+1)$) do not have any significant influence on the pressure convergence at point (i, j) (**Reddi** and **Chu** (1970)).

In effect, this method reduces the Jacobian matrix since the system equations comprise only five terms, which are represented at each of the five points (i.e. point (i, j) and its immediate adjacent neighbouring points). Furthermore, reducing the number of influential points also results in the reduction of memory space utilised (**Hou** *et al* (1985)), thus decreasing the computational time. Furthermore, it must be pointed out that the inversion of the Jacobian matrix increases the memory space for larger grid points if the Gaussian elimination method is used (**Nakamura** (1992)). Therefore, to prevent this, an alternative solution procedure, which employs the Gauss-Seidel iterative method is utilised. This method provides highly efficient storage and is very effective for the solution of the system of equations.

If nx and ny are number of nodes, defining the computational grid in X and Y directions respectively, then the pressure acting on each of these nodes can be defined as:

$$P_{(i,j)} \equiv \left[P_{(2,2)}, P_{(3,2)}, P_{(4,2)}, \cdots, P_{(nx-1, ny-1)} \right] \qquad [4.74]$$

It must be noted that the pressures at the first and the last row in axial and lateral directions are set to zero as they fall within the boundary conditions as defined in sections 4.5.2 and 4.6.2. Since the solution of the Reynolds' equation is obtained by minimising the differences in the pressures between the actual and the numerical solutions, the following relationships can be expressed:

- Analytical solution for the Reynolds' equation at point (i, j) is denoted as:

$$f^{R^a}{}_{(i,j)} = f\left[\overline{P}^a_{(2,2)}, \overline{P}^a_{(3,2)}, \ldots, \overline{P}^a_{(nx-1,ny-1)}\right] = 0 \qquad [4.75]$$

- Numerical solution of the Reynolds' equation at point (i, j) is written as:

$$f^{R^n}{}_{(i,j)} = f\left[\overline{P}^n_{(2,2)}, \overline{P}^n_{(3,2)}, \ldots, \overline{P}^n_{(nx-1,ny-1)}\right] = \varepsilon_r \qquad [4.76]$$

where f^R is the function defining the dimensionless Reynolds' equation, the superscripts "a" and "n" denote the analytical and the numerical solutions respectively, and ε is the user-specified error tolerance.

Since the numerical solution obtained should be comparable with the analytical solution, equations [4.75] and [4.76] can be equated by expressing them in the form of the Taylor series for multi-variable functions as:

$$f^{R^a}{}_{(i,j)} = f^{R^n}{}_{(i,j)} + \frac{\partial f^{R^n}{}_{(i,j)}}{\partial \overline{P}^n_{(i+1,j)}}\left(\overline{P}^a_{(i+1,j)} - \overline{P}^n_{(i+1,j)}\right) + \frac{\partial f^{R^n}{}_{(i,j)}}{\partial \overline{P}^n_{(i-1,j)}}\left(\overline{P}^a_{(i-1,j)} - \overline{P}^n_{(i-1,j)}\right) + \frac{\partial f^{R^n}{}_{(i,j)}}{\partial \overline{P}^n_{(i,j+1)}}\left(\overline{P}^a_{(i,j+1)} - \overline{P}^n_{(i,j+1)}\right)$$

$$+ \frac{\partial f^{R^n}{}_{(i,j)}}{\partial \overline{P}^n_{(i,j-1)}}\left(\overline{P}^a_{(i,j-1)} - \overline{P}^n_{(i,j-1)}\right) + \frac{\partial f^{R^n}{}_{(i,j)}}{\partial \overline{P}^n_{(i,j)}}\left(\overline{P}^a_{(i,j)} - \overline{P}^n_{(i,j)}\right) + \varepsilon_r = 0$$

$$[4.77]$$

In equation [4.77], the difference in the pressures can be expressed as:

$$\Delta \overline{P}_{(i,j)} = \left(\overline{P}^a_{(i,j)} - \overline{P}^n_{(i,j)}\right) \qquad [4.78]$$

This formulation for the pressure difference can be substituted back into equation [4.77] to give:

$$f^{R^a}{}_{(i,j)} = f^{R^n}{}_{(i,j)} + \frac{\partial f^{R^n}{}_{(i,j)}}{\partial \overline{p}^n_{(i+1,j)}} \Delta \overline{p}_{(i+1,j)} + \frac{\partial f^{R^n}{}_{(i,j)}}{\partial \overline{p}^n_{(i-1,j)}} \Delta \overline{p}_{(i-1,j)} + \frac{\partial f^{R^n}{}_{(i,j)}}{\partial \overline{p}^n_{(i,j+1)}} \Delta \overline{p}_{(i,j+1)}$$

$$+ \frac{\partial f^{R^n}{}_{(i,j)}}{\partial \overline{p}^n_{(i,j-1)}} \Delta \overline{p}_{(i,j-1)} + \frac{\partial f^{R^n}{}_{(i,j)}}{\partial \overline{p}^n_{(i,j)}} \Delta \overline{p}_{(i,j)} + \varepsilon_r = 0 \qquad \text{[4.79]}$$

The derivatives shown in the above equation are given by the Jacobian matrix as shown in section 4.4.8 (equation [4.86]) and can be expressed for the above equation as:

$$\overline{J}_{(ij,kl)} = \frac{\partial f^R{}_{(i,j)}}{\partial \overline{p}_{k,l}} \qquad \text{[4.80]}$$

The objective is to solve for the difference in pressures as denoted by equation [4.78]. The smaller the difference, the closer is the numerical solution to the analytical one. Since the two solutions cannot be identical due to the numerical errors, an error tolerance is specified, which marks the criterion for convergence. The error tolerance is usually very small and can be seen in the next section.

By assuming that the truncated error, ε_r in the Taylor series is very small; equation [4.79] can be re-written as:

$$-f^{R^n}{}_{(i,j)} = \frac{\partial f^{R^n}{}_{(i,j)}}{\partial \overline{p}^n_{(i+1,j)}} \Delta \overline{p}_{(i+1,j)} + \frac{\partial f^{R^n}{}_{(i,j)}}{\partial \overline{p}^n_{(i-1,j)}} \Delta \overline{p}_{(i-1,j)} + \frac{\partial f^{R^n}{}_{(i,j)}}{\partial \overline{p}^n_{(i,j+1)}} \Delta \overline{p}_{(i,j+1)} + \frac{\partial f^{R^n}{}_{(i,j)}}{\partial \overline{p}^n_{(i,j-1)}} \Delta \overline{p}_{(i,j-1)} + \frac{\partial f^{R^n}{}_{(i,j)}}{\partial \overline{p}^n_{(i,j)}} \Delta \overline{p}_{(i,j)}$$

$$\text{[4.81]}$$

In the above equation [4.81], left-hand term forms the residual function f^R and the right-hand side differentials form the Jacobian term f^J. Therefore, equation [4.81] can be simplified and written as:

$$\sum_{k=2}^{nx-1} \sum_{l=2}^{ny-1} \left[\overline{J}_{(ij,kl)} \right] \cdot \Delta \overline{p}_{(k,l)} = -f^R{}_{(i,j)} \qquad \text{[4.82]}$$

100

In the following two sections, derivation of the residual equation and Jacobian matrix are shown.

4.4.7 Residual Function

Referring back to equation [4.70], gathering all the terms to the left-hand side and rearranging for the pressure terms, the residual function $f^R_{(i,j)}$ is written as:

$$
f^R = \frac{\alpha^2}{2b^2\Delta\bar{x}^2}
\left\{
\begin{array}{l}
\bar{P}_{(i+1,j)}\left(\left(\dfrac{\bar{\rho}\bar{h}^3}{\bar{\eta}}\right)_{(i+1,j)} + \left(\dfrac{\bar{\rho}\bar{h}^3}{\bar{\eta}}\right)_{(i,j)}\right) \\[2ex]
- \bar{P}_{(i,j)}\left(\left(\dfrac{\bar{\rho}\bar{h}^3}{\bar{\eta}}\right)_{(i+1,j)} + 2\left(\dfrac{\bar{\rho}\bar{h}^3}{\bar{\eta}}\right)_{(i,j)} + \left(\dfrac{\bar{\rho}\bar{h}^3}{\bar{\eta}}\right)_{(i-1,j)}\right) \\[2ex]
+ \bar{P}_{(i-1,j)}\left(\left(\dfrac{\bar{\rho}\bar{h}^3}{\bar{\eta}}\right)_{(i,j)} + \left(\dfrac{\bar{\rho}\bar{h}^3}{\bar{\eta}}\right)_{(i-1,j)}\right)
\end{array}
\right\}
$$

$$
+ \frac{1}{2\Delta\bar{y}^2}
\left\{
\begin{array}{l}
\bar{P}_{(i,j+1)}\left(\left(\dfrac{\bar{\rho}\bar{h}^3}{\bar{\eta}}\right)_{(i,j+1)} + \left(\dfrac{\bar{\rho}\bar{h}^3}{\bar{\eta}}\right)_{(i,j)}\right) \\[2ex]
- \bar{P}_{(i,j)}\left(\left(\dfrac{\bar{\rho}\bar{h}^3}{\bar{\eta}}\right)_{(i,j+1)} + 2\left(\dfrac{\bar{\rho}\bar{h}^3}{\bar{\eta}}\right)_{(i,j)} + \left(\dfrac{\bar{\rho}\bar{h}^3}{\bar{\eta}}\right)_{(i,j-1)}\right) \\[2ex]
+ \bar{P}_{(i,j-1)}\left(\left(\dfrac{\bar{\rho}\bar{h}^3}{\bar{\eta}}\right)_{(i,j)} + \left(\dfrac{\bar{\rho}\bar{h}^3}{\bar{\eta}}\right)_{(i,j-1)}\right)
\end{array}
\right\}
\qquad [4.83]
$$

$$
- \quad 12\bar{u}_x \frac{p_l^3}{a^2 b\Delta\bar{x}}\left[\left(\bar{\rho}\bar{h}\right)_{i+1,j} - \left(\bar{\rho}\bar{h}\right)_{i-1,j}\right]
$$

4.4.8 The Jacobian Terms

The Reynolds' equation for the Jacobian term is discretised in similar manner to that for the residual function, except for the Couette flow term, which is discretised using the standard backward difference scheme for the purpose of achieving good numerical stability. Therefore, re-writing the discretised Reynolds' equation for the Jacobian term, denoted by f^J becomes:

$$
f^J = \frac{a^2}{2b^2\Delta\overline{x}^2}
\left\{
\begin{aligned}
&\overline{P}_{(i+1,j)}\left(\left(\frac{\overline{\rho}\overline{h}^3}{\overline{\eta}}\right)_{(i+1,j)} + \left(\frac{\overline{\rho}\overline{h}^3}{\overline{\eta}}\right)_{(i,j)}\right)\\
-\ &\overline{P}_{(i,j)}\left(\left(\frac{\overline{\rho}\overline{h}^3}{\overline{\eta}}\right)_{(i+1,j)} + 2\left(\frac{\overline{\rho}\overline{h}^3}{\overline{\eta}}\right)_{(i,j)} + \left(\frac{\overline{\rho}\overline{h}^3}{\overline{\eta}}\right)_{(i-1,j)}\right)\\
+\ &\overline{P}_{(i-1,j)}\left(\left(\frac{\overline{\rho}\overline{h}^3}{\overline{\eta}}\right)_{(i,j)} + \left(\frac{\overline{\rho}\overline{h}^3}{\overline{\eta}}\right)_{(i-1,j)}\right)
\end{aligned}
\right\}
$$

$$
+ \frac{1}{2\Delta\overline{y}^2}
\left\{
\begin{aligned}
&\overline{P}_{(i,j+1)}\left(\left(\frac{\overline{\rho}\overline{h}^3}{\overline{\eta}}\right)_{(i,j+1)} + \left(\frac{\overline{\rho}\overline{h}^3}{\overline{\eta}}\right)_{(i,j)}\right)\\
-\ &\overline{P}_{(i,j)}\left(\left(\frac{\overline{\rho}\overline{h}^3}{\overline{\eta}}\right)_{(i,j+1)} + 2\left(\frac{\overline{\rho}\overline{h}^3}{\overline{\eta}}\right)_{(i,j)} + \left(\frac{\overline{\rho}\overline{h}^3}{\overline{\eta}}\right)_{(i,j-1)}\right)\\
+\ &\overline{P}_{(i,j-1)}\left(\left(\frac{\overline{\rho}\overline{h}^3}{\overline{\eta}}\right)_{(i,j)} + \left(\frac{\overline{\rho}\overline{h}^3}{\overline{\eta}}\right)_{(i,j-1)}\right)
\end{aligned}
\right\}
\qquad [4.84]
$$

$$
-\ 12\overline{u}_x\frac{\overline{p}_i^{\,3}}{a^2b\Delta\overline{x}}\left[\left(\overline{\rho}\overline{h}\right)_{i,j} - \left(\overline{\rho}\overline{h}\right)_{i,j-1}\right]
$$

The Reynolds' equation in Jacobian form has to be expressed in terms of Taylor series expansion, as shown in equation [4.81]. Therefore, equation [4.84] has to be differentiated with respect to $\partial\overline{p}_{(i+1,j)}$, $\partial\overline{p}_{(i-1,j)}$, $\partial\overline{p}_{(i,j)}$, $\partial\overline{p}_{(i,j+1)}$ and $\partial\overline{p}_{(i,j-1)}$. This in turn yields a large equation, therefore, only one of the expressions, differentiation of $\partial f_{(i,j)}^{\,J}$ with respect to $\partial\overline{p}_{(i+1,j)}$ yields:

$$\frac{\partial f_{(i,j)}{}^{J}}{\partial \overline{p}_{(i+1,j)}} = \frac{a^2}{2b^2 \Delta \overline{x}^2} \frac{\partial}{\partial \overline{p}_{(i+1,j)}} \left\{ \begin{array}{l} \overline{p}_{(i+1,j)} \left(\left(\frac{\overline{\rho} \overline{h}^3}{\overline{\eta}} \right)_{(i+1,j)} + \left(\frac{\overline{\rho} \overline{h}^3}{\overline{\eta}} \right)_{(i,j)} \right) \\[1em] - \overline{p}_{(i,j)} \left(\left(\frac{\overline{\rho} \overline{h}^3}{\overline{\eta}} \right)_{(i+1,j)} + 2 \left(\frac{\overline{\rho} \overline{h}^3}{\overline{\eta}} \right)_{(i,j)} + \left(\frac{\overline{\rho} \overline{h}^3}{\overline{\eta}} \right)_{(i-1,j)} \right) \\[1em] + \quad \overline{p}_{(i-1,j)} \left(\left(\frac{\overline{\rho} \overline{h}^3}{\overline{\eta}} \right)_{(i,j)} + \left(\frac{\overline{\rho} \overline{h}^3}{\overline{\eta}} \right)_{(i-1,j)} \right) \end{array} \right\}$$

$$+ \quad \frac{1}{2 \Delta \overline{y}^2} \frac{\partial}{\partial \overline{p}_{(i+1,j)}} \left\{ \begin{array}{l} \overline{p}_{(i,j+1)} \left(\left(\frac{\overline{\rho} \overline{h}^3}{\overline{\eta}} \right)_{(i,j+1)} + \left(\frac{\overline{\rho} \overline{h}^3}{\overline{\eta}} \right)_{(i,j)} \right) \\[1em] - \overline{p}_{(i,j)} \left(\left(\frac{\overline{\rho} \overline{h}^3}{\overline{\eta}} \right)_{(i,j+1)} + 2 \left(\frac{\overline{\rho} \overline{h}^3}{\overline{\eta}} \right)_{(i,j)} + \left(\frac{\overline{\rho} \overline{h}^3}{\overline{\eta}} \right)_{(i,j-1)} \right) \\[1em] + \overline{p}_{(i,j-1)} \left(\left(\frac{\overline{\rho} \overline{h}^3}{\overline{\eta}} \right)_{(i,j)} + \left(\frac{\overline{\rho} \overline{h}^3}{\overline{\eta}} \right)_{(i,j-1)} \right) \end{array} \right\} \quad [4.85]$$

$$- \quad \frac{\partial}{\partial \overline{p}_{(i+1,j)}} \left[12 \overline{u}_x \frac{p_l^3}{a^2 b \Delta \overline{x}} \left[\left(\overline{\rho} \overline{h} \right)_{i,j} - \left(\overline{\rho} \overline{h} \right)_{i,j-1} \right] \right]$$

103

The differentiation of the term $\dfrac{\partial f_{(i,j)}{}^{J}}{\partial \overline{p}_{(i+1,j)}}$ yields the following equation:

$$
\begin{aligned}
\frac{\partial f_{(i,j)}{}^{J}}{\partial \overline{p}_{(i+1,j)}} = \quad & \frac{a^2}{2b^2 \Delta \overline{x}^2}
\left\{
\begin{array}{l}
\left(\left(\dfrac{\overline{\rho}\overline{h}^3}{\overline{\eta}} \right)_{(i+1,j)} + \left(\dfrac{\overline{\rho}\overline{h}^3}{\overline{\eta}} \right)_{(i,j)} \right) \\[3ex]
-\overline{p}_{(i,j)} \left(\dfrac{\partial \left(\dfrac{\overline{\rho}\overline{h}^3}{\overline{\eta}} \right)_{(i+1,j)}}{\partial \overline{p}_{(i+1,j)}} + 2\dfrac{\partial \left(\dfrac{\overline{\rho}\overline{h}^3}{\overline{\eta}} \right)_{(i,j)}}{\partial \overline{p}_{(i+1,j)}} + \dfrac{\partial \left(\dfrac{\overline{\rho}\overline{h}^3}{\overline{\eta}} \right)_{(i-1,j)}}{\partial \overline{p}_{(i+1,j)}} \right) \\[4ex]
+\overline{p}_{(i-1,j)} \left(\dfrac{\partial \left(\dfrac{\overline{\rho}\overline{h}^3}{\overline{\eta}} \right)_{(i,j)}}{\partial \overline{p}_{(i+1,j)}} + \dfrac{\partial \left(\dfrac{\overline{\rho}\overline{h}^3}{\overline{\eta}} \right)_{(i-1,j)}}{\partial \overline{p}_{(i+1,j)}} \right)
\end{array}
\right\} \\[6ex]
+ \quad & \frac{1}{2\Delta \overline{y}^2}
\left\{
\begin{array}{l}
\left(\dfrac{\partial \left(\dfrac{\overline{\rho}\overline{h}^3}{\overline{\eta}} \right)_{(i,j+1)}}{\partial \overline{p}_{(i+1,j)}} + \dfrac{\partial \left(\dfrac{\overline{\rho}\overline{h}^3}{\overline{\eta}} \right)_{(i,j)}}{\partial \overline{p}_{(i+1,j)}} \right) \\[4ex]
-\overline{p}_{(i,j)} \left(\dfrac{\partial \left(\dfrac{\overline{\rho}\overline{h}^3}{\overline{\eta}} \right)_{(i,j+1)}}{\partial \overline{p}_{(i+1,j)}} + 2\dfrac{\partial \left(\dfrac{\overline{\rho}\overline{h}^3}{\overline{\eta}} \right)_{(i,j)}}{\partial \overline{p}_{(i+1,j)}} + \dfrac{\partial \left(\dfrac{\overline{\rho}\overline{h}^3}{\overline{\eta}} \right)_{(i,j-1)}}{\partial \overline{p}_{(i+1,j)}} \right) \\[4ex]
+\overline{p}_{(i,j-1)} \left(\dfrac{\partial \left(\dfrac{\overline{\rho}\overline{h}^3}{\overline{\eta}} \right)_{(i,j)}}{\partial \overline{p}_{(i+1,j)}} + \dfrac{\partial \left(\dfrac{\overline{\rho}\overline{h}^3}{\overline{\eta}} \right)_{(i,j-1)}}{\partial \overline{p}_{(i+1,j)}} \right)
\end{array}
\right\} \\[6ex]
- \quad & \left[12\overline{u}_x \frac{p_i^3}{a^2 b \Delta x} \left[\frac{\partial \left(\overline{\rho}\overline{h} \right)_{i,j}}{\partial \overline{p}_{(i+1,j)}} - \frac{\partial \left(\overline{\rho}\overline{h} \right)_{i,j-1}}{\partial \overline{p}_{(i+1,j)}} \right] \right]
\end{aligned}
\qquad [4.86]
$$

104

The partial differentiation $\partial\bar{\eta}_{(i+1,j)}$, $\partial\bar{p}_{(i+1,j)}$ and $\partial\bar{h}_{(i+1,j)}$ with respect to $\partial\bar{p}_{(i+1,j)}$, in the second line of equation [4.86] is as shown below:

$$\frac{\partial\left(\frac{\bar{p}\bar{h}^3}{\bar{\eta}}\right)_{(i+1,j)}}{\partial\bar{p}_{(i+1,j)}} = \left(\frac{\bar{h}^3_{(i+1,j)}}{\bar{\eta}_{(i+1,j)}}\cdot\frac{\partial\bar{p}_{(i+1,j)}}{\partial\bar{p}_{(i+1,j)}} - \frac{\bar{h}^3_{(i+1,j)}}{\bar{\eta}^2_{(i+1,j)}}\cdot\frac{\partial\bar{\eta}_{(i+1,j)}}{\partial\bar{p}_{(i+1,j)}} + \frac{3\bar{h}^2_{(i+1,j)}}{\bar{\eta}_{(i+1,j)}}\cdot\frac{\partial\bar{h}_{(i+1,j)}}{\partial\bar{p}_{(i+1,j)}}\right) \qquad [4.87]$$

In equation [4.87], the first differential term is the variation of density with pressure; the second differential term is the variation of viscosity with pressure; the final differential term is the variation lubricant film thickness with pressure.

Referring to equation [4.1], the density, expressed in terms of non-dimensional pressure is:

$$\bar{p} = 1 + \frac{5.83\times10^{-10}\,\bar{p}E'}{1+\left(1.68\times10^{-9}\,\bar{p}E'\right)} \qquad [4.88]$$

where the coefficients 5.83×10^{-10} and 1.68×10^{-9} were obtained experimentally (**Hamrock** and **Dowson** (1994)). Since the pressures generated in large conformal contacts such as piston against bore (**Li** *et al* (1981), **Knoll** *et at* (1982) and **Xie** *et al* (1998)), is appreciably smaller than that in counterformal contacts, variation of density due to rise in pressure is small and therefore can be ignored. Non-dimensional viscosity in terms of non-dimensional pressure can be written; by referring to equation [4.7] as:

$$\bar{\eta} = \exp^{(\ln\eta_o+9.67)\left(-1+\left(1+5.1\times10^{-9}\,\bar{p}E'\right)\right)} \qquad [4.89]$$

Therefore, variation of viscosity with respect to pressure can be expressed by differentiating equation [4.89] as:

$$\frac{\partial\bar{\eta}_{(i,j)}}{\partial\bar{p}_{(k,l)}} = \left[Z_1\cdot(\ln\eta_0+9.67)\cdot\left(5.1\times10^{-9}\right)\cdot\left(1+5.1\times10^{-9}E'\bar{p}_{(k,l)}\right)^{Z_1-1}\right]\cdot\bar{\eta}_{(i,j)} \qquad [4.90]$$

Variation of film thickness with respect to pressure is attributed to the deflection of the contiguous bodies. This is described by the elasticity of the bodies, as shown in section 4.3. The value for the differential is the influencing point in the deflection co-efficient matrix, given by equation [4.32]. Thus, the film shape variation in equation [4.87] is written as:

$$\frac{\partial \overline{h}_{(i,j)}}{\partial \overline{P}_{(k,l)}} = D_{(m,n)} \qquad [4.91]$$

Therefore, for the point $(i+1,j)$, the above differential can be written as:

$$\frac{\partial \overline{h}_{(i+1,j)}}{\partial \overline{P}_{(i+1,j)}} = D(1,1) \qquad [4.92]$$

where:

$$i = (i+1), k = (i+1)$$
$$j = (j), l = (j)$$

Substituting equations [4.91] and [4.90] into equation [4.87] for point $(i+1,j)$ results in:

$$\frac{\partial \left(\frac{\overline{p}\,\overline{h}^3}{\overline{\eta}} \right)_{(i+1,j)}}{\partial \overline{P}_{(i+1,j)}} = \left(\begin{array}{c} \dfrac{\overline{h}^3_{(i+1,j)}}{\overline{\eta}_{(i+1,j)}} \cdot \dfrac{\partial \overline{P}_{(i+1,j)}}{\partial \overline{P}_{(i+1,j)}} \\[2ex] -\dfrac{\overline{h}^3_{(i+1,j)}}{\overline{\eta}^2_{(i+1,j)}} \cdot \left[Z_1 \cdot \left(\ln \eta_0 + 9.67 \right) \cdot \left(5.1 \times 10^{-9} \right) \cdot \left(1 + 5.1 \times 10^{-9}\, E' \overline{p}_{(k,l)} \right)^{Z_1 - 1} \right] \cdot \overline{\eta}_{(i,j)} \\[2ex] +\dfrac{3\overline{h}^2_{(i+1,j)}}{\overline{\eta}_{(i+1,j)}} \cdot D(1,1) \end{array} \right)$$

[4.93]

Equation [4.93] is one of the many partial differential terms, solved for and shown here. For the remaining terms, similar approach is employed to complete the formulation of the Jacobian terms for the rest of the influencing points; substituted back into equation [4.86] for the respective parameters to complete the expression.

106

4.5.1 Simulation Condition for Quasi Static Analysis

Simulations were carried out for a high performance V10, 2.99 Litres racing engine and a commercial/passenger, inline 4-cylinder, 1.8 litres diesel engine. Piston of the high performance engine is of a hollow construction, made out of a high grade aluminium alloy, with modulus of elasticity of 78 GPa, (**Howell-Smith** (2002)). Although, the piston is hollow, it is of sufficient thickness for the semi-infinite assumption to hold. It should be noted that for semi-infinite counterformal circular contact the ratio $\frac{a}{R}$ less than 0.5 (where a is the Hertzian radius and r is the equivalent radius) represents semi-infinite condition. When this value exceeds 2, a layered contact results. For the case of conformal contacts here, the dimensions of contact are large, but far less than the equivalent radius (typically piston skirt length is 37mm and the equivalent radius is 200m). Therefore, the aforementioned ratio is quite small and semi-infinite assumption is deemed valid. This is also inline with the arguments put forward in section 4.3.2. The piston liner is made out of an Al-based Metal-Matrix-Composite, with electrolytic coating of Nickel and Silica. Piston skirt and liner are honed to super-finish. In some cases surface modification is carried out to form lubricant trapping grooves. Although maximum combustion pressure for these types of engine can reach 120MPa (shown in figure 3.4), for this study, it was set at 50 MPa for a lower-mid-range engine speed. Number of computation points used for numerical analysis was 200X100, the former in the direction of entraining motion. Maximum combustion pressure occurs 13 degrees (in terms of crank-angle past TDC). Piston skirt has a nominal diameter of 92.143 mm, with a nominal clearance of 57.5 micrometer with bore. Out-of-roundness of the piston is incorporated in the analysis. Average temperature gradient from the ring pack to the bottom of piston skirt, measured at Perfect Bore Ltd (**Howell-Smith** (2002)) was found to be approximately 245° and 125° correspondingly. This variation of temperature led to a maximum expansion of the piston diameter by 84 micrometer (**Golya** (2000)).

Pistons of the diesel engine are, however, of sturdy construction and are made out of cast iron, with modulus of elasticity of 210 GPa, (**Hayes Refence Manual** (1992)). Except for

relief radii at extremities, there are no special surface features on this piston. The maximum combustion pressure for this engine can reach 34.5MPa (shown in figure 3.3), at engine speed of 3700rpm. Number of computation points used is the same as in section 4.5.2, 200 by 160 nodes. Maximum combustion pressure occurs 13 degrees (in terms of crank-angle past TDC).

Three conditions in a cycle is carefully investigated for both the engines; these are at:
- top dead centre position (TDC)
- combustion position
- bottom dead centre position (BDC)

Further instantaneous parameters, such as the entraining speed, load and geometry are described in chapter 5, at each condition investigated.

4.5.2 Boundary Conditions for Quasi Static Analysis

The boundary conditions employed to limit the solution domain in this analysis are:

- At the *edges* of the rectangular computational zone, shown in figure 4.9, the pressures are considered to be equal to zero, therefore for a mesh of 200 by 160;

$$\bar{P}_{(i,1)} = \bar{P}_{(201,j)} = \bar{P}_{(i,161)} = \bar{P}_{(1,j)} = 0$$

- To avoid tensile pressures in the fluid film (which are negative) at the cavitation boundary, the Reynolds' condition $\bar{p} = \dfrac{\partial \bar{p}}{\partial x} = \dfrac{\partial \bar{p}}{\partial y} = 0$ is used. This condition prevails, when a negative pressure value is encountered during the iteration and is set to zero.

The chosen boundary conditions are consistent with that employed by **Li** *et al* (1981) and **Knoll** and **Peeken** (1982).

4.5.3 Convergence Criteria for Quasi Static Analysis

To approximate a solution to the equation [4.79], an error tolerance must be specified. If the roots obtained are within the limits of the required tolerance, then the numerical procedure is deemed to have converged and a solution found.

There are two roots required in order to attain the overall solution to the coupled non-linear equations. The first root obtained is for the pressure, which in turn is fed back into the numerical procedure to evaluate the second root. This second root is for the load and should be approximately equal to the initial input load. The flowchart shown in figure 4.12 provides a graphical representation of the convergence procedure.

$$\sum\sum \left| \frac{p_{i,j}^{n+1} - p_{i,j}^{n}}{p_{i,j}^{n+1}} \right| \leq 0.1 \qquad \boxed{\text{No}} \qquad \Longrightarrow \qquad \boxed{\begin{array}{c}\text{Continue}\\ \text{iterative}\\ \text{process}\end{array}}$$

$$\boxed{\text{Yes}}$$

$$\left| \frac{W - F_r}{F_r} \right| \leq 10^{-5} \qquad \boxed{\text{No}} \qquad \Longrightarrow \qquad h^{n+1} = h^{n} + \left(F_r - W \right)\wp'$$

$$\boxed{\text{Yes}}$$

$$5.0 \times 10^{-11} \leq \wp' \leq 5.0 \times 10^{-10}$$
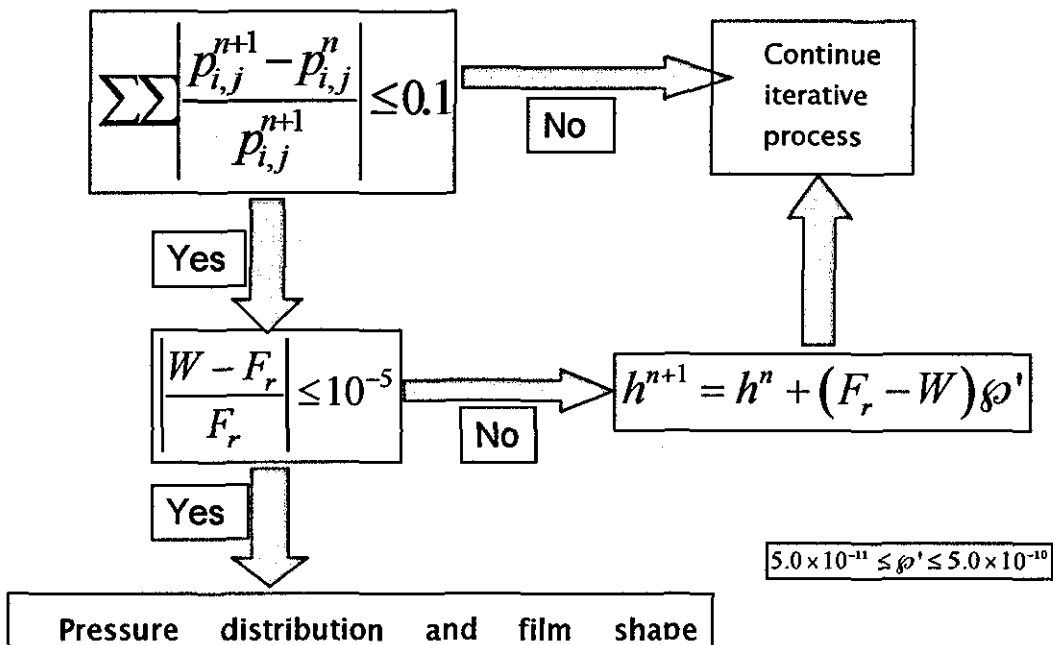
Pressure   distribution   and   film   shape

Figure 4.12: Flowchart of convergence

109

Therefore, for the pressures to converge, the following criterion is employed:

$$\frac{\sum_{i=1}^{nx}\sum_{j=1}^{ny}\left|p_{(i,j)}^{n}-p_{(i,j)}^{o}\right|}{\sum_{i=1}^{nx}\sum_{j=1}^{ny}p_{(i,j)}^{n}} \leq \varepsilon_{rp}$$

[4.94]

where, the error tolerance for the pressure ε_{rp} is set equal to **0.0001**. If the convergence is not achieved, the input pressures into the next iteration loop are updated, using the following expression:

$$p_{(i,j)}^{n} = p_{(i,j)}^{o} + \wp_{p}\Delta p_{(i,j)}$$

[4.95]

where $\wp_{p}$ is the under-relaxation factor, which ranges from 0.1 to 1.0, depending on the type of EHL problem at hand. Similarly, for the load to reach a converged solution, the criterion used is:

$$\left|W - F\right| \leq \varepsilon_{L}$$

[4.96]

Here, the error tolerance for load convergence ε_{L} is set equal to **0.0001**. If the load has not converged, then the central film thickness is adjusted according to the evaluated unbalanced load, using the following formulation:

$$h^{n+1} = h^{n} + \left(F - W\right)\wp_{L}$$

[4.97]

where $\wp_{L}$ is the damping co-efficient used to dampen the fluctuations in central oil film thickness. Hence, if the evaluated load W is less than F, then the central film thickness is further reduced.

4.6.1 Reynolds' Equation with Elastic Squeeze Effect for Transient Analysis

As the name suggests, quasi-static analysis of lubrication problem solves for the pressures generated in a lubricated conjunction for an applied load at an instant in time (see section 4.4). Therefore, by nature, it does not possess the element of time or history of lubricant film shape, whereas this is not true for a transient lubrication analysis (**Christensen** (1961, 1970) and **Herrebrugh** (1970)). Rewriting the equation [4.53], the partial differential terms of variation of density and lubricant film thickness with time can be expressed as:

$$\frac{\partial}{\partial x}\left(\frac{\rho h^3}{\eta}\frac{\partial p}{\partial x}\right)+\frac{\partial}{\partial y}\left(\frac{\rho h^3}{\eta}\frac{\partial p}{\partial y}\right)=12\left[u_{AV}\frac{\partial}{\partial x}(\rho h)+v_{AV}\frac{\partial}{\partial y}(\rho h)+\frac{\partial\rho}{\partial t}(h)+\frac{\partial h}{\partial t}(\rho)\right] \quad [4.98]$$

Variation of density with time, $\frac{\partial\rho}{\partial t}$, can be ignored as it was found to make no significant difference in the final results (**Jalali-Vahid** (2000)).

The term $\frac{\partial h}{\partial t}$ is known as the squeeze velocity. As the body is deflected due to pressure, lubricant is assumed to fill the gap. The elastic squeeze term, $\frac{\partial h}{\partial t}$, describes the mutual approach or separation of surfaces. Studies by **Christensen** (1961, 1970) and **Herrebrugh** (1970), **Jalali-Vahid** (1999) and **Kushwaha** (2000) have all shown that a larger lubricant film was predicted when the elastic squeeze was taken into account.

Referring to equation [4.98] and ignoring the density variation with time, the dimensionless Reynolds' equation, including the effect of elastic squeeze can be expressed as:

$$\frac{a^2}{b^2}\frac{\partial}{\partial\bar{x}}\left(\frac{\overline{\rho h}^3}{\bar{\eta}}\frac{\partial\bar{p}}{\partial\bar{x}}\right)+\frac{\partial}{\partial\bar{y}}\left(\frac{\overline{\rho h}^3}{\bar{\eta}}\frac{\partial\bar{p}}{\partial\bar{y}}\right)=12\bar{u}_x\frac{P_l^3}{a^2 b}\frac{\partial}{\partial\bar{x}}\left(\overline{\rho h}\right)+12\frac{P_l^2}{a^2}\bar{\rho}\frac{\partial}{\partial\bar{t}}\left(\bar{h}_t-\bar{h}_{t-1}\right) \quad [4.99]$$

The discretised Reynolds' equation, similar to that in equation [4.70], is written as:

$$
\frac{a^2}{b^2}\left[\frac{\left(\dfrac{\overline{\rho}\overline{h}^3}{\overline{\eta}}\right)_{(i+\frac{1}{2},j)}\left(\dfrac{\overline{P}_{(i+1,j)}-\overline{P}_{(i,j)}}{\Delta\overline{x}}\right)-\left(\dfrac{\overline{\rho}\overline{h}^3}{\overline{\eta}}\right)_{(i-\frac{1}{2},j)}\left(\dfrac{\overline{P}_{(i,j)}-\overline{P}_{(i-1,j)}}{\Delta\overline{x}}\right)}{\Delta\overline{x}}\right]
$$

$$
+\left[\frac{\left(\dfrac{\overline{\rho}\overline{h}^3}{\overline{\eta}}\right)_{(i,j+\frac{1}{2})}\left(\dfrac{\overline{P}_{(i,j+1)}-\overline{P}_{(i,j)}}{\Delta\overline{y}}\right)-\left(\dfrac{\overline{\rho}\overline{h}^3}{\overline{\eta}}\right)_{(i,j-\frac{1}{2})}\left(\dfrac{\overline{P}_{(i,j)}-\overline{P}_{(i,j-1)}}{\Delta\overline{y}}\right)}{\Delta\overline{y}}\right]
\qquad [4.100]
$$

$$
= \quad 12\overline{u}_x\frac{p_l^3}{a^2 b\Delta\overline{x}}\left[\left(\overline{\rho}\overline{h}\right)_{i+1,j}-\left(\overline{\rho}\overline{h}\right)_{i-1,j}\right]+12\frac{p_l^2\overline{\rho}_{(i,j)}}{a^2\Delta\overline{t}}\left(\overline{h}_{t_{(i,j)}}-\overline{h}_{t-1_{(i,j)}}\right)
$$

Therefore, the residual function, $f^R_{(i,j)}$, including the elastic squeeze term can be expressed as:

$$
f^R = \frac{a^2}{2b^2\Delta\overline{x}^2}\left\{
\begin{array}{l}
\overline{P}_{(i+1,j)}\left(\left(\dfrac{\overline{\rho}\overline{h}^3}{\overline{\eta}}\right)_{(i+1,j)}+\left(\dfrac{\overline{\rho}\overline{h}^3}{\overline{\eta}}\right)_{(i,j)}\right)\\[3ex]
-\;\overline{P}_{(i,j)}\left(\left(\dfrac{\overline{\rho}\overline{h}^3}{\overline{\eta}}\right)_{(i+1,j)}+2\left(\dfrac{\overline{\rho}\overline{h}^3}{\overline{\eta}}\right)_{(i,j)}+\left(\dfrac{\overline{\rho}\overline{h}^3}{\overline{\eta}}\right)_{(i-1,j)}\right)\\[3ex]
+\quad\overline{P}_{(i-1,j)}\left(\left(\dfrac{\overline{\rho}\overline{h}^3}{\overline{\eta}}\right)_{(i,j)}+\left(\dfrac{\overline{\rho}\overline{h}^3}{\overline{\eta}}\right)_{(i-1,j)}\right)
\end{array}
\right\}
$$

$$
+\;\frac{1}{2\Delta\overline{y}^2}\left\{
\begin{array}{l}
\overline{P}_{(i,j+1)}\left(\left(\dfrac{\overline{\rho}\overline{h}^3}{\overline{\eta}}\right)_{(i,j+1)}+\left(\dfrac{\overline{\rho}\overline{h}^3}{\overline{\eta}}\right)_{(i,j)}\right)\\[3ex]
-\;\overline{P}_{(i,j)}\left(\left(\dfrac{\overline{\rho}\overline{h}^3}{\overline{\eta}}\right)_{(i,j+1)}+2\left(\dfrac{\overline{\rho}\overline{h}^3}{\overline{\eta}}\right)_{(i,j)}+\left(\dfrac{\overline{\rho}\overline{h}^3}{\overline{\eta}}\right)_{(i,j-1)}\right)\\[3ex]
+\quad\overline{P}_{(i,j-1)}\left(\left(\dfrac{\overline{\rho}\overline{h}^3}{\overline{\eta}}\right)_{(i,j)}+\left(\dfrac{\overline{\rho}\overline{h}^3}{\overline{\eta}}\right)_{(i,j-1)}\right)
\end{array}
\right\}
\qquad [4.101]
$$

$$
-\quad 12\overline{u}_x\frac{p_l^3}{a^2 b\Delta\overline{x}}\left[\left(\overline{\rho}\overline{h}\right)_{i+1,j}-\left(\overline{\rho}\overline{h}\right)_{i-1,j}\right]\;+\;12\frac{p_l^2\overline{\rho}_{(i,j)}}{a^2\Delta\overline{t}}\left(\overline{h}_{t_{(i,j)}}-\overline{h}_{t-1_{(i,j)}}\right)
$$

and the Jacobian term as:

$$
\begin{aligned}
f^J = \quad & \frac{a^2}{2b^2\Delta\overline{x}^2}\left\{
\begin{array}{l}
\overline{P}_{(i+1,j)}\left(\left(\dfrac{\overline{\rho}\overline{h}^3}{\overline{\eta}}\right)_{(i+1,j)}+\left(\dfrac{\overline{\rho}\overline{h}^3}{\overline{\eta}}\right)_{(i,j)}\right) \\[1.5em]
- \;\overline{P}_{(i,j)}\left(\left(\dfrac{\overline{\rho}\overline{h}^3}{\overline{\eta}}\right)_{(i+1,j)}+2\left(\dfrac{\overline{\rho}\overline{h}^3}{\overline{\eta}}\right)_{(i,j)}+\left(\dfrac{\overline{\rho}\overline{h}^3}{\overline{\eta}}\right)_{(i-1,j)}\right) \\[1.5em]
+ \quad \overline{P}_{(i-1,j)}\left(\left(\dfrac{\overline{\rho}\overline{h}^3}{\overline{\eta}}\right)_{(i,j)}+\left(\dfrac{\overline{\rho}\overline{h}^3}{\overline{\eta}}\right)_{(i-1,j)}\right)
\end{array}\right\} \\[3em]
+ \quad & \frac{1}{2\Delta\overline{y}^2}\left\{
\begin{array}{l}
\overline{P}_{(i,j+1)}\left(\left(\dfrac{\overline{\rho}\overline{h}^3}{\overline{\eta}}\right)_{(i,j+1)}+\left(\dfrac{\overline{\rho}\overline{h}^3}{\overline{\eta}}\right)_{(i,j)}\right) \\[1.5em]
- \;\overline{P}_{(i,j)}\left(\left(\dfrac{\overline{\rho}\overline{h}^3}{\overline{\eta}}\right)_{(i,j+1)}+2\left(\dfrac{\overline{\rho}\overline{h}^3}{\overline{\eta}}\right)_{(i,j)}+\left(\dfrac{\overline{\rho}\overline{h}^3}{\overline{\eta}}\right)_{(i,j-1)}\right) \\[1.5em]
+ \quad \overline{P}_{(i,j-1)}\left(\left(\dfrac{\overline{\rho}\overline{h}^3}{\overline{\eta}}\right)_{(i,j)}+\left(\dfrac{\overline{\rho}\overline{h}^3}{\overline{\eta}}\right)_{(i,j-1)}\right)
\end{array}\right\} \\[3em]
- \quad & 12\overline{u}_x\frac{p_l^3}{a^2b\Delta x}\left[\left(\overline{\rho}\overline{h}\right)_{i,j}-\left(\overline{\rho}\overline{h}\right)_{i,j-1}\right]+12\frac{p_l^2\overline{P}_{(i,j)}}{a^2\Delta\overline{t}}\left(\overline{h}_{t_{(i,j)}}-\overline{h}_{t-1_{(i,j)}}\right)
\end{aligned}
\qquad [4.102]
$$

Note that the same procedure is followed throughout as that in sections 4.4.7 to section 4.4.8 in the formulation of the *residual* and *Jacobian* terms shown above.

113

Therefore, differentiating $\partial f_{(i,j)}{}^J$ with respect to $\partial \overline{p}_{(i+1,j)}$ yields:

$$
\frac{\partial f_{(i,j)}{}^J}{\partial \overline{p}_{(i+1,j)}} = \frac{a^2}{2b^2\Delta \overline{x}^2} \left\{ -\overline{P}_{(i,j)} \left[\frac{\left(\left(\frac{\overline{\rho}\overline{h}^3}{\overline{\eta}}\right)_{(i+1,j)} + \left(\frac{\overline{\rho}\overline{h}^3}{\overline{\eta}}\right)_{(i,j)} \right)}{} \frac{\partial\left(\frac{\overline{\rho}\overline{h}^3}{\overline{\eta}}\right)_{(i+1,j)}}{\partial \overline{p}_{(i+1,j)}} + 2\frac{\partial\left(\frac{\overline{\rho}\overline{h}^3}{\overline{\eta}}\right)_{(i,j)}}{\partial \overline{p}_{(i+1,j)}} + \frac{\partial\left(\frac{\overline{\rho}\overline{h}^3}{\overline{\eta}}\right)_{(i-1,j)}}{\partial \overline{p}_{(i+1,j)}} \right] + \overline{P}_{(i-1,j)}\left[\frac{\partial\left(\frac{\overline{\rho}\overline{h}^3}{\overline{\eta}}\right)_{(i,j)}}{\partial \overline{p}_{(i+1,j)}} + \frac{\partial\left(\frac{\overline{\rho}\overline{h}^3}{\overline{\eta}}\right)_{(i-1,j)}}{\partial \overline{p}_{(i+1,j)}} \right] \right\}
$$

$$
+ \frac{1}{2\Delta \overline{y}^2}\left\{ \frac{\partial\left(\frac{\overline{\rho}\overline{h}^3}{\overline{\eta}}\right)_{(i,j+1)}}{\partial \overline{p}_{(i+1,j)}} + \frac{\partial\left(\frac{\overline{\rho}\overline{h}^3}{\overline{\eta}}\right)_{(i,j)}}{\partial \overline{p}_{(i+1,j)}} - \overline{P}_{(i,j)}\left[\frac{\partial\left(\frac{\overline{\rho}\overline{h}^3}{\overline{\eta}}\right)_{(i,j+1)}}{\partial \overline{p}_{(i+1,j)}} + 2\frac{\partial\left(\frac{\overline{\rho}\overline{h}^3}{\overline{\eta}}\right)_{(i,j)}}{\partial \overline{p}_{(i+1,j)}} + \frac{\partial\left(\frac{\overline{\rho}\overline{h}^3}{\overline{\eta}}\right)_{(i,j-1)}}{\partial \overline{p}_{(i+1,j)}} \right] + \overline{P}_{(i,j-1)}\left[\frac{\partial\left(\frac{\overline{\rho}\overline{h}^3}{\overline{\eta}}\right)_{(i,j)}}{\partial \overline{p}_{(i+1,j)}} + \frac{\partial\left(\frac{\overline{\rho}\overline{h}^3}{\overline{\eta}}\right)_{(i,j-1)}}{\partial \overline{p}_{(i+1,j)}} \right] \right\}
$$

$$
- \left[12\overline{u}_x \frac{p_i^3}{a^2 b\Delta \overline{x}}\left[\frac{\partial\left(\overline{\rho}\overline{h}\right)_{i,j}}{\partial \overline{p}_{(i+1,j)}} - \frac{\partial\left(\overline{\rho}\overline{h}\right)_{i,j-1}}{\partial \overline{p}_{(i+1,j)}} \right] + 12\frac{p_i^2 \overline{P}_{(i,j)}}{a^2 \Delta \overline{t}}\left(\frac{\partial \overline{h}_{(i,j)}}{\partial \overline{p}_{(i+1,j)}} - \frac{\partial \overline{h}_{t-1(i,j)}}{\partial \overline{p}_{(i+1,j)}} \right) \right]
$$

[4.103]

114

4.6.2 Initial Condition for the Transient Analysis

In transient analysis, the piston was set just after TDC, with a crank-angle being $0.01°$. The piston was assumed to have a tilt angle of $0.1°$ (**Knoll** and **Peeken** (1981), **Goenka** *et al* (1994), **Xie** *et al* (1998)). At such position (shown by experience), the cylinder pressures maintain the contact load, helping to attain better convergence for displacement.

4.6.3 Boundary Conditions for Transient Analysis

The boundary condition for the transient analysis is similar to that in section 4.5.2

4.6.4 Convergence Criteria for Transient Analysis

For transient analysis, the convergence criterion is similar to the quasi-static analysis, with the exception that the load convergence is not carried out (**Al-Samieh** *et al* (2002), **Jalali-Vahid** et al (2001)). The computed pressures are integrated over the contact domain to obtain the lubricant reaction forces and moments. These reaction forces, f_{r1} (in the major thrust side) and f_{r2} (in the minor thrust side) and moments, m_{fr1} and m_{fr2}, are substituted into equations [3.25] and [3.26] to solve for $\ddot{e}_t$ and $\ddot{e}_b$. The lateral displacement, e_t and tilt β obtained from equations [3.10] or [3.11] provide the instantaneous profile at any given time-step.

Convergence is achieved, for any time-step t, when difference in the lateral accelerations $\ddot{e}_{t,u} - \ddot{e}_{t,u-1}$ and $\ddot{e}_{b,u} - \ddot{e}_{b,u-1}$ within iteration loop, is appreciably small. This is expressed as:

$$\left| \frac{\ddot{e}_{t,u} - \ddot{e}_{t,u-1}}{\ddot{e}_{t,u}} \right| \times 100 \le 1.0 \qquad [4.104]$$

and:

$$\left| \frac{\ddot{e}_{b,u} - \ddot{e}_{b,u-1}}{\ddot{e}_{b,u}} \right| \times 100 \leq 1.0 \qquad\qquad [4.105]$$

If both these conditions are not satisfied within a time-step, new iterative values of the tilt and lateral displacement are obtained from equations [3.10] or [3.11], and are used to update the profile in equation [4.60], thereby varying the elastic film shape equation.

4.7 Closure

In this chapter, a description of lubricant properties and its significance to lubrication problem was highlighted. A methodology to obtain the elasticity equation to define the deflection of two conforming bodies was presented. The validation of this equation in approximating deflections in conformal contacts is carried out in section 5.5. The Reynolds' equation was derived from the Navier-Stokes equation and the continuity of flow assumptions. A discretisation technique was described to enable numerical solution of the two dimensional Reynolds' equation for pressures generated in a lubricated contact. The initial conditions, boundary conditions and convergence criterion employed in both the quasi-static and transient analysis were highlighted.

Chapter 5

5.1 Introduction

Using the theory outlined in chapters 3 and 4, a numerical model to simulate the 3 degrees of freedom model of piston assembly was developed. As piston assembly accounts for a sizeable proportion of mechanical and frictional losses in internal combustion engines (IC) (as highlighted in chapter 1), it is essential to undertake remedial actions in order to minimise these.

Modern material science and technology allows for use of high performance alloys that provide light-weight, but structurally durable components, for instance, the use of special grade aluminium alloys or Metal Matrix Composites, which may be aluminium based (as described later on). Therefore, low inertial dynamics can be achieved. Current technology is also available in some applications to provide high BMEP and low emissions than the conventional diesel engines, for example through EGR or HCCI (**Taylor** 1993). Therefore, all the conditions mentioned above can be satisfied and are attainable. The reason that these stated objectives are not being achieved, are in part due to problems encountered in tribo-dynamics of piston-to-cylinder bore contact. High combustion pressures result in severe impact dynamics problem, such as in piston to cylinder liner slapping action. This impact, not only induces structural vibration and noise emission problems, but can also lead to component degradation due to contact fatigue spalling or scuffing failures, resulting from bridging of lubricant film. Nevertheless, the technology of having high combustion pressures, even in gasoline engines, low inertial dynamics per construction configuration, is already available in high performance compact engines, such as in racing vehicles. It, therefore, appears like many other engineering solutions, that a transfer of technology from high to lower levels should be strived for. This is possible even with a reduction in cost due to use of diesel as opposed to gasoline. After all, the philosophy in racing cars was originally to use them as a test-bed for commercial developments.

To achieve the above mentioned objectives, however, a fundamental understanding of the tribo-dynamics problem is necessary, which contrary to many reported initial investigations, advocating a simplified approach, invariably a very detailed analysis would yield a practical solution. In such a detailed analysis, elastic deformation of contiguous bodies, geometrical profile of mating members and effect of surface features should be considered, in order to retain a coherent film. Therefore, this chapter outlines such a detailed approach for high technology precision piston systems, and attempts to ascertain the performance difference between these, and those used in commercial vehicles.

5.2 Simulation Conditions

A number of simulation studies are carried out in this chapter to investigate the tribo-dynamic conditions in piston-skirt to cylinder liner conformal contact. The conditions pertain to quasi-static analysis. The dynamic forces are calculated separately for given positions in the piston cycle and used as an input for the analysis. The instantaneous tilt angle of the piston and the speed of entraining motion are also the other input parameters into a quasi-static analysis. Although, such an analysis is a good representation of actual prevailing conditions, it carries no history of lubricant film from a space-time location to another, and lacks the increased load carrying capacity of the contact due to squeeze film action. However, as opposed to the fully transient conditions, thus described, the quasi-static analyses have the advantage of considerably lower computational intensity, both in terms of CPU times and memory allocation. Therefore, a greater amount of output data, at considerably reduced analysis time can be obtained. Transient tribo-dynamic analysis has been carried out in chapter 6. The key point is to undertake such an investigation at piston positions of interest, where significant adverse condition, either in terms of wear or contact fatigue performance occur, such as at entraining motion reversals (**Priebsch** 2001) at TDC or BDC. The latter position has the additional loss of contact load, which results in reduced contact deformation, which in turn can yield very low lubricant film thickness. Another position of interest is at the peak combustion pressure, where the

118

generated pressures can lead to lateral and tilting motion of the piston, and the subsequent aforementioned slapping problem.

The quasi-static analysis is also mostly carried out under isothermal conditions. However, thermal distortion of the system can lead to the diminution of the clearance and lead to diminishing film thickness, leading to asperity interactions, a mixed regime of lubrication or even boundary lubrication. A few analyses have been carried out to investigate such conditions, but a thermoelastohydrodynamic analysis has not been carried out, as most studies have shown that isothermal analyses yield results that deviate from actual conditions by only a small amount. Since lubricant behaviour is considered to be Newtonian, its tractive response has been ignored. Fully flooded inlet conditions cannot be assured, as in reality the speed of entraining motion continually alters and reversals take place at both TDC and BDC, and in most cases the inlet distance required will be far in excess of the piston-skirt length. The simulated conditions, in fact, represent real situation in this regard.

All simulation studies were carried out with a 200 X 100 computational mesh density, the former in the axial direction (i.e. along the length of the piston skirt). The CPU time depended upon the contact load and the speed of entraining motion (i.e. the type of piston described in this chapter and the position of it within the cylinder bore). This varied in the range 16-28 hours on a Pentium 800 MHz machine. A typical analysis output requires 4 MB of computer storage.

The results presented in this chapter for each simulation case follows a particular template, consisting of a number of figures. These include a three dimensional contact pressure distribution, which is used as a visualisation aid to show the effects of piston skirt profile, its tilt, thermal distortion, ovality and the inclusion of any introduced surface feature upon generated pressures. Other figures include more quantitative representation of generated pressures as isobar plots, the corresponding oil film contours, indicating regions of minimum film thickness, certain two dimensional representations of these contour plots through sections of interest and flow patterns to study the physics of motion of the lubricant action.

119

Two simulation studies are reported below, one in respect of a 4-cylinder diesel engine (being a typical large volume automobile engine) and the other for a 10-cylinder high performance gasoline racing engine.

5.3 Results for a Diesel Engine

Tribo-dynamic analysis of piston assembly of a 4-cylinder, 4-stroke, in-line, 1.81 Litre direct injected diesel engine is considered in this section. This engine is employed for a range of models of volume manufactured vehicles. The maximum combustion pressure is 34 MPa, occurring during the piston cycle, $11°$ past the TDC, as measured in terms of crank-angle rotation. Note that the crank-angle of zero degrees denotes the TDC position. The combustion pressure curve is shown in figure 3.3. The pressure curve was measured by a pressure sensor fitted into the combustion chamber at Ford Werke AG, Köeln, Germany.

Both the cylinder and the piston are made of Steel, with Young's modulus of elasticity being 211 GPa, and Poisson's ratio of 0.3. The cylinder bore has a circular profile with a radius of 92.3 mm. The piston skirt has a nominal radius of 92.25 mm, providing a nominal clearance of 50 μm. The length of piston skirt is 52 mm. The piston gudgeon pin is offset by 10 μm. The piston profile in the circumferential direction is, in fact, oval, owing to deviations from this nominal radius. For the purpose of this simulation study, the ovality of the piston is ignored. The longitudinal profile of the piston skirt incorporates relief radii at its axial extremities. Figure 5.1 depicts the axial profile of the piston skirt. The surfaces of the contiguous bodies in contact are considered to be perfectly smooth. The connecting rod length is 126 mm and the crank-throw is 32 mm.
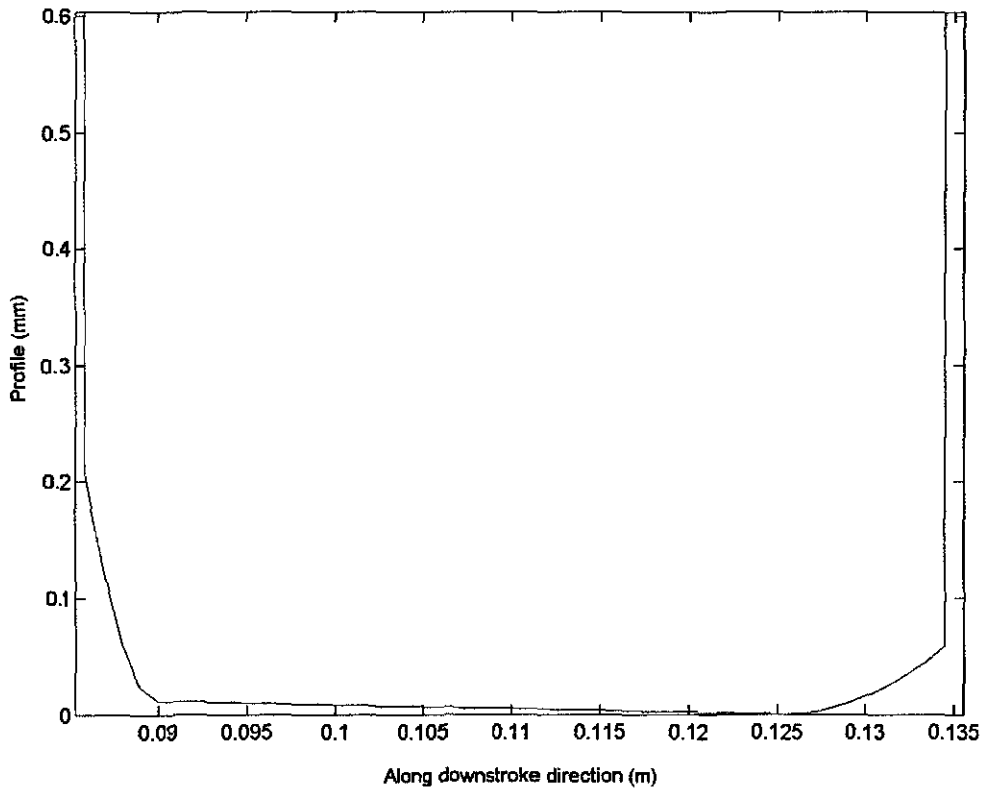
Figure 5.1: Undeformed piston skirt profile of 1.81L diesel engine

For this diesel engine piston, the number of computational mesh points along the longitudinal direction is 200 and along the circumferential direction is 100. In the profiled regions, the computational mesh points at the upper end of the skirt is 16 and 12 for and lower ends respectively.

The lubricant used is a mineral oil with its viscosity at atmospheric pressure, being $0.04 Pa \cdot s$. The piezo-viscosity of the lubricant is 10^{-9} Pa^{-1}. The density of the lubricant at atmospheric pressure is $860 Kg.m^{-3}$.

5.3.1- Analysis Results for TDC

At the TDC the contact load is quite low and sharply rises as the piston moves downwards towards the position, where the combustion takes place. At the TDC the

speed of entraining motion momentarily ceases, and any lubricant film is retained by squeeze film action. In a quasi-static analysis, the squeeze film velocity will not be known as the history of lubrication from a previous time step is not taken into account. Therefore, the analysis is carried out after motion reversal, very close to the TDC position. The velocity of the piston translational motion is approximately 26 mm/s (or the speed of entraining motion being 13 mm/s). which is very low indeed, when compared with its maximum mid-span velocity being 12 m/s and load of 46 N (obtained from analysis, see Chapter 3). Therefore, for all intent and purposes, the results would be quite representative of what takes place at the TDC, given that motion reversal is almost instantaneous. The tilt of the skirt towards the cylinder liner on the major thrust side, obtained through dynamic analysis is approximately $0.00175°$. Figure 5.2 shows the three dimensional pressure distribution for this condition. The pressure region occurs in the inlet region to the contact, which is on the bottom of the skirt, owing to the lubricant being pulled into the contact by wedge effect. Because of low load the pressure values are very low, and spread over a sizeable circumferential domain due to the almost aligned contact, owing to the small tilt angle.

Figure 5.3 is a two dimensional representation of the 3D pressure distribution, often referred to as pressure isobar or an isobaric pressure plot. Note that the high pressure inlet region, described above, is on the right-hand side of the figure.

Pressure distribution can also be viewed through axial and circumferential sections of the 3D pressure distribution. These are illustrated in figures 5.4 and 5.5 respectively, through the region of maximum pressure. It can be seen that the axial domain of pressure extends over 45 mm of the skirt of length 52 mm. In the circumferential direction, it extends for a π-film region.
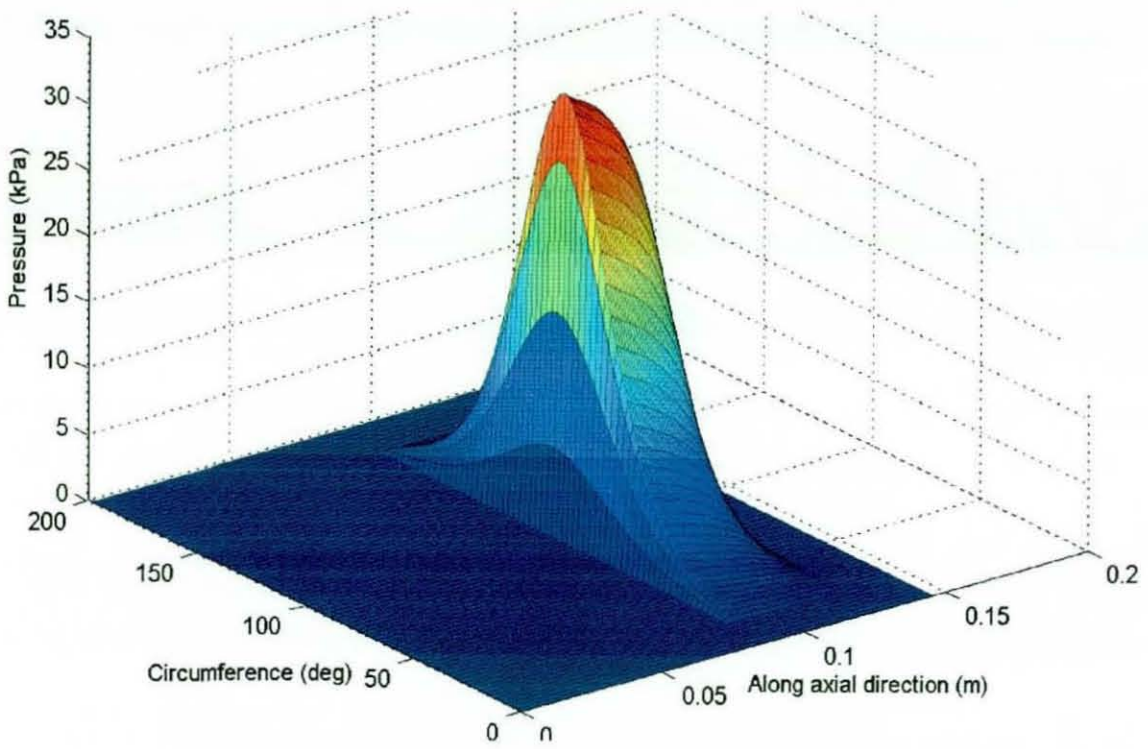
Figure 5.2: Three dimensional pressure distribution during reversal at TDC (entraining direction: from left to right along the axial direction)
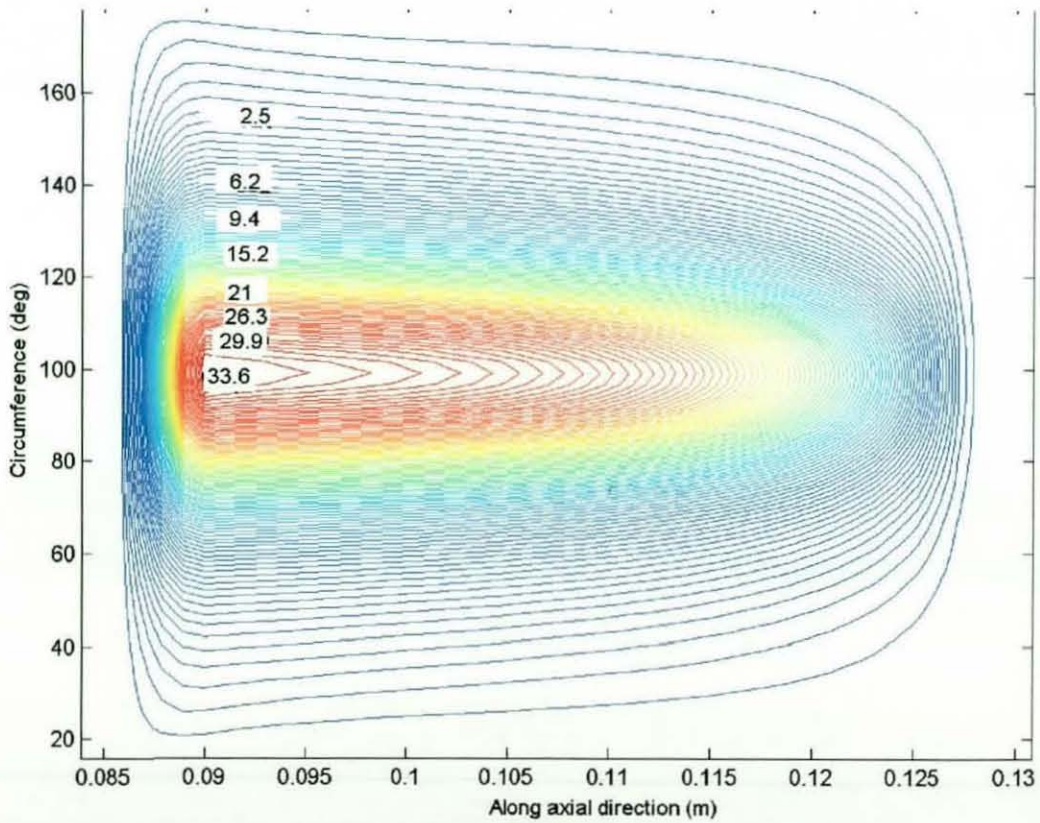

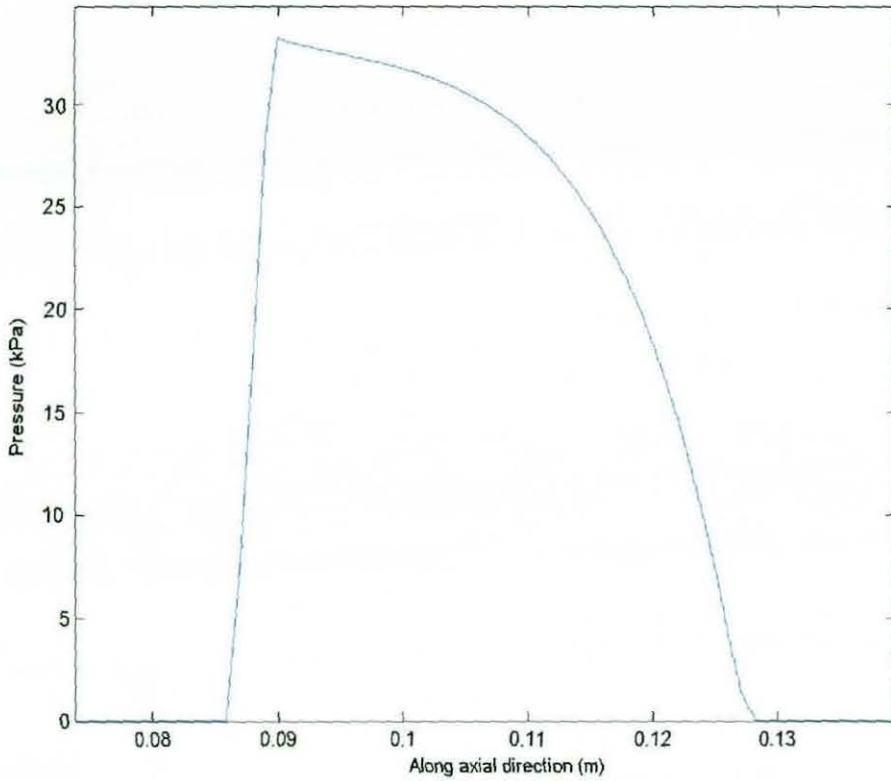Figure 5.3: Pressure isobar (in KPa) during reversal at TDC

123

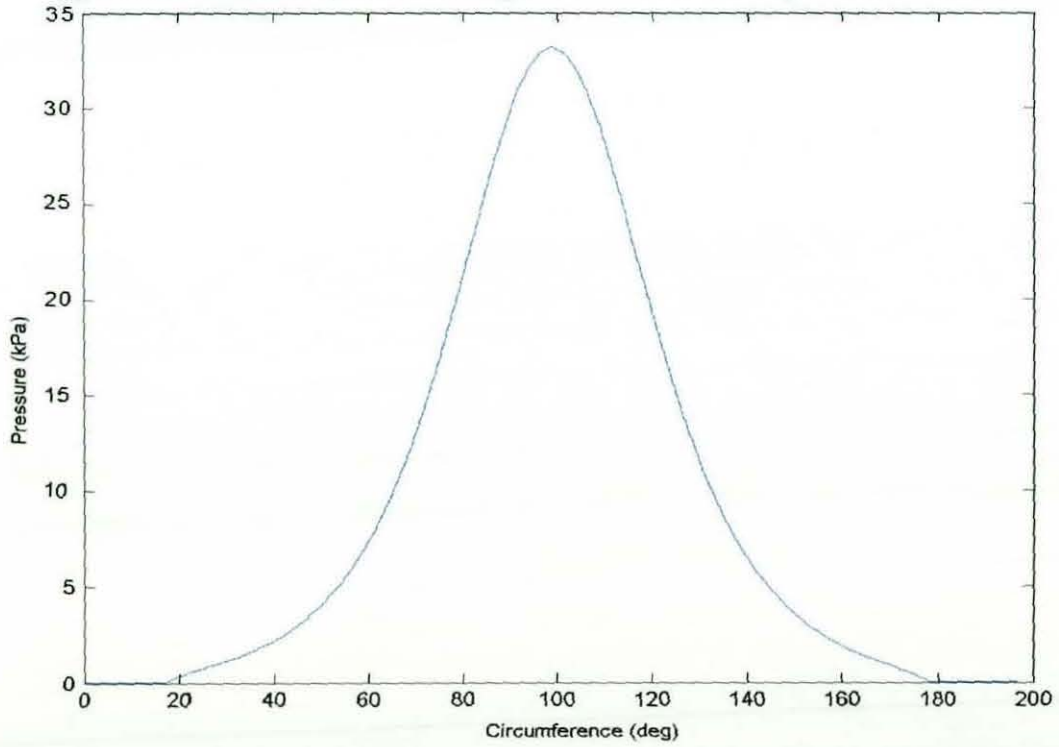Figure 5.4: Maximum pressure along axial direction during reversal at TDC

Figure 5.5: Maximum pressure along circumferential direction during reversal at TDC

The corresponding lubricant film contour is shown in figure 5.6. The region of minimum film is indicated by the contour level at 10.53 μm film thickness. In fact, the minimum film is less than this value, but it is difficult to show, owing to the required number of contour levels, which when implemented render the contour plot indecipherable. It is far easier to show the minimum film thickness by cutting through the oil film contour values from the computed numerical data. This is shown in figure 5.7a, where the minimum film at the exit region has fallen to a value of 9.5 μm. It is interesting to note the wedge shape of the lubricant film in this figure, extending all the way to the exit region, indicating that no deformation has taken place. This minimum film thickness is also shown in the circumferential cut of the oil film shape in the circumferential direction. The shape indicates the iso-viscous rigid nature of lubrication condition, which would not be easily surmised from the axial pressure distribution in figure 5.4, which can incorrectly be taken as being reminiscent of an elastohydrodynamic regime of lubrication. Note that the pressures are in KPa range.
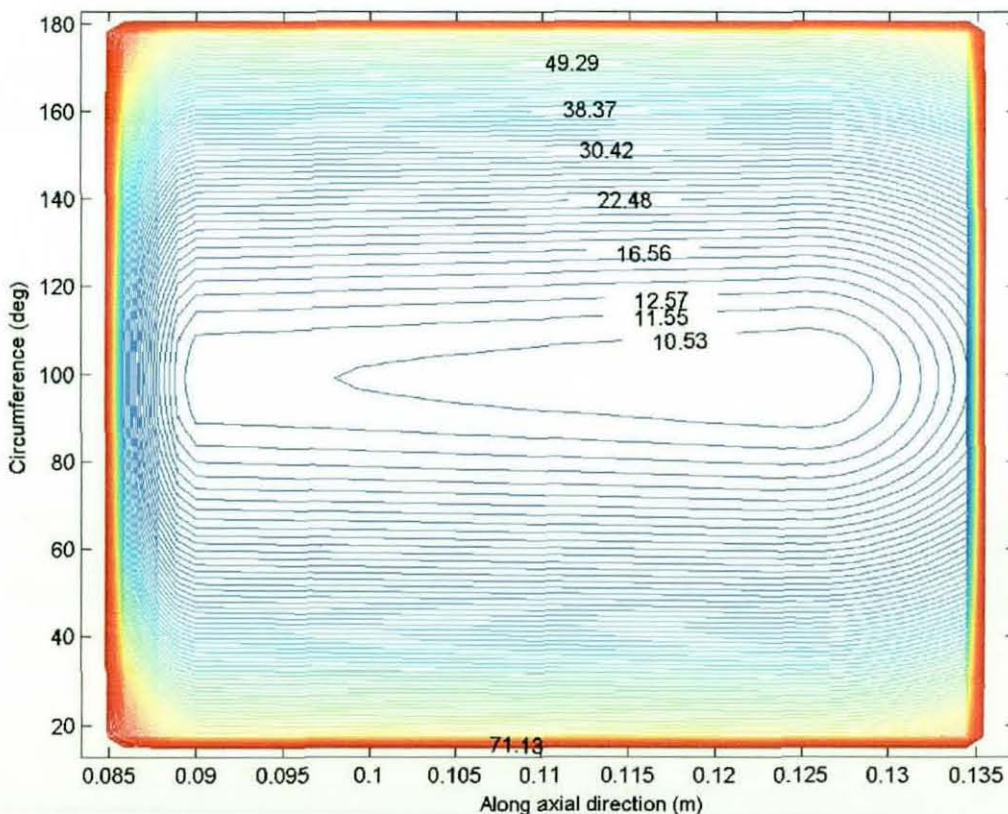
Figure 5.6: Lubricant film contour (in μm) during reversal at TDC
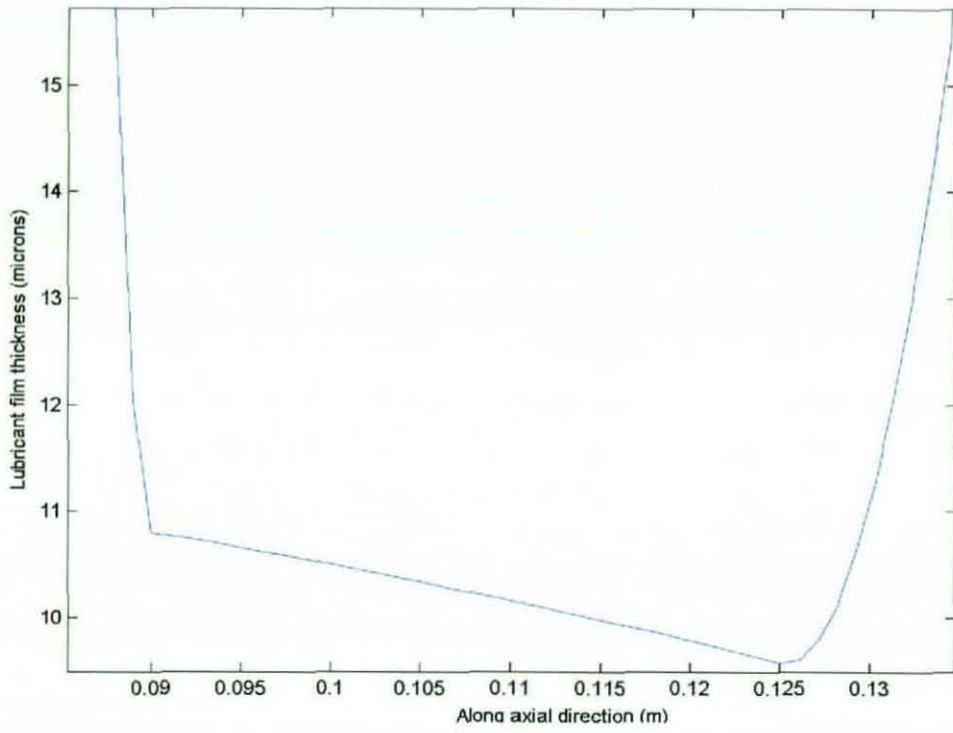
Figure 5.7(a): Minimum lubricant film along axial direction during reversal at TDC
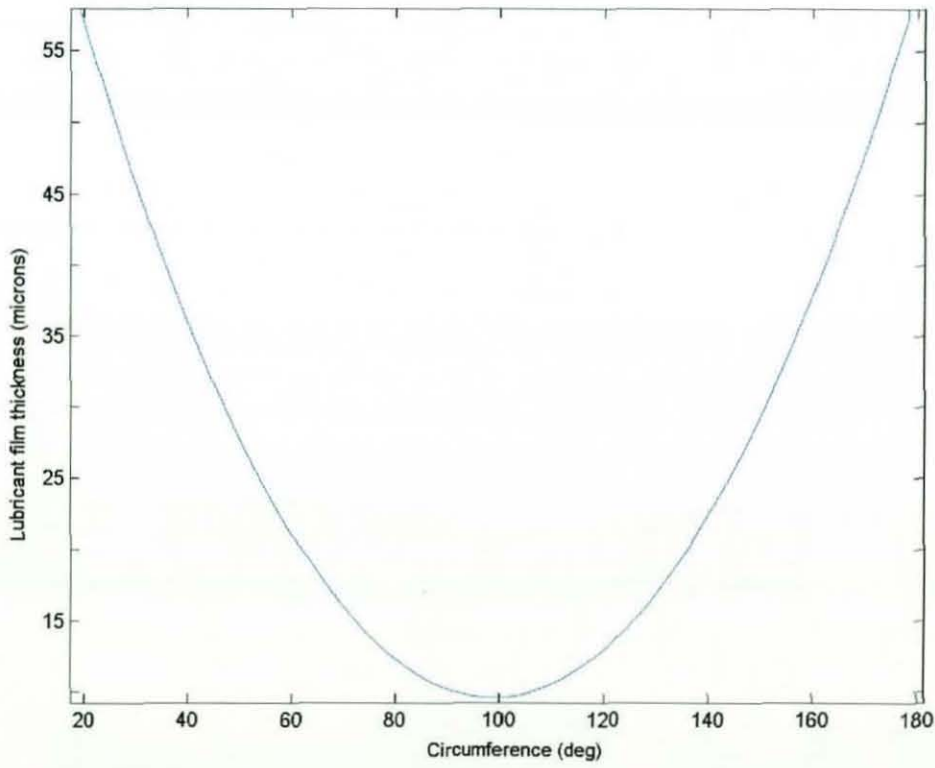
Figure 5.7(b): Minimum lubricant film along circumferential direction during reversal at TDC

The flow pattern can be superimposed upon the oil film contour to study the physics of motion of the lubricant in the contact domain. In figure 5.8, the flow pattern is indicated by black arrows (the arrow heads are not easily discernible, owing to the small magnitude of flow through the centre of the contact), whilst the oil film contour is the same plot as that in figure 5.5. The flow pattern in the inlet region shows the deviation of flow towards the shoulders of the contact to the sides of the higher contact pressure region. The flow through the contact is much smaller in magnitude than that to its sides, even though the pressures are not that high at all. This pattern is noted more poignantly in later examples, where higher pressures are generated. In general, lubricant takes the path of least resistance. This can be seen in figure 5.9, where the same flow pattern is superimposed on the isobaric pressure plot. The low magnitudes of lubricant flow are due to the Newtonian slow viscous action, which is the fundamental basis for the Reynolds' hydrodynamic equation. The interesting flow pattern around the axial position indicated by $x=0.08$ m in figure 5.8 is because the rising inlet slope commences in this region as can be seen in figure 5.9. In this figure, the flow is rather stagnant in the pressure generating region, with increased magnitude prior to the inlet and after the exit, a characteristic of hydrodynamic lubrication.
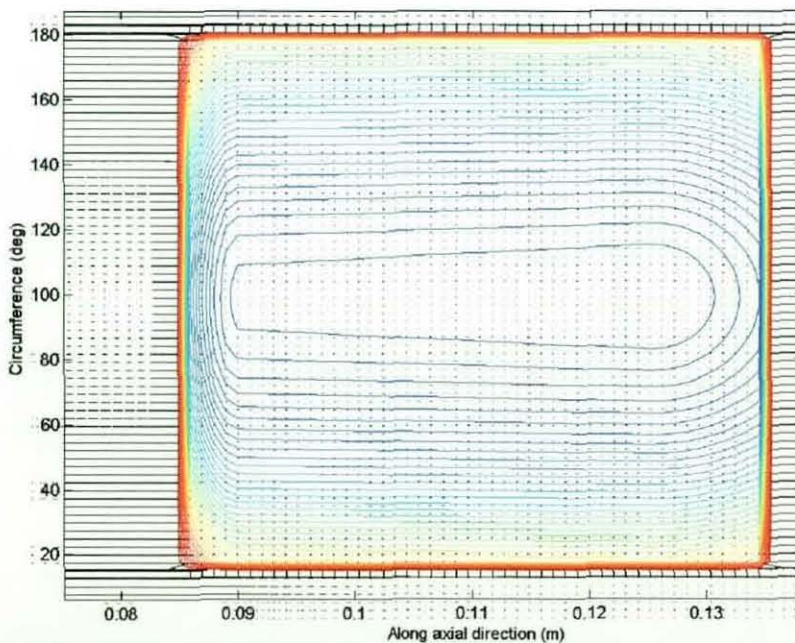

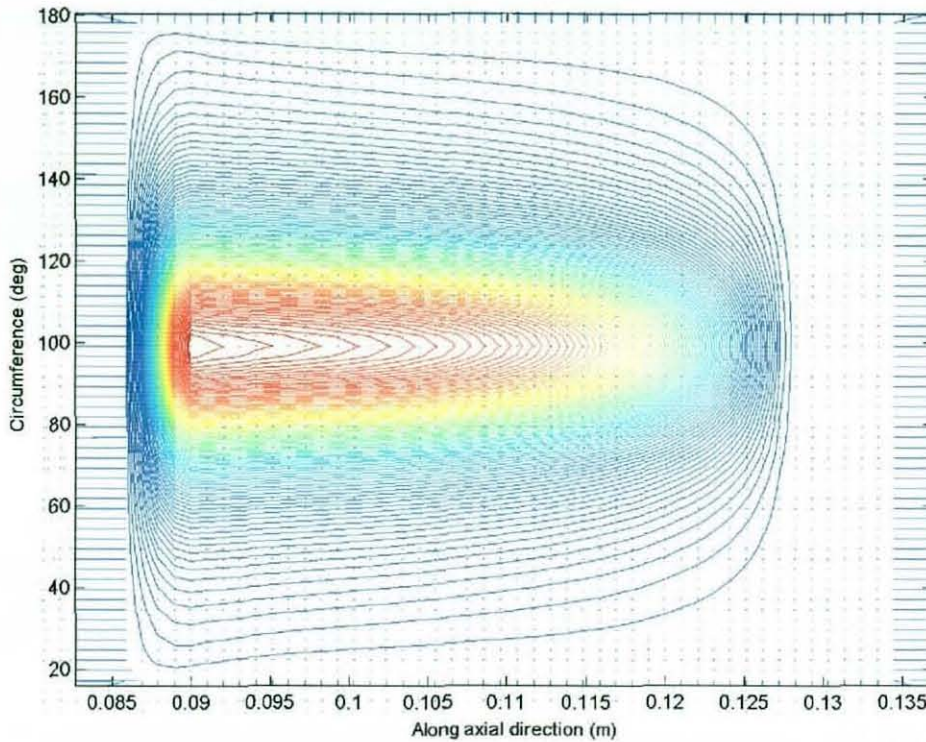Figure 5.8: Lubricant flow superimposed on lubricant film thickness during reversal at TDC

Figure 5.9: Lubricant flow superimposed on lubricant film thickness during reversal at TDC

5.3.2 Analysis Results for Combustion

At the combustion, the contact load is increased to a value of 1691 N, with the speed of entraining motion at 1.29 m/s, and with the piston misalignment being 0.1°. These conditions are much more severe than the previous case, leading to the three-dimensional pressure distribution shown in figure 5.10. The same pattern is observed as in the previous case, but with much increased pressures, in the order of 0.73 MPa, and with emerging pressure peaks both in the inlet and the outlet regions of the contact. There is contact deformation in this case, of the order of 4 μm, contributing to an elastic film shape with thickness in the region of 20-30 μm. The shape of the pressure distribution and the existence of contact deformation suggests prevailing elastohydrodynamic lubrication. However, the variation of lubricant viscosity in the region of pressure maxima indicates very small rise, which would be expected at such low pressures, using either of the viscosity-pressure dependence formulae of **Barus** (1895) or **Roelands** (1966). The high value of piezo-viscosity index at 10^{-9} Pa^{-1} may be in part responsible for
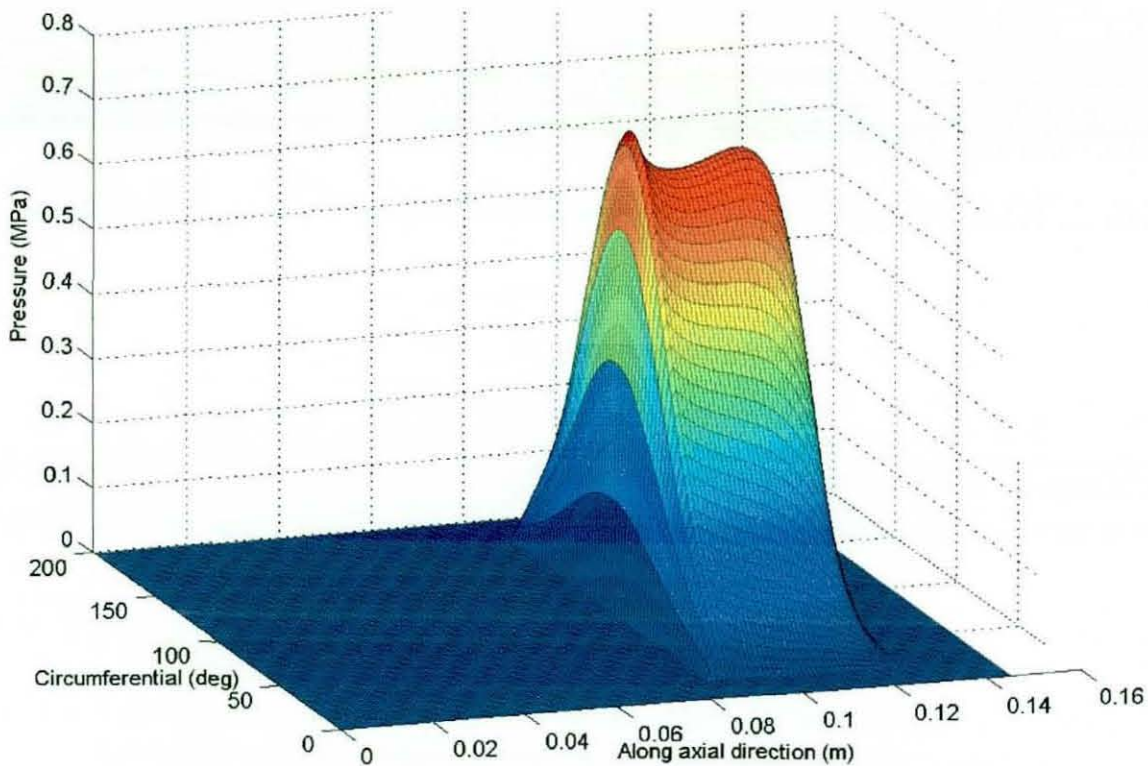
this outcome.

Figure 5.10: Three dimensional pressure distribution during combustion (entraining direction: from left to right along the axial direction)

To confirm this, figure 5.11 illustrates little rise in the dimensionless viscosity above its iso-viscous value of unity. The prevailing conditions are, therefore, iso-viscous elastic. The pressure isobar shows the regions of pressure maxima more clearly. The inlet region is on the left-hand side of the figure. It is interesting to note that unlike concentrated contacts, such as in ball or roller-to-races or cam-to-follower, here the maximum pressure spike occurs in the inlet domain.

Two dimensional pressure cuts in the circumferential and axial directions are shown in figures 5.13 and 5.14 respectively. The corresponding film shapes are shown in figures5.15 and 5.16 respectively. The minimum film thickness is in the exit side of the contact and after the pressure spike at the exit. This film thickness is 24 µm.
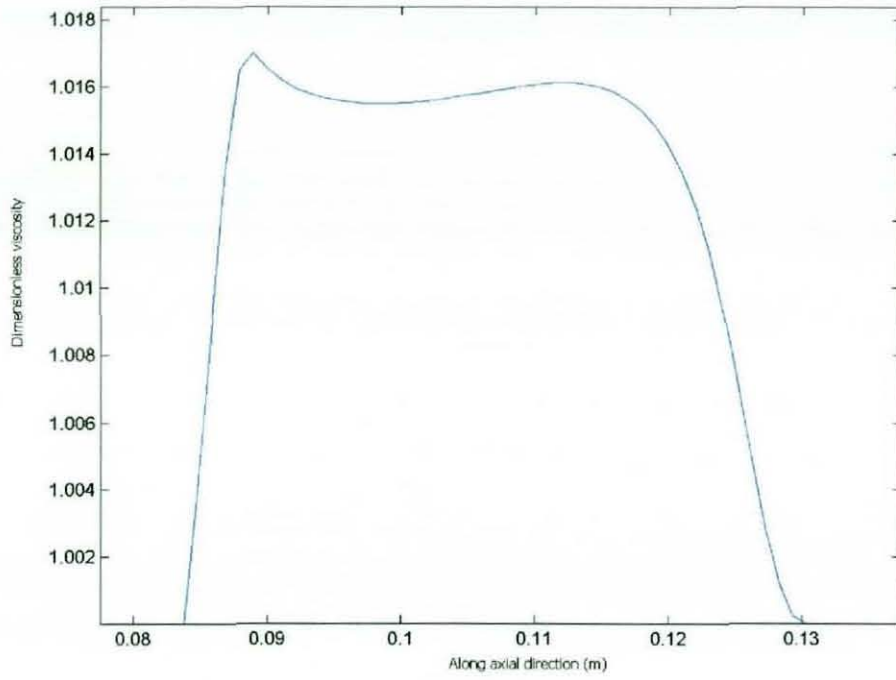
Figure 5.11: Dimensionless viscosity along the axial direction in the region of high pressure
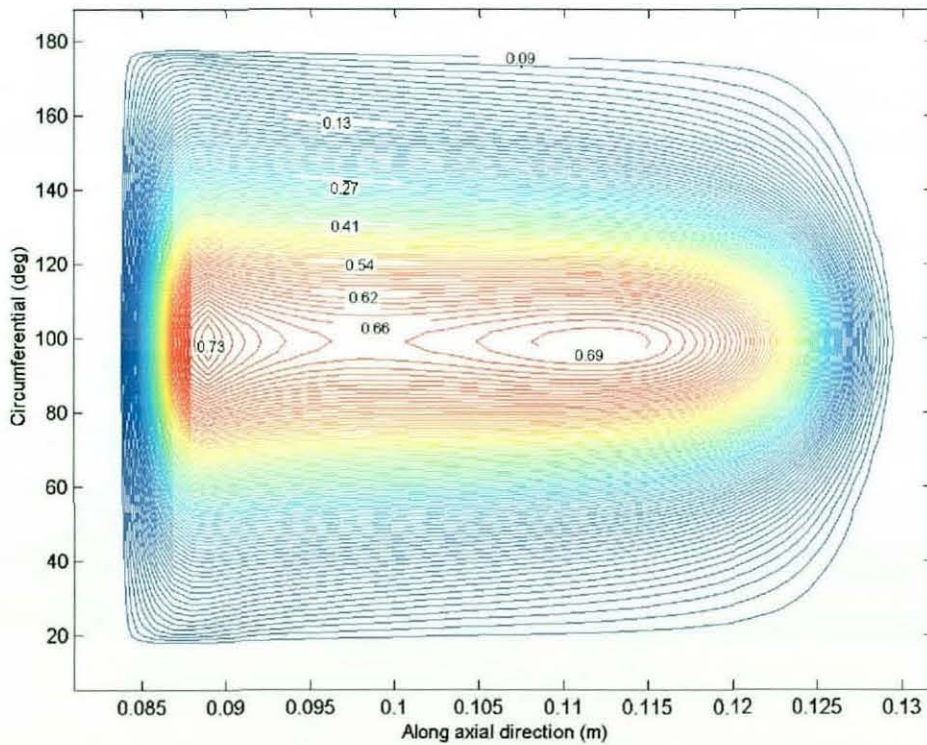

Figure 5.12: Pressure Isobar (in MPa) during combustion

The oil film contour in figure 5.17 shows the island of minimum film thickness. The next contour level extends to the inlet region, owing to the leading edge pressure pip due to the discontinuity in profile there, with a thickness of 24.6 μm. The lubricant film is formed in these regions due to retention by squeeze caving effect, because of deformation caused by high pressures. Low flow rate helps to promote this mechanism. This is illustrated in figure 5.18, where the volumetric flow is superimposed upon the isobaric pressure plot. The high flow rate on the shoulders of the contact can be clearly observed. The outward dispersion of the lubricant by the generated high pressures is visible. In contrast, the low and almost stagnant flow through the contact is also evident.
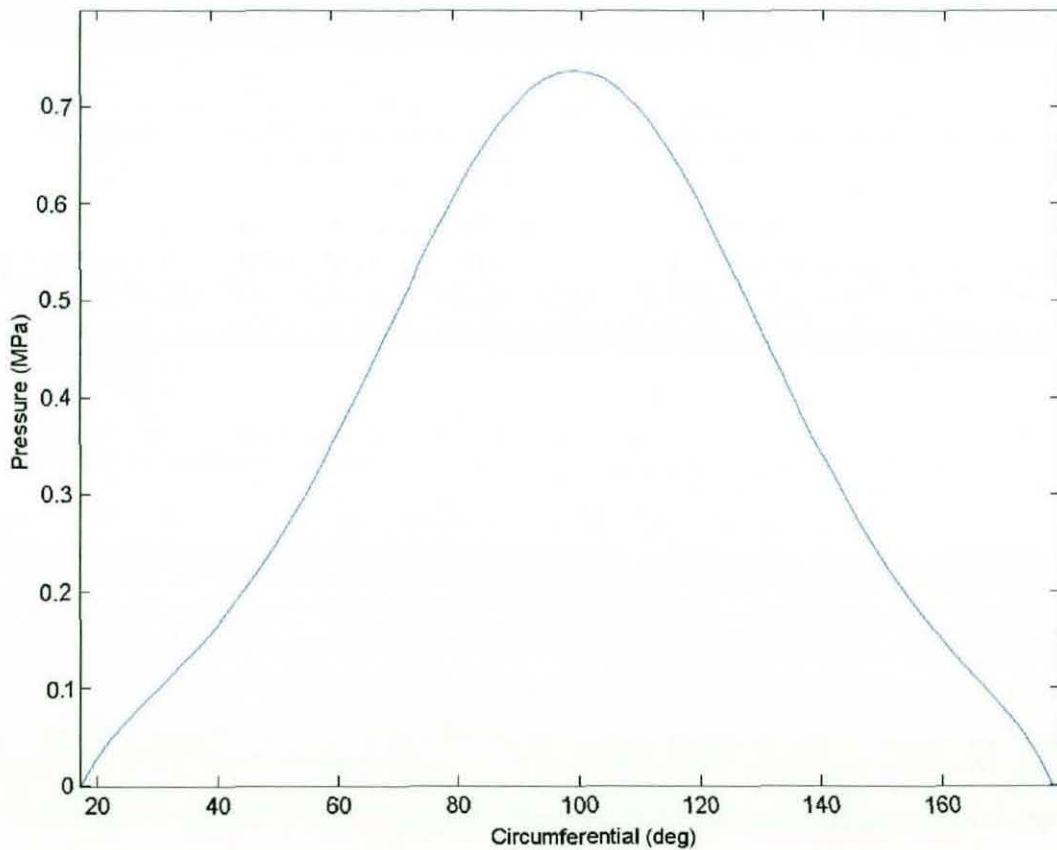
Figure 5.13: Maximum pressure along circumferential direction during combustion
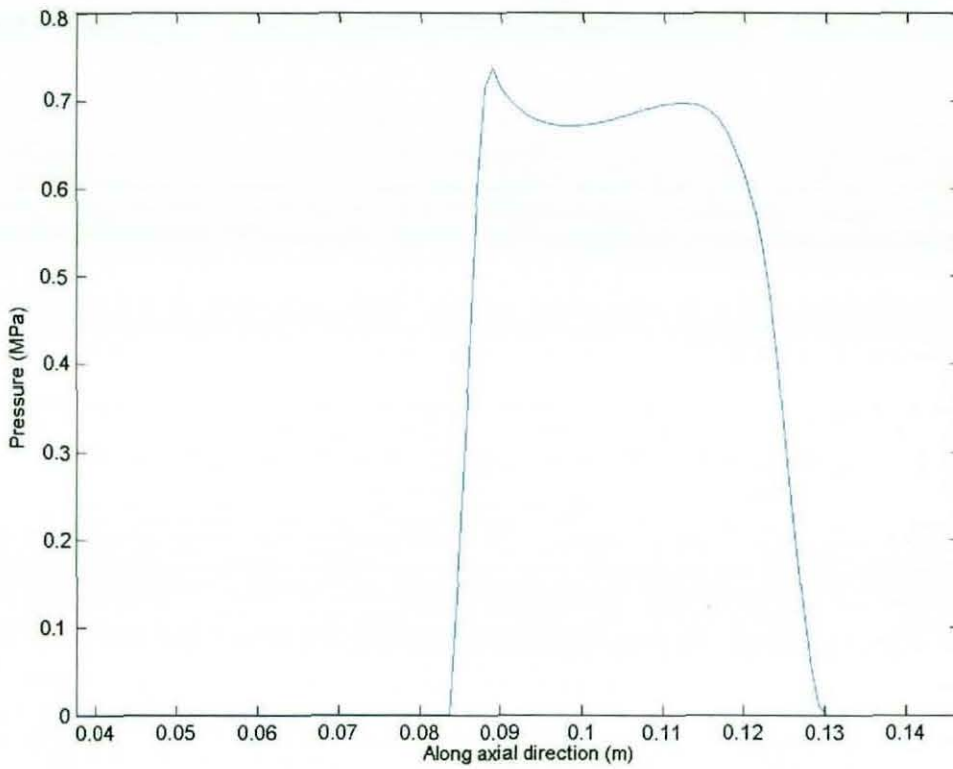
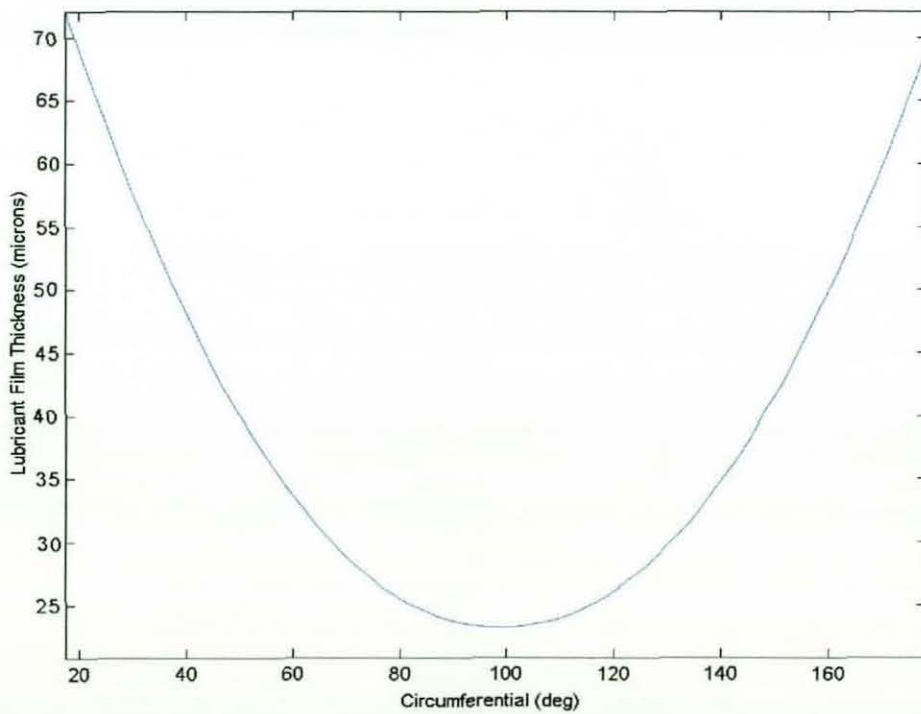Figure 5.14: Maximum pressure along axial direction during combustion

Figure 5.15: Minimum circumferential lubricant film thickness during combustion
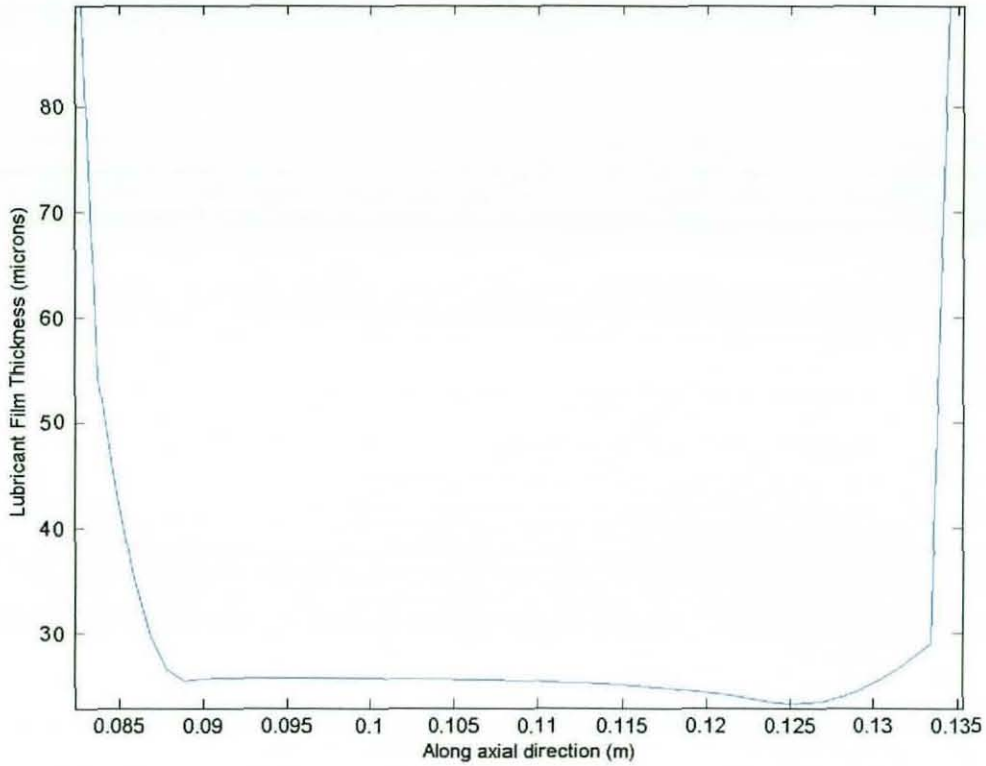
132

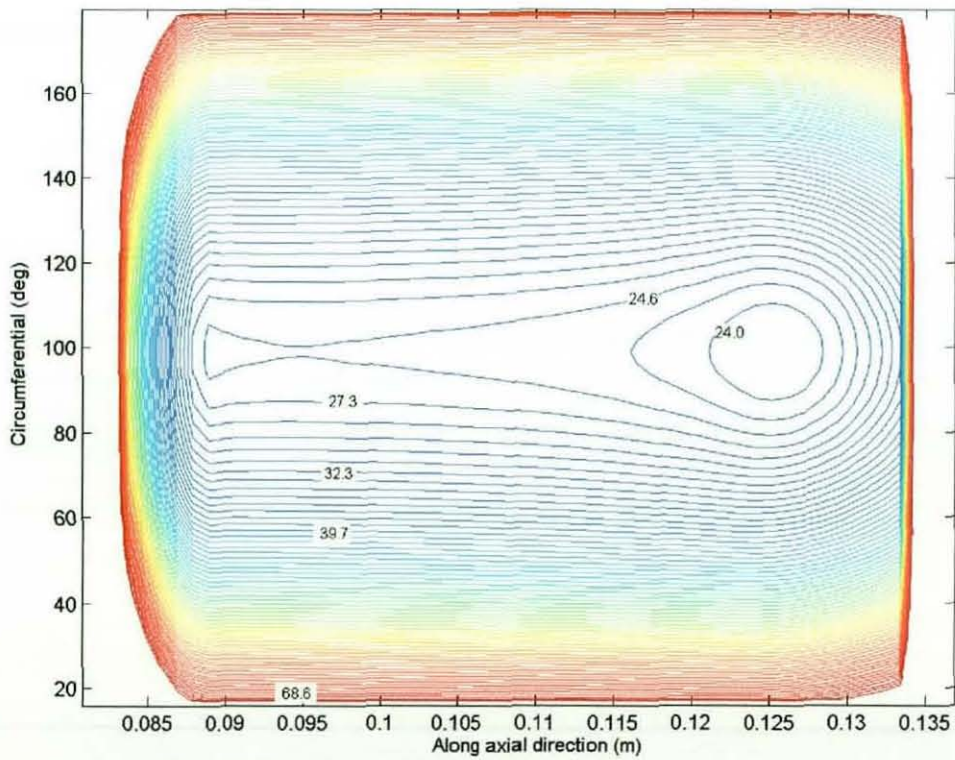Figure 5.16: Minimum circumferential lubricant film thickness along axial direction during combustion

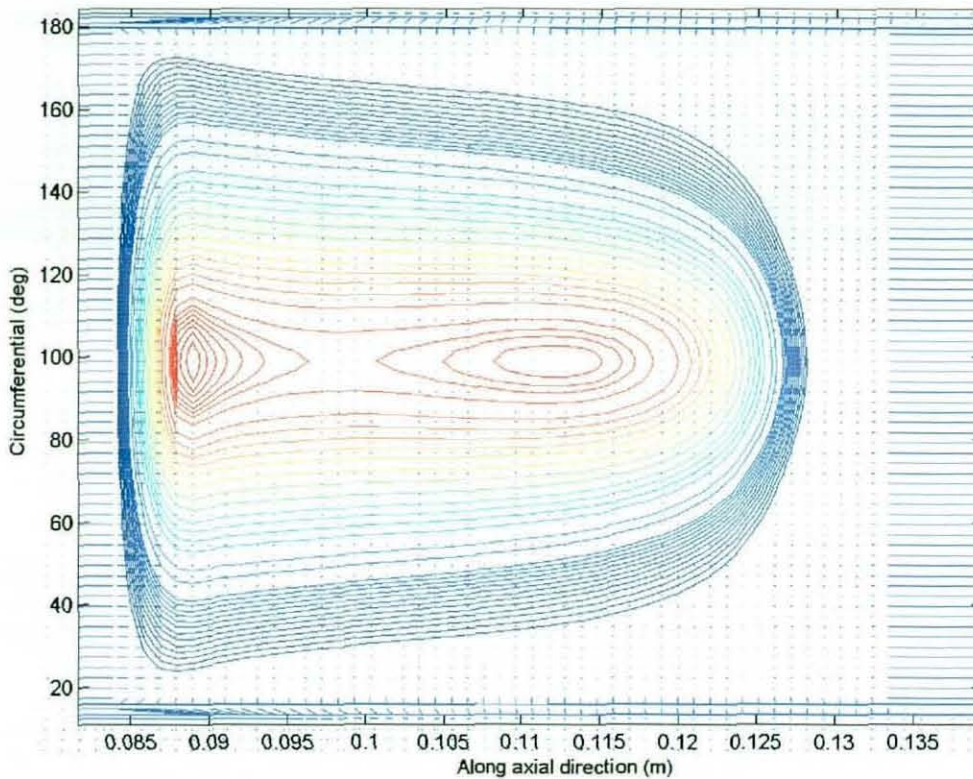Figure 5.17: Lubricant film contour (µm) during combustion

Figure 5.18: Lubricant flow superimposed on pressure isobar during combustion

5.3.3 Analysis Results for Piston Mid-cycle

When the piston is at mid-cycle (where the speed of entraining motion reaches its maximum value of 12.17 m/s), the lubricant film reaches its maximum thickness. The piston misalignment reduces to a value of 0.0024°, therefore, the chance of occurrence of pressure pip is also reduced, as the edge stress discontinuity effect is diminished. Due to the reduction in applied combustion pressure, the contact load has decreased to a value of 531.65 N. The mechanism of fluid film formation is dominated by iso-viscous rigid regime of lubrication, as the contribution of local deformation in the minimum film thickness of 63.1 µm is merely 1 µm. The same trend in fluid flow pattern is seen as in the previous case (see figure 5.19). In this figure the flow pattern is indicated by arrows, which are more clear than in the previous cases, showing outward flow to the sides of the contact and to the rear exit at the right-hand side of the figure. An interesting feature of flow pattern occurs in the inlet region. The flow appears to be mostly pushed away in the direction of the piston travel, rather than entrained into the contact.
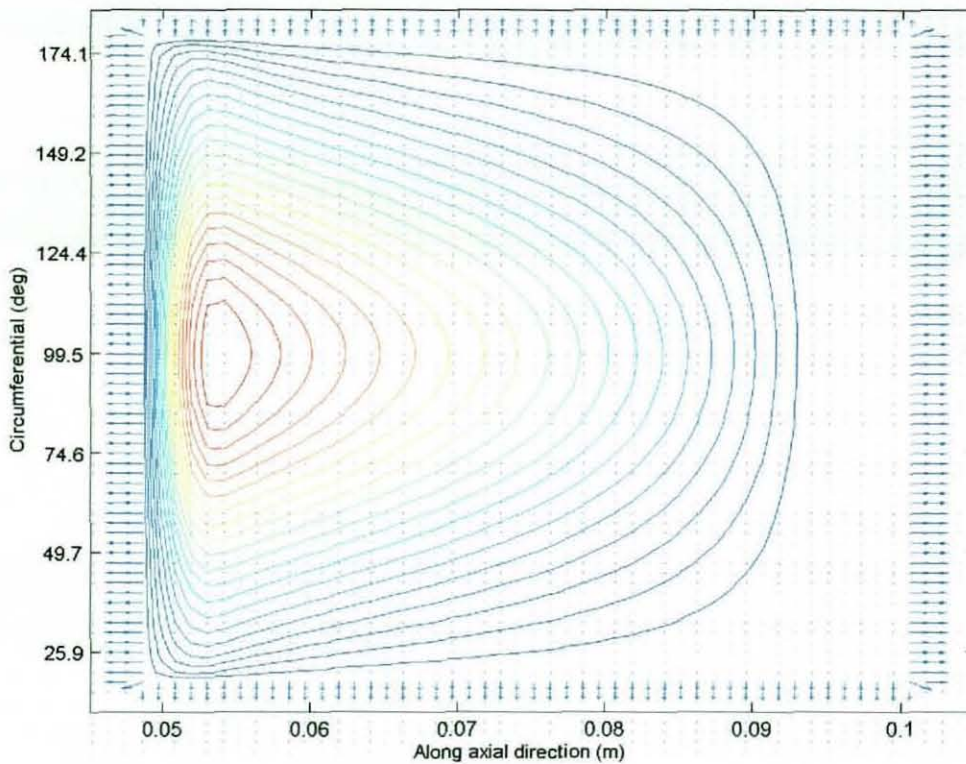
Figure 5.19: Lubricant pressure generated in the contact superimposed on lubricant film flow at mid-stroke

This is due to the presence of the maximum pressure at the leading edge of the contact, caused by the sharp profile change, which should ideally promote a wedge effect. The wedge effect, of course, is less effective in sliding motion than the usual rolling action in most load bearing lubricated contacts. The pressure isobars are also shown in the same figure, with the island of maximum pressure. The pressure isobar with various pressure levels and the corresponding 3D plot are shown in figures 5.20 and 5.21 respectively. The 2D pressure profiles in the axial and circumferential directions are also shown in figures 5.22 and 5.23 respectively, the former indicating a leading high pressure acting as a barrier to lubricant entry into the contact. This seems to cause a backflow of the lubricant in the inlet region. Due to reduced pressures, an insufficient squeeze caving effect emerges in order to entrap the lubricant, but because of high entraining velocity, compared with the previous case the film thickness has increased. This trend is also reported by all previous analysis work (see: **Knoll** and **Peeken** (1982), and **Xie** et al (1998)). The oil film contour and the corresponding cuts in the axial and circumferential directions are shown in figures 5.24, 5.25 and 5.26 respectively.
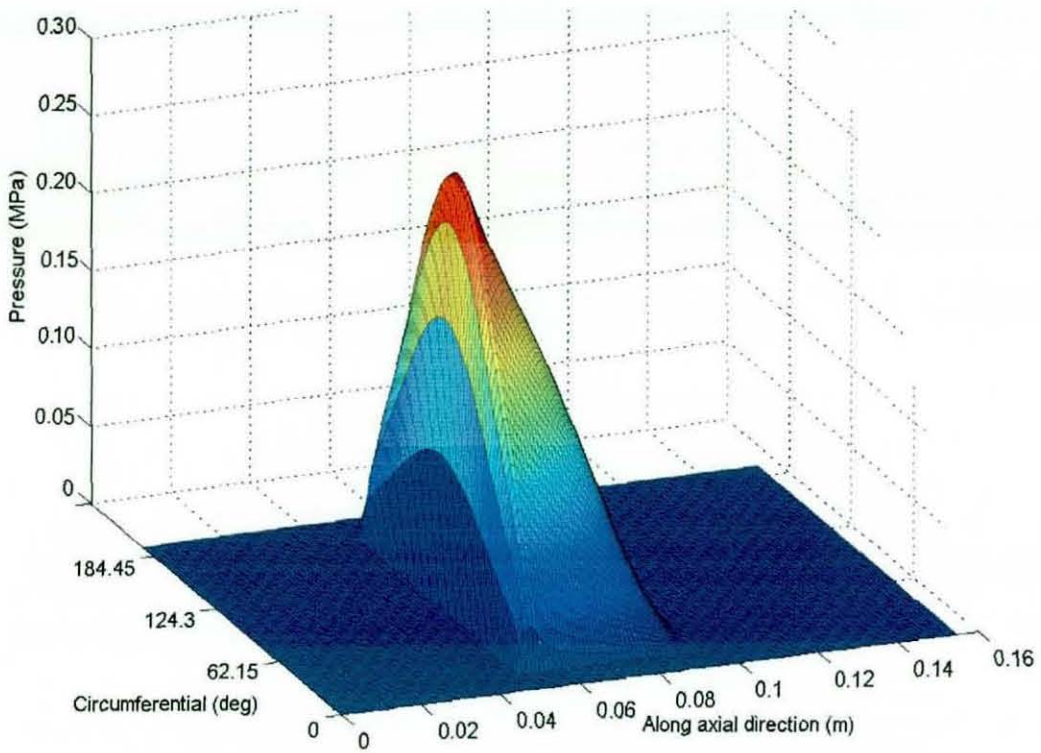
Figure 5.20: Three dimensional pressure distribution at mid-stroke (entraining direction: from left to right along the axial direction)
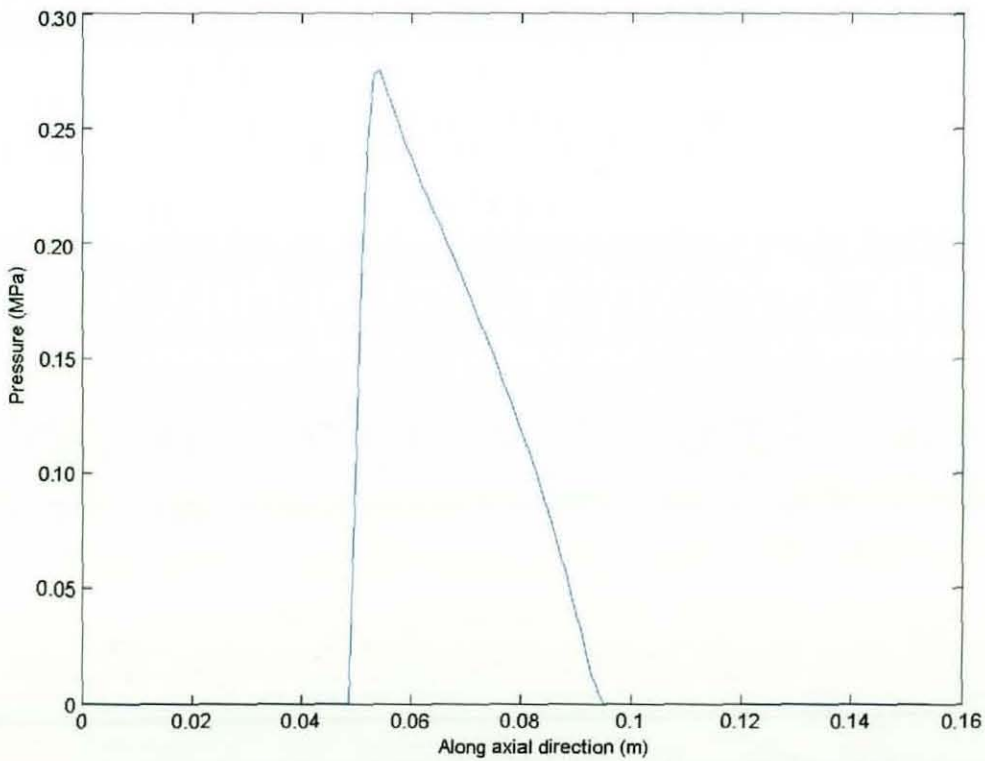

Figure 5.21: Pressure profile along axial direction at mid-stroke
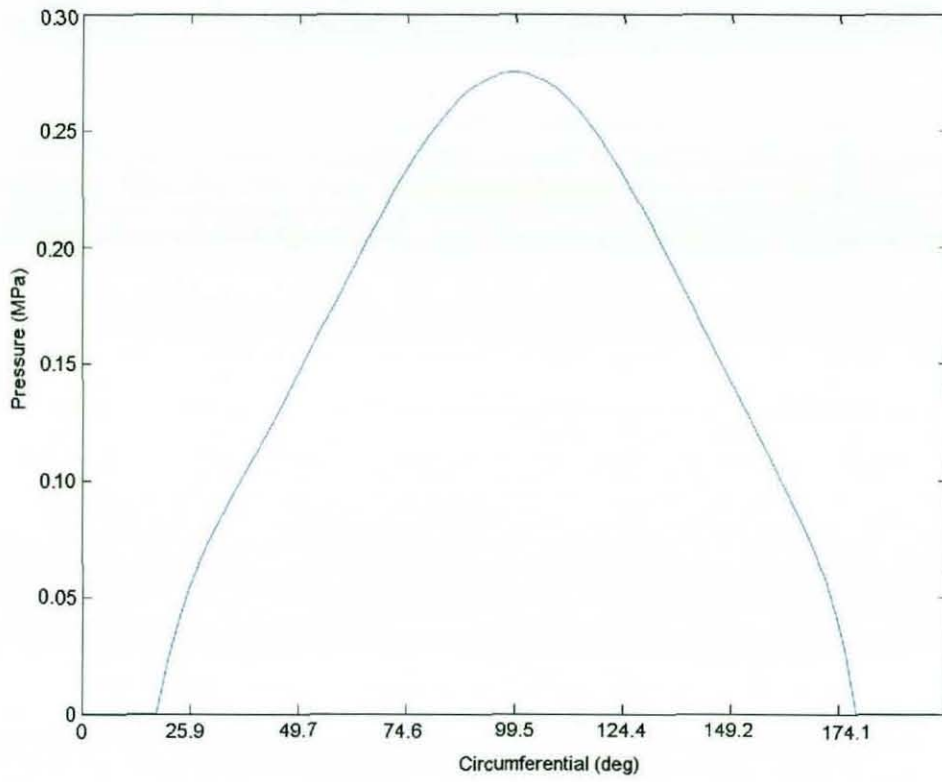
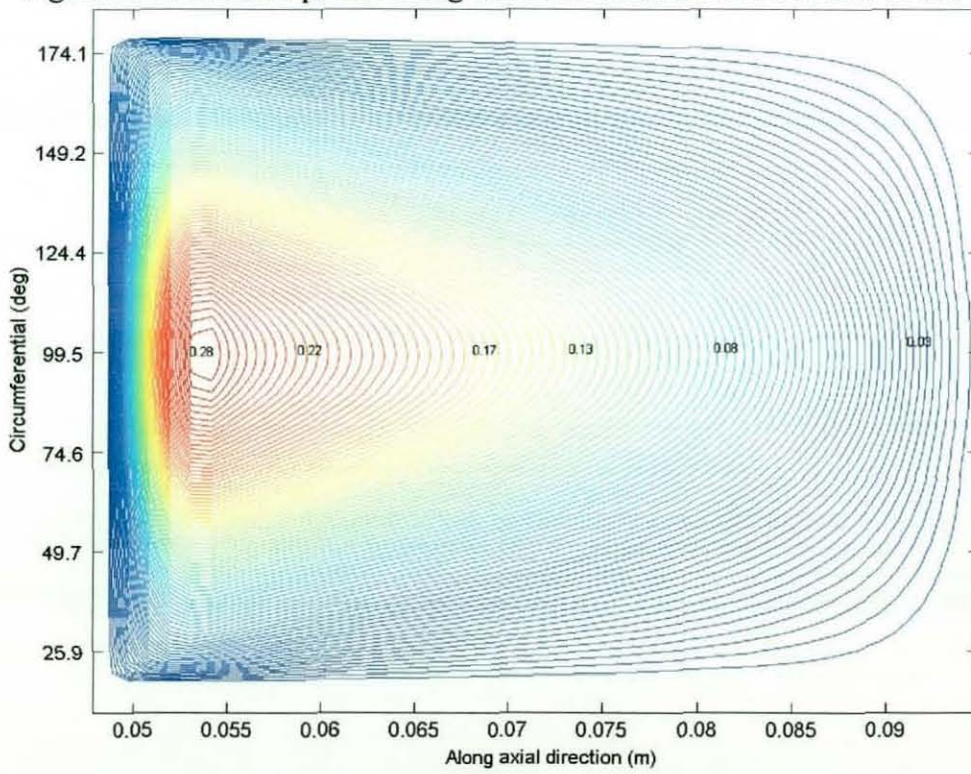Figure 5.22: Pressure profile along circumferential direction at mid-stroke

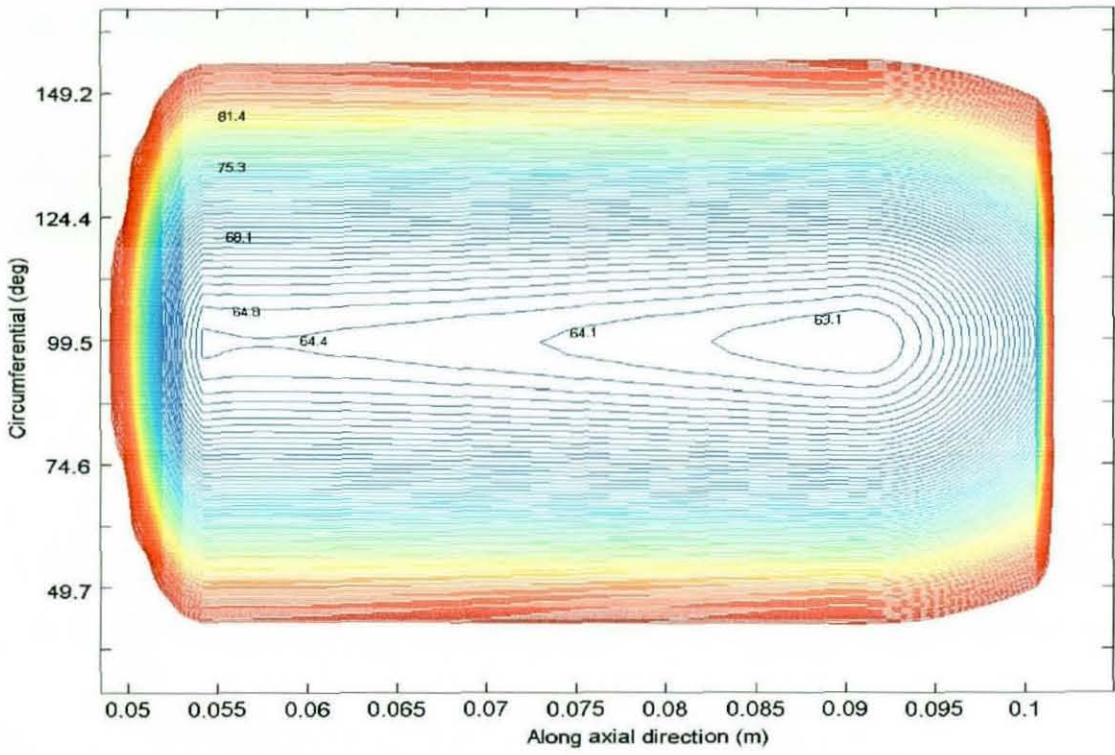Figure 5.23: Pressure isobar (MPa) at mid-stroke

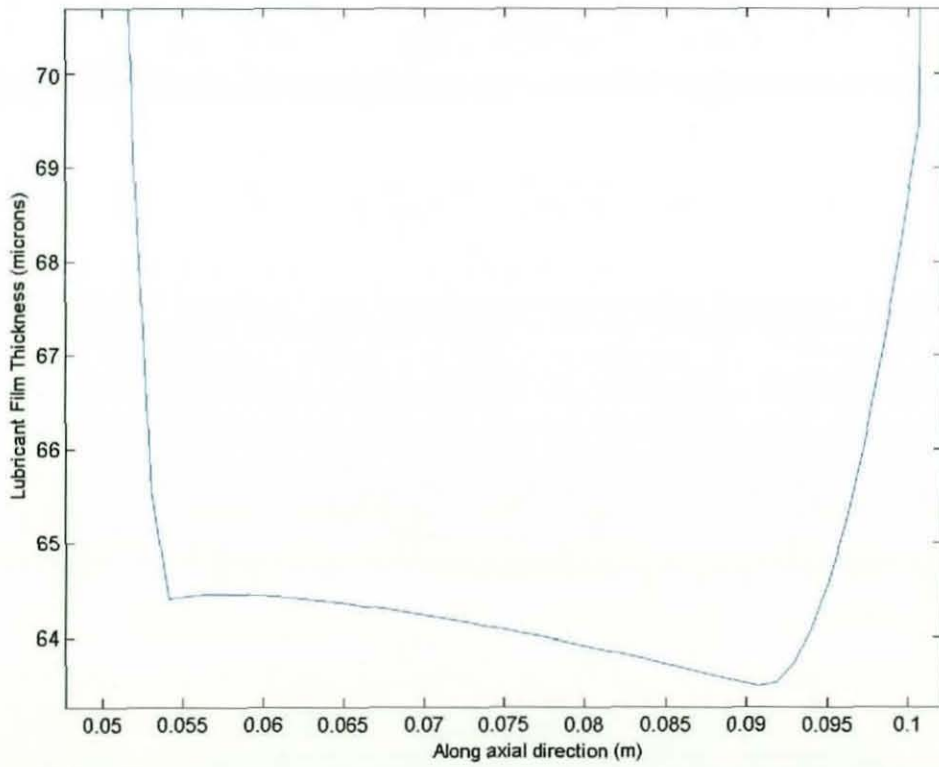Figure 5.24: Lubricant film contour (μm) at mid-stroke

Figure 5.25: Lubricant film thickness along axial direction at mid-stroke
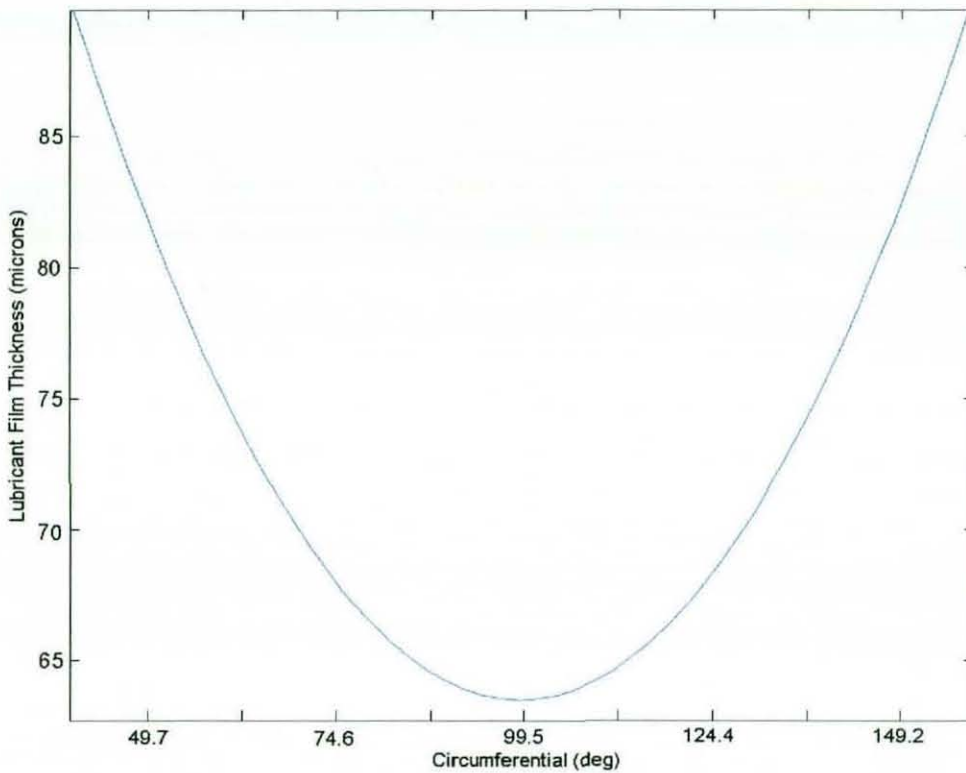
138

Figure 5.26: Lubricant film thickness along circumferential direction at mid-stroke

5.3.4- Analysis Results for BDC

The conformal contact of the piston with cylinder liner is investigated at the BDC with the major thrust side. At this location the entraining motion reverses. The speed of entraining motion ceases momentarily and the lubricant film is maintained by pure squeeze film action, similar to that reported above for the TDC position, but at considerably reduced load. An appropriate study of this position (as well as at TDC) is through transient analysis, which would provide a proper value for elastic squeeze film

velocity, $\dfrac{\partial h}{\partial t}$ at all locations in the contact. Note that a first order approximation of

squeeze velocity at each location, in a transient analysis is obtained as: $\dfrac{\partial h}{\partial t} = \dfrac{h_{n+1} - h_n}{\Delta t}$,

where n is any time step, and h varies throughout the contact. In a quasi-static analysis, a value must be assumed, as no film history from a previous calculation time is available. Arbitrary imposition of squeeze film velocity, which is common in quasi-static analyses

is likely to lead to misleading conclusions. A transient analysis, such as that reported in chapter 6 overcomes this shortcoming. A detailed analysis, more manageable under quasi-static conditions (as described in section 5.2) can be carried out with a very low speed of entraining motion, and with no assumed value for squeeze film velocity. The results will be quite representative of prevailing conditions, as the fast speed of reversal means that lubricant film is replenished rapidly. Furthermore, even under transient conditions to capturing the exact point of reversal with no entraining motion is very difficult. Thus, a very slow speed of entraining motion analysis would be acceptable, so long as this value is representative of the piston velocity relative to the cylinder bore. Therefore, the speed of entraining motion for this analysis, very close to the BDC in the downward motion of the piston is 0.045 m/s, where the piston is tilted at its bottom extremity with an angle of $0.085°$ towards the major thrust side. The resulting contact load is 21 N.

Figure 5.27 shows the three dimensional pressure distribution. Due to the tilt of the piston and low cylinder pressure at BDC (i.e. low contact force), the load bearing contact area has diminished considerably. The diminished contacting region is often as the result of starved rather than fully flooded conditions, as described by **Hamrock** (1994). The degree of starvation depends upon the inlet distance and the thickness of the lubricant film at the meniscus, ahead of the contact. Determination of the boundary at which onset of starvation occurs requires rigorous simulation and experimental studies. Such work has been reported by **Wedeven** (1968), **Wolveridge** *et al* (1971), **Hamrock** and **Dowson** (1976) and **Brewe** and **Hamrock** (1982), all for counterformal circular and elliptical point contact configurations. For a conformal contact as studied here, it is important to note that the inlet boundary is governed by the geometrical realities of the system. In other words, the inlet meniscus for the piston skirt to cylinder liner contact, advancing towards BDC, cannot be practically extended beyond the bottom of the cylinder bore. Therefore, given that a sufficient supply of lubricant exists, the inlet meniscus can be assumed at such a position, which is the assumption made in this analysis. As the piston advances toward BDC, the inlet distance is progressively reduced and the speed of entraining action also diminishes. It is, therefore, axiomatic that at reversal the contact

would be necessarily starved of a sufficient supply of lubricant. The pressure generating region should therefore become narrow, which is the case here.

Figure 5.28 shows the tilted undeformed piston profile. It is clear that the region of high pressures is confined to a small portion of the piston skirt length. The contact pressures are indeed quite low, with the maximum value being around 22 KPa.

A clearer representation of the pressure distribution is made by an isobar plot. This is shown in figure 5.29. Note that significant pressures occur over merely 7 mm of the 52 mm skirt length. It is interesting to note that the area of contact is much smaller than the principal radii of contact of the conforming bodies in contact. Thus, Hertzian approximation can be employed for such a contact, but this is not true of all the instances and localities during the piston cycle, and thus the need for the solution of the problem, using generalised solution for the contact mechanics of the problem, as highlighted in chapter 4. Figures 5.30 and 5.31 illustrate two dimensional cuts through the maximum contact pressure region in circumferential and axial contact directions respectively.
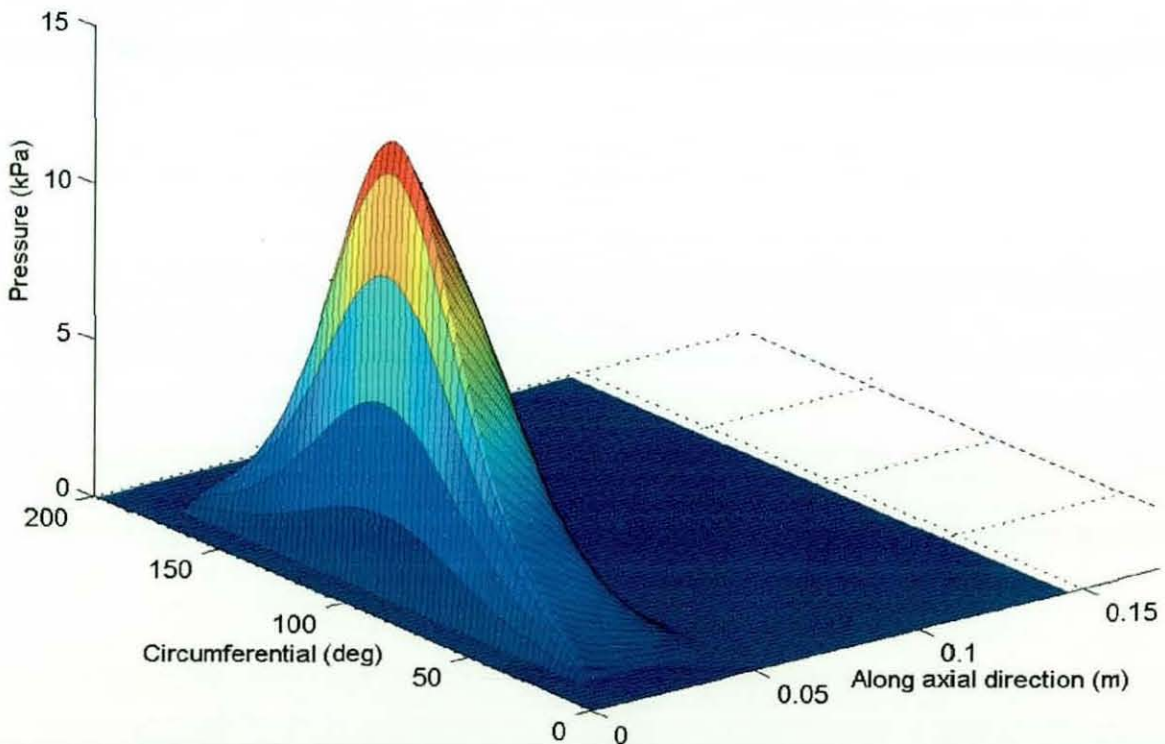

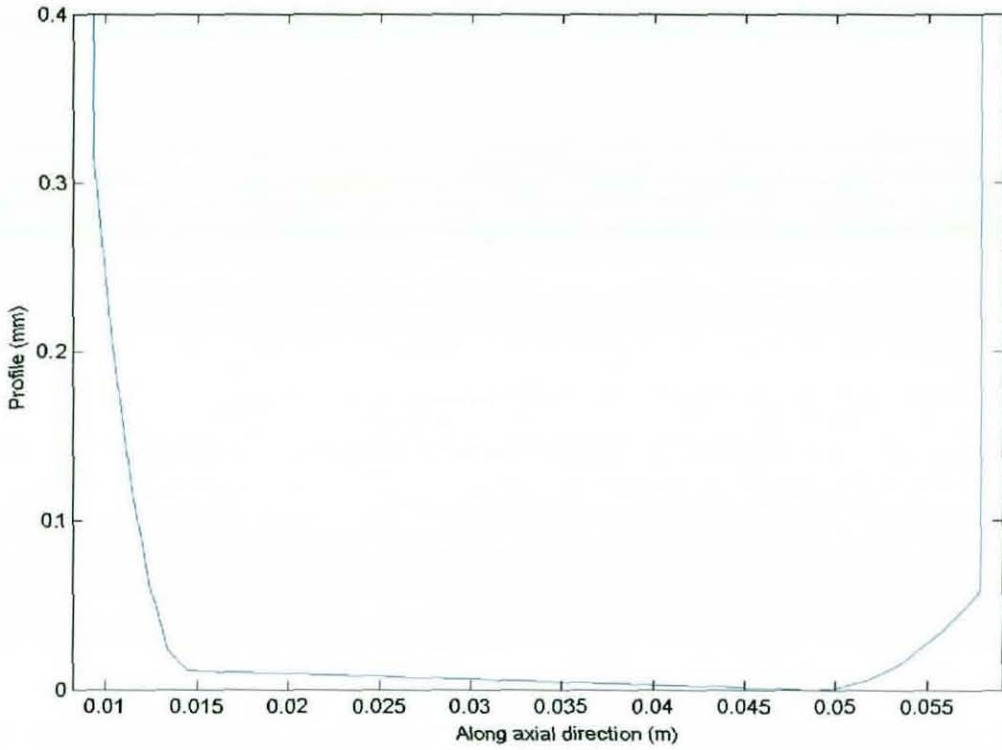Figure 5.27: The 3D pressure distribution at BDC (reversal position)

Figure 5.28: Undeformed tilted piston axial profile at BDC, as seen from major thrust side
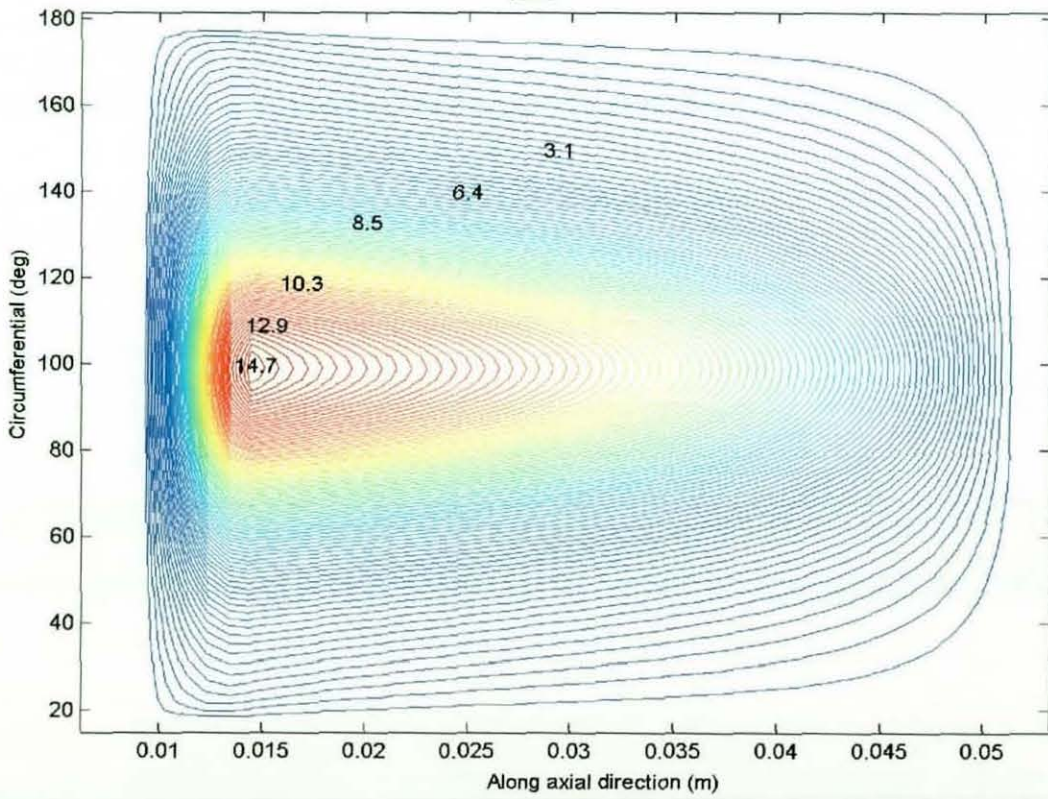

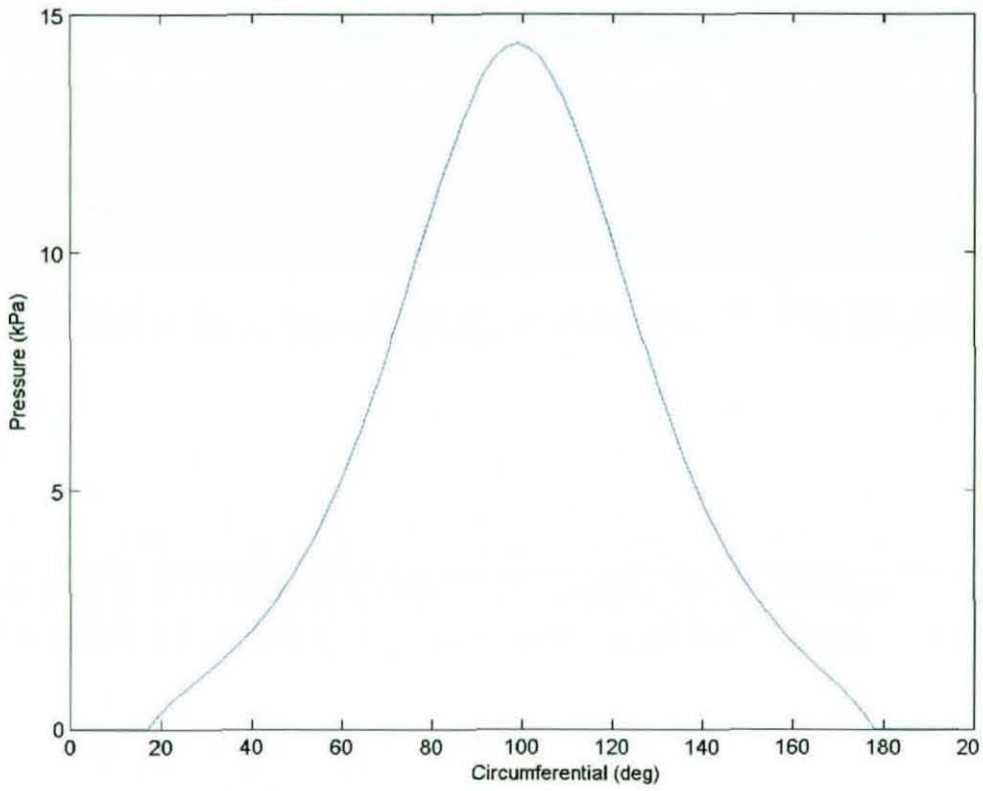Figure 5.29: Isobar plot of generated pressures (KPa) at BDC

Figure 5.30: Circumferential pressure distribution at BDC
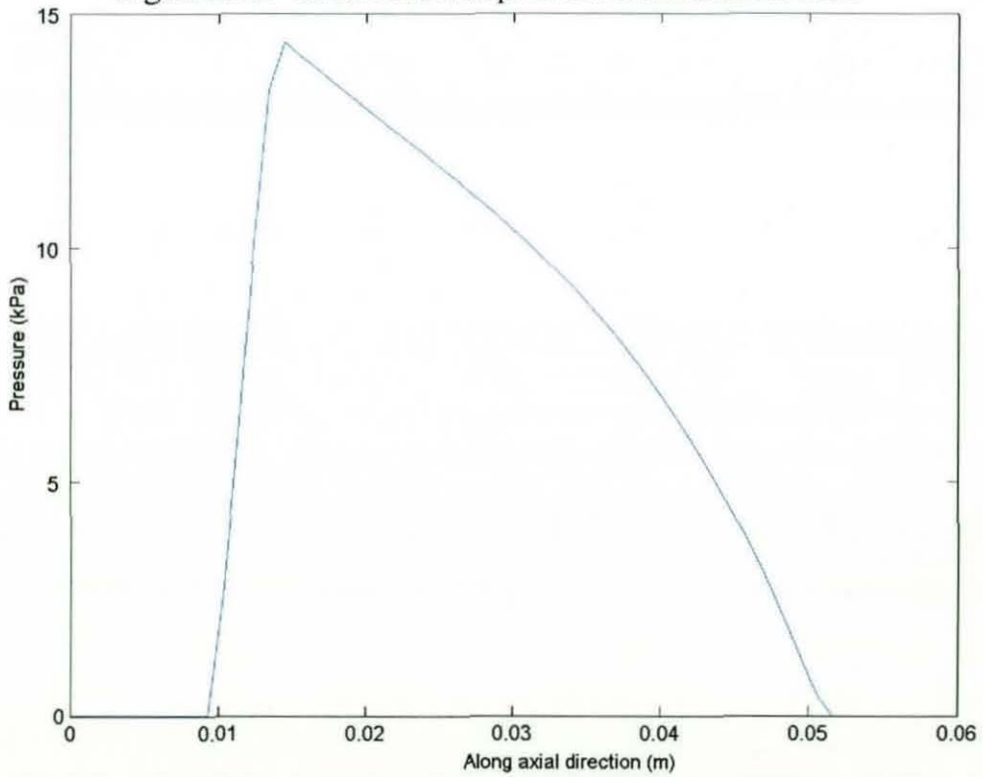
Figure 5.31: Axial pressure distribution at BDC

143
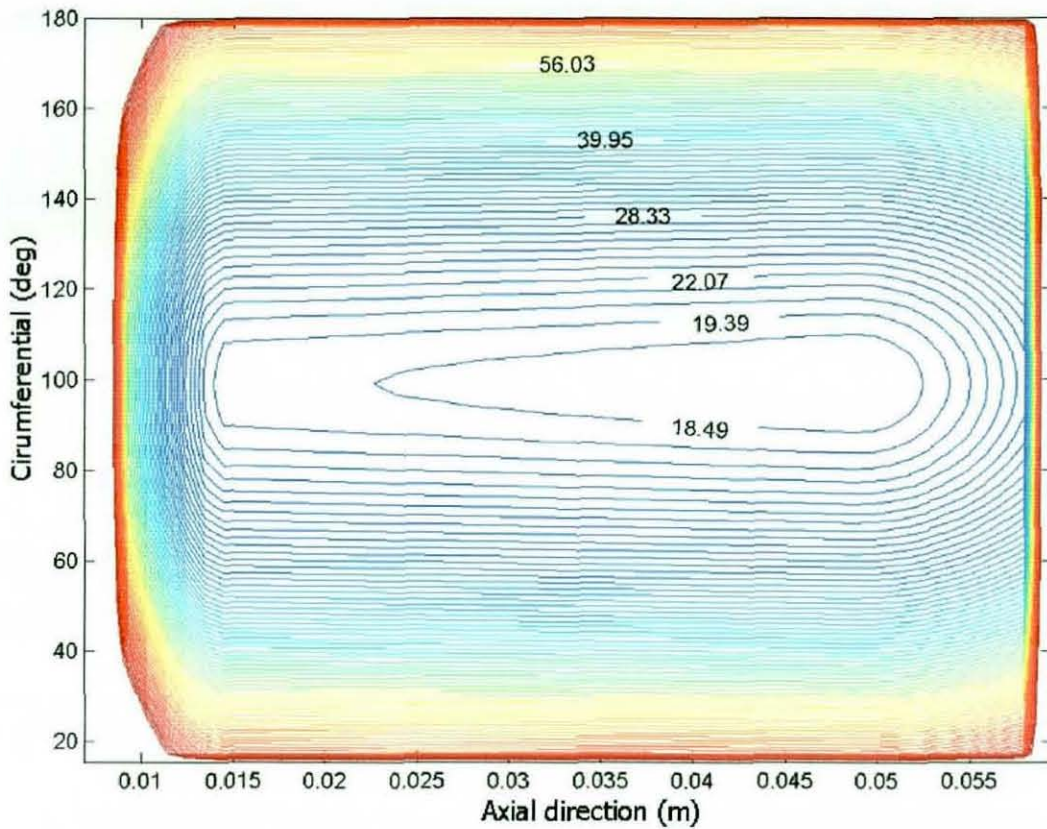
Figure 5.32: Zoomed (central region) lubricant film contour (μm) for piston at BDC position

The extent of pressure generated region is much broader in the circumferential direction, as it occurs over nearly 160°, although the significant pressures are confined to the

region 80°-120 °. The lubricant film contour is shown in figure 5.32. The minimum film thickness is approximately 45.3 μm and occurs in the immediate vicinity and after (i.e. on the exit side) of the maximum pressure region. The maximum pressure region is around 0.0495 m from the bottom of the bore (see figure 5.31). The minimum film is at the position 0.0525 m from the bottom of the bore.

Figures 5.33 and 5.34 show the film shape profiles through the minimum film thickness in the circumferential and axial directions respectively. Both pressure profiles are of a hydrodynamic shape. In fact low pressures result in no elastic deformation of contiguous

bodies. No variation in lubricant viscosity is also noted. Therefore, the prevailing regime of lubrication at the BDC is iso-viscous rigid.

Figure 5.33: Lubricant film thickness along the circumferential direction

Figure 5.34: Lubricant film thickness along the axial direction

145

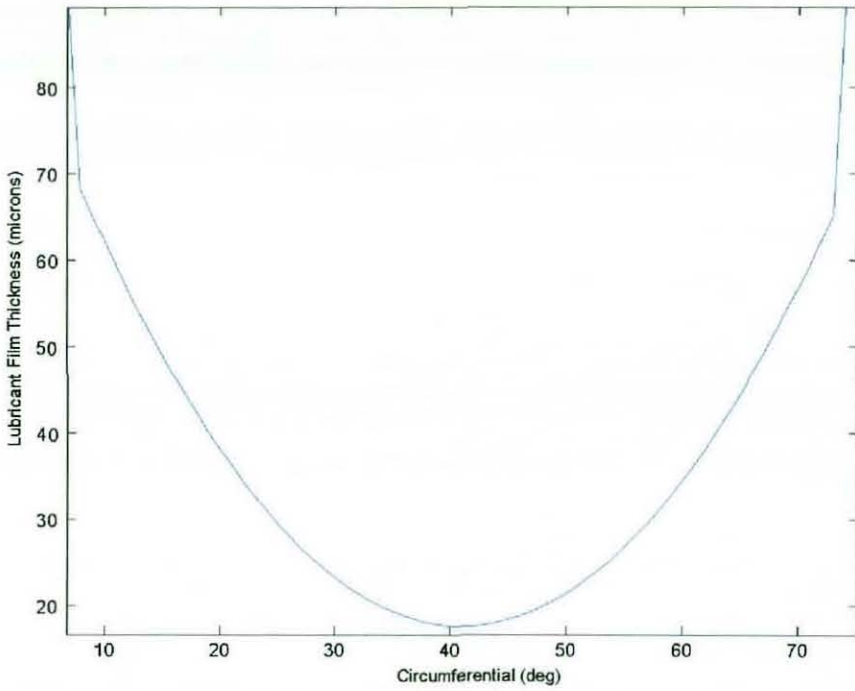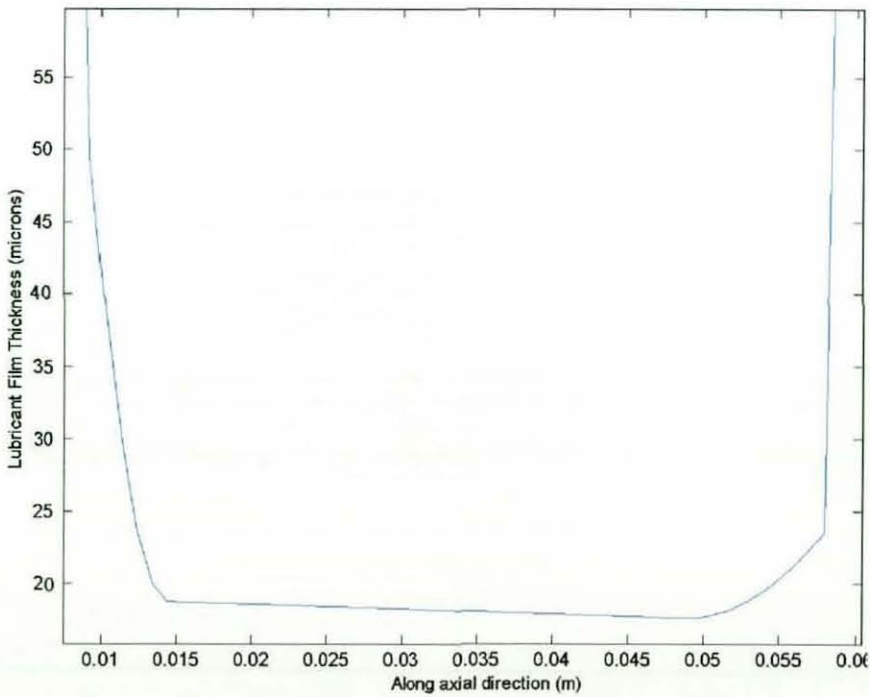Returning to the theme of starvation in such reversal positions as BDC, it is clear that in practice the cessation of entraining motion would result in starvation of contact, where a lubricant film can only be retained through squeeze film action. Theoretically, with no entraining motion and without significant squeeze film effect, a dry contact condition would result, which is the ultimate case of starvation. The most general theoretical corroboration of this is to determine the film thickness ratio between that at the inlet meniscus, ahead of the minimum (or central) film thickness and itself, or: $\dfrac{h_{c\infty}}{h_c}$. **Birkhoff**

and **Hayes** (1992) have indicated that a minimum ratio of approximately 11.3 is required for a fully flooded contact. One can see from figure 5.34 that the film thickness just before the closure film at the relief radii of the piston axial profile is around 76 μm (also see on the oil film contour of figure 5.32), whereas the minimum film in the contact region is about 45 μm, indicating a much lower ratio than that suggested for fully flooded contacts. In fact in the circumferential direction, a much higher ratio, with the lubricant film thickness at the sides of the contact reaching a value of approximately 225 μm (not shown in this figure, but obtained numerically), but the ratio is still far below the limit stated by **Birkhoff** and **Hayes** (1992).

5.4 Results for a high performance engine

The above mentioned analysis is extended to a high performance engine. Tribodynamic analysis of piston-connecting rod-crank sub-system of a 10-cylinder, 4-stroke, 2.98 Litre engine is considered in this section. This 824 bhp engine is used in formula one motorsport. The combustion pressure, unlike the conventional spark ignition engine, is 50 MPa, occurring during the piston cycle, 13° past the TDC, as measured in terms of crank-angle rotation. The combustion pressure curve is shown in figure 3.4 (see Chapter 3). The pressure curve was measured by a pressure sensor fitted into the combustion chamber at the Perfect Bore Ltd., Andover, UK.

Both the cylinder and the piston are made of high grade aluminium alloy, with Young's modulus elasticity of 78 GPa, and Poisson's ratio of 0.33. The cylinder bore has a circular profile with a radius of 89.13 mm. The piston skirt has a nominal radius of 89.073 mm, providing a nominal clearance of 57.5 μm. The large clearance is compensated by the relatively large thermal expansion of the Aluminium alloy than that of Steel used in conventional engines, such as that reported in the previous simulation study. The length of piston skirt is 52 mm. The piston gudgeon pin is offset by 10 μm. The piston profile in the circumferential direction is, in fact, oval, owing to deviations from this nominal radius. The longitudinal profile of the piston skirt incorporates relief radii at its axial extremities.
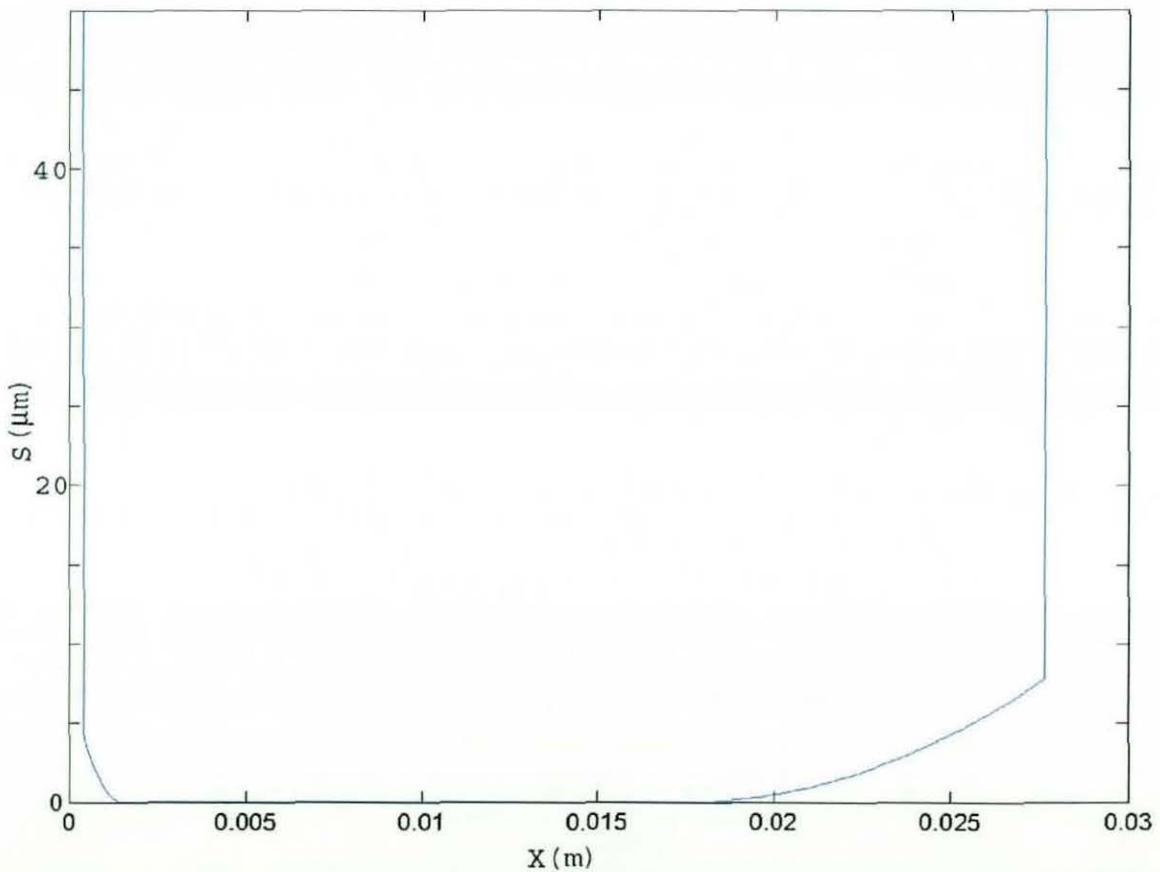
Figure 5.35: Undeformed profile of piston

The piston skirt axial profile is asymmetrical (see figure 5.35), with the top and bottom end sections having radii that deviate from the principal nominal radius by 80 μm on the top and 46 μm at the bottom. The bottom section is merely a chamfer. This chamfer creates the wedge effect for lubricant entrainment as the piston traverses toward the BDC.

The actual profile is shown in figure 4.5(a) and (b). This represents an aligned conforming profile of the skirt against the cylinder bore. The contact domain is quite large in many instances and in order to obtain convergence and realistic pressure distributions, it is necessary to use as refined a computational mesh as possible. Therefore, the selected mesh density accommodated 8 nodes in this region of lower skirt end relief and 77 nodes at the upper tapered end of the skirt.

The mesh density of the profiled sections, lower skirt relief profile and tapering at the top, are shown in figures 5.36 and 5.37.

Figure 5.36: Number of nodes at lower end relief

The speed of piston in this engine reaches a maximum of 42.1 m/s. The entraining motion ceases at TDC and BDC momentarily and the lubricant is retained in these instances by entrapment, squeeze film motion and rapid replenishment due to short lived stop time.

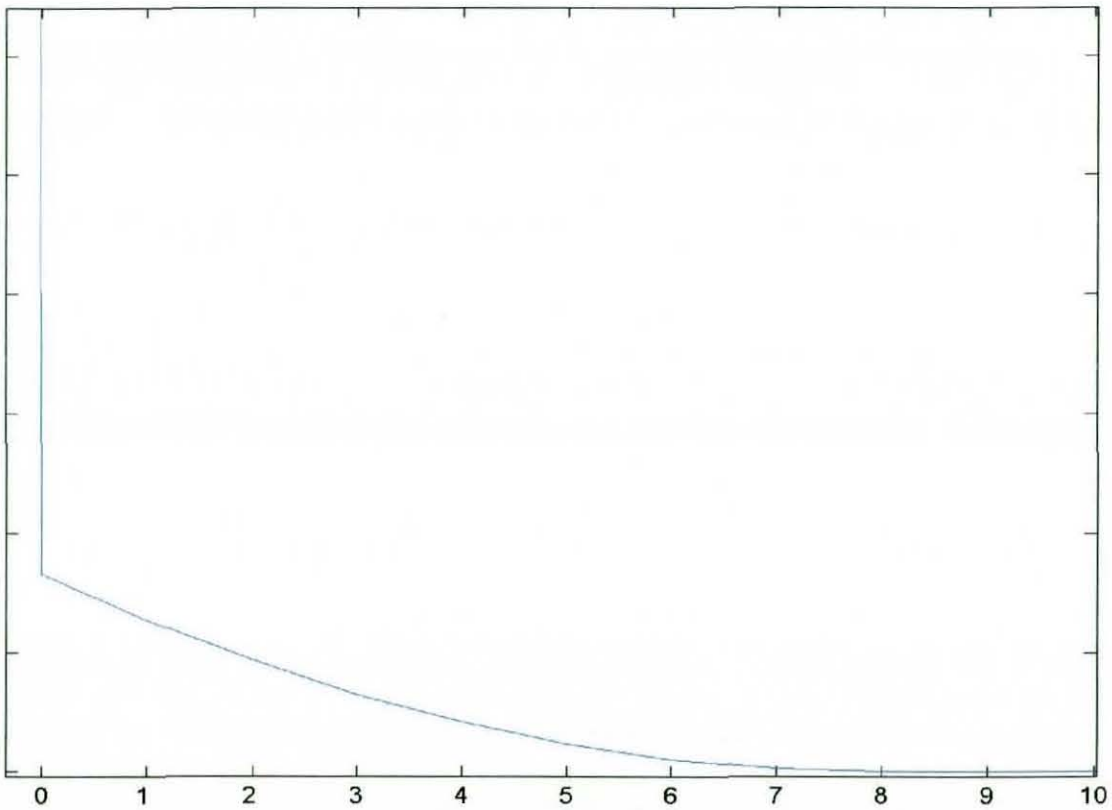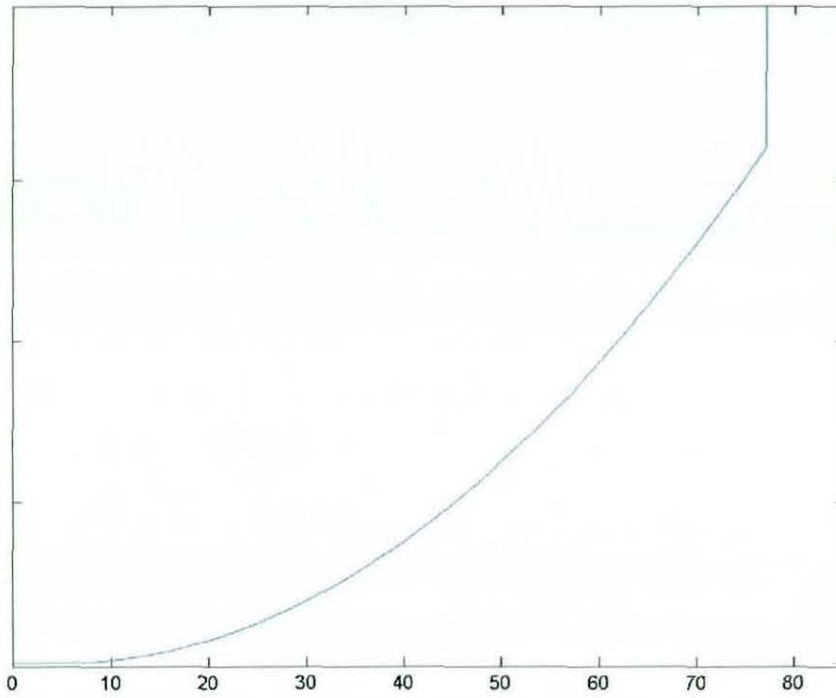Figure 5.37: Number of nodes tapered top end of piston skirt

The connecting rod length and the crank radius are 105.8 mm and 21.14 mm respectively.

5.4.1 Analysis at combustion

A position of interest in any tribodynamic analysis of piston skirt or ring-pack to cylinder liner contact is at the piston instantaneous locality, corresponding to peak combustion pressure, which occurs as the air-fuel mixture detonates. This position, as already described previously in the thesis is usually designed to occur, a few degrees (in terms of contact angle) past the TDC, in order to lessen the effect of piston slapping action. The combustion pressure rises dramatically just prior to this location, resulting in corresponding high contact forces. At the same time the velocity of the piston relative to the stationary liner, and consequently the speed of entraining motion of the lubricant is still comparatively low in its downward direction. The combination of high contact load and low speed of entraining motion usually translates to some of the worst tribological conditions encountered in IC engine, and as rated in chapter 1, account for the major source of frictional loose.

The downward sliding velocity is designated to be positive, and is 2.9 m/s at this position, which is still relatively low, given the sliding nature of the contact. The position investigated corresponds to the crank-angle of 13°, where the maximum combustion pressure of 50 MPa is applied, resulting in an extreme case, with a piston misalignment of 0.1° with respect to the vertical axis of the cylinder bore, and with a contact force of 2.5 KN.

Figure 5.38 shows the three dimensional pressure distribution. The contact area is extended circumferentially over approximately a π-film and in the axial direction over the skirt length of 28 mm. Note the edge pressure spikes, which are reminiscent of edge stress discontinuities in counterformal contact of a roller to a flat semi-infinite elastic half-space (see **Johns** (1979), **Johns** and **Gohar** (1981), **Rahnejat** and **Gohar** (1979), **Heydari** and **Gohar** (1980)). The abrupt change in the axial profile of the piston skirt in the vicinity of its leading and trailing edges gives rise to this pressure spikes. The relief radii or chamfer are used precisely for the reason of reducing these edge effects. Any tilt of the piston accentuates the problem at the skirt end penetrating into the liner, whilst relieving the high pressures at the lifted end. This has been shown by **Harris** (1985), **Johns** (1979) and **Johns** and **Gohar** (1981) for dry elastostatic counterformal contact of rollers to flats and under lubricated conditions under steady state entraining motion by **Kushwaha** (2000) and **Kushwaha, Rahnejat** and **Gohar** (2002). It should be noted that under lubricated condition the pressure spikes increase from their elastostatic levels for the same load, whilst mid-span contact pressures reduce in magnitude. This has been shown for the counterformal contact of rolling element bearings by **Mostofi** (1981), **Mostofi** and **Gohar** (1982), **Rahnejat** (1984) and **Kushwaha** (2000).
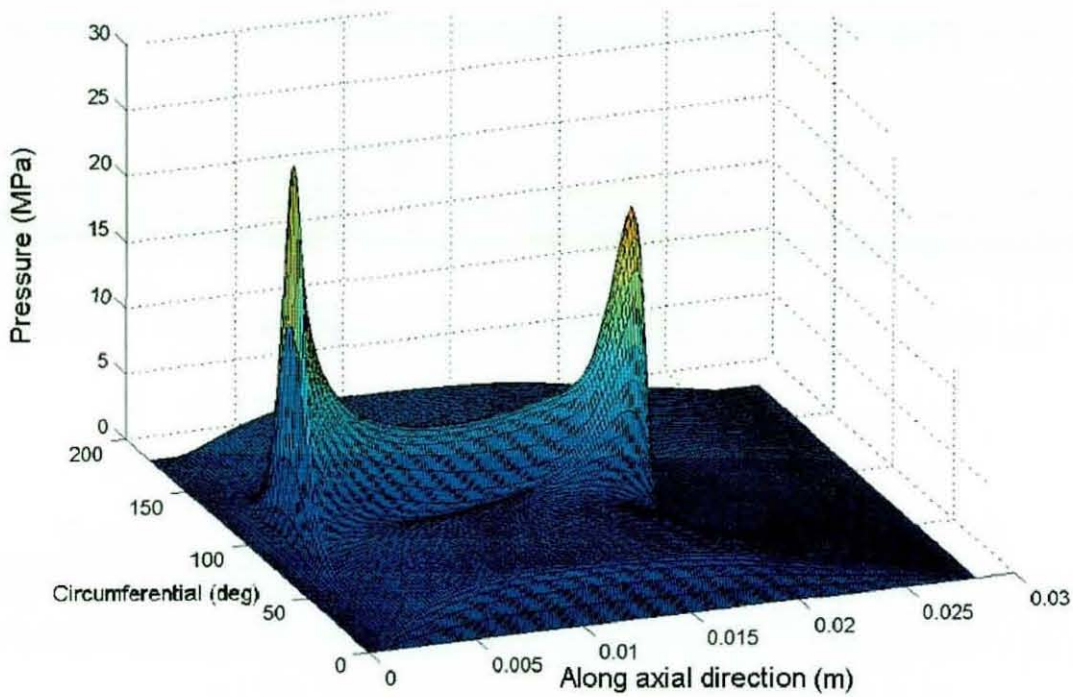
Figure 5.38: Three dimensional pressure distribution at maximum combustion pressure
(direction of entraining motion: left to right along axial direction)

The three dimensional pressure distribution in figure 5.38 can be regarded as a good visualisation tool. A quantitative description of the generated contact pressures can be provided by an isobar plot. Such a plot is a two dimensional representation of figure 5.38 over the pressure generating domain. It depicts regions of constant pressure or in other words isobars. This is shown in figure 5.39. The direction of entraining motion is from left to right in this figure. This corresponds to the down-stroke sense of the piston, with the inlet being on the bottom side of the skirt. Unlike normal lubricated conjunctions the maximum pressure is on the inlet side due to the more abrupt profile here than at the exit. The regions of high pressures occur over the flat region of the piston skirt axial profile. This is indicated by the islands of pressure spikes to either side of the contact and along the centreline of the contact in the circumferential direction. Note that the asymmetry in the axial pressure distribution is due to the differences between the relief radii at the top and the bottom of the skirt. The maximum pressures occur on the left-hand side of figure 5.39, which correspond to the bottom of the piston skirt, and in the vicinity and prior to the commencement of the relief radius. The maximum pressure value is 29.2 MPa. The

corresponding maximum pressure isobar on the other end of the skirt is in a similar location with a value of 22.9 MPa.
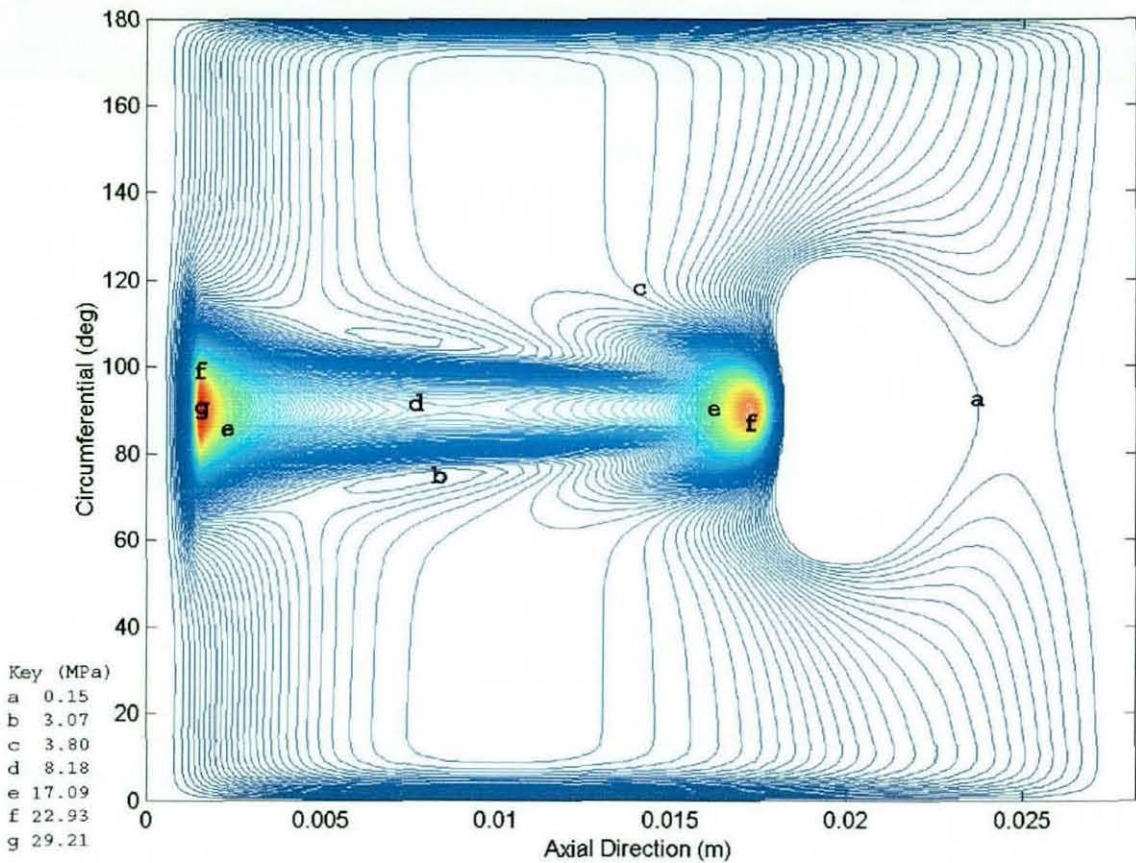
Figure 5.39: Pressure isobar plot at combustion

Due to piston ovality and the degree of its conformance to the cylinder bore, the region of high pressures is concentrated in the domain $60°-120°$, whilst lower pressures extend for all the π-film region. Figures 5.40 and 5.41 show two-dimensional pressure profiles for the inlet and the outlet regions of the contact in the circumferential direction respectively. The corresponding minimum film thickness values in these contact cross sections occur in the vicinity of the maximum pressures, with the lowest film thickness of 1.97 μm. The minimum film thickness occurs here, because the existence of pressure spikes inhibits flow of lubricant into this region (figures 5.42 and 5.43).

152
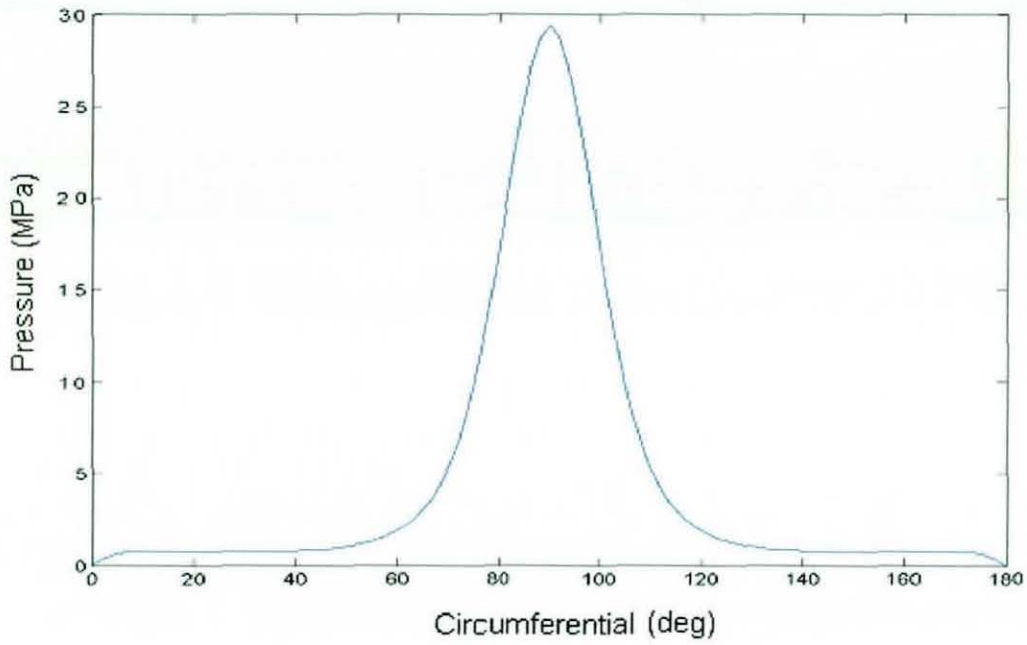
Figure 5.40: Circumferential pressure distribution at inlet region
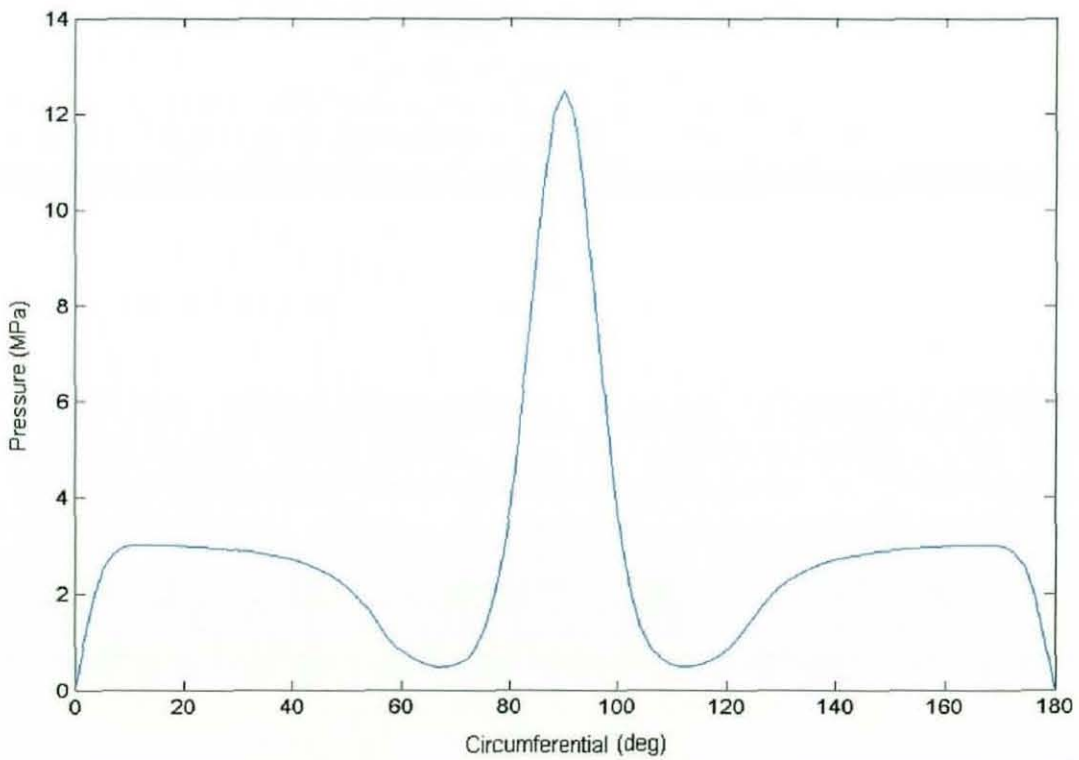
Figure 5.41: Circumferential pressure distribution at outlet region
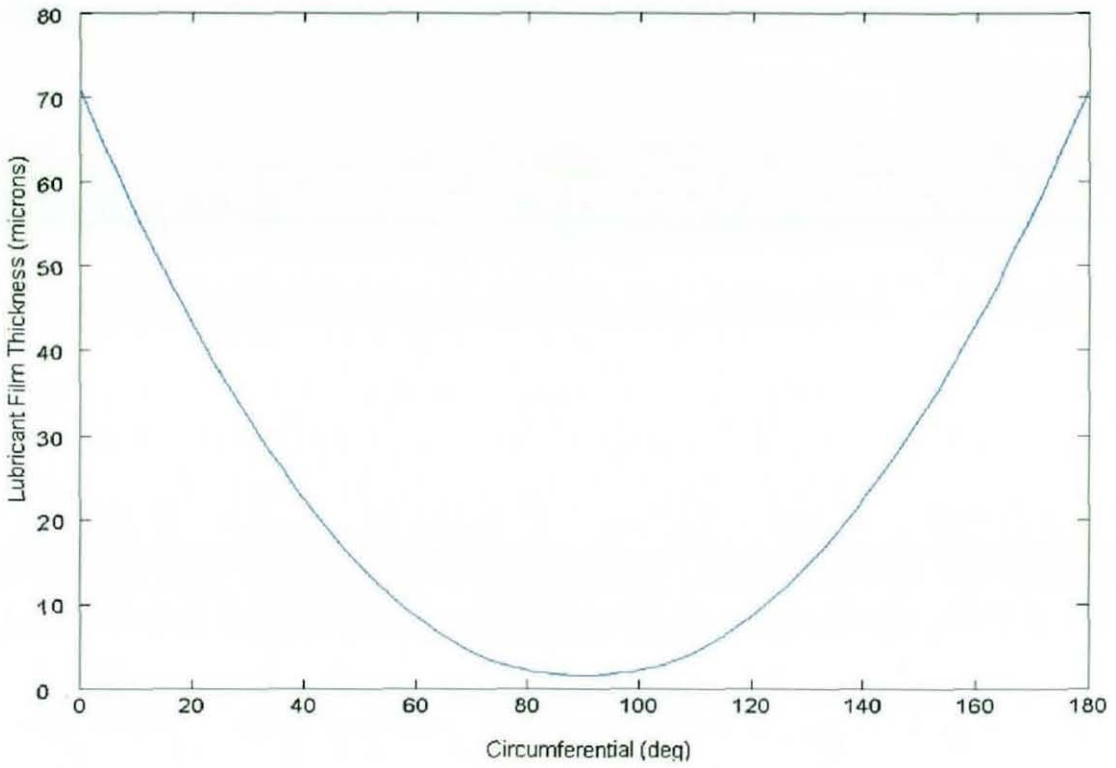
Figure 5.42: Circumferential thickness at inlet region
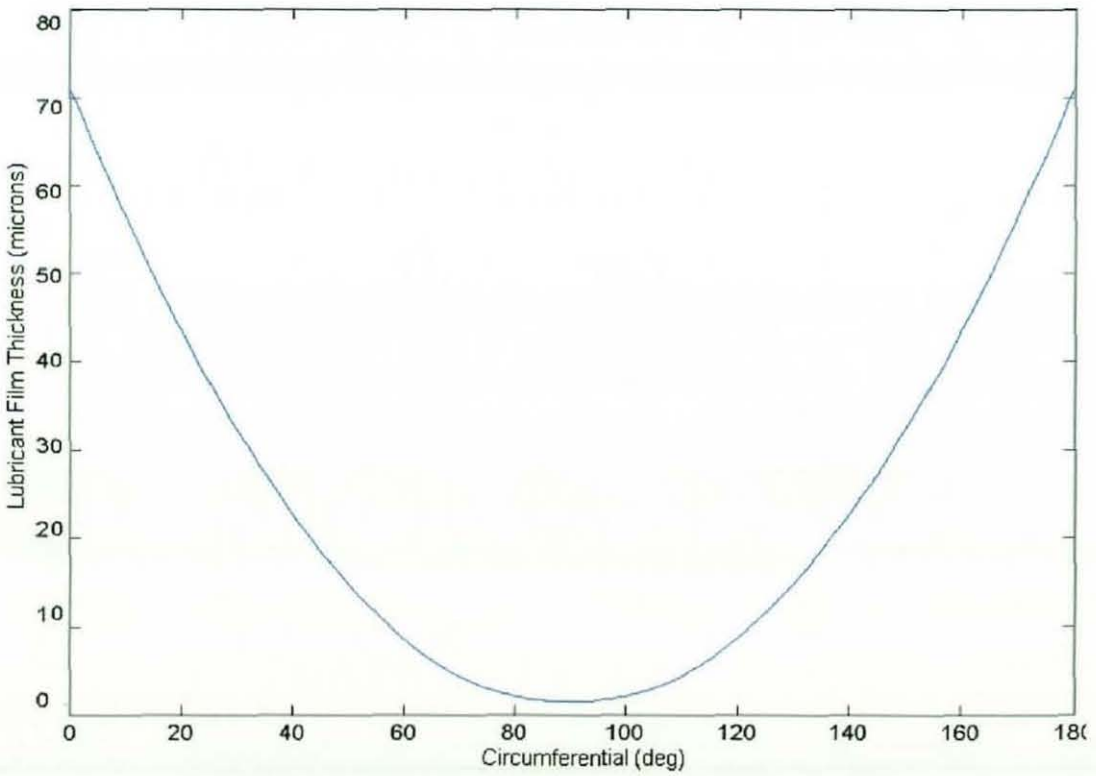
Figure 5.43: Circumferential thickness at outlet region

154

Figures 5.44 and 5.45 show the axial pressure distribution and the corresponding lubricant film thickness through the centre of the contact. Note the pressure spikes at the extremities of the contact, which occur in the vicinity of sudden change from the flat profile to that of the relief radii. The continuity or smoothness of this change ensures a reduction in the magnitude of pressure "pips". This problem has been tackled in higher pressure concentrated counterformal lubricated conjunctions such as in rolling element and tapered roller bearings. Edge blending of rollers is now common place, after initial studies carried out by **Lundberg** (1947), resulting in a proposed "idealised Lundberg Profile", which has been proven to be impractical to manufacture. Subsequent studies have concentrated in the approximation of this profile by a series of intersecting radii, see for example **Johns** (1979) and **Johns** and **Gohar** (1981). More common form of relieving has been undertaken by central crown radii, covering the entire length of the roller, known as self-aligning rollers and for some pistons, referred to as barrelled profiles. The minimum axial film thickness occurs within the vicinity of these edge pressure spikes.
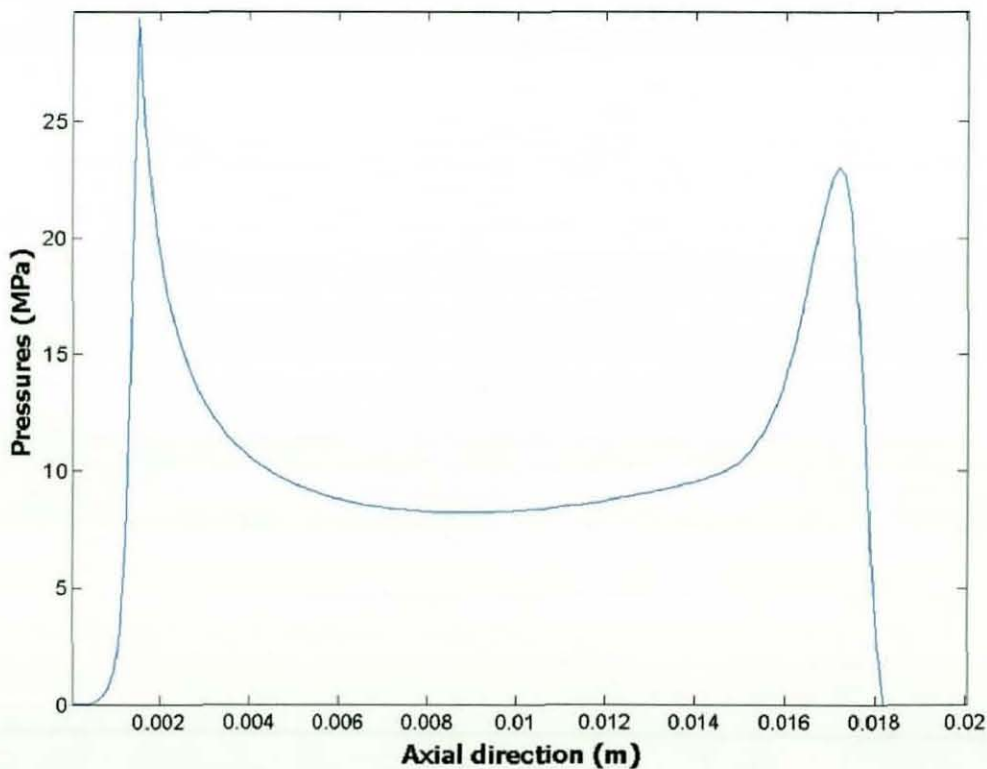
Figure 5.44: Pressure distribution along axial direction at maximum combustion pressure
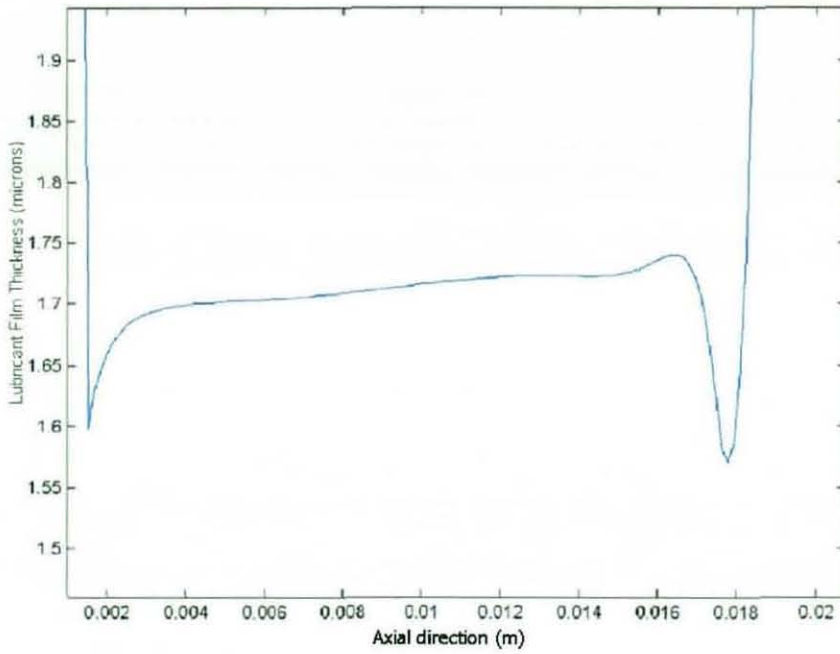
Figure 5.45: Minimum lubricant film along axial direction at maximum combustion pressure
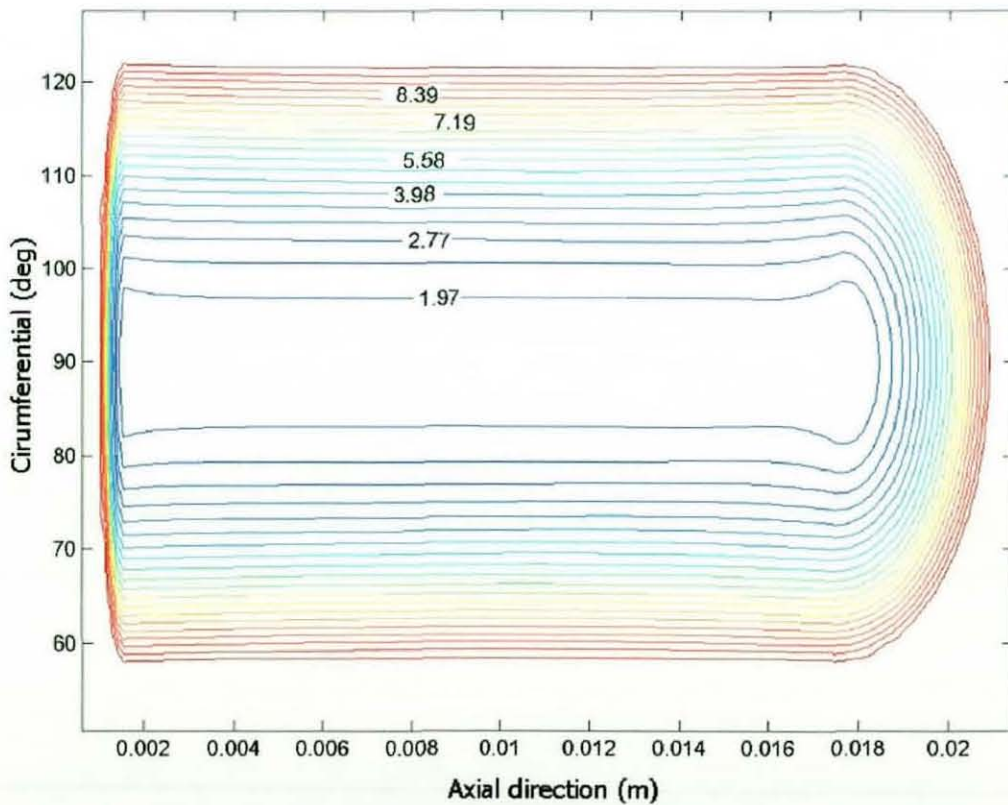
Figure 5.46: Film contour plot for the entire contact region at combustion

The island of minimum film thickness extends between the pressure peaks, when referring back to the pressure isobar plot of figure 5.39. Figures 5.47 and 5.48 show the inlet and outlet regions of the pressure isobars with superimposed flow pattern, indicated by a vector plot. In figure 5.47 the inward flow is pulled into the contact by entraining motion, but little flow ingresses into the region of high pressures. Most of the flow goes onto the "shoulders" of the high pressure region. Note that the length of the arrows indicates the magnitude of flow, which are much larger in the converging inlet gap than those in the high pressure region. The same pattern is observed at the outlet region in reverse mode, where the outflow is much larger than those in the rear high pressure domain. Flows on the side-lobes (i.e. shoulders of the contact) are inward bound in the inlet region (see figure 5.47) and outward bound in the outlet region (see figure 5.48).
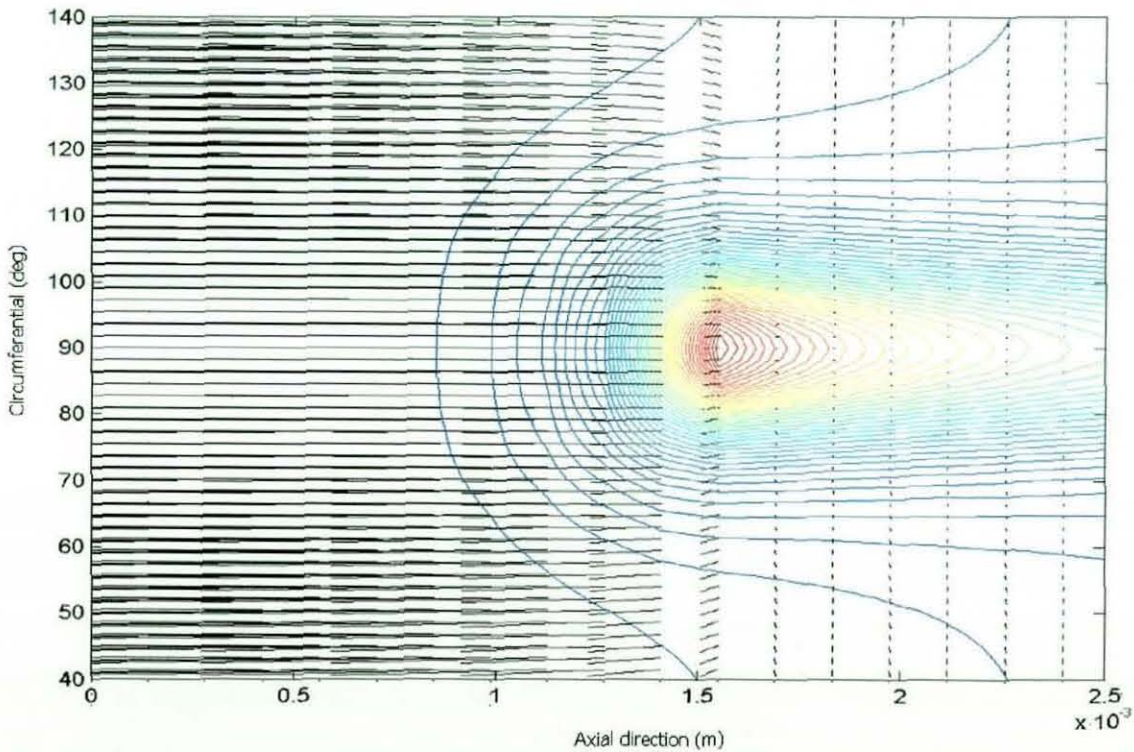
Figure 5.47: Magnification of flow pattern superimposed on pressure isobar plot at inlet region

157
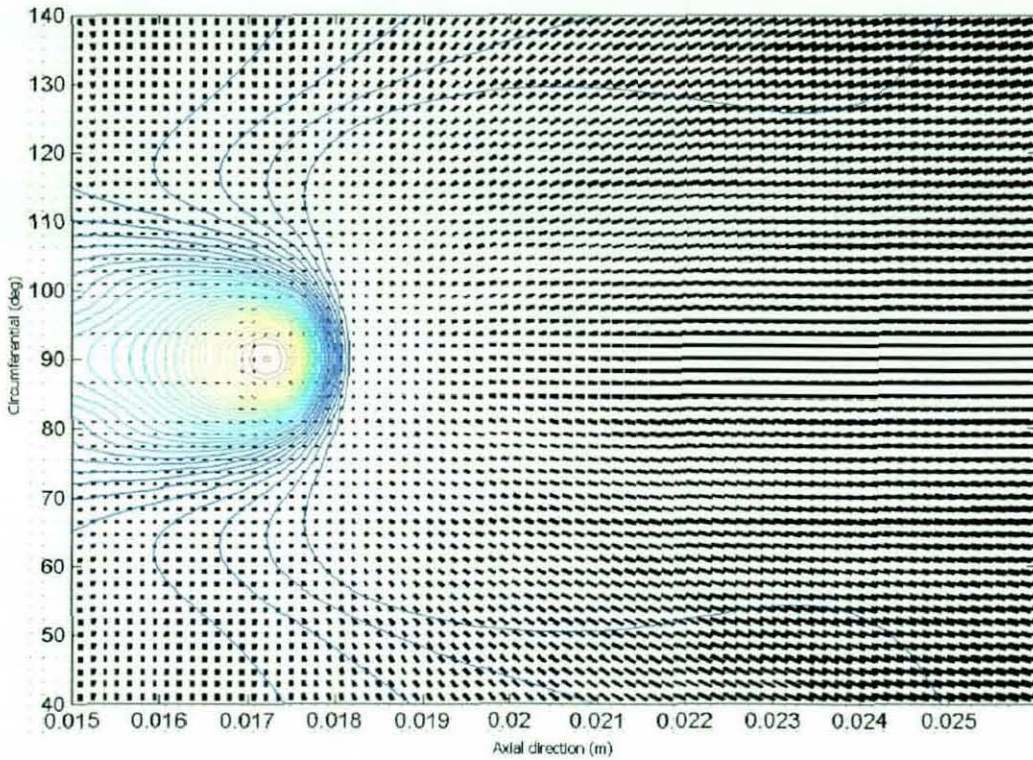
Figure 5.48: Magnification of flow pattern superimposed on pressure isobar plot at outlet region

The total deflection of the bodies is approximately 1.92 µm, accounting for more than 90% of the gap size between them. The value of $\alpha p \approx 0.03$, which corroborates the insignificant increase in lubricant viscosity at even the maximum value of pressures. Thus, the prevailing conditions are iso-viscous elastic.

5.4.2 *Effect of Thermal Expansion*

When the effect of thermal expansion of the piston is taken into account (see section 4.5.1), the contact conformity is enhanced. To obtain the deformed shape of the piston skirt, it is necessary to compute both thermal loading as well as deformation due to generated lubricant pressure. The latter is computed according to the contact deformation theory described in chapter 4. The former is obtained by thermo-elastic finite element analysis of hollow piston construction under quasi-static conditions for given value of combustion force. This analysis was carried out by Golya (2000) using an in-house

developed finite element code. The deformed profile of the piston skirt after thermo elastic analysis was imported as the initial profile for the subsequent analysis. This thermal expansion results in an increase in the area of contact. Therefore, the domain of pressure generation has increased, yielding lower pressure peaks, as evident in figure 5.49. The peak pressure, to the rear of the contact is approximately 13 MPa, which is less than half of the peak pressure of 29MPa observed under the isothermal solution. The effect of spreading of the pressure generating domain with thermal expansion of the piston skirt can also be observed by comparison of isobar plot of figure 5.50 with the previous isothermal solution, under the same contact conditions depicted by figure 5.39.
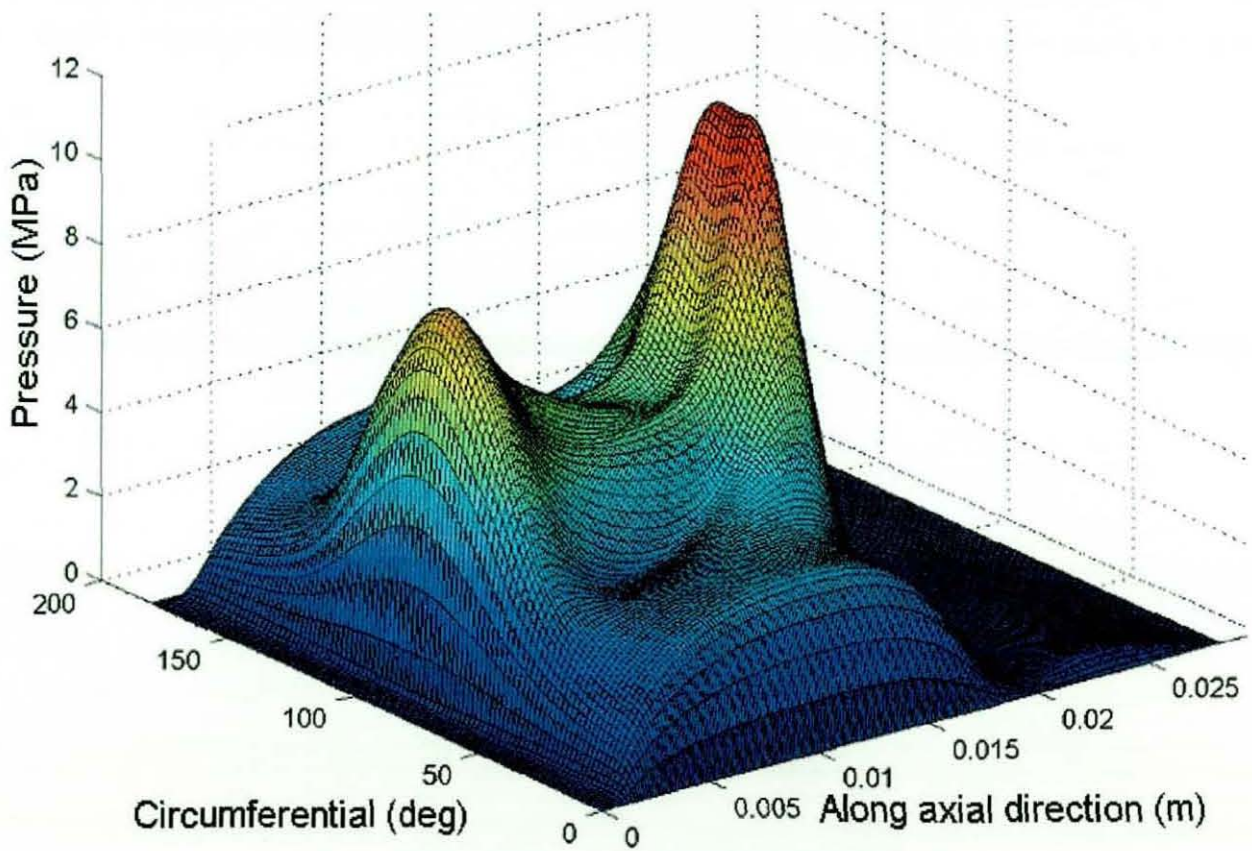
Figure 5.49: 3-Dimensional pressure distribution during combustion with considering thermal distortion (entraining motion from left to right along axial direction)

Figures 5.51 and 5.52 show the two-dimensional pressure profiles through the region of peak pressures along the axial and circumferential direction respectively. A comparison of the results in figure 5.51 with those in figure 5.44 indicates an increase in the pressure generating region towards the exit constriction by a length of nearly 2mm. A comparison of two pressure isobars show that in the case of isothermal solution, the exit region exhibits a closed low pressure region, indicated by a heart-shaped island, whereas in the current case, a pressure generating region has evolved.
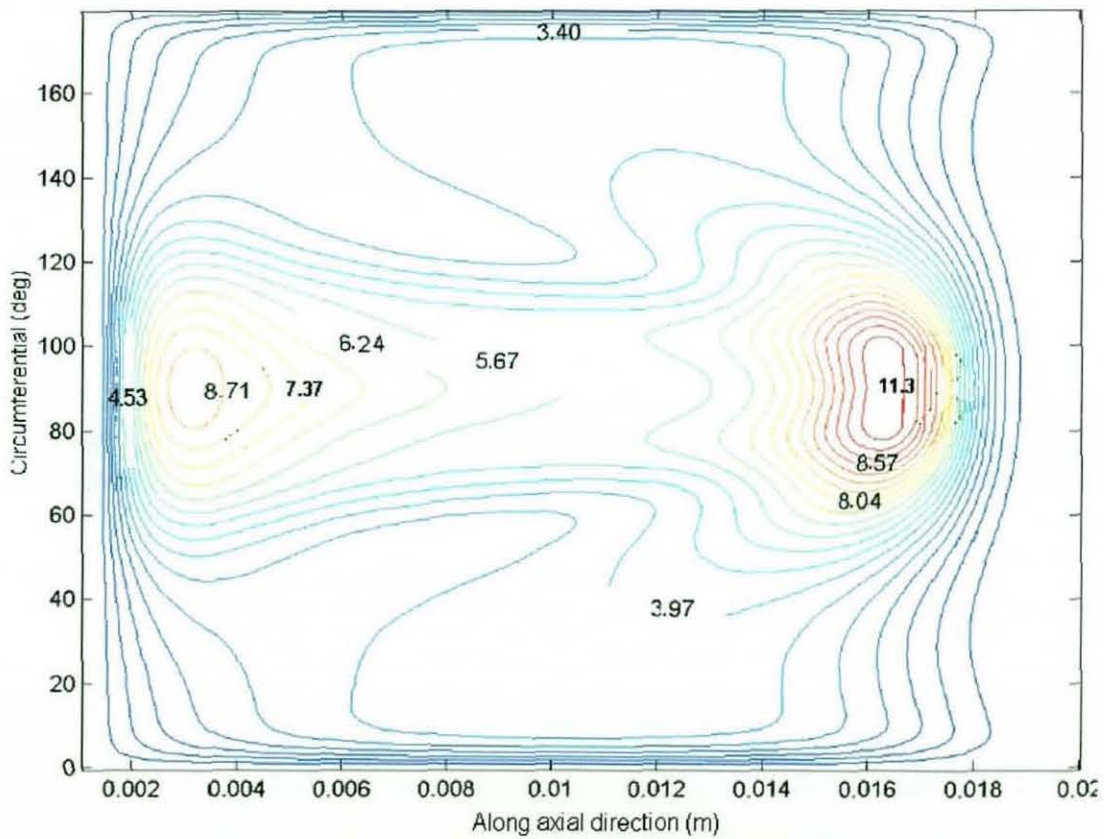
Figure 5.50: Isobaric pressure plot (MPa) at combustion with considering thermal distortion

The increased pressure generating region indicates that a higher load carrying capacity would be attained due to thermal deformation of the hollow piston skirt. In the circumferential direction, the pressure generating region in both figures 5.41 and 5.52 corresponds to a full π-film, but with thermal expansion, the proportion of the load carried at the contact extremities beyond the pressure peaks has been enhanced.
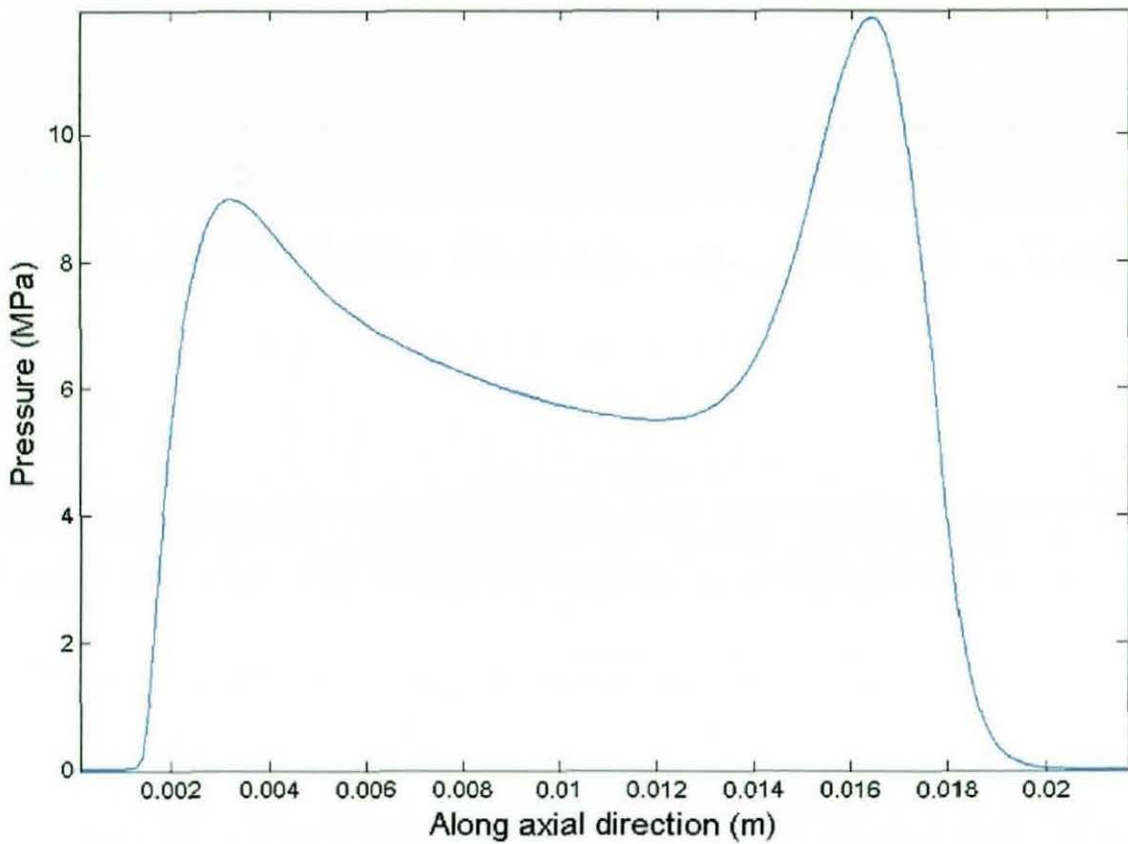
Figure 5.51: Maximum pressure distribution along axial direction during combustion with considering thermal distortion

Figures 5.53, 5.54, 5.55 and 5.56 show the lubricant film contour, and the axial and circumferential cuts through the regions of minimum lubricant film thickness correspondingly. A comparison of these with the case of isothermal solution indicates the overall film thickness has hardly altered, irrespective of the reduced pressures in the current case. Under the prevailing hydrodynamic conditions, one would expect the lubricant film thickness to decrease with reducing pressures. However, the regime of lubrication is at the border of iso-viscous elastic condition with little deformation in the case of isothermal solution. With thermal distortion, the global deformation due to thermal action has increased, whilst, elastic deformatiuon due to hydrodynamic pressures is reduced, with the net effect being that the overall gap size has hardly altered. The

implication of this finding are twofolds. Firstly, higher load carrying capacity can be achieved
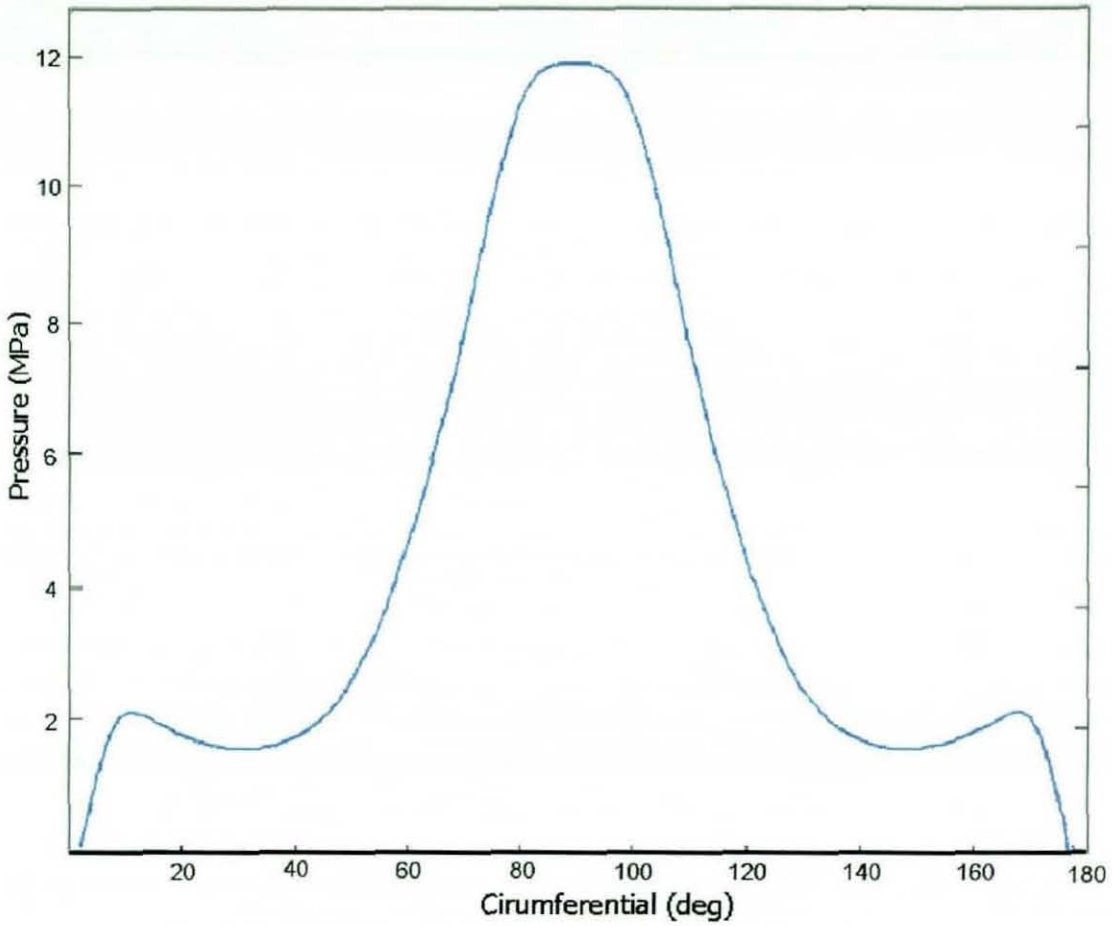
Figure 5.52: Maximum pressure distribution along circumferential direction during combustion with considering thermal distortion

with thermal distortion, yielding more contact conformity and deformation, thus yielding a thicker film. This means that the prevailing regime of lubrication can be shifted more towards iso-viscous elastic conditions, which is beneficial. Secondly, due to insignificant observed differences between isothermal and thermal solutions, it is clear that the need for full thermo-hydrodynamic solution is alleviated and the lubricant falls well within the fold of Newtonian behaviour. The lubricant behaviour is iso-viscous and the inclusion of thermal distortion of the contiguous solids would suffice.
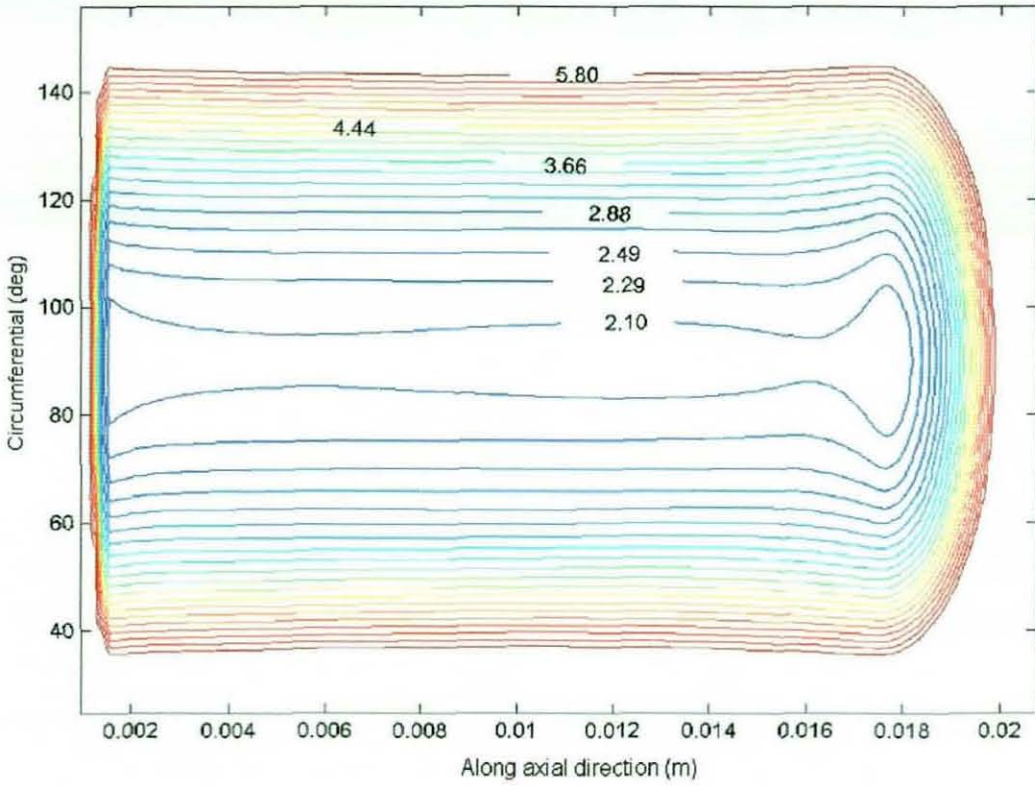
Figure 5.53: Lubricant film contour (μm) during combustion with considering thermal distortion
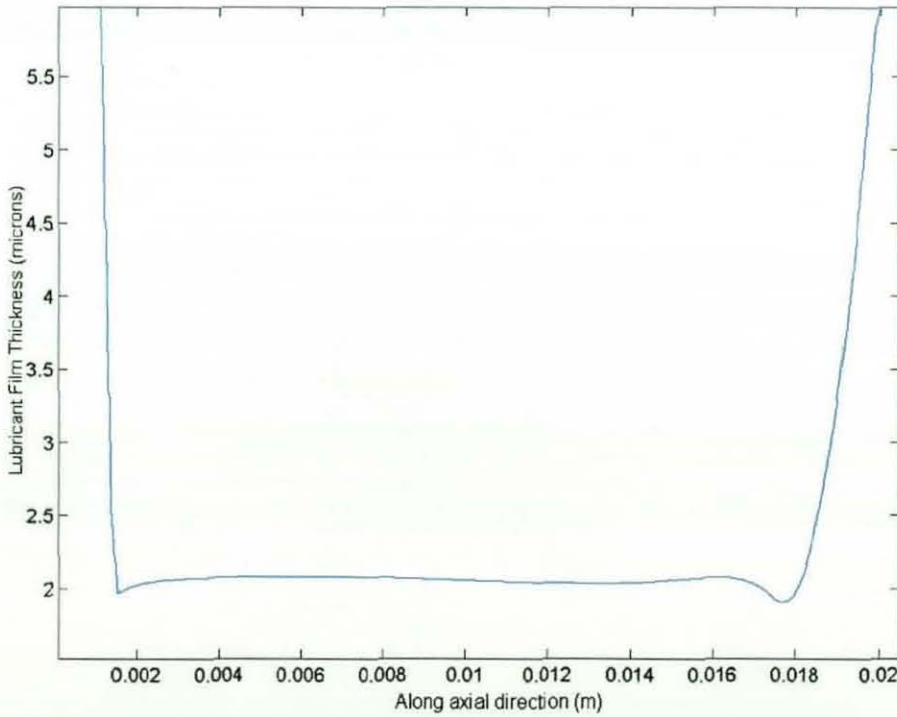
Figure 5.54: Minimum lubricant film thickness along axial direction during combustion with considering thermal distortion
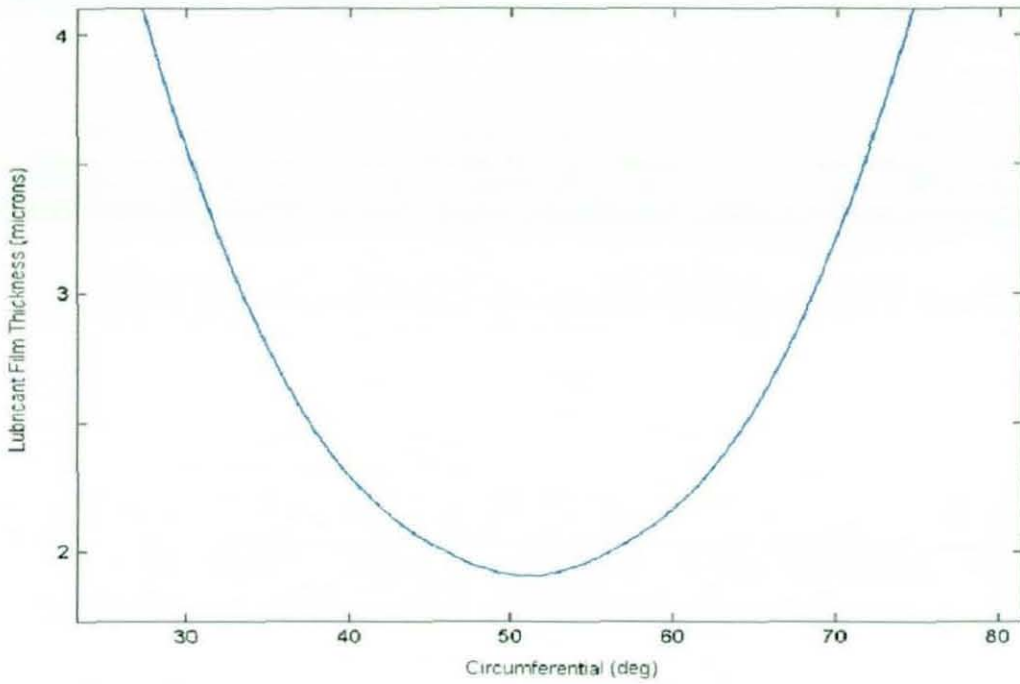
Figure 5.55: Lubricant film thickness at upper end of skirt along circumferential direction with the effect of thermal expansion
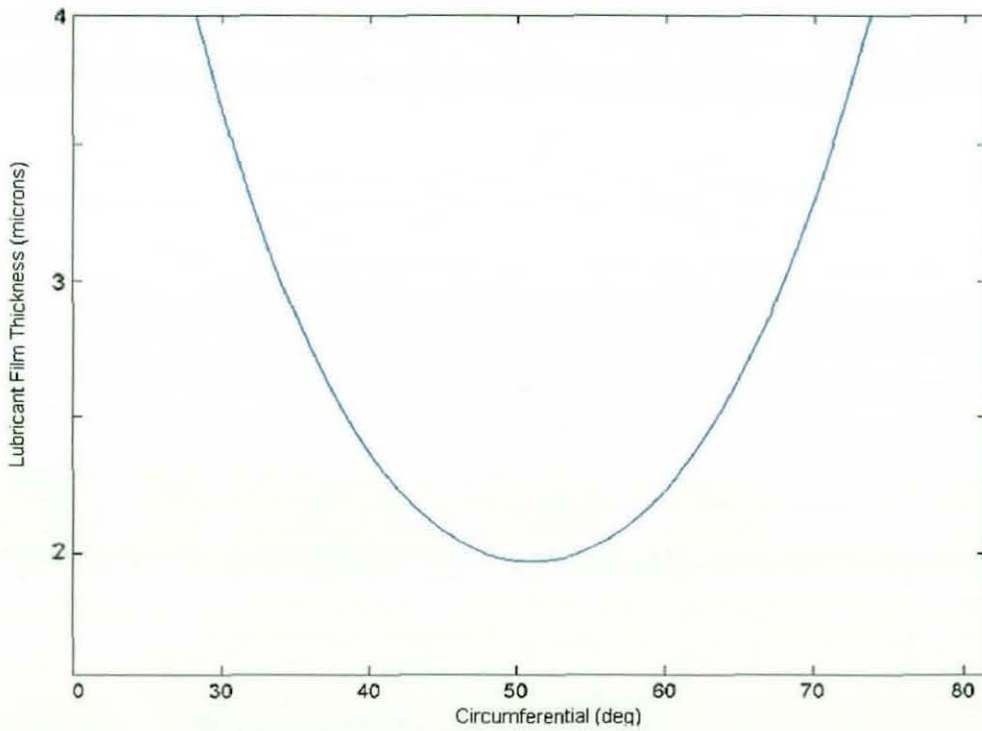
Figure 5.56: Lubricant film thickness at bottom end of skirt along circumferential direction with the effect of thermal expansion

164

In figure 5.57, the flow pattern is superimposed upon the isobaric pressure plot. As in the previous cases, the region of high volumetric flow rate remains on the shoulders of the contacting region. Due to the close conformity of the contact and slight increase in gap to the sides of the contact due to thermal distortion, more flow than in the previous case (see figures 5.47 and 5.48) ingresses into the contacting region. However, this is still not sufficient as the flow inside the high pressure region remains almost stagnant as represented by very small arrows (dots in the figure). The arrow shape, almost indicates the thermally distorted and conforming contact region.
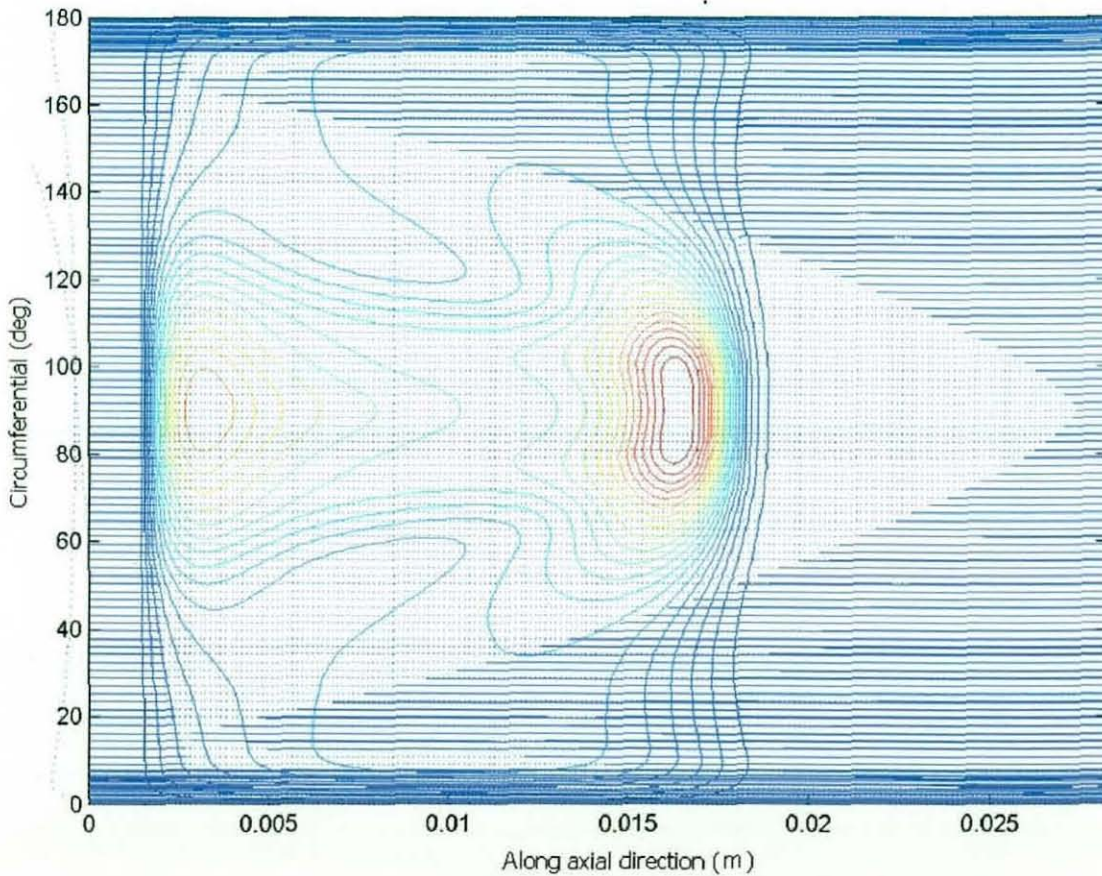
Figure 5.57: Lubricant film flow superimposed upon isobaric pressure plot

5.5 Verification of Methodology

Due to relatively high speed of sliding motion and the curved conformal contact of piston skirt to cylinder liner, measurement of lubricant film thickness has always posed difficulties, for example by optical interferometry, which is often used for counterformal contact of ball and rollers against optically flat glass races. Other methods developed for this purpose, chiefly LIF (see section 2.4.5.1), require extensive experimental set ups and dedicated research in measurement work, which are outside the aims and objectives of the current research. However, sufficient results have been obtained by other research workers that provide a basis for judgement to be made in respect of numerical findings reported in this thesis. Furthermore, monitoring of component performance, removed from the engine after service can be used as a measure of verification of numerical predictions. This is highlighted in section 5.5.1.

Other validation/verification of numerical predictions is ideally carried out against analytical solution or other numerical methods. For this purpose the case of an engine journal bearing, employed as the main crankshaft support is used, where the solution methodology was initially developed by **Gupta** (2002) for a thin shell journal bearing construction. **Gupta** (2002) verified his solution methodology for elastohydrodynamics of the 4th engine bearing by predicting the conical whirl of the flywheel, using a multi-body dynamics model of the same 1.8 litre, 4-stroke, 4-cylinder engine (also investigated here), against experimental measurements of the same flywheel motions obtained by **Kelly** (2000). **Gupta** (2002) showed that the component of the rigid body motion of the flywheel in the axial direction of the crankshaft towards the clutch friction disc, referred to as flywheel nodding action, had a predicted amplitude of 0.127 mm due to distortion of the thin bearing shell induced by generated elastohydrodynamic pressures. **Kelly** (2000) had measured the same motion to have an amplitude of 0.14 mm for the same engine operating conditions, thus a remarkable agreement was found.

The solution of the EHL of conforming contact of the journal against the thin shell bearing, made of Babbit, a Tin based alloy of low elastic modulus (in the range 50-60

GPa) was carried out by **Gupta** (2002) and **Gupta** *et al* (2002), and also reported by **Rahnejat** (2000), using a column method solution for the determination of shell deformation. The column method is based upon calculation of local deformation at any location, being only dependent on the column of pressure directly acting upon it. In this manner, an analytic expression can be obtained for contact deflection. The method is only approximate, but computationally efficient, and is quite accurate for contact of bodies of low elastic moduli. A numerical solution of this type is, of course, essential in case of engine bearings of thin shell construction and of finite width, where the length to diameter ratio falls in between the short and long bearing approximations, making either the approximation methods inappropriate for the determination of contact pressure distribution. The engine bearing in the aforementioned diesel engine has a length to diameter ratio of 1.67.

The deformation of contacting bodies: piston skirt to cylinder liner contact, is based on a generalised solution of the elasticity of conforming solids, where the localised deformation at any location is due to all columnar pressure elements. This approach is applied in the next section to show the conformity of the analysis approach with that reported by **Gupta** (2002) for the case of thin shell engine bearing, under the operating conditions. This is, therefore, a validation of the methodology developed in this thesis. When the engine bearing bush has a greater thickness than the thin solid shell used in the analysis by **Gupta** (2002) and **Kelly** (2000), or its modulus of elasticity is increased, the validity of the column method comes to question, and deviations are observed between its predictions and those obtained by the methodology developed in this thesis.

5.5.1 Tribodynamics of Engine Journal Bearings

In the simulation study carried out in this section, the thin shell engine journal bearing has a Babbit shell 5 mm thick, with a Young's modulus of elasticity of 60 GPa, and a Poisson's ratio of 0.33. The journal is considered to be Steel for this simulation runs, with the radius of 31.75 mm. The bearing width is set at 70 mm, making a width-diameter ratio of 1.11. The journal clearance is 40 μm (a ratio of approximately 1/800 th of the

journal radius). The engine speed is considered to be 1800 rpm, with the maximum combustion pressure of 32 MPa. Detonation takes place 13° crank-angle rotation past the TDC. The 4th journal bearing nearest to the position of the flywheel is subjected to combined direct and moment loading, mainly due to the 4th cylinder firing. From TDC to the combustion position, the pressure rises sharply, effectively applying a contact force of 6-13 KN to the 4th journal bearing. Generated lubricant pressures and elastic deformation of the shell resist this applied load, when the centre of the journal traces an eccentric orbital path around the centre of the bearing shell.

Figures 5.58 and 5.59 show the results obtained from both: (i) a column method solution and (ii) a full finite difference solution of the conformal contact of journal to bearing shell, for the conditions described in the preceding paragraph. The two dimensional pressure distributions are cross-sectional results through the maximum pressure and in the circumferential direction (i.e. the direction of entraining motion of the lubricant) (see figure 5.58). The results are for the various loaded conditions. Those in full line (as indicated by the key to the figure) correspond to the full solution of the elasticity equation. Those as dotted lines are obtained at the same conditions, but with column method assumption. Note that both sets of results indicate good concordance at lower values of load, which can be taken as a verification of the generalised methodology outlined for piston skirt to cylinder liner contact. As expected the column method under-estimates contact deformation, which in turn results in lower generated pressures in the iterative solution. It should be noted that thickness of the shell will make a difference in the column method solution, but has no influence in the finite difference solution, which is based upon the assumption of the mating bodies being semi-infinite elastic half-spaces. Note that as the load is increased the deviations between the two methods have become significant, owing to the simplifications of the column method. At high loads (i.e. 13 KN), the minimum lubricant film thickness is quite low with the full solution because of high pressures (see figure 5.59). With the column method the minimum film thickness is higher in value, for lower predicted pressures (see figure 5.59). The percentage difference between the predicted minimum film thickness values is, nevertheless quite low. This is because the thin shell is made of Babbit. To show greater deviation between the two

methods, thus indicating the importance of the full solution, the thin shell can be considered as a Steel bush, with a Young's modulus of elasticity of 212 GPa and a Poisson's ratio of 0.3. The Steel-on-Steel contact will generate much higher pressures, which in turn result in greater inaccuracy in column method evaluation of contact deformation.
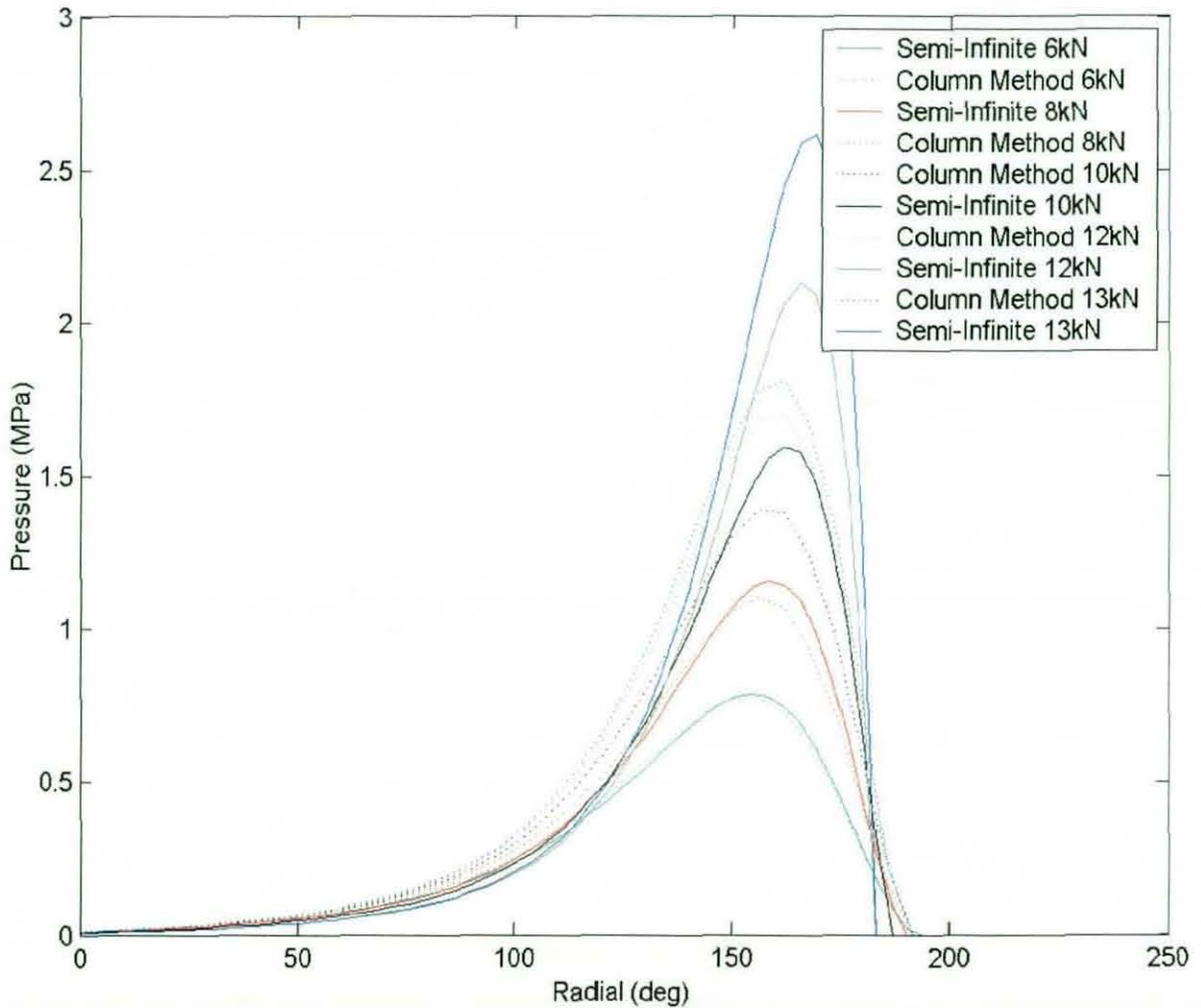
Figure 5.58: Comparison of maximum pressure variation with applied load obtained by using column method and semi-infinite theory (for steel on Babbit)
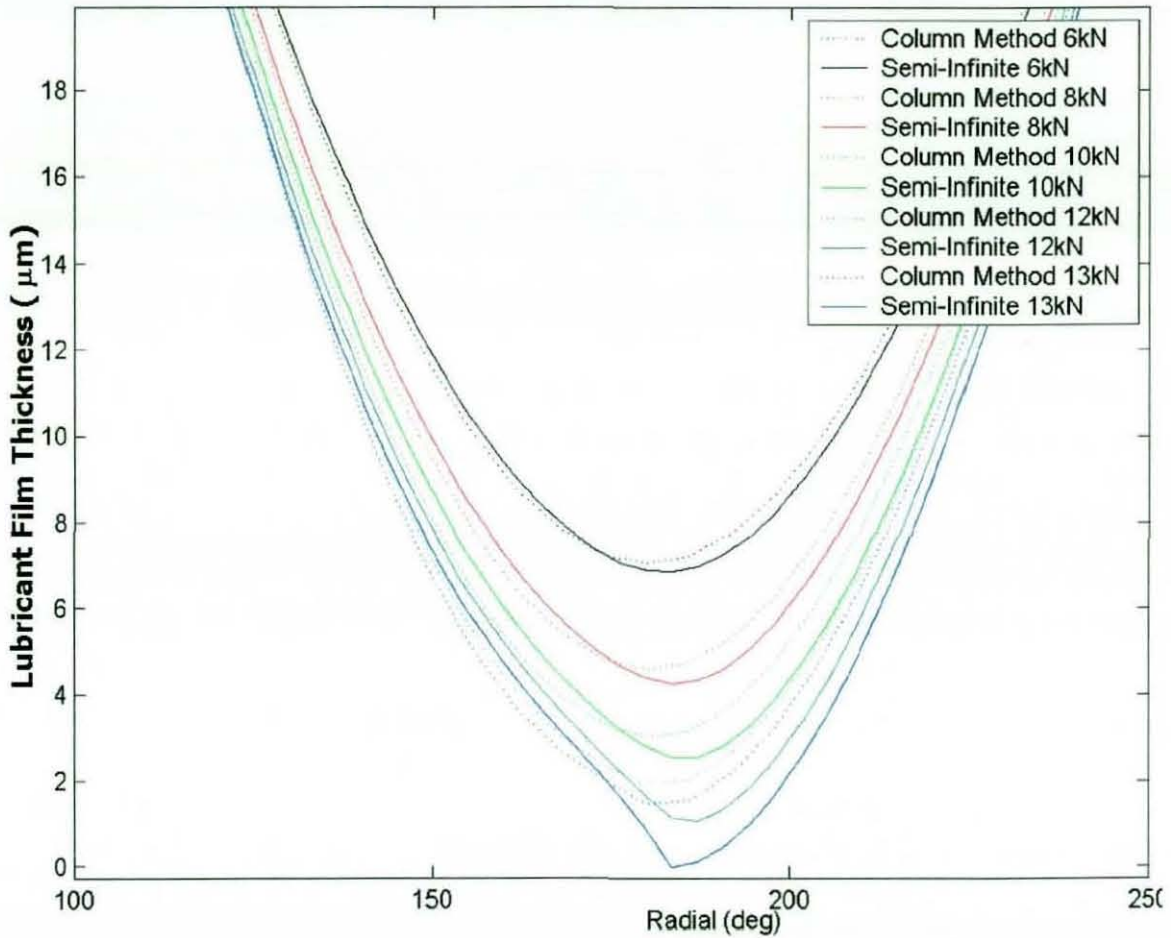
Figure 5.59: Comparison of minimum lubricant film variation with applied load obtained by using column method and semi-infinite theory (for steel on babbit)

Figures 5.60 and 5.61 illustrate the column method results for pressure distribution and the corresponding film shape for the same engine bearing configuration and operating conditions as for the previous case, with the exception of thin shell material, being made of Steel in this case. In this case higher contact reactions are used for the purpose of analysis. However, at the same contact load of 13 KN (used in both set of analyses), the region of maximum pressures (shown in circumferential cuts through the 3D pressure distributions) exhibit much higher pressures for Steel-on-Steel combination. This is expected owing to the higher effective reduced modulus of elasticity of the mating members (see figures 5.58, for column method solution at 13 KN, and figure 5.60 at the same load). In fact, the maximum pressure has increased nearly fifteen folds from a value of 1.75 MPa to 25 MPa. Note that the applied load is the same for both cases, meaning

the pressure distribution is more uniformly distributed over the softer (i.e. the lower elastic modulus) shell. This is evident by comparing the isobaric pressure plots with different shell materials (see figures 5.62 and 5.63), both having been obtained with use of column method approximation.
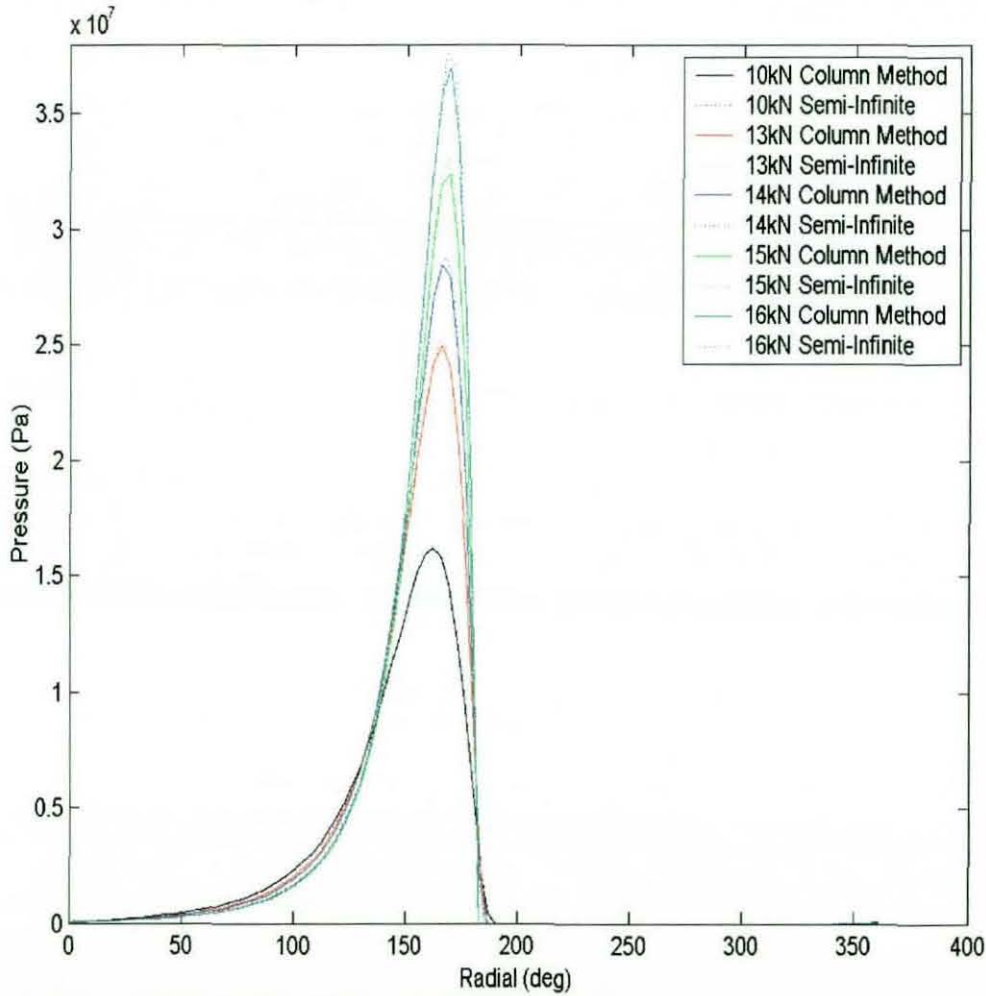
Figure 5.60: Comparison of maximum pressure variation with applied load obtained using column method for steel on steel

A similar comparison can be made in respect of corresponding oil film thickness profiles in the vicinity of the maximum pressures (see figures 5.59 for column method at 13 KN and figure 5.61 for the same load). It can be observed that greater pressures for Steel-on-

Steel combination have resulted in an increase of minimum film thickness from 1.8 μm to nearly 15.8μm.
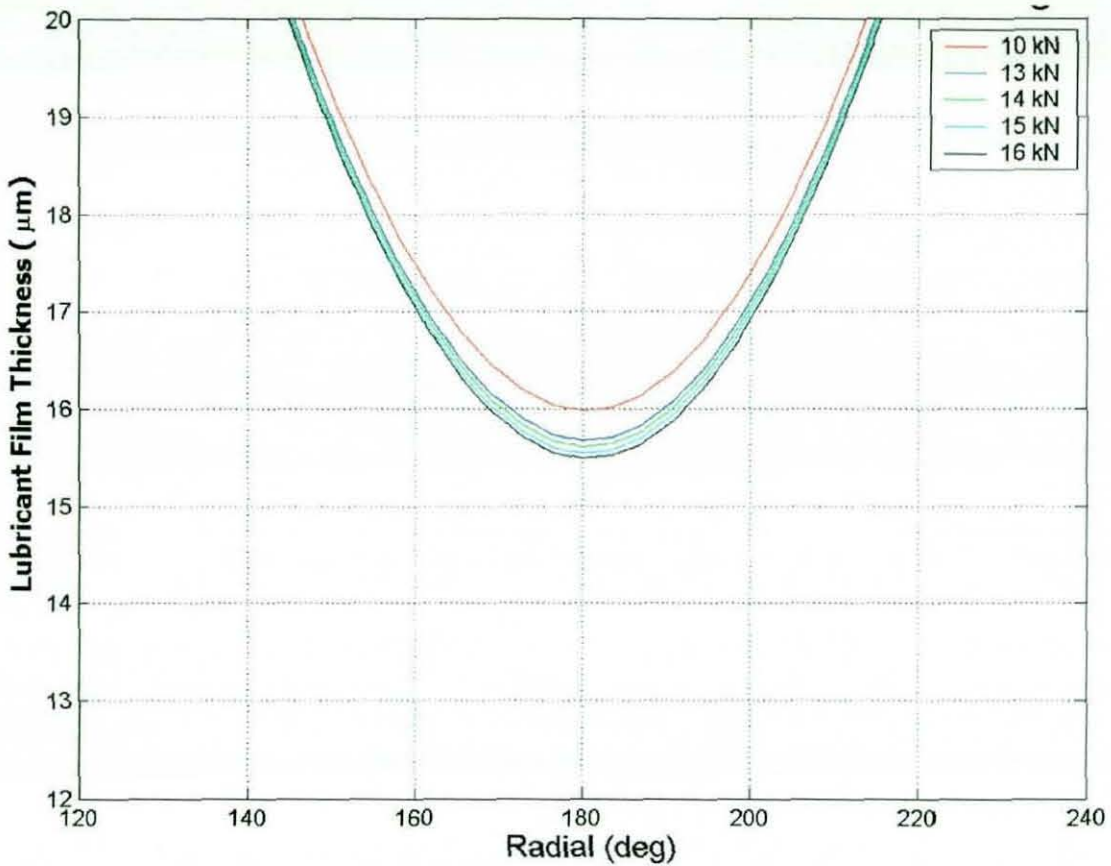
Figure 5.61: Comparison of minimum lubricant film variation with applied load obtained using column method (for steel on steel)

5.5.2 Observation of Piston Skirt Performance

The minimum film in some parts of the cycle in the case of the *F1* engine piston skirt contact falls at or near 2 μm thickness (see figures 5.46 and 5.62). The skirt is initially turned to a nominal diameter and then lapped to super finish. The bore is pressurised before machining, so that when the piston is fitted into the bore under operating conditions, the surfaces conform to each other by a combination of bending of the skirt and thermal expansion distortion. The surface finishes of the contiguous bodies render a

root mean square value of approximately 2 μm. Figures 4.8(a) and (b) show the compound out-of-roundness and surface roughness of the piston skirt, measured using a tallyround. Since the generated contact pressures in the conformal contact are not as large as those encountered in concentrated counterformal contacts of, for example, ball and rolling element bearings, cam-follower pairs and meshing gear teeth contacts, asperity deformation takes place to much lesser extent. It is, therefore, clear that with low lubricant film thickness of the same values as the composite RMS values of mating surfaces, the oil film would be bridged at various locations and at different times during the piston cycle. This has been observed on many piston skirts of the same or similar types in *F1* engines, a typical one of which is depicted in figure 4.8(a) and 4.8(b). Note the scuffing marks in the mid-span of the piston skirt profile, where the generated pressure distribution largely forms, and is intended to bend the hollow skirt in order to form a coherent film. Clearly, this aim is not achieved at all times.

It is clear that during a cycle the contact conditions go through various regimes of lubrication. These regimes of lubrication and transition from one to another appear on the **Stribeck** (1901) curve, which is a plot of coefficient of friction against a film parameter, usually denoted by the symbol λ, where: $\lambda = \dfrac{h_{min}}{\sqrt{R_a^2 + R_b^2}}$, R_a and R_b being the RMS value of surface finish of contiguous contacting surfaces: a and b respectively. Figure 5.62 shows what a Stribeck curve looks like. Note that boundary lubrication, corresponding to rubbing of two surfaces, often regarded to have formed an oxide surface layer, exhibits the maximum value of friction for any pair of contiguous bodies in contact. Soft oxide layers would provide oxide particles that roll in between them, providing third body lubricating action. However, it is generally thought that fluid film layers are always present in any lubricated machine element, even in the absence of entraining motion, owing to squeeze film action under loaded conditions or entrapment of pockets of lubricant in between surface undulations. Recent experimental work by **Sugimura** *et al* (1998), studying very thin films and at even low loads (where insignificant elastic deformation takes place) has shown that the lubricant film does not completely diminish in stop-start or acceleration-deceleration entraining action, for even

protracted periods of cessation of entraining motion. **Al-Samieh** (2002) has provided an explanation for Sugimura's experimental investigation in terms of transient behaviour of these thin films. These conditions are similar to reversals at TDC or BDC. The results presented in this chapter indicate that in certain locations during the piston cyclic action, a mixed regime of lubrication may be prevalent.
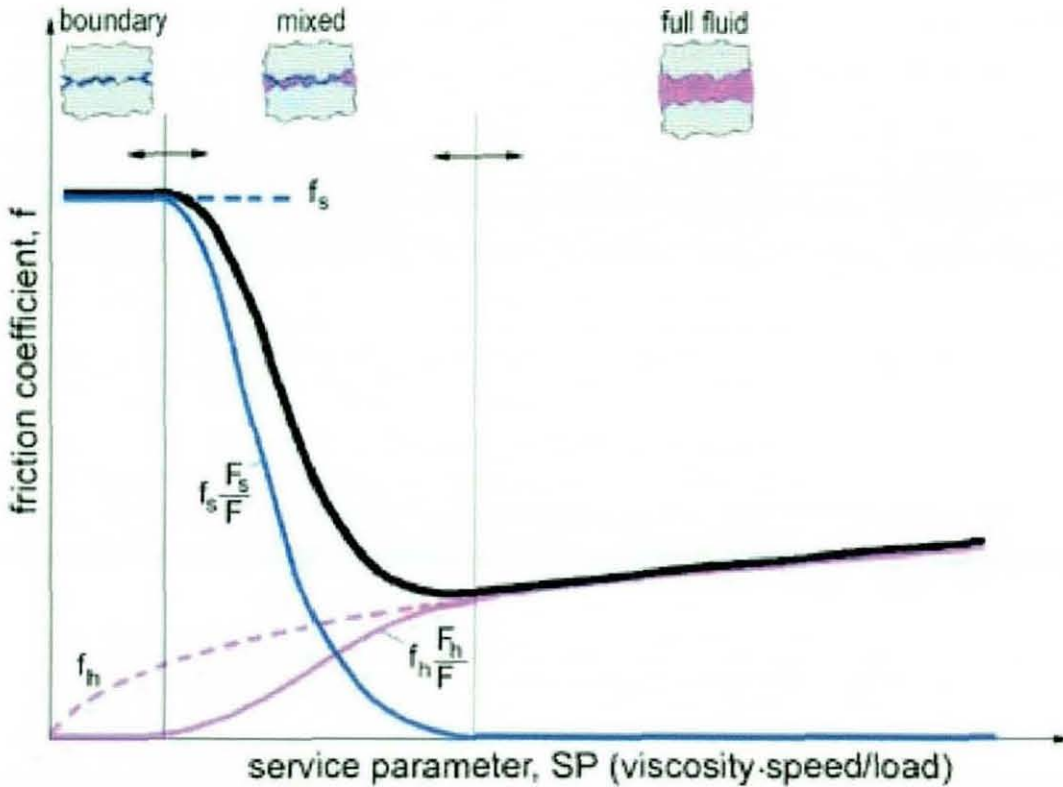
Figure 5.62: A typical Stribeck curve for regimes of lubrication

The aforementioned film parameter increases with elastic deformation of surfaces, rendering elastohydrodynamic conditions or if a large clearance gap exists for films to be maintained under hydrodynamic action, as observed in the study of BDC. In general, however, low hydrodynamic pressures and low clearance or diminution of gap with no elastic deformation, for example due to thermal expansion of the piston, can lead to gradual increase in hydrodynamic traction and an increase in coefficient of friction. This is often indicated in the *Stribeck curve*.

5.6- Inclusion of Surface Features

The above discussions show the difficulty in ensuring full fluid film lubrication in the conformal contact of piston skirt to cylinder liner throughout the piston cyclic operation. The analyses reported above show that film thickness can fall within the composite RMS value of mating surfaces or very close to it, so that asperity interactions may take place, leading to scuffing of surfaces as shown in the previous section. Traditionally, it was thought that improved surface quality, thereby reducing the surface roughness of mating members would improve the situation. Therefore, super-finishing surface treatment methods have been used, such as lapping or honing. However, as the analyses in this chapter have shown lubricant entrapment in parts of the cycle, where cessation of entraining motion takes place or low piston velocities exist can account for a significant contribution to fluid film lubrication, such as at TDC and particularly at or in the vicinity of BDC. For the remaining part of the cycle smoother surfaces would be desirable. Therefore, super-finishing together with inclusion of surface features on the piston skirt or cylinder liner or both is regarded as a possible solution to the problem of wear of piston skirts.

The F1 piston described in this chapter is often honed and then regular surface grooves introduced by diamond turning, using precision numerical control lathes. The depth of the grooves is approximately 2 μm. They are introduced circumferentially with regular spacing of 2 μm. There is no particular scientific reason behind this configuration of grooves. Indeed, their introduction was not based upon any tribological study, prior to the work carried out in the current study. In fact, from a tribological viewpoint, it is clear that introduction of sharp edged grooves/ridges would tend to induce stress discontinuities and sharp rises in contact pressures. It would be prudent to introduce the grooves prior to honing, thus rounding/blending the sharp edges. Nevertheless, the analysis reported below considers the existing procedure, rather than what would be desirable.

In order to see the effect of the introduction of these surface features the profile of the piston shown in figure 5.35 is modified to include the introduced undulations (see figure 5.63). The methodology employed for the tribological study remains unchanged. Therefore, the included features are also subjected to deformation of the contiguous surfaces, analogous to a micro-elastohydrodynamic analysis, with the difference that other surface roughness of the contiguous bodies is not taken into account, and that the generated pressures (as can be seen from the analyses described thus far) do not promote viscous-elastic conditions, rather iso-viscous elastic regime of lubrication for most of the loaded part of the cycle. To gauge the effect of these introduced features the quasi-static analysis is carried out at the same "maximum combustion" position as that reported in section 5.4.1.
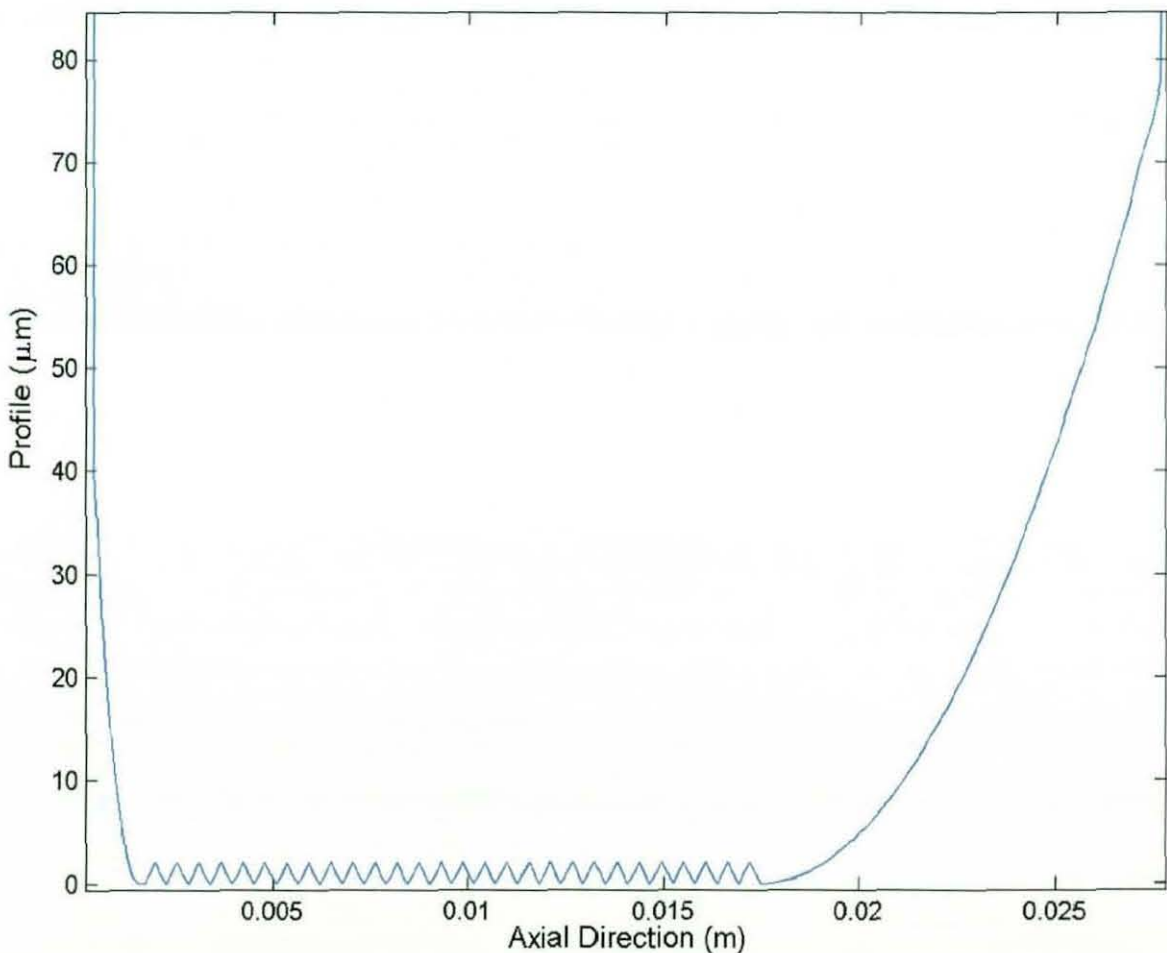
Figure 5.63: Profile of piston with surface features

Figure 5.64 shows the three dimensional pressure distribution for this case. This result is directly comparable with the same condition, but without the introduced surface features, depicted by figure 5.38. Two interesting initial observations can be made. Firstly, the generated pressures are affected by the introduction of these surface grooves. Secondly, the comparison with figure 5.38 shows increased edge pressure magnitudes, reduced central region pressures and a reversal in the disposition of pressure spike magnitudes. In other words the pressure spike at the contact outlet (to the right hand side of the figure) is larger in magnitude than that at the inlet, opposite to the behaviour noted in figure 5.38.
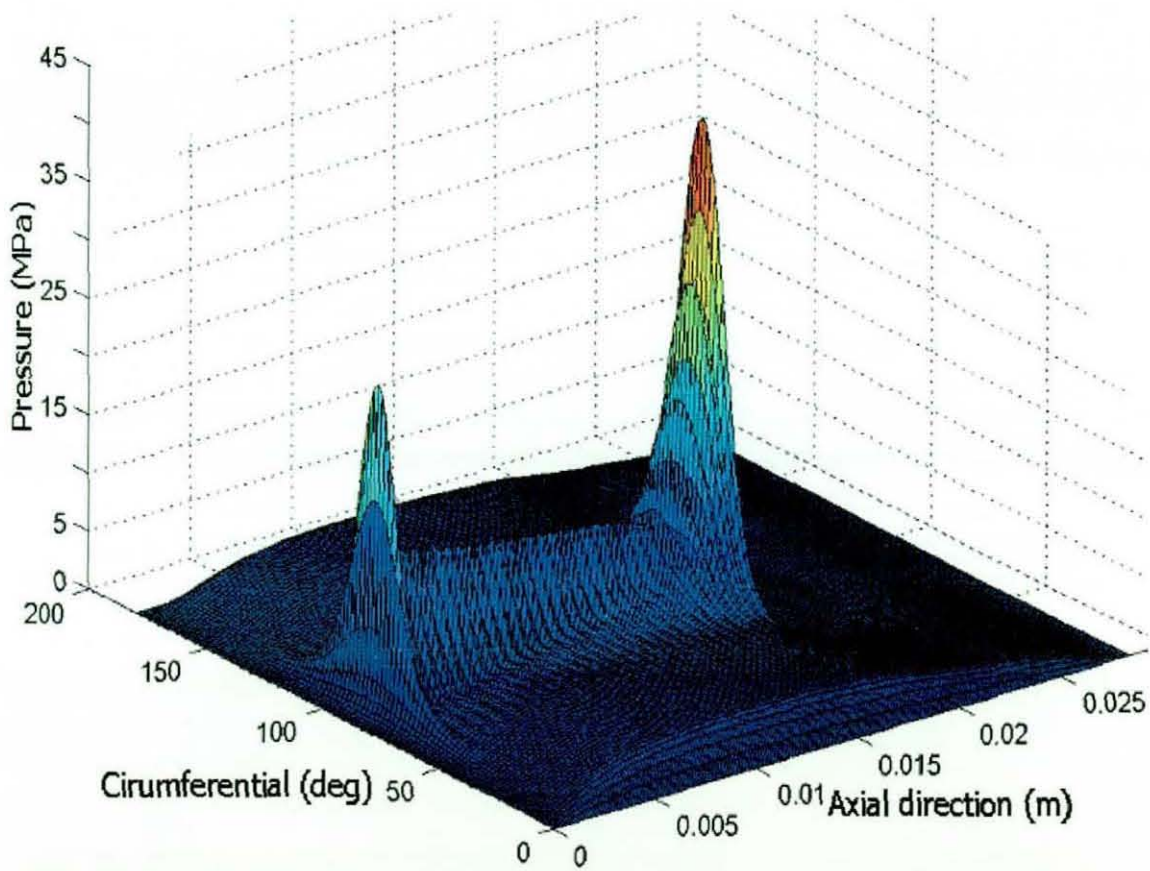
Figure 5.64: 3-Dimensional pressure distribution plot for a piston with surface modification during combustion (entraining direction from left to right along the axial direction)

The pressure undulations observed in the figure, between the inlet and outlet pressure maxima are as the result of edge stress discontinuities, introduced by the sharp groove edges. These can be observed more clearly in figure 5.65, depicting the isobaric pressure

plot. There are numerous is loads of pressure, each introduced by the circumferential grooves. A better picture emerges when the axial pressure distribution is viewed (see figure 5.66). There are numerous pressure pips, interspersed by regions of very low pressure due to a plentiful supply of lubricant trapped in the grooves.
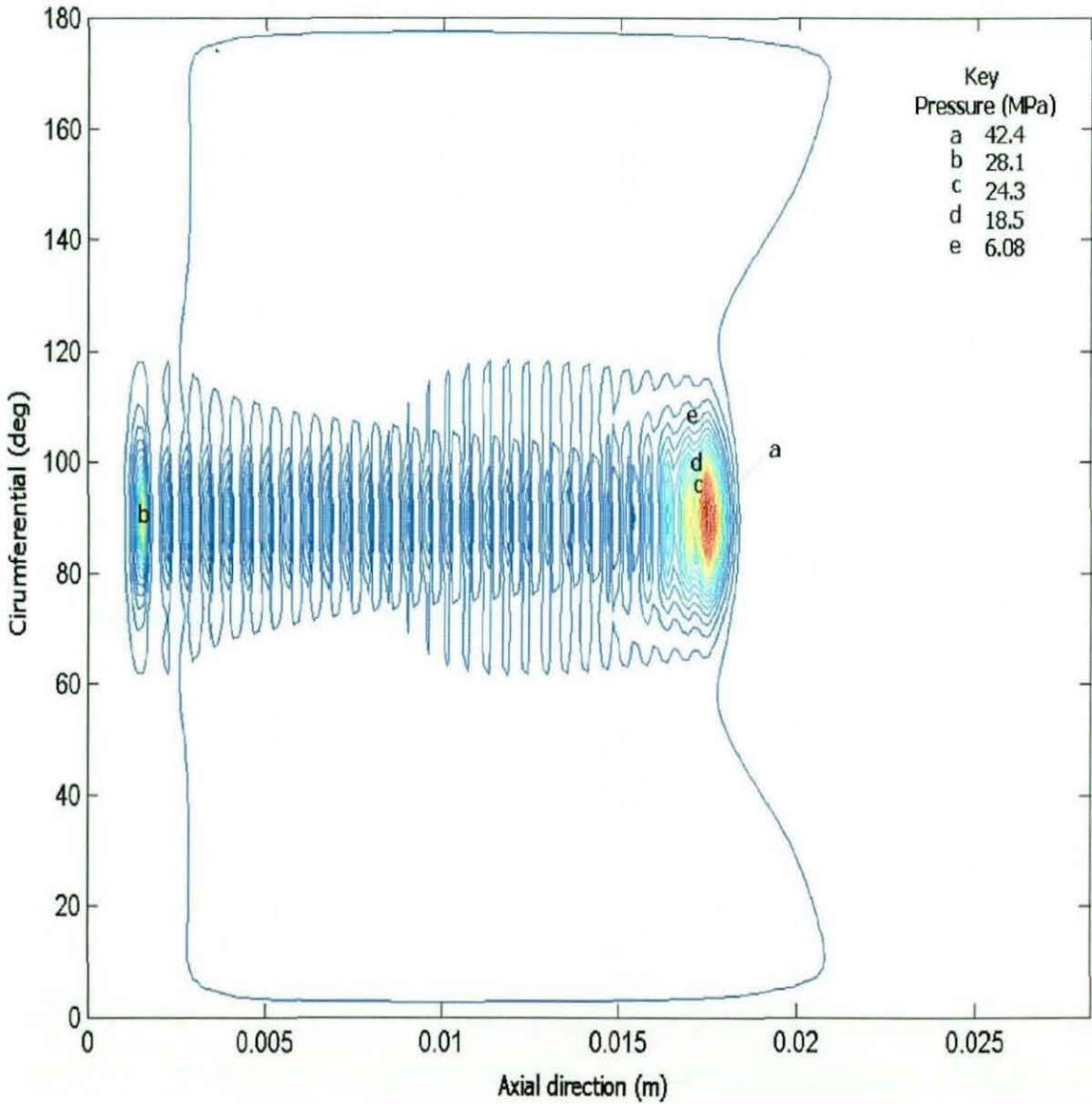
Figure 5.65: Isobaric pressure plot for a piston with surface modification during combustion
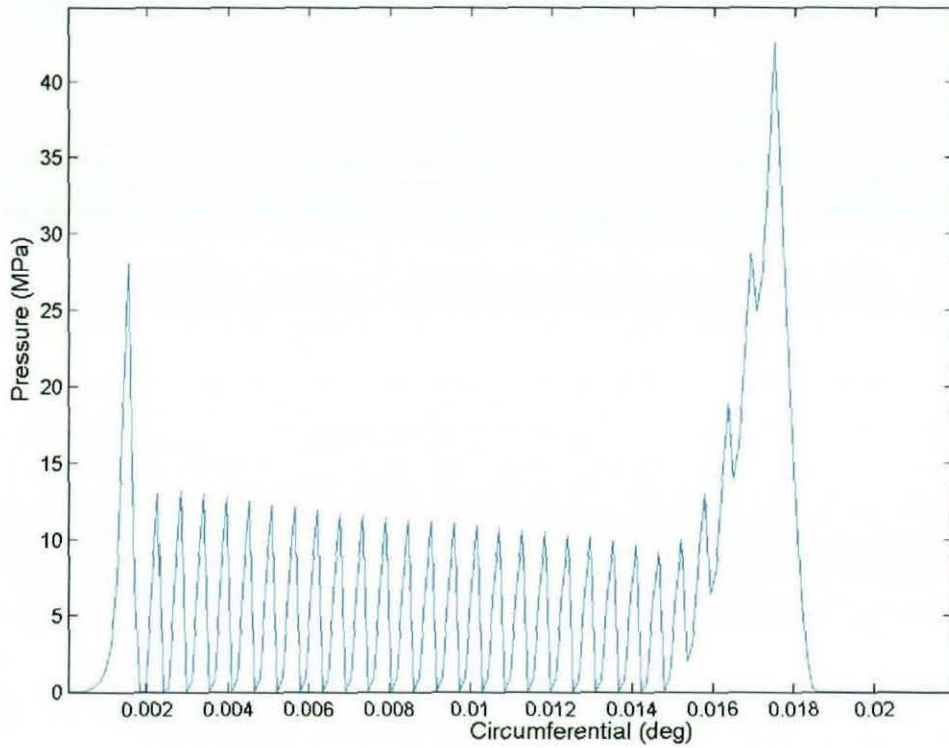
Figure 5.66: Axial plot along the maximum pressure for a piston with surface modification during combustion
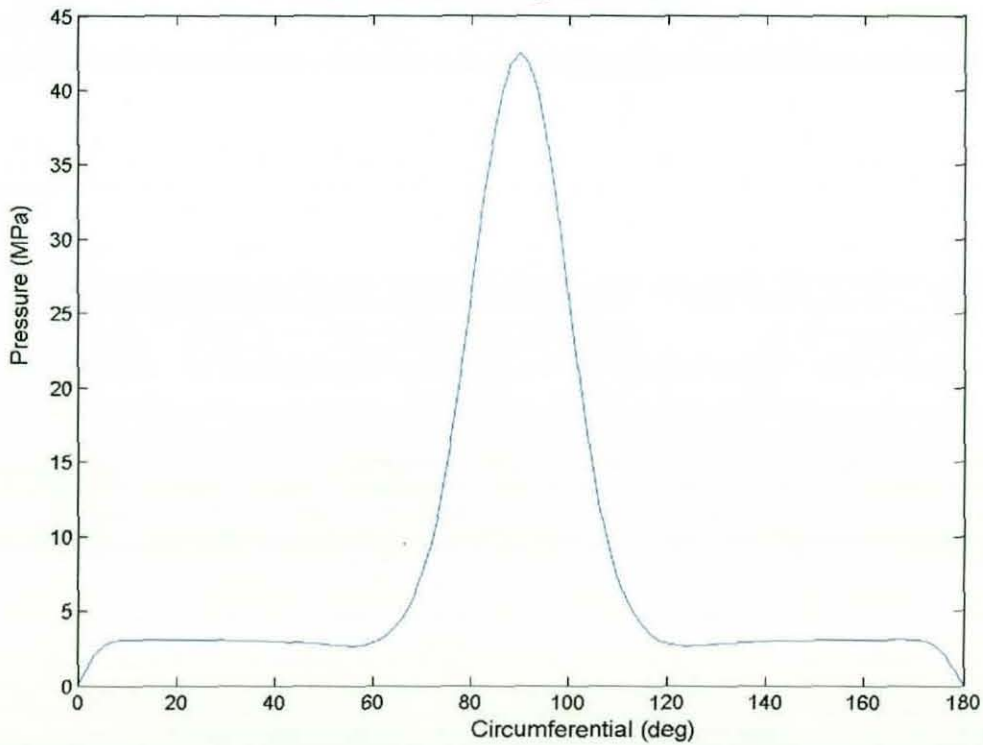
Figure 5.67: Circumferential maximum pressure along the outlet region for a piston with surface modification during combustion
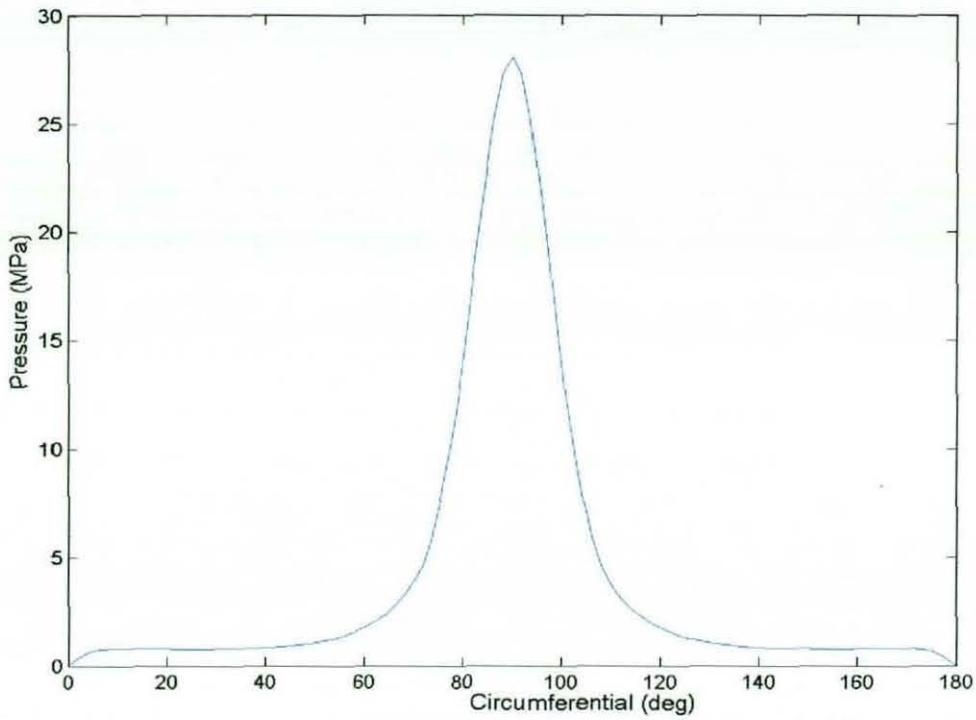
Figure 5.68: Circumferential maximum pressure along the outlet region for a piston with surface modification during combustion
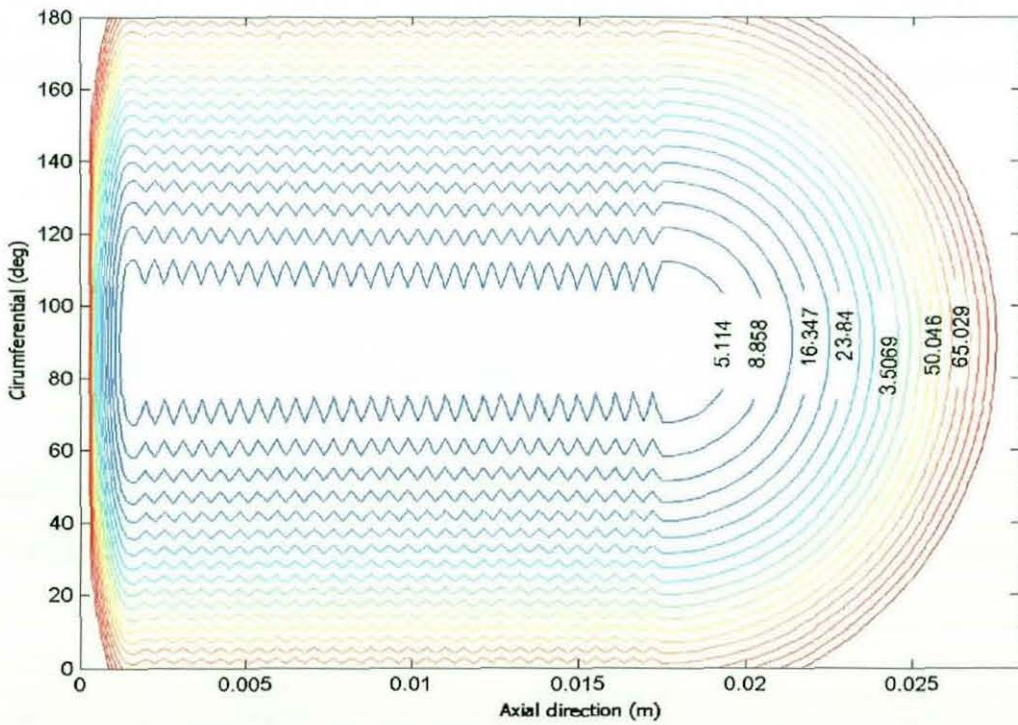
Figure 5.69: Lubricant film contour (μm) plot for a piston with surface modification during combustion

Figure 5.69 shows the lubricant film thickness contour. This is comparable to the isothermal solution without surface features in figure 5.53 and that with thermal distortion of the piston, again without any surface features in figure 5.62. The overall film thickness has increased from around 2 μm to 3-5μm (see figure 5.70), although the absolute minimum film thickness occurs in the vicinity of the maximum pressure and is still of similar value to the previous cases. However, the overall increase in the thickness of the lubricant film would result in a corresponding improvement in fuel efficiency of the vehicle. This has been obscured by trials of pistons with such surface features, and thus the reason for their introduction in F1 engines.
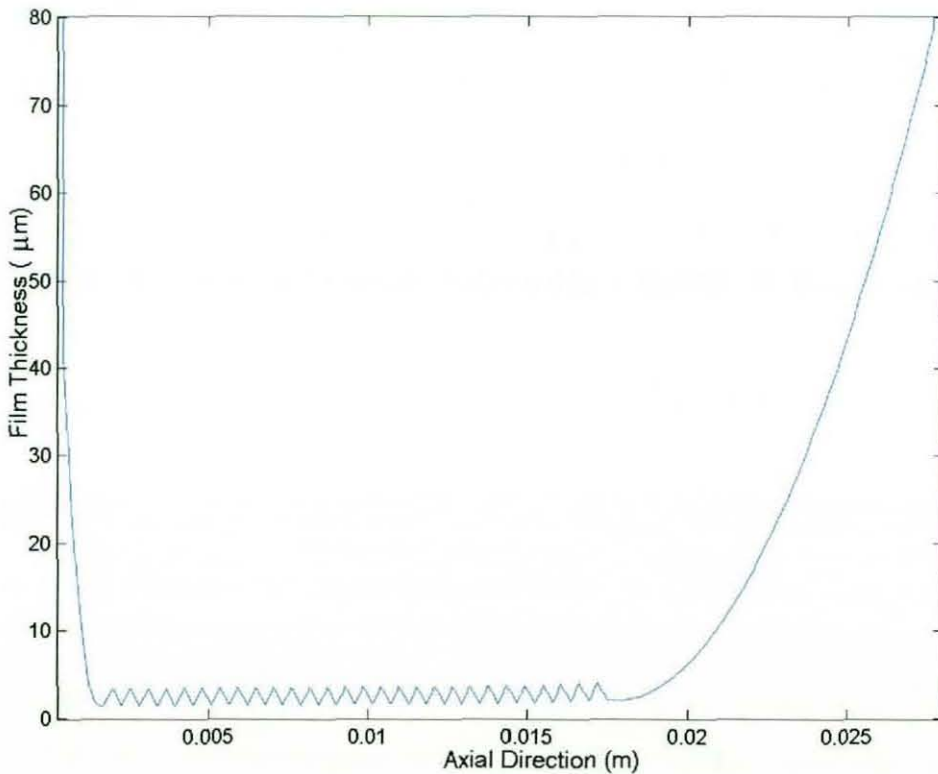
Figure 5.70: Lubricant film thickness along the axial direction for a piston with surface modification during combustion
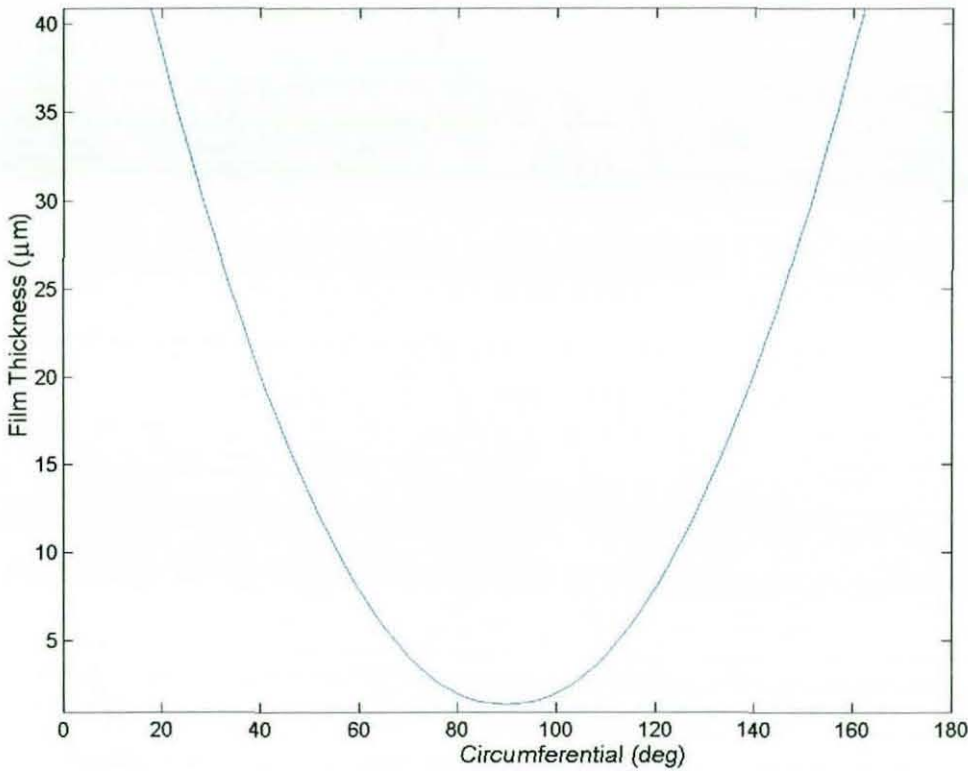
Figure 5.71: Lubricant film thickness along the circumferential direction for a piston with surface modification during combustion

5.7 Closure

The above detailed quasi-static analyses are useful to understand the effect of various parameters: geometric and operating conditions upon the tribodynamic performance of *piston-connecting rod-crank subsystem*. The analyses carried out in this chapter in respect of two such systems and at various locations within the piston cycle, have shed light on a number of key issues. Firstly, higher combustion pressures will result in greater elastic deformation in the contacting region, promoting the formation of more coherent lubricant films. This finding indicates that for better tribological performance one would normally require higher pressures. However, this is not necessarily the case as high pressures, whilst guarding against wear by promotion of an elastic gap between the contiguous bodies, can also lead to sub-surface stresses that can exceed the elastic limits set by

182

maximum shear stresses and cyclic orthogonal reversing shear stresses (see **Johns-Rahnejat** (1988) and **Johns-Rahnejat** and **Gohar** (1997)). Since the generated pressures in such conformal contacts are well below those required to initiate fatigue spalling, increased combustion appears to be an ideal solution in tribological terms. This finding happens to be quite fortuitous, as it coincides with the growing trend for increased combustion power and increasing use of materials of lighter construction, which also coincides with a desire to reduce inertial imbalance by reduction of component weight in the system. However, component flexibility has the drawback of structural vibration and coupled noise propagation, which is not desirable. Therefore, a major pointer from the results obtained in this chapter is that conditions that promote good lubrication conditions and inertial balance do not necessarily lead to a solution for their ideal combined characteristics. It should be noted that the tribological studies embodied here are based upon the determination of elastic deformation of the contiguous solids as a local effect, or in other words, within the contact domain. Such an approach is based upon the classical assumptions of **Hertz** (1896). In reality, the impact dynamics of the system causes propagation of structural waves due to global distortion of the elastic solids, an approach which was promoted by **St Venant** (1868).

The analyses in this chapter cover a large spectrum of tribodynamics of piston assemblies; from mass manufactured diesel engines to high performance *F1* racing cars. Yet all the analyses show that the prevailing regimes of lubrication are iso-viscous rigid or iso-viscous elastic. With relatively low contact pressures, as the result of contact conformity, lubricant piezo-viscous action hardly manifests itself. This problem has already promoted use of magnetic based fluids as additives to increase the polarity of lubricants to adhere to surfaces and promote the formation of a thin surface film, particularly at positions, where relatively low contact loads and diminished lubricant entraining action can lead to mixed regimes of lubrication, for example at TDC and BDC.

Verifications of the results of this chapter are difficult to achieve through experimentation, particularly within the time constraints of a PhD study, which requires in the first instance to develop the numerical predictions as a pre-requisite. Therefore,

section 5.5 has been included, which shows good agreement for special cases of use of the methodology against numerical predictive work of **Gupta** (2002), **Kelly** *et al* (2001) and **Gupta** *et al* (2002). Other verification work have been undertaken with respect to observation of piston skirt performance, as indicated in section 5.5. These corroborate the findings of the reported numerical predictions in this chapter.

Finally, it has been noted on a number of occasions, in this chapter, that more representative tribodynamic analysis necessitates an investigation of the transient behaviour of the system as a whole. This approach is reported in chapter 6.

Chapter 6

6.1 Transient tribodynamics

A transient analysis of piston skirt to cylinder liner is undertaken in this chapter. Such an analysis is more representative of prevailing contact conditions than that reported in chapter 5 by virtue of the fact that the lubricant film thickness at any instant of time depends on its historical values. In other words, the film thickness formed in the contact of contiguous bodies has a continuous behaviour which is carried forward from one step of analysis to the next. Such an analysis necessitates the evaluation of inertial forces and their induced moments that determine the contact loads carried by the load bearing surfaces. In a quasi-static analysis the effect of these inertial contributions are not taken into account. **Jalali-Vahid** *et al* (2000) have shown that owing to the aforementioned differences the lubricant film thickness has a higher value, with increased contact forces under transient conditions. They have indicated that under-estimation of contact pressures and film thickness under quasi-static analysis can lead to erroneous predictions with respect to fatigue spalling life of bearing surfaces and early prediction of wear.

In chapter 3, a transient analysis is reported, but for the case of dry elastic contact of contiguous bodies. The problem with that analysis is that impact loads are not resisted by the presence of a lubricant film, resulting in high frequency repetitive impacts. Therefore, in this chapter, a transient lubricated analysis is reported. The methodology employed is highlighted in chapter 4. It includes simultaneous solution of inertial rigid body dynamics, the transient form of the Reynolds' equation and the elastic film shape.

6.2 Transient tribodynamics of piston skirt to cylinder liner contact

The transient analysis is carried out with respect to the same 1.8L diesel engine as that reported in chapters 3 and 5. The operating conditions are given in section 3.3.4. A

computational grid of 180 nodes in the direction of entraining motion and 80 nodes in the circumferential direction was employed. A cycle time of piston translational motion at the engine speed of 3700 rpm is 0.0162 s. 934 time steps of simulations were carried out at a fixed integration time of 1.74 µs. The number of space-time computational nodes is 13435200, disregarding the number of iterative cycles for spatial domain pressure convergence and time domain tilt and lateral motions' convergence. It should also be noted that simultaneous solution is undertaken for both piston to cylinder contacts on the major and minor thrust sides with the same computational space time mesh density (i.e. the mesh density is twice the aforementioned value). The total CPU time for a cycle of piston motion was 150 hours on a Pentium IV 1.8GHz workstation with a RAM size of 512 MB. When compared to other transient analyses reported in chapter 2 and later on this chapter, the current analysis embodies no significant assumption and is considerably more detailed. The main assumptions are concerned with perfectly smooth surfaces of contiguous bodies and the isothermal nature of the analysis. The former assumptions have been dealt with in some detail in chapter 5. The same chapter also includes, to some, extent the effect of thermal distortion, although a full thermohydrodynamic analysis has not been undertaken, the justification for which is explained in the previous chapter. Another assumption made concerns the existence of a clearance fit between the piston and the cylinder bore, which is applicable to start-up conditions and not usually observed in hot-running pistons, where instances of interference may be encountered. The isothermal conditions with larger clearances, in fact, represent worst experienced contact conditions due to generation of higher impact forces with increased lateral and tilting inertial effects. These lead to exacerbated conditions, since it has been shown that contact deformation is larger in lubricated contacts than that under dry impacting conditions (see **Dowson** and **Wang** (1994), **Larsson** and **Högland** (1995) and **Al-Samieh** and **Rahnejat** (2002)). Although the contribution due to film thickness due to elastic deformation has been found to be less than 20% of the film during the piston cycle and that only at high combustion pressures, nevertheless, the prevalent conditions in many instances is iso-viscous elastic. Therefore, a hydrodynamic solution for piston to cylinder liner is inappropriate, although the same has been undertaken by some authors such as Li et al (1982)). Some authors have assumed similar iso-viscous elastic conditions obtained in

this thesis to be elastohydrodynamic by the virtue of small increase in the viscosity of the lubricant. Although, this is, by definition true for $\alpha p_0 > 1$, the viscous effect can be considered almost negligible at such low pressures. This means that the effect of viscosity variation may be ignored in future solutions similar conditions to those in this thesis are encountered.

6.3 Results and Discussion

Under the simulated conditions, the piston's translational displacement and velocity are shown in figures 6.1 and 6.2 respectively. This figure shows momentary cessation of piston motion at the extremes of its travel (i.e. at TDC and BDC). The maximum piston's translational velocity is at its mid cycle, which provides the highest rate of lubricant entrainment into the contact. At TDC and BDC, the lubricant film is retained by a combination of squeeze film action and rapid commencement of entraining motion.
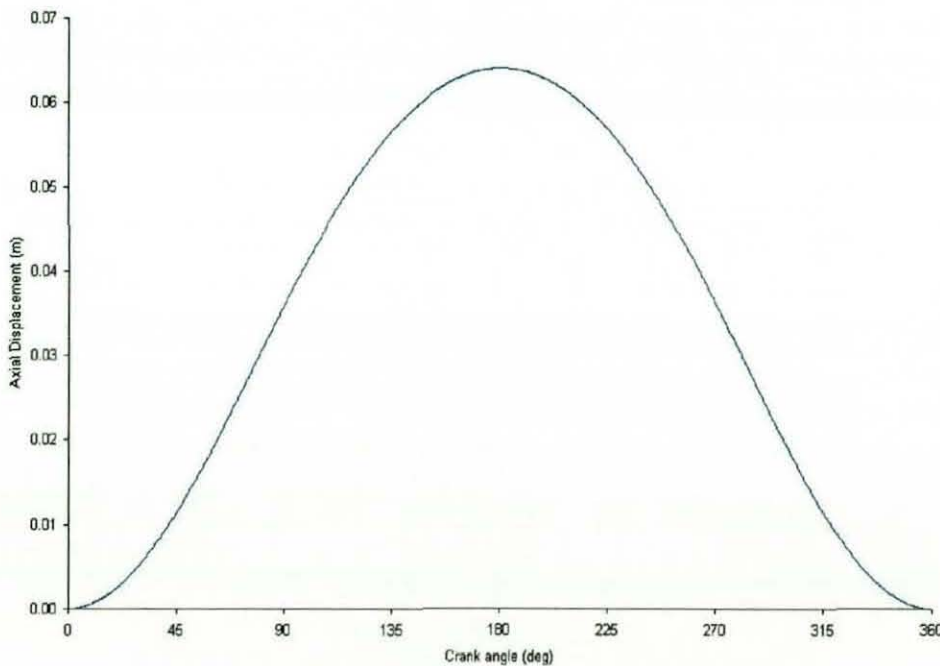
Figure 6.1: Translational displacement of piston

187
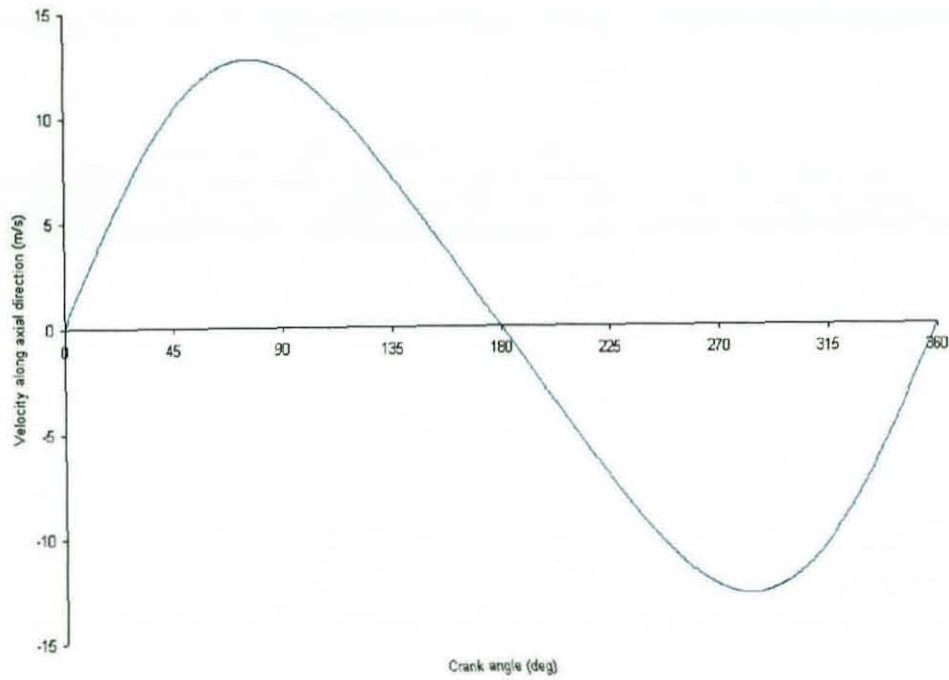
Figure 6.2: Translational velocity of piston
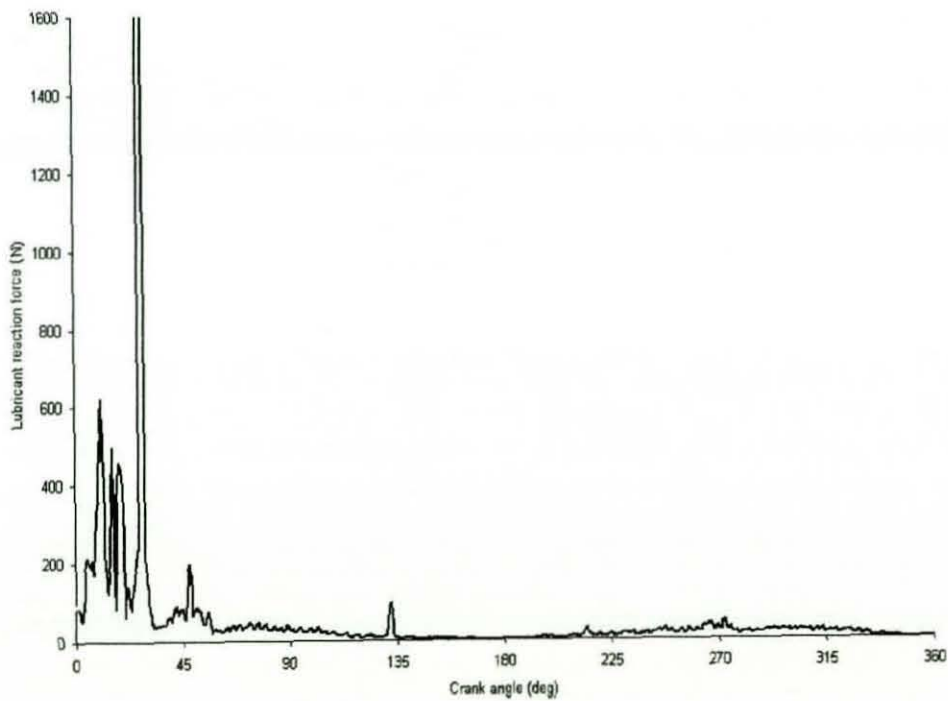
Figure 6.3: Lubricant reaction force on the major thrust side

188
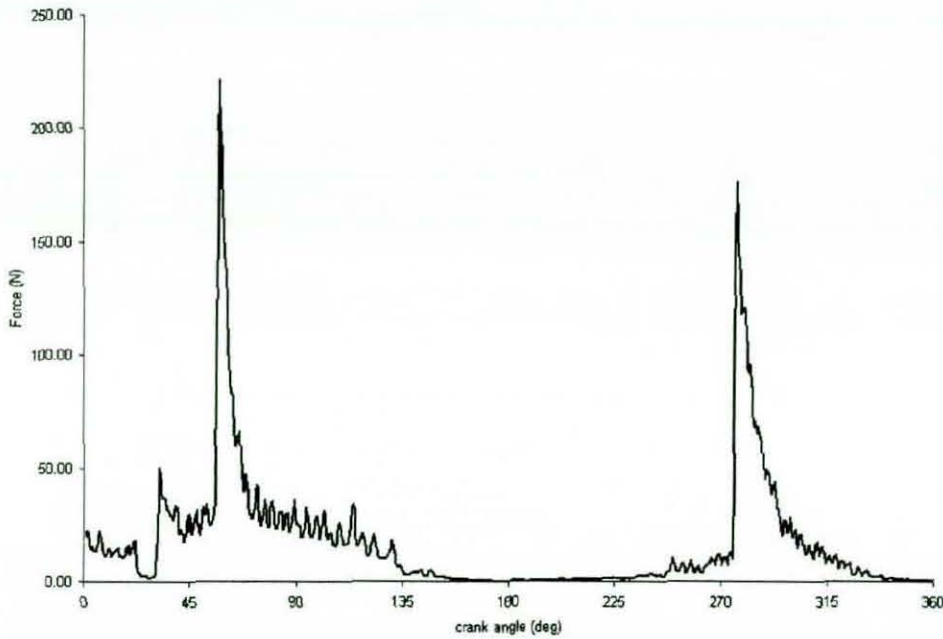
Figure 6.4: Lubricant reaction force on the minor thrust side

The other contributory factor in the formation of lubricant film is the contact load, induced by the inertial dynamics of the piston in combined lateral and tilting motion, caused by direct and moment loading of the contacting regions due to offset location of the gudgeon pin (refer to chapter 3). Figures 6.3 and 6.4 show the contact force variation on the major and minor thrust sides respectively. Due to the eccentric location of the gudgeon pin, the impact force on the major thrust side is considerably higher than the corresponding values on the minor thrust side. This is because the offset position of the gudgeon pin creates a larger clearance on the major thrust side, thus the impact velocity is greater there. This is analogous to a ball falling upon an oily plate falling from a greater height, resulting in a larger impact force. It can be observed that, on the major thrust side, the contact force attains its maximum value at the combustion maximum pressure with a value tending to 2KN. On the minor thrust side and at the same position, the load bearing surfaces encounter an almost insignificant force (see figure 6.1 at 13°). As the contact force dramatically decreases on the major thrust side, the corresponding value on the minor thrust side begins to increase, culminating in a maximum value of 225N at around the crank angle of 60 deg, which is nearly 1/3 of piston travel down stroke. A clearer picture emerges when piston lateral and tilting motions are observed (see figures 6.5 and

6.6 respectively). Figure 6.5 shows that at the top dead centre a lateral displacement of 20 µm has taken place with an almost aligned piston (see figure 6.6 for the crank angle of 0 deg). As the piston traverses downwards, the lateral displacement increases dramatically with increased pressure towards the major thrust side, culminating in a lateral displacement of approximately 37 µm (see fig 6.5), with a corresponding tilt of 0.07 deg towards the major thrust side. These motions are responsible for the high impact force of 2kN described above. After the combustion, the piston tilting motion reverses, as shown in figure 6.6 in concert with rapid emergence of clearance on the major thrust side (i.e. a reduction in lateral displacement with respect to the major thrust side). The piston continues in this vain, where the combination of lateral approach towards the minor thrust side and reversal of tilting motion away from the major thrust side leads to the diminution of gap on the minor thrust side, thus the reason for the emergence of high impact forces on the minor thrust side, as described above. From mid-cycle at 90° crank angle, the lateral motion reverses to one approaching the minor thrust side. This is indicated in figure 6.5 by the negative values of the lateral displacement.
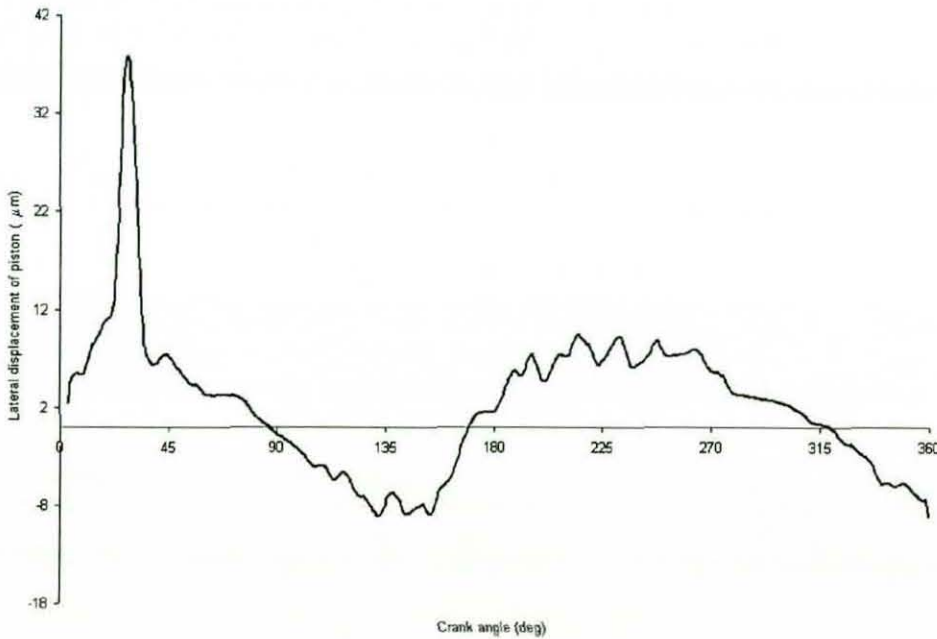
Figure 6.5: Lateral displacement of piston from the centre line
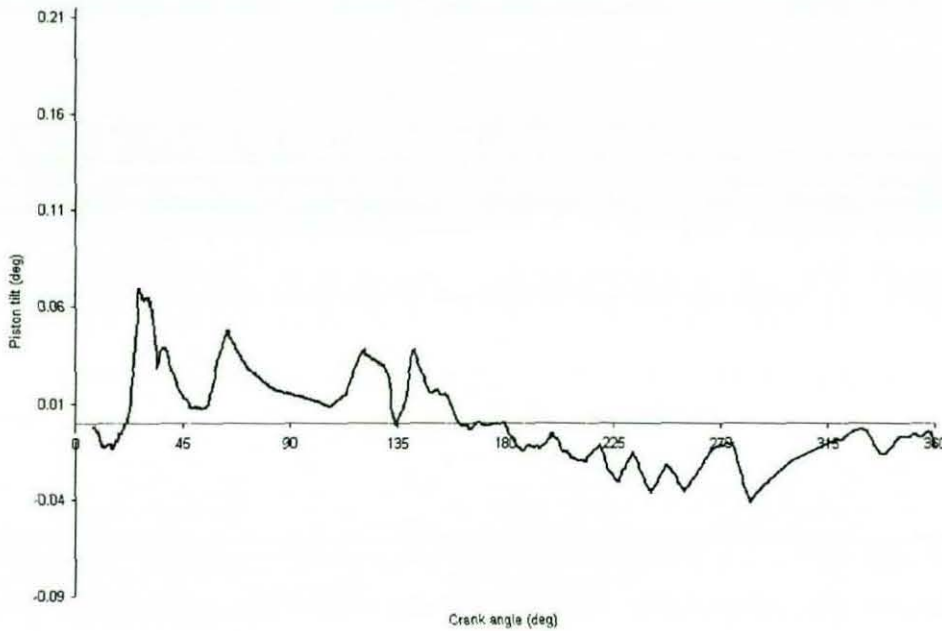
Figure 6.6: Piston tilt about the gudgeon pim

At the same time, the tilt angle is generally reducing, until a totally aligned configuration is observed at the BDC, as is expected. This is shown in figure 6.6, where the few undulations in the tilt angle is due to increased lubricant reactions due to the approach of the piston towards the liner on the minor thrust side. On the upstroke of the piston from BDC (i.e. for crank angle greater than 180°) the piston aligns itself to the minor thrust side with small tilt angles due to low combustion pressures. The inertial dynamics of the system displaces the piston laterally; motion towards the major thrust side (see figure 6.5). At 360 deg the power stroke cycle is complete. The tilt angle and the corresponding lateral displacement values at 0 and 360 degrees should ideally be the same, if the transient analysis is to yield a repeatable cycle. Although this is nearly the case for piston tilt in figure 6.6, it is clear that a number of such cycles should be included in the transient analysis. However, due to the computational time and memory constraint, it is clear that such an undertaking is impractical and that a clear picture of transient contact behaviour has already emerged with this initial analysis. Any further extension of the current analysis can only lead to refinement of the results in a quantitave sense, but not in a fundamental understanding of the physical phenomena.

191

Of particular importance in such a transient analysis as the one reported here, is the estimation of the lubricant film thickness and the corresponding pressures during the piston cycle. Investigation of film thickness can be carried out in two ways. First, the minimum film thickness under transient conditions can be obtained. Second, the lubricant film shape and the extent of the contact can be studied at specific location, since storage of lubricant film contour at all locations would require very large computing storage capacity and in any case would not be of interest in parts of the cycle, where sufficient lubricant entrainment yields a coherent and thick lubricant film.

Figure 6.7 shows the transient minimum film thickness variation. The film thickness at the TDC is approximately 50 μm.
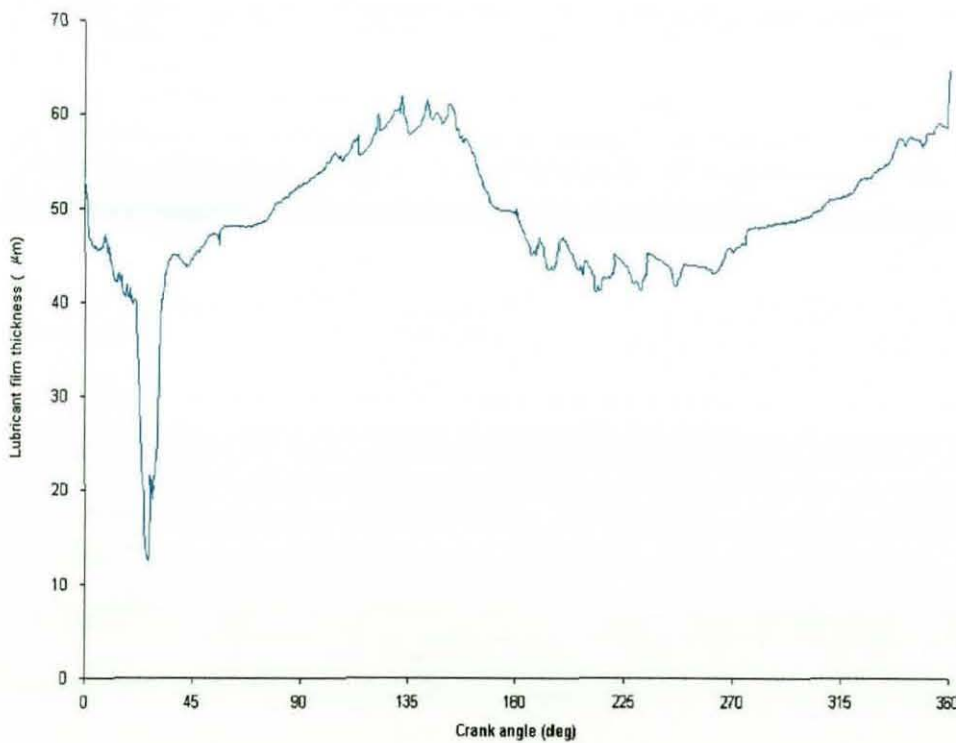
Figure 6.7: Lubricant film thickness at the majot thrust
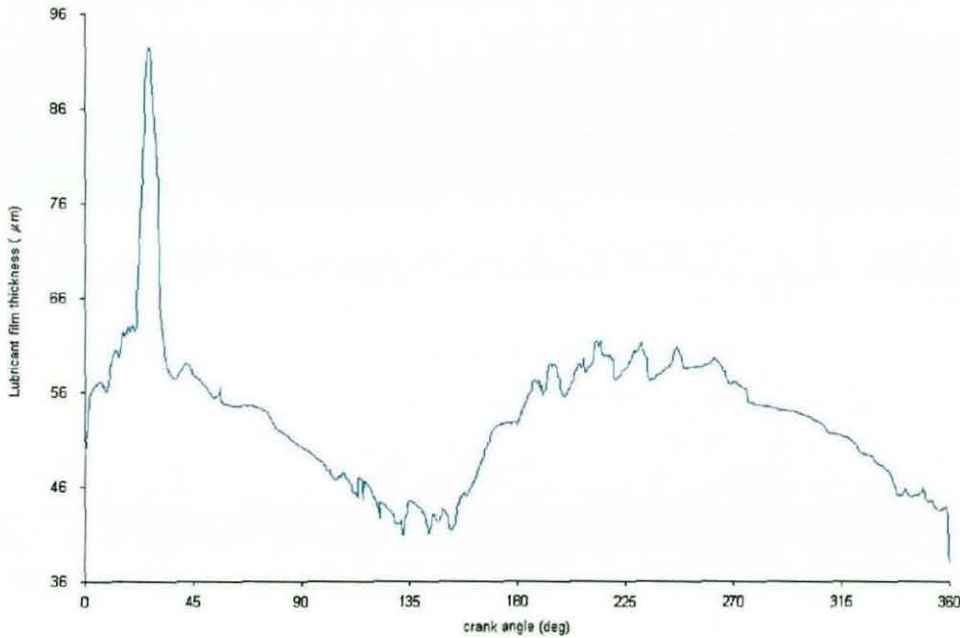
Figure 6.8: Lubricant film thickness at the minor thrust

As the piston tilts and undertakes lateral motion towards the major thrust side, the rigid body motion diminishes the gap and the lubricant film reduces dramatically to a value of nearly 13 µm. Although the impact force reaches a value of 2kN (as previously shown), the corresponding elastic deformation is quite small due to the large area of conformal contact. Therefore, main contributory factor for the retention of a lubricant film is the wedge action due to entraining motion. This is confirmed by a subsequent rise in the film thickness after combustion, when the speed of entraining motion increases, the contact load decreases and the lateral displacement takes place away from the major thrust side. The rise and fall of lubricant film thickness almost reciprocally with variation of contact load is indicative of hydrodynamic regime of lubrication. If elastohydrodynamic conditions were encountered, the lubricant film behaviour would have been insensitive to load variation. In fact, as already shown in chapter 5, the prevailing regime of lubrication is either iso-viscous rigid or just isoviscous elastic. The remaining parts of the cycle show minimum film thickness variation is in line with rigid body motions (lateral and tilting motions) as described in figures 6.5 and 6.6. Figure 6.8 shows the minimum film thickness variation on the minor thrust side. Owing to the dominance of the rigid body

193

motions, the minimum oil film thickness history shows an almost reverse characteristics to that in figure 6.7. Figures 6.9 and 6.10 show the corresponding maximum pressure time history on the major and minor thrust sides respectively. Clearly in-line with hydrodynamic behaviour, wherever maximum pressure is encountered during the cycle, minimum film thickness exhibits its least values. The maximum pressure on the major thrust side is much greater that that in the minor thrust side, reaching a value of approximately 2MPa at maximum combustion (at 13 deg crank angle). The maximum pressure on the minor thrust side reaches a value of 0.12 MPa, which is quite insignificant given the extent of contact conformity. In figure 6.10, the many pressure reversals are due to many repetitive approach and separations, and are not due to computational inaccuracies, although the latter may have some contribution. Referring back to figure 6.7, the film thickness at TDC is 52 μm at the beginning of simulation (during down stroke) and 57 μm at the cessation of upstroke. This anomaly is due to the aforementioned nature of the single-cycle analysis, but can be observed not to be very significant.
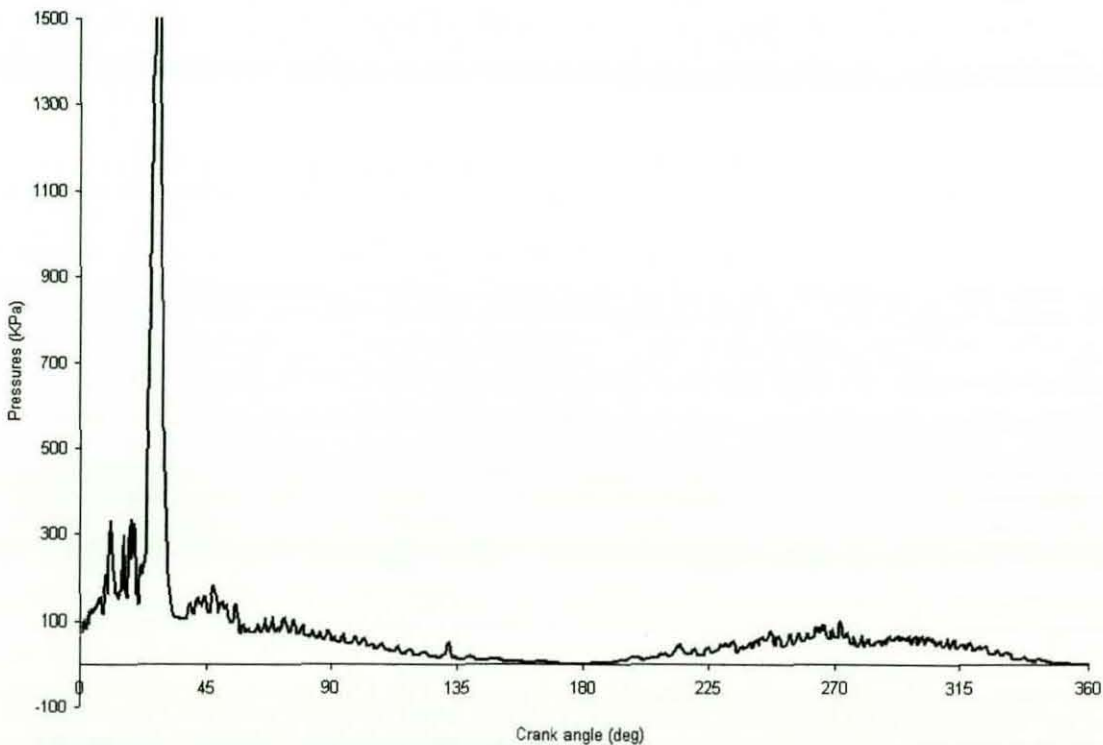
Figure 6.9: Maximum pressure distribution on the major thrust side
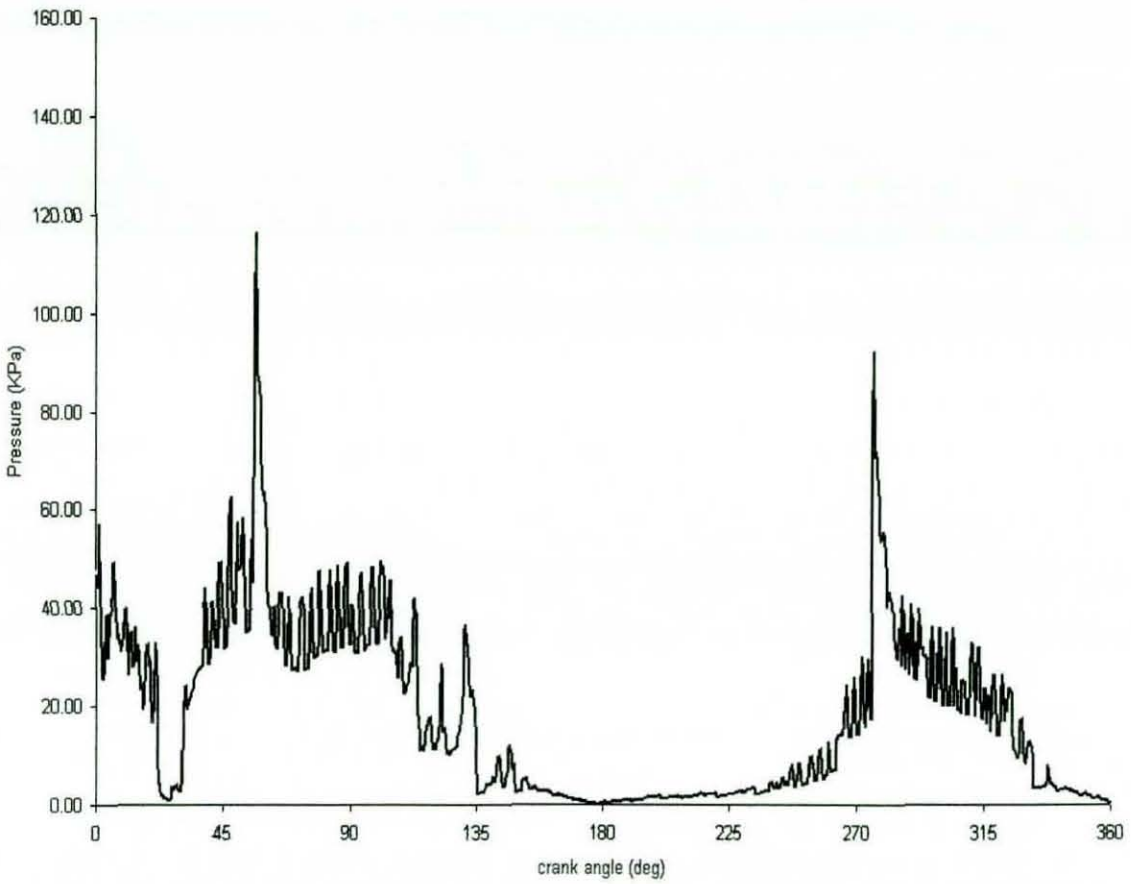
Figure 6.10: Maximum pressure distribution on the major thrust side

To encapsulate the tribodynamic behaviour of the lubricant film, the locus of the position of the minimum film thickness can be obtained using a radar plot. Such a plot, as its name suggests, traces the position of the minimum lubricant film thickness as the piston undertakes its combined primary and secondary motions. A radar plot is essentially a polar plot, in which, the radius of the plot is divided into a number of concentric circles, the perimeter of each of which represent a spatial nodal position (see figure 6.11). In figure 6.11, the total radius represents the 80 nodes used in the circumferential direction. The locus of the minimum film thickness appears, during the entire cycle, on the radius representing the mid computational nodal point, in this case node number 40. The circular locus of the minimum film thickness indicates that for all combinations of rigid body motions, the minimum film thickness remains at the centre of the contact with the major thrust side.
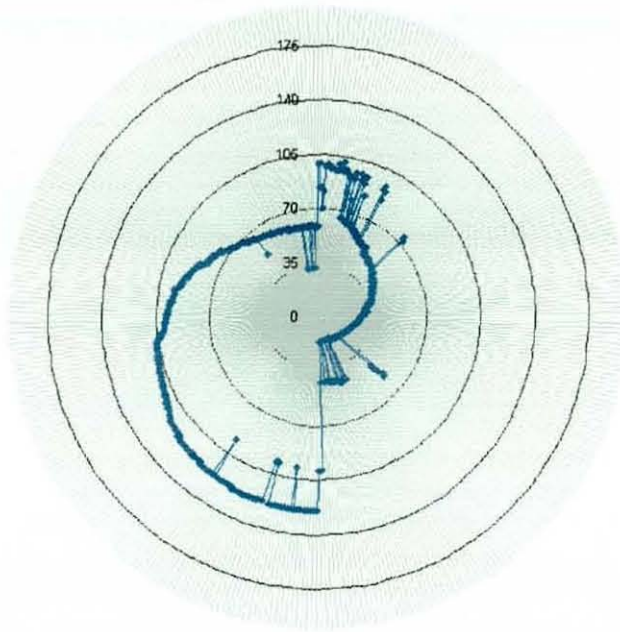
Figure 6.11: Radar plot indicating variation of minimum film along entraining direction at the major thrust side
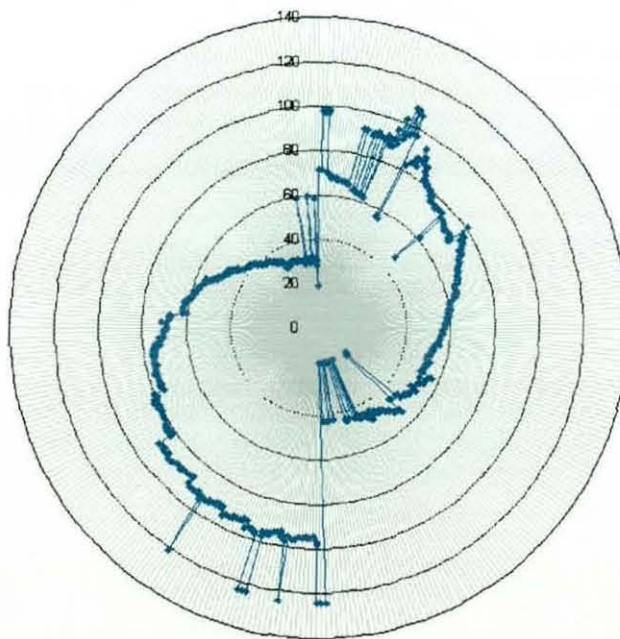
Figure 6.12: Radar plot indicating variation of minimum film along entraining direction at the minor thrust side

This is as expected, since in rigid body approach or separation of two concentric cylinders with insignificant deformation, the shortest distance between them always

remains along their centre-lines. If significant deformation had taken place, the circularity of the locus would have been breached, such as the minimum film thickness dip at the exit of a flattened region in the concentrated counterformal contact, for example, of a ball to race contact. Therefore, figure 6.11 is an affirmation of the above stated prevailing hydrodynamic conditions. Figure 6.12 is a similar radar plot in the axial entraining direction. A much more complex locus is observed in this case. The deviation from circularity is due to combined lateral and tilting motion, as well as the upstroke and down-stroke sense of the piston. 180 spatial nodes are represented as the radius of the radar plot. 934 radii represent the time transient condition. The radial disposition of the minimum film thickness from the centre of the plot indicates the extent of lateral motion of the piston towards or away from the major thrust side. The top right-hand side of the figure indicates the position of TDC, whilst the bottom of the figure represents BDC. The minimum film locus right of the vertical diagonal corresponds to the down-stroke action of the piston, whilst the region on the left-hand side of the same diagonal refers to the upstroke sense of the piston. The locus of the minimum film is in a clockwise sense in this radar plot. It follows a 'kidney–like shape, which indicates adherence to the major thrust side from TDC to mid-cycle, followed by lateral motion to BDC and adherence to the minor thrust side in the upstroke sense. Any deviations, indicated on the plot by points away from the prescribed path are due to tilting motion of the piston. The instances that such action is prevalent are in the region of maximum combustion and as the piston reverses; its tilting motion.

Figure 6.13 shows the lubricant oil film contour at the TDC. The piston tilt angle has a value of -0.005^0 (the negative tilt angle represents rotation away from the from the major thrust side). This is shown in figure 6.6. The contact load is obtained as approximated 80N see figure 6.3. These values are different to those estimated by the multi-body analysis in chapter 3 and used in the quasi-static analysis of lubricated contact in section 5.3.
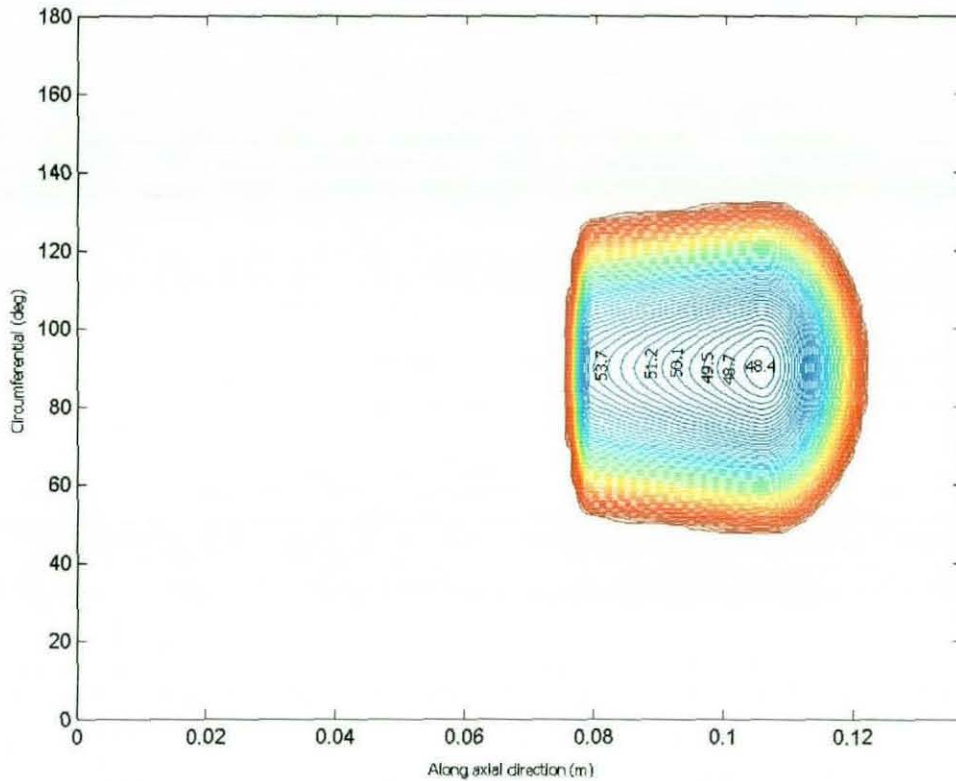
Figure 6.13: Oil film contour during reversal at TDC along major thrust side

The reason for the difference is that the contact model in the multi-body analysis is based on a dry elastostatic model, using **Petrenko's** (1916) analytic approximation, which is incidentally more applicable to counterformal contact configurations. The analysis in this chapter is based on fully transient conditions, thus, the input conditions for the estimation of the film thickness and pressure distribution are more representative. Figure 6.13 is, therefore, only qualitatively comparable to the equivalent quasi-static predictions, illustrated in figure 5.6. The extent of the contact is reduced under transient conditions, particularly in the circumferential direction, owing to a greater misaligned condition. The minimum film, however, has increased by more than 4 folds in value, because of the greater gap predicted in the transient analysis than that obtained by the assumed static equilibrium in chapter 5. The increase in the film thickness is not due to enhanced contact deformation and fluid film retention under transient conditions, reported by Jalali-**Vahid** (2000). Furthermore, under transient conditions, there is squeeze film action due

198

to the existence of historical film thickness data, which is not the case in quasi-static analysis. It is now generally accepted that squeeze film motion enhances the load carrying capacity of the contact, yielding a higher film thickness. This has been shown by other authors, including **Al-Samieh** (2002), **Jalali-Vahid** (2000) and **Kushwaha** (2000). The squeeze film motion plays a significant role in the absence of entraining motion, for example, at TDC here. The fact that the contact load has increased from 46 N under elasto-static analysis to 80 N under transient condition with squeeze effect is itself a corroboration of increased load carrying capacity.
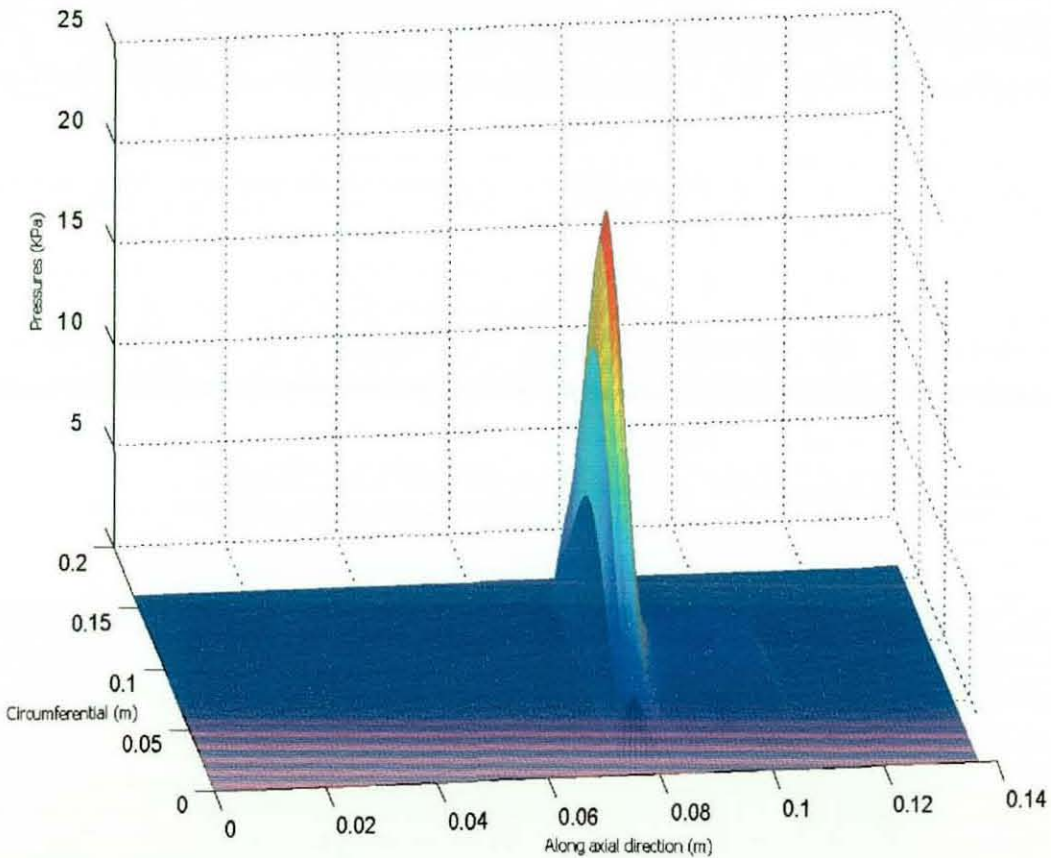
Figure 6.14: 3D Pressure distribution during reversal at TDC along major thrust side (entraining direction is from left to right along axial direction)

The lubricant film is trapped between approaching surfaces, because its slow viscous motion (almost non-existence at TDC) is not sufficient to allow it to escape from the

closing   gap   between   the   approaching   bodies.
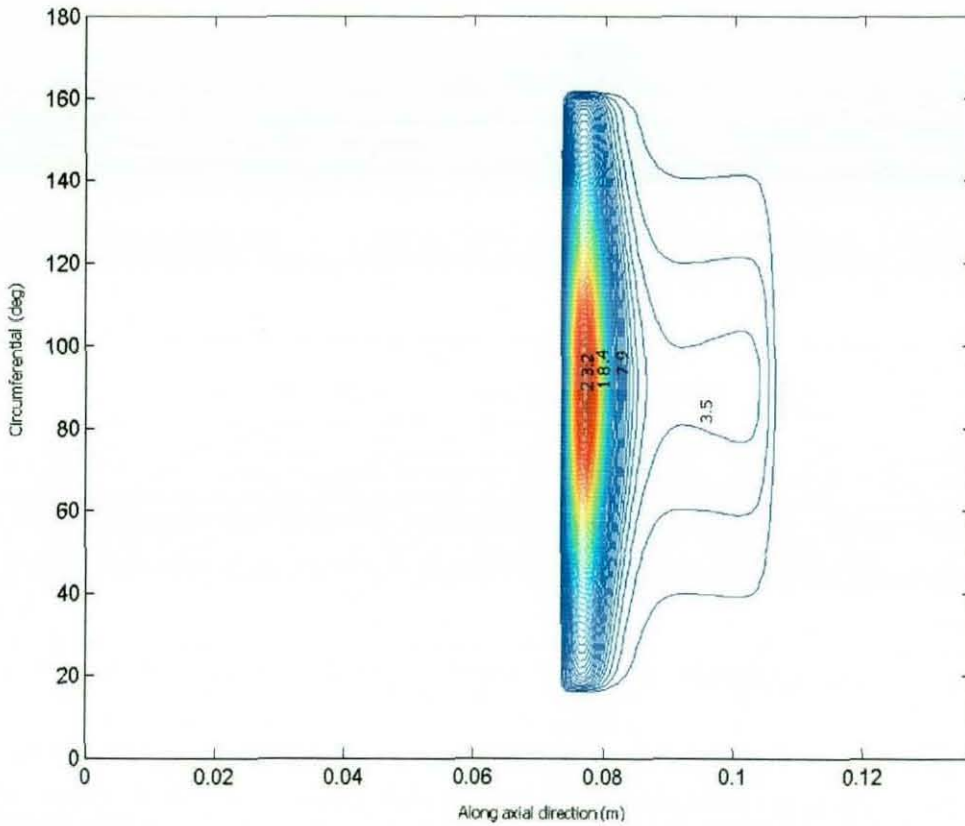
Figure 6.15: 3D Pressure distribution during reversal at TDC along major thrust side

Due to increased hydrodynamic lubricant film thickness, when compared with the quasi-static analysis in chapter 5, the pressure distribution exhibits lower pressures, the maximum being 23.2 KPa, as opposed to 33.6 KPa in chapter 5 (see the 3D pressure distribution in figure 6.14 and the isobaric pressure in 6.15).

Figure 6.16 shows the 3D pressure distribution at the position of maximum combustion pressure. The distribution is very similar to that obtained under quasi-static analysis. The contact load and the misalignment of the piston are of the same order to those predicted in the quasi-static analysis (tilt angle of 0.15 as opposed to 0.11 in chapter 5, contact load of 2 KN as opposed to 1.7 KN). However, the effect of squeeze film action is only considered in the current transient analysis, this being the major difference that has led to the increase of contact pressures from a maximum value of 0.7 MPa in the quasi-static analysis to 1.7 MPa here. Furthermore, due to a greater tilt angle, the contact load

200

intensity has been enhanced, with a reduced pressure generating region in the case of transient analysis, this being the reason for the corresponding increase in the magnitude of generated pressures. Figure 6.17 corroborates these findings in an isobaric pressure plot. Figure 6.18 illustrates the corresponding oil film contour, with the minimum film thickness of 10.6 am. the film thickness under quasi-static analysis was predicted to be 23.6 µm (see fig. 5.17). The increased pressure magnitudes under transient conditions and due to combined entraining and squeeze film action is in-line with the findings of other workers for example **Jalali-Vahid** *et al* (2001) and **Wijnant** and **Venner** (1997). The increased pressures contribute to an increased lubricant film thickness in most highly loaded contacts, as described by **Jalali-Vahid** *et al* (2001), **Jalali** (2001) and **Wijnant** and **Venner** (1997) due to elastic squeeze film action.
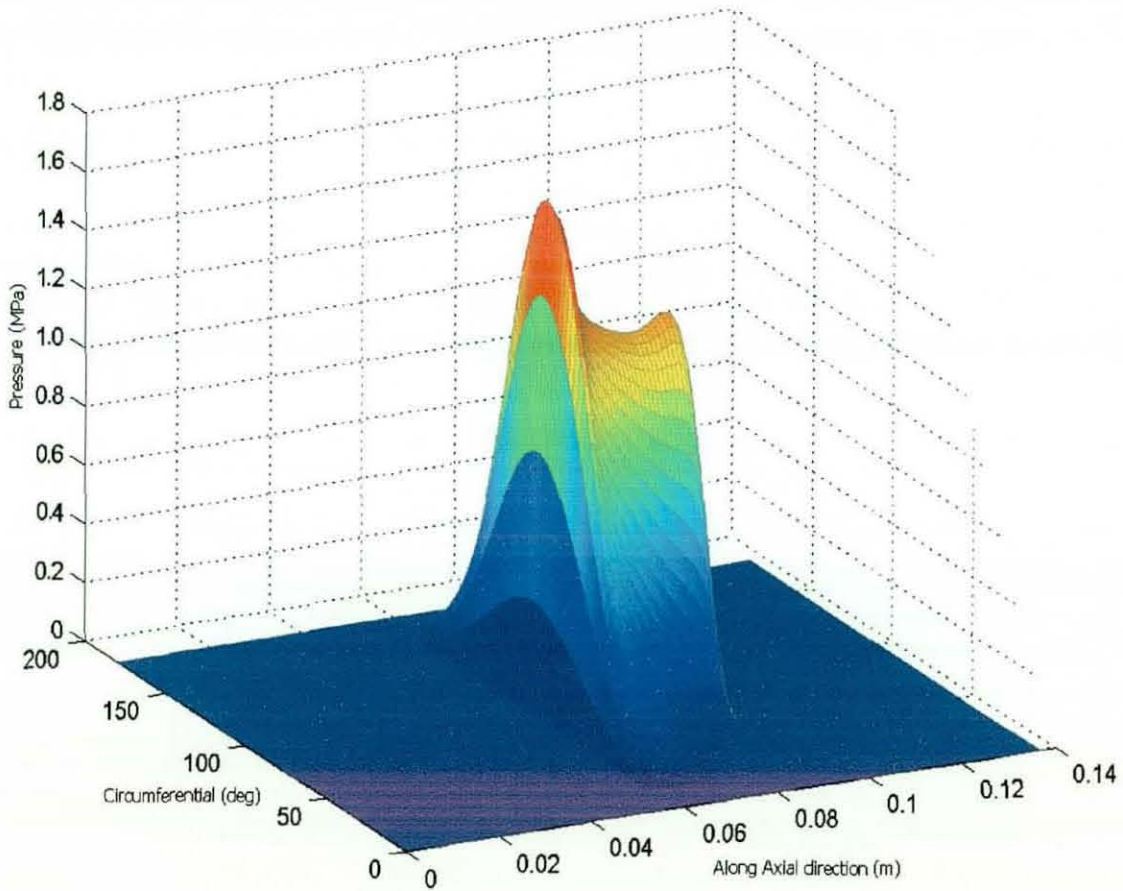
Figure 6.16: 3D pressure distribution at the position of maximum combustion pressure along major thrust side

However, in the case of the reported piston skirt to cylinder liner contact due to the close conformity of the contact and the size of the contact, the increased pressures from their quasi-static levels contribute little to the elastic deformation of contiguous solids. Therefore, the minimum film thickness in fact decreases due to the dominant rigid body action.
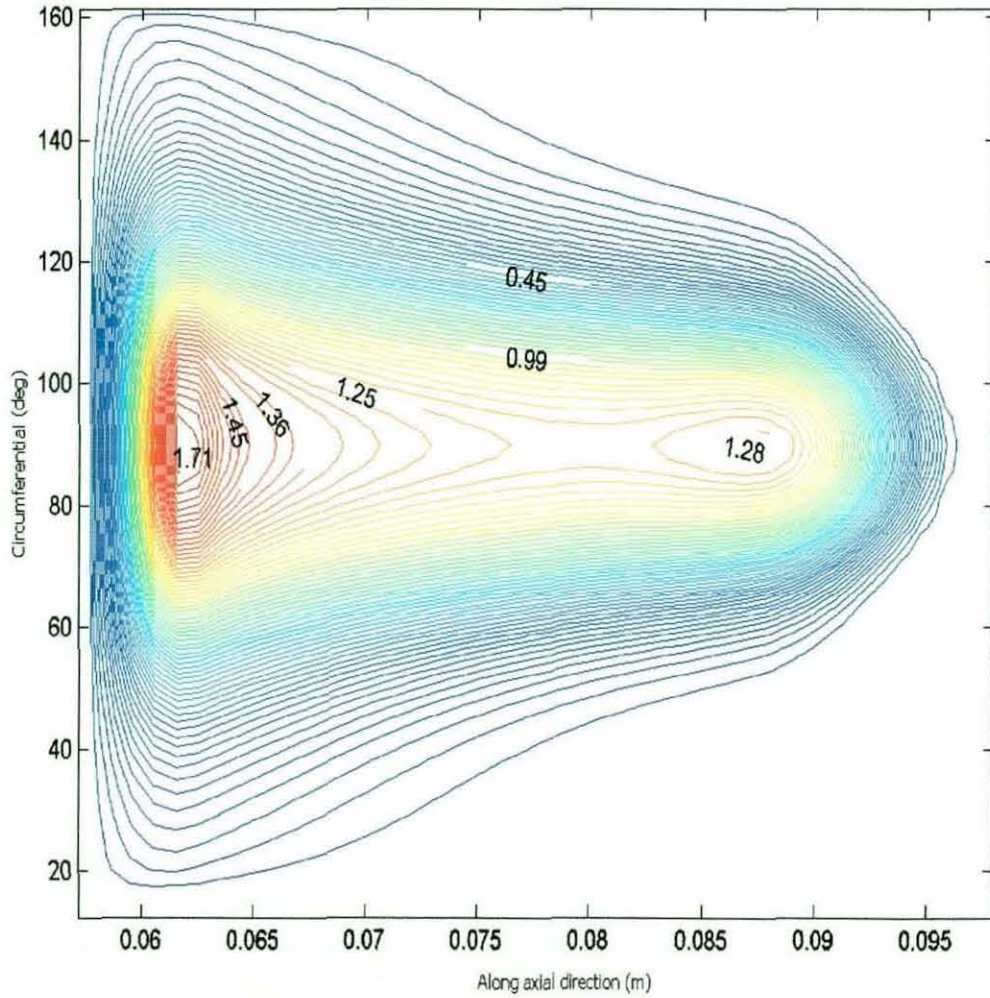
Figure 6.17: Isobaric pressure plot at the position of maximum combustion pressure along major thrust side
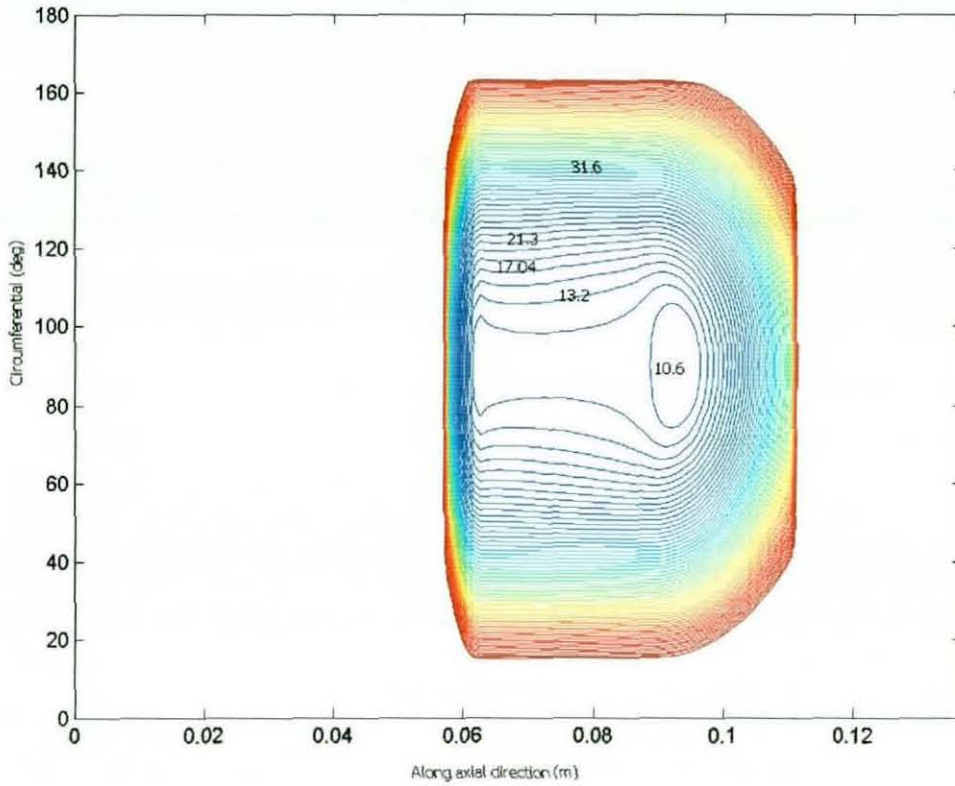
Figure 6.18: Oil film contour at the position of maximum combustion pressure along major thrust side

Al-Samieh and **Rahnejat** (2002) and **Dowson** and **Wang** (1994) have shown that in the initial rigid body approach of contiguous solids in contact the film thickness reduces in-line with hydrodynamic regime of lubrication, and it only increases in thickness when the inertial forces are large enough to cause an elastic squeeze film effect, which deforms the contacting surfaces to create a squeeze caving effect. Such is not the case in the conformal contact of the piston skirt to cylinder liner investigated in this chapter.

6.4 Closure

The main conclusion of the transient analysis is the reaffirmation of the findings of the quasi static analysis outlined in chapter 5. However, the predictions made with a transient analysis is deemed more accurate due to the inclusion of the effect of inertial dynamics , secondary motions of the piston and the effect of rigid body approach and separation of

203

the contiguous load bearing surfaces. In practical terms, a quasi-static analysis, which is considerably less computing time intensive, would be preferred, particularly where commercial pressures in engine development are paramount such as in the motor sport arena. This would particularly be true, if detailed analysis of surface quality and modification is to be included in the analysis, such as those reported in chapter 5. However, it should be noted that quasi-static analysis is only scientifically justifiable, if the predicted contact load or surface deformation profile is based upon an accurate dynamic contact model. This has led to some simplified solutions, using finite element analysis for deformation profiles, prior to the determination of the pressure distribution that would induce such deformation. There are two problems with this approach. First, the contact load has still to be estimated for the finite element analysis, and the analysis in chapter 3 indicates the crudity of this approach (see work by **Goenka** and **Meenik** (1992), **Dursunkaya** and **Keribar** (1992) and **Offner** and **Priebsch** (2000).). Second, the investigations in this thesis has shown that the prevailing regime of lubrication is hydrodynamic, iso-viscous rigid in most instances, with little deformation in other instances. Therefore, determination of pressures, based on contact deformation rather than precise rigid body inertial dynamics appears to be inappropriate. Finally, to determine contact deformation using finite element would necessitate a considerable mesh density or one that would re-mesh the contact domain as the boundary conditions alter due to piston primary and secondary motions. Such undertakings makes the computational time in this approximate methods comparable to a full transient analysis reported here with the added disadvantage of embodied assumptions that are not made in the current analysis.

Chapter 7

7.1 Overall Conclusions

The investigations in the thesis have highlighted the complexity of the piston-connecting-rod-crank sub-system dynamics. The problem is multi-variate in nature, drawing upon its multi-disciplinarity. It involves multi-degrees of freedom motion, including translational rigid body dynamics of the piston, which is an unbalanced motion. Although in the current analysis this is a prescribed motion (i.e. kinematic condition), it is affected by the inertial dynamics of the crankshaft system, the elastic distortion of the crank system and the complex power torque, comprising many harmonics. Therefore, the prescribed kinematics of this motion includes many harmonics of engine order, or in other words, multiples of crankshaft rotational speed. The piston is also subjected to small amplitude lateral and tilting motions, which are induced by interactions between it and the cylinder bore, and are referred to as secondary motions. These interactions include direct force and moment loading contributions at contacting surfaces, referred to as the major and minor thrust sides. The contacts are lubricated domains under transient conditions. Therefore, the analysis includes physical disciplines such as tribology, contact mechanics (elasticity), constrained multi-body dynamics and small amplitude vibration.

The complexity of the problem is in combined solution of all the involved phenomena, all of which are non-linear in nature. The solution is in space-time co-ordinates for full transient analysis. This has been carried out in chapter 6. A simpler, but more detailed quasi-static analysis is provided in chapter 5. Both analyses indicate the same overall findings. It is noted that two problems dominate concerns with use of pistons. First, the frictional losses and wear are as a result of conditions that lead to breakdown or diminution of a coherent lubricant film in the load bearing surfaces. Second, large impact forces can contribute significantly to generation of noise in certain localities within the

piston cycle. The thesis is concerned with the former, but the results obtained also give a good pointer for the further investigation of the latter.

All the results obtained point to the dominance of the hydrodynamic regime of lubrication, with relatively low generated pressures in the range of tens of KPa to tens of MPa, distributed over an area (in most instances) that would invalidate the usual Hertzian assumptions. Due to good contact conformity and the aforementioned pressure distributions, the prevailing regime of lubrication is iso-viscous rigid. This is certainly the case in the more unloaded parts of the piston cycle, such as the BDC. Where the speed of entraining motion is significant such as in the mid-cycle of piston motion, a coherent lubricant film can be retained and the frictional losses will be small. Elsewhere, with diminished or ceased entraining motion, the lubricant film thickness would not be sufficient to ensure fluid film lubrication (such as at BDC or TDC), unless the contact load is sufficiently high to cause elastic deformation of contiguous bodies, thereby retaining a fluid film by the squeeze caving phenomenon. However, this mechanism is most potent at high values of pressure, usually encountered in non-conforming contacts. The results of the analyses in this thesis have indicated that such elastohydrodynamic conditions are unlikely in most piston skirt configurations, and that best attained conditions at high combustion pressures only yield small deformation, and little piezo-viscous action, pertaining to the iso-viscous elastic regime of lubrication.

Making the piston skirts out of material of lower elastic moduli, and of hollow construction have shown to marginally improve the elastic nature of such conforming gaps, even at quite high combustion pressures encountered in F1 racing engines. It is, therefore, no wonder that surface modification in terms of inclusion of artificial cavities and grooves in either the cylinder liner or piston surface or both have become a part of the empirical approach for high performing engines. Prior to this approach, and still commonplace in volume manufactured vehicles, profiling of the piston with leading and trailing relief radii were seen (and still envisaged to) improve the lubrication by wedge effect. Although this is true, the main contribution of this approach is during parts of the cycle that significant speed of entraining motion exists. Elsewhere, the effect of profiling

is minimal, simply shifting the edge stress discontinuity to a different region of the contact, but still with insufficient pressure magnitudes to render any noticeable elastic deformation. The thermal distortion of the hollow piston skirt also does not help the situation, as it merely spreads the area of the contact and reduces the generated pressures.

The inclusion of surface features appears to be the right approach to pursue. However, this can be quite complex in nature and an expensive option. The analyses contained in this thesis indicate that inclusion of such features can be beneficial in certain parts of the piston cycle. Much detailed work would be necessary as to the formation, pattern and alignment of such features, but the thesis contains a good start in this direction.

Finally, the results show that the piston skirt lubrication suffers from fundamental starvation problem, particularly if one is to include the effect of the piston oil control ring. If such effect were to be introduced in the current formulation, reported in the thesis, a bleaker picture of inadequate piston lubrication would emerge.

7.2 Achievement of Aims

The thesis has achieved its original aims and objectives, but in the process has arrived at many other important issues which form the basis for the suggested future work. One such issue is the interference conditions between the piston skirt and the cylinder liner, surmised under real running conditions and noted by the thermal distorted conditions in chapter 5. The increased contact contiguity there suggests that far thinner films than those predicted in the current analysis may be prevalent in reality under inlet reversal positions and at relatively low contact loads, such as the BDC, where severe wear patterns are often noted in failed F1 racing engines. This suggests that clearance conditions taken in the thesis represent mostly start-up conditions. The use of a relatively high value of piezo-viscosity index oil, as suggested by the industrial partners of this reported research, and non-inclusion of effect of temperature upon this power index may have led to the non-

emergence of elastohydrodynamic conditions, even at high impact forces. Although, most other studies with lower values of piezo-viscosity, and particularly experimental work, have found the same trends as those indicated in this thesis.

It is also noted that inlet boundary condition may be seriously affected by the inclusion of the oil control ring, within the piston ring-pack. Therefore, it would have been more representative to model the piston skirt to cylinder liner in conjunction with the oil control ring to cylinder liner.

7.3 Contributions to Knowledge

There are various aspects in the analyses carried out in the thesis, which may be regarded as contribution to the current understanding of piston tribodynamic problem. In this section a number of such contributions are highlighted, but these are not regarded as the only contributions made.

The quasi-static analysis carried out in chapter 5 is novel in the sense of its detailed approach, including many key practical features not incorporated in other analyses, hitherto reported in literature and cited in chapter 2. These features include first and foremost the development of a generic contact mechanics model for evaluation of conforming contacts, which is in agreement with that reported by Hashemi and Paul (1979), but never employed for case of pistons, particularly with misaligning conditions, at high impact forces, and with complex three-dimensional geometry. Secondly, the quasi-static analysis includes many practical features not encountered in other literature on the subject, such as detailed surface irregularities and modification features, and with thermal distortion. The analysis, therefore, has been extended to thermohydrodynamics, as well as micro-hydrodynamics, all with high computational mesh densities, and robust methods of solution in space and time domains, including effective influence Newton-Raphson method and linear acceleration integration scheme.

The transient tribo-elasto-multi-body dynamics problem includes physics of motion study from film thickness prediction and secondary motion evaluation of the order of micrometers and minutes of arc to large rigid body dynamics, including simultaneous solution of the contact problem at both major and minor thrust sides. Such a comprehensive solution has not hitherto been reported in literature.

The thesis discusses many aspects of piston dynamics problem, throughout the broad spectrum of vehicle manufacture, with many pertinent practical engineering issues. In particular, it provides solutions for high performance Formula 1 racing engines. This is the first ever comprehensive analysis of piston tribodynamics for this range of engines at very high combustion pressures.

The methodology has also been applied to engine bearings in chapter 5 and compared to solutions for thin shell constructions of these against the column method, indicating the extent of the validity of the latter, while confirming the generic nature of the generalised methodology itself.

7.4 Suggestions for Future Work

As already highlighted above, some salient features of piston require further investigation. These include thermal distortion of the piston and the liner resulting in interference conditions, particularly at low loaded regions. In such narrow conjunctions, may be of the order of tens of nanometre and with particular lubricant rheology (including the use of additives), other kinetic actions due to molecular behaviour may become prominent. **Al-Samieh** and **Rahnejat** (2001) have carried out fundamental study of such conjunctions at very low loads. With ever improving surface quality and at very low loads such actions may become important in future pistons, perhaps for other applications than automobiles (for example in precision mechanisms). It is already

claimed that ester based lubricating fluids improve upon frictional characteristics of piston conjunctions, such as magnetic based fluids. Therefore, a fundamental study of these fluids in conjunction with hydrodynamic action is proposed. Some preliminary research into these effects is being carried out by **Al-Samieh**, **Rahnejat** and **Dowson** for very lightly loaded contacts of molecular smoothness.

The inclusion of tractive action and non-Newtonian fluid behaviour may also be important, although the results obtained thus far indicate this to be less important than has been suggested in some literature. A much more significant issue is contact starvation when a simultaneous solution of piston skirt and oil control ring to cylinder liner would be undertaken. The frictional losses in the ring-pack contacts are likely to be quite significant. A methodological approach to surface modification for high performing high power engines should form the basis of future work. This should include the effect of surface features, their shape, orientation and positioning within the cycle. The analysis should be carried out with the view of optimising such parameters as discussed.

The existing experimental work, mostly based on LIF or capacitance method (see chapter 2) do not show the physics of motion of the lubricant through the contact, which is the cornerstone of piston profiling and skirt construction. It is important to device optical interferometric or spectroscopic methods for precise observation of the contact under controlled laboratory conditions. Such experimental investigations have been carried out in recent years in case of point contact counterformal geometry, for example by **Sugimura** *et al* (1998). These approaches should be extended to the case of conforming contacts.

The close conformance of the results of column method approximation (for the determination of contact deformation) with those of generalised solution paves the way for its use in the case of piston-liner contacts of lower elastic moduli and liners of thin construction. This will reduce the computational time burden and would pave the way for the inclusion of many other features, such as detailed thermal distortion and propagation of elastic waves in thin structures that are not included in the current analyses. If such an

approach is taken, the coincidence of elastic propagating waves with sound pressure waves in the combustion chamber, possibly through either finite element or boundary element analysis can render in-depth study of piston slapping noise.

Reference

Al-Samieh, M.F. and **Rahnejat, H.** (2002): Physics of lubricated impact of a sphere on a plate in narrow continuum to gaps of molecular dimensions. *J.Phys. D: Appl. Phys.*, 35 , pp 2311-2326 .

Al-Samieh, M.F. and **Rahnejat, H.** (2001): Ultra-thin Lubricating Films Under Transient Conditions *J.Phys. D: Appl. Phys.*, 34 , pp 2610-2621 .

Al-Samieh, M.F., Balakrishnan, S. and **Rahnejat, H.** (2001): Transient impact dynamics of ball on a drop of oil. in *452 EUROMECH Conference*, Aberdeen, UK

Andersson, B.S. (1991): Company's perspective in vehicle tribology. *Leeds-Lyon Symposium on Tribology*, Eds. Dowson, D., Taylor, C.M. and Godet, M, Elsevier (Oxford), pp. 503-506

Balakrishnan, S. and **Rahnejat, H.** (2002): Transient elastohydrodynamic lubrication of piston skirt to cylinder liner under combined reciprocating and slapping motions. in 3rd *AIMETA International Tribology Conference*, Salerno, Italy

Barus, C. (1893): Isothermal, Isopiestics and Isometrics relative to Viscosity. *American Journal of Science*, Volume 45, pp. 87

Betts, H. (1997): Offset piston pins in reverse rotation engines. *The Edge*, Engine-tech Inc, Texas, November

Blair, W.L., Hoult, D.P. and **Wong, V.W.** (1990): The role of piston distortion on lubrication in a reciprocating engine. *ASME Journal of Engineering for Gas Turbines and Power*, Volume 112, pp. 287-300

Blok, H. (1965): Inverse problems in hydrodynamic lubrication and design directions for lubricated flexible surfaces. *Proceedings of the International Symposium on Lubrication and Wear*, D. Mester and B. Sternlicht (eds.,), McCutchan, Berkeley, pp. 1-151

Boussinesq, J. (1885): Essai théorique sur l'équilibre des massifs pulvérulents comparé à celui des massifs solides, et sur la poussée des terres sans cohesion. 2nd ed. Brussels

Bovington, C. and **Spikes, H.** (1996): Prediction of the influence of lubricant formulations on fuel economy, from laboratory bench tests. In the proceedings of the International Tribology Conference, pp. 817

Boysal, A. and **Rahnejat, H.** (1997): Torsional vibration analysis of a multi-body single cylinder internal combustion engine model. *Journal of Applied Mathematical Modelling*, 21, pp. 481-493

Bremer, R.C. (1979): A practical treatise on engine crankshaft torsional vibration control. *SAE Transactions*, Pap. No. 790763

Brewe, D. and **Hamrock, B.J.** (1982): A simplified solution for stresses and deformations. *Journal of Lubrication Technology*, Volume 105, pp. 171

Brown M.A., McCann, H. and **Thompson, D.M.** (1993): Characterization of the oil film behaviour between the liner and piston of a heavy duty diesel engine. Tribological Insights and Performance Characteristics of Modern Engine Lubricants, SAE/SP-93/996/932784

Cameron, A. (1970): Basic Lubrication Theory. Longmans Group Ltd., London, ISBN 0-582-44479-9

Chance, M.A. (1967): Analysis of time-dependent of multi-freedom mechanical systems in relative coordinates. *ASME Journal of Eng. Industry*, No. 89, pp. 119-125

Christensen, H. (1961): The oil film in a closing gap. *Proceedings of the Royal Society*, Volume A-266, pp. 312-328

Christensen, H. (1970): Elastohydrodynamic theory of spherical bodies in normal approach. *Transactions of ASME Journal of Lubrication Technology*, Volume 92 (1)

Ciulli, E. (1992): A review of internal combustion losses. Part 1: Specific studies on the motions of pistons, valves and bearings. *Proc. Institution of Mechanical Engineers Part D*, Volume 206, pp. 223-226

Crouch, R.F. and **Cameron, A.** (1961): Viscosity-temperature equations for lubricants. *Journal of Institute of Petroleum*, Volume 47, pp. 307-313

Cusano, C. and **Wedeven, L.D.** (1982): The effect of artificially - produced defects on the film thickness distribution in sliding EHD point contacts. *Transactions of the ASME. Journal of Lubrication*, Vol. 104.

Dowson, D. and **Higginson, G.R.** (1959): A numerical solution to the elastohydrodynamic problem. *Journal of Mechanical Eng. Science*, Part 1, Volume 6

Dowson, D. and **Higginson, G.R.** (1960): The effect of material properties on the lubrication of elastic rollers. *Journal of Mechanical Eng. Science*, Volume 2

Dowson, D., Higginson, G.R., and **Whittaker, A.V.** (1962): Elastohydrodynamic lubrication: a survey of isothermal solutions. *Journal of Mechanical Eng. Science*, Volume 4

Dowson, D. and **Jones, D.A.** (1967): An optical-interference method of measurement of time-dependent elastohydrodynamic film profiles. *Rep. 3 Symposium on Experimental*

Methods in Tribrobology, Proceedings of the Institution of Mechanical Engineers, Vol. 182 (3G)

Dowson, D. (1968): <u>Tribology.</u> Cambridge University Press, Cambridge

Dowson, D., Taylor, C.M. and **Godet, C.M.** (1983): Tribology of Reciprocating Engines. *9th Leeds-Lyon Symposium on Tribology* (Butterworth, Oxford), pp. 348

Dowson, D. and **Wang, D**. (1994): An Analysis of the Normal Bouncing of a Solid Elastic Ball on an Oily Plate. *Proc. 6th Nordic Symposium on Tribology*, Volume 1, pp. 85-101

Dowson, D. (1995): Elastohydrodynamic and micro-elastohydrodynamic lubrication. *WEAR*, Elsevier Sciences S. A., Volume 190, pp. 125-138

Dursunkaya, Z. and **Keribar, R.** (1992): Simulation of secondary dynamics of articulated and conventional piston assemblies. SAE paper No. 920483

Dursunkaya, Z., Keribar, R. and **Ganapathy, V.** (1994): A model of secondary motion and elastohydrodynamic skirt lubrication. *Journal of Tribology*, Volume 116, pp. 777-785

Ertel, A.M. and **Grubin, A.N.** (1949): <u>Investigation of Scientific and industrial research.</u> Book 30, *Central Scientific Research Institute for Technology and Mechanical Engineering*, Moscow

Forbes, J.E. and **Taylor, E.S.** (1943): A method for studying piston friction. NACA Wartime Report W-37

Furuhama, S. and **Takiguchi, M.** (1981): Effect of piston and piston ring designs on the piston friction forces in a diesel engine. SAE 810997

Gear, C.W. (1971): Simultaneous numerical solutions of differential-algebraic equations. *Circuit Theory*, Volume 18, pp. 89-95

Gohar, R. and **Rahnejat, H.** (December 1979): Design of Profiled Tapered Roller Bearing. *Tribology International*

Gohar, R. (1974): A Numerical Method for Obtaining the Deformed Shape of the Roll in the Cold Rolling Process. *Journal of Mechanical Engineering Science*, Volume 16

Gohar, R. (1988): Elastohydrodynamics. Ellis Horwood Ltd., Chichester

Golya, S. (2002): Private communication

Golya, S. (2000): Design of a racing piston. MSc. Dissertation, Loughborough University

Goto, T.K. and **Kai, S.** (1990): Development of friction prediction model for high performance engines. *J. Soc Tribology Lubrication Engineers*, Volume 47, pp. 567-573

Graddage, M.J., Czysz, F.J. and **Killinger, A.** (1993): Field testing to validate models used in explaining a piston problem in a large diesel engine. Transactions of the ASME Journal of Engineering for Gas Turbines and Power, Volume 115, pp. 721-727

Greene, A.B. (1969): Initial visualization studies of piston-cylinder dynamic oil film behaviour. Wear, Volume 13, pp. 345

Grubin, A.N. and **Vinogradova, I.E** (1949): Investigation of scientific and industrial research. *Book 30, Central Scientific Research Institute for Technology and Mechanical Engineering*, Moscow

Gupta, G.K. (1974): Dynamic analysis of multi-body systems. *ASME Journal of Engineering Industry*, No. 9, pp. 809-811

Gupta, S. (2002): Elasto-Multi-body Dynamics of Internal Combustion Engines with Thin Shell Elastohydrodynamic Journal Bearings. PhD thesis, Loughborough University

Haddad S.D. Howard D.A. (1980): Analysis of piston slap induced noise and assement of some methods of control in diesel engines. SAE paper No. 800517

Hamrock, B.J. and **Dowson, D.** (1976): Isothermal elastohydrodynamic lubrication of point contacts, Part 1. *Journal of Lubrication Technology*, Volume 98, No. 2, pp. 223-229

Hamrock, B.J., Jacobson, B.O. and **Bergstrom, S.I.** (1987): Measurement of the density of base fluids at pressures to 2.2GPa. *ASLE Transactions*, Volume 30, No. 2, pp. 196-202

Hamrock, B.J. (1994): Fundamentals of fluid film lubrication, McGraw Hill Inc., International Edition

Harris, T.A. (1984), Rolling bearing analysis, 2nd Edition, John Wiley & Sons, Chichester

Hartfield-Wünsch, S.E., Tung, S.C. and **Rivard, C.J.** (1993): Development of bench wear test for the evaluation of engine cylinder components and the correlation with engine test results. Tribological Insights and Performance Characteristics of Modern Engine Lubricants, SAE/SP-93/996/932693

Hayes Reference Manual Series (1992): Reference manual for Ford 1.8L diesel engine. Hayes Reference Series.

Hegazy, S.H. (2000): Multi-body dynamic analysis for assessment of vehicle handling with aerodynamics interactions under transient manoeuvres. PhD thesis, University of Bradford

Herrebrugh, K. (1970): Elastohydrodynamic squeeze films between two cylinders in normal approach. *Transactions of ASME Journal of Lubrication Technology*, April, 292

Hertz, H. (1896): Miscellaneous papers by H. Hertz. Eds. Jones and Schort, Macmillan London

Heydari, M. and **Gohar, R.** (1979): Pressure Distribution on Radially Loaded Rollers. *Journal of Mechanical Engineering Science*, Volume 16

Hofbauer, P. (2002): Advanced Diesel Engines for the EU and US Automotive Markets, The United States Energy Association Energy Forum In Conjunction with the G-8 Ministerial Conference Proceedings, Johannesburg

Hooke, C.J. (1992): The minimum film thickness in lubricated line contacts during reversal of entrainment. *Proc. Institution of Mechanical Engineers Part J*, Volume 206, pp. 337-345

Hou, K., Zhu, D. and **Wen, S.** (1985): A New numerical technique for computing surface elastic deformation caused by a normal pressure distribution. *Journal of Tribology*, Volume 107, No.1, pp. 128-131

Hoult, D.P., Lux, J.P. Wong, V.W. and Billian, S.A. (1988): Calibration of laser fluorescence measurements of lubricant film thickness in engines. *SAE* 881587

Howell-Smith, S. (2002): Private Communication

Inoue, T., Maeda, Y., Takeda, M. and Nakada, M. (1989): Study of transient oil consumption of automotive engine. SAE 892110

Ioannides, E. and **Pareti, G.** (1986): Fatigue life predictions in line contacts with and without edge stresses. *Proc. International Conference on Fatigue of Engineering Materials and Structures, Proc. Institution of Mechanical Engineers*, Volume 1

Jalali-Vahid, D. (2000): Transient analysis of isothermal elastohydrodynamic point contact. PhD thesis, University of Bradford

Jalali-Vahid, D, Rahnejat, H and Jin Z.M. (1997): Elastohydrodynamic lubrication of point contact under combined rolling and squeeze film. H Rahnejat and R Whalley (eds), *Tri-Annual Conference on Multi-Body Dynamics: Monitoring and Simulation Techniques*, Mechanical Engineering Publications, London, ISBN 1-86058-064-5

Jalali-Vahid, D., Rahnejat, H., Jin, Z. M. and Dowson, D. (2001): Transient analysis of isothermal elastohydrodynamic circular point contacts" , *Proc. Instn. Mech. Engrs.*, Vol. 215, Part C: J. Mech. Engng. Sci., pp 1159-1173 .

Johns, P.M. and **Gohar, R.** (1981): Roller bearings under radial and eccentric loads. *Tribology International*, Volume 14, pp. 131

Johns-Rahnejat, P.M. (1988): Pressure and Stress Distribution Under Elastohydrodynamic Point Contacts. Ph.D. Thesis, Imperial College of Science and Technology, University of London

Johns-Rahnejat and **Gohar, R.** (1997): Point Contact Elastohydrodynamic Pressure Distribution and Sub-Surface Stress Field. in H Rahnejat and R Whalley (eds), *Multi-Body Dynamics: Monitoring and Simulation Techniques-II*, Mechanical Engineering Publications, London, ISBN 1-86058-064-5

Johnson, K.L. (1985): <u>Contact Mechanics</u>. Cambridge University Press, ISBN 0521-34796-3

Kelly, P (1999): <u>Multi-body dynamic analysis of engine induced automotive clutch pedal vibration</u>. PhD thesis, University of Bradford

Kelly, P. and **Rahnejat, H.** (1997): <u>Clutch pedal dynamic noise and vibration investigation</u>. in H. Rahnejat and R. Whalley (Eds.) *Multi-body dynamics: monitoring and simulation techniques*, Professional Engineering Publishing (UK), pp. 23-31.

Knoll, G.D. and **Peeken, H.J.** (1982): Hydrodynamic lubrication of piston skirts. *Transaction of the ASME*, Volume 104, pp. 504-509

Kushwaha, M. (2000): <u>Elasto-multi-body dynamics of valve train systems with transient elastohydrodynamic contact conditions</u>. PhD. Thesis, University of Bradford

Lagrange, D.F. (1982): An automotive piston lubrication model. *ASLE Transaction*, Volume 26, pp. 151-160

Larsson, R. and **Höugland, E.** (1995): Numerical simulation of a ball impacting and rebounding a lubricated surface. *Transactions of the ASME Journal of Tribology*, 117, pp. 94-102

Lee, R.T. and **Hsu, C.H.** (1993): A Fast Method for the Analysis of Thermal-Elastohydrodynamic Lubrication of Rolling/Sliding Line Contacts. *WEAR* (Elsevier Sequoia), Vol. 166, pp. 107-117

Lewicki, W. (1955): Some physical aspects of lubrication in rolling bearings and gears. Engineer, Vol. 200

Li, D.F., Rhode, S.M. and **Ezzat, H.A.** (1982): An automotive piston lubrication model. *ASLE Transaction,* Volume 26, pp. 151-160

Liu, K., Xie, Y.B. and **Gui, C.L.** (1998): A comprehensive study of the friction and dynamic motion of the piston assembly. *Proc. Institution of Mechanical Engineers Part J,* Volume 212, pp. 221-226

Love, A. E. H. (1934): A Treatise on the Mathematical Theory of Elasticity, 4th ed. Cambridge, England: Cambridge University Press

Lundberg, G. and **Palmgren, A.** (1947): Dynamic capacity of rolling bearings. *Acta. Polytechnica,* Mechanical Engineering Series, Royal Swedish Academy of Engineering Science, pp. 96

Kannel, J.W. (1965): Methods for determining pressure distributions in lubricated rolling contact. *Transactions of ASLE,* Vol. 8

Ma, M.T., Smith, E.H. and **Sherrington, I.** (1995a): A three dimensional analysis of piston ring lubrication, Part 1: Modelling. *Proc. Institution of Mechanical Engineers Part J,* Volume 209, pp. 1-14

Ma, M.T., Smith, E.H. and **Sherrington, I.** (1995b): A three dimensional analysis of piston ring lubrication, Part 2: Sensitivity analysis. *Proc. Institution of Mechanical Engineers Part J,* Volume 209, pp. 15-27

Mang, T. and **Dressel, W.** (2001): Lubricants and lubrication. Wiley-VCH GmbH, Weinheim, ISBN 3-527-29536-4

March, J.P. and **Croker, M.D.** (1998): Present and future perspectives of powertrain refinement. *IMechE Conf., Transactions on Vehicle Noise and Vibration, London,* pp. 23-40

MDI (1994): ADAMS/Solver – Users reference manual. MDI, Michigan

MDI (2001): Product guide. MDI, Michigan

Mostofi, A. (1981): Oil Film Thickness and Pressure Distribution in Elastohydrodynamic Elliptical Contacts. PhD. Thesis, Imperial College of Science and Technology, University of London

Muskhelishvili, N.I (1963): Some Basic Problems of the Mathematical Theory of Elasticity: Fundamental Equations, Plane Theory of Elasticity, Torsion, and Bending, 4th corr. and augm. ed. Groningen: P. Noordhoff

Nakada, M. (1994): Trends in engine technology and tribology. *Tribology International*, Volume 27, pp. 3-8

Nakamura, S. (1992): Applied Numerical Methods with Software. Prentice-Hall Inc., USA.

Navier, C.L.M.H. (1823): Memoire sur les du mouvement des fluides. *Mem. Académie des Inst. Sciences Fr.*, Volume 6, pp. 389-416

Newmark, N.M. (1962): A method of computation for structural dynamics. *Transaction of ASCE*, 127:1406-35, Paper No.3384

Newton, I. (1687): Mathematical principles of natural philosophy. *Lib. II, Sec. II*, London

Oh, K.P, Li, C. H. and **Goenka, P. K.** (1987): Elastohydrodynamic lubrication of piston skirts. *ASME Journal of Tribology*, Volume 109, pp. 356-362

Okamura, H. (1982): A contribution to the numerical analysis of isothermal elastohydrodynamic lubrication. *Tribology of Reciprocating Engines*, Proc. of the 9th Leeds-Lyon Symposium, Butterwoths, England, pp. 313-320

Okrent, E.H. (1964): Engine friction and bearing wear. The role of elasticity in bearing performance. *ASLE Trans*, No. 7, pp. 147-152

Okubo, M., Kanda, H. and **Yonezawa, T.** (1989): Analysis and reduction of piston slap noise in diesel engines. SAE paper No. 890127

Orlandea, N., Chace, M. A. and **Calahan, D. A** (1977): A sparsity oriented approach to dynamic analysis and design of mechanical systems. *ASME Journal of Engineering Industry*, No. 99, pp. 773-784

Parker, D.A. and **Adams D.R.** (1982): Friction losses in Reciprocating Internal Combustion Engine. IMechE Conference on Tribology: Key to the efficient engine, Mechanical Engineering Publications, pp. 31-39

Hashemi, J. and **Paul, B.** (1979): Numerical determination of contact pressures between closely conforming wheels and rails. *Technical Report No. 8*, Federal Railroad Administration Washington

Petroff, N.P. (1883): Friction in machines and the effect of the lubricant. *Inzh. Zh. St. Petersburg*, Volume 1, pp. 71-140; Volume 2, pp. 227-279; Volume 3, pp. 337-463; Volume 4, pp. 535-564

Phen, R.V., Richardson, D. and **Borman, G.** *et al* (1993): Measurement of cylinder liner oil film thickness in a motored diesel engine. *Tribological Insights and Performance Characteristics of Modern Engine Lubricants*, SAE/SP-93/996/932789

Pirro, D.M. and **Wessol, A.A.** (2001): Lubrication Fundamentals. Marcel Drekker Inc., New York, ISBN 0-8247-0574-2

Offner, G. and Priebsch, H.H. (2000): Elastic body contact simulation for predicting piston slap induced noise in an IC engine. in H Rahnejat and R Whalley (eds), *Multi-Body Dynamics: Monitoring and Simulation Techniques-II*, Mechanical Engineering Publications, London, ISBN 1-86058-253-3

Quinn, T.F.J. (1991): Physical analysis for tribology. Cambridge University Press, Cambridge

Rahnejat, H. (1984): Influence of Vibration on Oil Film in Concentrated Contacts. PhD. Thesis, Imperial College of Science and Technology, University of London

Rahnejat, H. (1998): Multi-body dynamics: Vehicles, machines and mechanisms. Professional Engineering Publishing, Bury-St. Edmunds, U.K.

Reddi, M.M and **Chu, T.Y.** (1970): Finite-element solution of the steady-state incompressible problem. *Transactions ASME, Journal of Lubrication Technology*, Volume 94, pp. 495-503

Roelands, C.J.A. (1966): Correlation Aspects of Viscosity-Temperature-Pressure Relationship of Lubricating Oils. Ph.D. Thesis, Delft University of Technology, The Netherlands.

Reynolds, O. (1886): On the theory of lubrication and its application to Mr. Beauchamp Tower's experiments, including and experimental determination of the viscosity of olive oil. *Phil. Transaction of Royal Society*, London, Volume 177, pp. 157-234

Ryan, R.R. (1989): ADAMS multibody system analysis software. *MDI Technical Publications*, Volume 2

St Venant (1868): Historique abrege des recherches sur la resistance et sur l'elasticite des corps solides.

Safa, M.M.A. and **Gohar, R.** (1986): Pressure distribution under a ball impacting a thin lubricant layer. *Trans. ASME Journal of Tribology*, July, Vol. 108

Schiehlen, W.O. (1990): Multi-body system handbook. Springer-Verlag, Berlin

Shabana, A.A. (1989): Dynamics of multi-body systems. Wiley, New York

Stachowiak, G.W. and **Batchelor A.W.** (2001): Engineering tribology. Butterworth Heinemann, Boston, ISBN 0-7506-7304-4

Stokes, G.G. (1845): On the theories of the internal friction of fluids in motion, and of the equilibrium and motion of elastic solids. *Transaction of Cambridge Philosophic Society*, Volume 8, pp. 287-341

Stolarski, T.A. (1990): Tribology in machine design. Heinemann Newnes, Oxford

Stribeck, R. (1901): Kugellager fur beliebige belastungen. *Z. Ver. Deutsche Ing.*, Volume 45, pp. 73-125

Sugimura, J., Jones, W. R. and **Spikes, H. A.** (1998): EHD film thickness in non-steady state contact conditions. *Trans. ASME, J. Tribology*, Vol. 120, pp. 442-452

Taylor, C.M (1993): Engine Tribology. Tribology Series, Elsevier, Oxford, 26

Taylor, R.I. and **Coy, R.C.** (1996): Improved fuel efficiency by lubricant design: a review. *Proc. Institution of Mechanical Engineers Part J*, Volume 214, pp. 1-15

Taylor, R.I. (1998): Engine friction lubricant sensitivities: a comparison of a modern diesel and gasoline engines. *In Proceedings of the 11th International Colloquium on Industrial and Automotive Lubrication*, Esslingen

Timoshenko, S.P. and **Goodier, J.N.**(1951): Theory of Elasticity. McGraw Hill, New York

Ting, L.L. (1980): Development of laser fluorescence technique for measuring piston ring oil film thickness. *Journal of Lubrication Technology*, Transactions ASME, Volume 102, No. 2, pp 165-171

Toshihide, O., Mamoru, T. and **Yamamoto, M.** (1993): Influence of engine oil viscosity on piston ring and cam face wear. *Tribological Insights and Performance Characteristics of Modern Engine Lubricants*, SAE/SP-93/996/932782

Tower, B. (1883): First Report on Friction Experiments (Friction of Lubricated Bearings). *Institution of Mechanical Engineers Part J*, pp. 632-659

Uras, H.M. and **Patterson, D.J.** (1983): Measurement of piston and ring assembly friction. SAE paper 830416

Wijnant, Y.H. and **Venner, C.H.** (1997): Analysis of an EHL circular point contact incorporating rolling element vibration. *Proc. 23rd Leeds-Lyon Symposium on Tribology*, pp. 445-456

Wedeven, L.D and **Cameron, A.** (1968): A study of elastohydrodynamic lubrication in rolling bearings using optical interference. *Symposium on Experimental Methods in Tribology, Proc. Institution of Mechanical Engineers*, Rep. 15, Volume 3G

Wittenburg, J. (1977): Dynamics of systems of rigid bodies. Teubner, Stuttgart

Wolveridge, P.E. and **Archard J. F.** (1971): The starved lubrication of cylinders in line contact. *Symposium on Experimental Methods in Tribology, Proc. Institution of Mechanical Engineers*, Volume 185, No. 81/71, pp. 1159-1169

Younggren, P.J. and **Schwartz, S.E.** (1993): The effect of trip length and oil type (synthetic versus mineral oil) on engine damage and engine-oil degradation in a driving test of a vehicle with a 5.7L V-8 engine. *Tribological Insights and Performance Characteristics of Modern Engine Lubricants*, SAE/SP-93/996/932838

Zhu, D., Cheng, H.S., Arai, T. and **Hamai, K.** (1992): Numerical analysis for piston skirts in mixed lubrication. Part I: Basic modeling. *Journal of Tribology, Transactions of the ASME*, Vol. 114, No. 3, pp. 553-562

Zhu, D., Cheng, H.S., Arai, T. and **Hamai, K.** (1993): Numerical analysis for piston skirts in mixed lubrication. Part I: Basic modeling. *Journal of Tribology, Transactions of the ASME*, Vol. 115, No. 1, pp. 125-133

Zienkiewicz, O.C. and **Taylor, R.L.** (2000): The finite element method Vol. 1, 5th Ed., Butterworth Heinnemann, Oxford

Internet references

Environmental Protection Agency: http:// www.epa.gov

Honda: http:// www.honda.com

Hunters Betts: http:// www.aera.org/Members/EngineTech

Inventors: http:// inventors.about.com/library/inventors/blcar.htm

McLaren: http:// www.mclaren.co.uk

Mercedes: http:// www.mercedes-benz.de

University Karlsruhe: http:// iamlasun8.mathematic.uni-karlsruhe.de

Visteon : http:// www.visteon.com

Volkswagen: http:// www.volkswagen.de